UNIVERSITY OF SOUTHAMPTON

FACULTY OF ENGINEERING, SCIENCE AND MATHEMATICS

INSTITUTE OF SOUND AND VIBRATION RESEARCH

WAVE PROPAGATION IN RAILWAY TRACKS AT HIGH FREQUENCIES

by

Jungsoo Ryue

Thesis for the degree of Doctor of Philosophy

March 2008

UNIVERSITY OF SOUTHAMPTON

ABSTRACT

FACULTY OF ENGINEERING, SCIENCE AND MATHEMATICS
INSTITUTE OF SOUND AND VIBRATION RESEARCH

Doctor of Philosophy

WAVE PROPAGATION IN RAILWAY TRACKS AT HIGH FREQUENCIES

by Jungsoo Ryue

In order to understand long range wave propagation in railway tracks, it is required to identify how far vibrations can travel along a rail. To answer this question, the main wave types that propagate along rails and their attenuation characteristics are determined as a function of frequency. In this work the effective wave types and their decay rates are investigated for frequencies up to 80 kHz.

Two numerical methods, the conventional finite element method and the wave-number finite element method, are utilized to predict the predominant wave types and their decay rates for a rail on a continuous foundation. From these simulations, the waves that are measurable on various regions of the rail cross-section are identified. Also, to improve the simulated results, the frequency dependent damping loss factor of a rail has been measured up to 80 kHz on several short rail samples. The predominant wave types predicted have been validated by experiments performed on a short test track. The measured group velocities present very good agreement with the predicted ones so that it is identified which wave types predominantly propagate in various regions of the rail cross-section. Another measurement has been performed on an operational track to validate the simulated decay rates. In this experiment, train-induced rail vibrations were acquired for several trains running over a long section of rail. The measured decay rates are presented for comparison with the output of the simulations and good agreement is found between them.

A feasibility study is carried out of wave reflection and transmission due to cracks in rails. These are estimated for various cracks of progressively larger size by means of numerical simulation. Through this simulation, the relative efficiency of various incident and reflected waves for detecting defects in rails is determined.

Contents

List of Tables

ACKNOWLEDGEMENTS

I would like to thank deeply my supervisors, Professors D. J. Thompson and P. R. White, for their solid and continual guidance and support throughout the course of this research work. My greatest gratitude should go to them.

I am also very grateful to the sponsor of this research project, Balfour Beatty Rail Technologies, and my industrial supervisor, Dr. D. R. Thompson, for giving much valuable advice in practical points of view.

I wish to acknowledge to Dr. Chris Jones and Dr. Tim Waters for their advice and opinions on this work. Also I really thank Dr. C. M. Nilsson for his advice on numerical problems.

I would like to share my pleasure with my family in Korea. I also thank many Korean colleagues who gave me great comfort and consolation.

I dedicate this thesis to my wife who has always supported and encouraged me with her endless love.

List of Symbols and Abbreviations

A list of symbols is presented, although most of them are defined in the text. Vectors and matrices are denoted by bold letters.

*	complex conjugate
$\otimes$	Hadamard product, an element-wise multiplication of two matrices
$\|\ \|$	norm of vector
diag( )	vector created from its argument's diagonal terms
^{T}	transpose
^{H}	Hermitian transpose (transpose and complex conjugate)
$\mathbf{a}$	wave amplitude vector
c	phase velocity
c_g	group velocity
c_L	phase velocity of longitudinal wave
f	frequency
$\mathbf{f}_b$	blocked force
g	acceleration of gravity
j	unit imaginary number
k	stiffness
k_p^d	dynamic stiffness of rail pad
$k_p^{'d}$	damped dynamic stiffness of rail pad
l_x	half length of finite waveguide structure
h	thickness of structure
n_j	number of nodes on region j of FE or WFE model
$_p$	subscript for rail pad
$_r$	subscript for rail
r_{ij}	power reflection coefficient of wave i for an incident wave j
$\mathbf{s}$	relation between stress and strain
t	time
t_{ij}	power transmission coefficient of wave i for an incident wave j
u, v, w	displacements in Cartesian coordinates
x, y, z	Cartesian coordinates

A	cross-sectional area
$\mathbf{A}$	matrix used in WFE analysis
$\mathbf{D}_C$	dynamic stiffness matrix of combined SSE/FE model
$\mathbf{D}_f$	dynamic stiffness matrix of FE model
$\mathbf{D}_F$	condensed dynamic stiffness matrix of FE model
$\mathbf{D}_S$	dynamic stiffness matrix of WFE model
E	Young's modulus
E'	complex Young's modulus
$\mathbf{E}(x)$	diagonal matrix consisted of $e^{-j\kappa x}$ for all eigenvalues of κ
$\mathbf{E_I}$	$= \int_{-l_x}^{l_x} \text{diag}(\mathbf{E}(x))\text{diag}(\mathbf{E}(x))^T dx$
F	force at boundary
$F(\ )$	function of its argument
$\mathbf{F}$	external force vector
G	shear modulus
I	wave incident
$\mathbf{I}$	identity matrix
$\mathbf{K}$	$= \mathbf{K_2}(-j\kappa)^2 + \mathbf{K_1}(-j\kappa) + \mathbf{K_0}$
$\mathbf{K_2}$, $\mathbf{K_1}$, $\mathbf{K_0}$	stiffness matrices of WFE model
$\mathbf{K_d}$	damped stiffness matrix of WFE model, $= \mathbf{K}(1 + j\eta)$
$\mathbf{K}_{fe}$	stiffness matrix of FE model
L	length of FE model
$\mathbf{M}$	mass matrix of WFE model
$\mathbf{M}_{fe}$	mass matrix of FE model
N	number of degrees of freedom in WFE model
N_s	number of nodes on rail surface of FE or WFE model
$Q_{z,j}$	energy ratio for the z directional deformation in region j of FE or WFE model
R	waves reflected
S	contacting area between rail and foundation in FE model
T	waves transmitted
$\mathbf{V}(x)$	displacement of cross-section at x
$W(x,t)$	energy carried by waves propagating in space and time
$\mathbf{W}$	nodal displacement vector at boundaries
X_m	full scale level of A/D converter

β	material damping parameter input to ANSYS
δ	step size of quantifier in A/D converter
ϵ	strain
ε_{mn}	matrix used in WFE analysis
ζ_n	modal damping ratio of the n^{th} mode of FE model
η	damping loss factor
η_n	modal damping loss factor of the n^{th} mode of FE model, $= 2\zeta_n$
κ	wavenumber
κ_d	damped wavenumber
κ_+	wavenumber travelling in the positive x direction
κ_-	wavenumber travelling in the negative x direction
λ	wave length
ν	Poisson's ratio
ρ	density
$\boldsymbol{\sigma}$	stress
σ_n	imaginary part of $\omega_{d,n}$
χ, ψ, ξ	displacements of cross-section in Cartesian coordinates
ω	angular frequency
ω_n	natural frequency of the n^{th} mode of FE model
$\omega_{d,n}$	damped natural frequency of the n^{th} mode of FE model
Δ	decay rate in dB/m
Δf	increment of discrete frequency
$\Delta\kappa$	increment of discrete wavenumber
Θ	matrix used in WFE analysis
Π^j_{inc}	power contained in incident wave j
Π^i_{ref}	power contained in reflected wave i
Π^i_{trn}	power contained in transmitted wave i
$\boldsymbol{\Phi}$	matrix consisted of all eigenvectors of $\tilde{\boldsymbol{\Phi}}$
$\boldsymbol{\Phi}_{fe}$	eigenvector of FE model
$\tilde{\boldsymbol{\Phi}}$	eigenvector of WFE model (mode shape of cross-section)
$\tilde{\boldsymbol{\Phi}}_+$	eigenvector of WFE model for κ_+
$\tilde{\boldsymbol{\Phi}}_-$	eigenvector of WFE model for κ_-
$\tilde{\boldsymbol{\Phi}}_s$	eigenvector at nodes on rail surface of WFE model

$\tilde{\mathbf{\Phi}}_L$	left eigenvector of WFE model
$\tilde{\mathbf{\Phi}}_R$	right eigenvector of WFE model
$\tilde{\mathbf{\Psi}}$	$= -j\kappa\tilde{\mathbf{\Phi}}$

A/D	analogue to digital
DS	dynamic stiffness
EMAT	electromagnetic acoustic transducer
FE	finite element
PZT	piezoceramic transducer
SE	spectral element
SFE	spectral finite element
SSE	spectral super element
WFE	wavenumber (or waveguide) finite element

Chapter 1

Introduction

1.1 Background

The structural integrity of rails is a major concern for the railways of the world. Even though there are several rail inspection techniques and rail inspections are performed routinely, they do not yet give the desired reliability. The various types of NDE (Non-Destructive Evaluation) rail inspection techniques that are currently used or could be used in the future are outlined in ref. [1].

Ultrasonic waves have been used for the inspection of rails for many years. The most commonly used ultrasonic testing technique is pulse-echo, where sound in the megahertz frequency range is introduced into a test object and reflections (echoes) returned from internal imperfections or from the geometrical surfaces are analysed. This conventional method, however, has some drawbacks. They are associated with the attenuation characteristics and limited volumetric coverage. Conventional ultrasonic waves with wavelengths of a few millimetres can travel only a few hundred millimetres in any direction within a rail. Hence these ultrasonic waves can only be used to inspect the region of a rail close to the transducer location. Moreover this testing is limited by the speed of inspection. Dedicated ultrasonic inspection trains which have onboard devices can inspect the two rails with one or several ultrasonic probes at train speeds of 50 to 100 km/h [2, 3].

On the other hand, the use of relatively low frequency ultrasonic waves, sometimes called 'guided waves', has been attempted recently for long range inspection of

rails. A brief discussion on the history, recent application and potential of this type of testing is presented in ref. [4]. The application of these waves for rail inspection is discussed in refs [5–10]. In the low ultrasonic frequency range, a rail becomes an effective waveguide due to the presence of a boundary, i.e., the rail surface, which traps the wave energy and makes it propagate efficiently along the rail. Hence these waves, in the tens of kilohertz frequency range, enable a large area of structure to be tested from a single transducer position, thereby avoiding the time consuming scanning required by conventional ultrasonic methods. These waves are particularly sensitive to transverse vertical defects since they travel along a rail. A further advantage is that at the frequencies used, attenuation which occurs in weld material is very low and hence weld material can be readily penetrated and tested. These benefits make this testing using relatively low frequency ultrasonic waves very attractive. This technique is used effectively to inspect pipe systems but application to rails has been limited because of the presence of many possible wave modes in rails, most of which are dispersive. Also there has been little study on the wave propagation along rails regarding the effect of the rail support and damping loss factors of a railway track. Furthermore, it has not yet been clearly specified in the literature which wave types and which frequency range would be most effective for the propagation over long distances in the railway track. It is apparent that the answers to these questions are highly related to the sources of damping in the track.

The work in this thesis aims to investigate the propagation of waves in railway tracks in the tens of kilohertz frequency range. It focuses towards addressing the following fundamental question that needs to be answered before anything else. *How far along a rail can vibration travel?* This simple but essential question requires three specific answers: in which wave type, at which region of a rail cross-section and at which frequencies is it most effective. The frequency range considered in this study spans up to 80 kHz based on the findings in ref. [11]. In fact, at higher frequencies, e.g., around 80 kHz, a railway track may behave less clearly as a waveguide, because the wavelength becomes shorter than the dimensions of the rail cross-section. For instance, the wavelength of a shear wave in steel will be about 38 mm at 80 kHz, which is about a half of the width of the railhead and a quarter of the rail height. Moreover, as frequency increases it can be anticipated that spatial attenuation will increase. The frequency range of interest is therefore unlikely to extend beyond 80 kHz and will probably be limited to less than this. Nevertheless, in this thesis

the frequency range is chosen simply by following the findings in the literature, discussed in Chapter 2.

1.2 Structure of the thesis

As a first step towards the goals established above, in Chapter 3, the conventional finite element method is employed to analyse the rail. Using this method, a relevant cross-sectional model is specified and then a track model is set up as a rail on a continuous foundation. To simulate the waves in an infinite rail, a short length of the track is considered with symmetric and/or antisymmetric boundary conditions at both ends of its length. Modal analysis for this short length of track will produce natural frequencies and their mode shapes of the rail section. These results are used to obtain the frequency-wavenumber relation and the deformation profiles of each wave. The FE analysis results also exhibit the effect of the damping in the track model on propagating waves in terms of modal damping. These can also be converted into the form of a spatial decay rate.

Although the dispersion relations and decay rates are predictable using FE analysis, it has several drawbacks for dealing with wave propagation in structures. So, a two-dimensional finite element method called the wavenumber finite element (WFE) method is used as an alternative to the conventional FE method in Chapter 4. This method only requires cross-sectional modelling of a railway track and imposes a significantly smaller computational burden than the classical FE method, both in terms of time and memory. Since the increment of discrete wavenumber can be specified arbitrarily, unlike the FE method, this method enables dispersion curves, group velocities and decay rates to be evaluated on a finer grid. The results produced by the WFE method will be compared initially with those simulated by the FE method. Furthermore, since dynamic responses are usually measured normal to the rail surface, waves that are measurable at various positions on the rail surface are identified using the energy distributions around the rail surface quantified from the predicted displacements.

In the FE and WFE simulations, the structural damping loss factor of a rail is assumed initially simply as a constant value for the entire frequency range. However, damping is expected to be a frequency-dependent quantity rather than a constant.

So, in order to improve the simulation results, in Chapter 5 structural damping loss factors are measured up to 80 kHz from impact hammer tests conducted on rail samples of three different types. Then improved predictions of the decay rates are found using the WFE method with the measured damping loss factors for the rail.

In order to validate the predominant wave types simulated, two experiments are conducted up to 80 kHz on a test track, of approximate length 32 m, using different input excitation schemes: an impact hammer and piezoceramic transducers (PZTs). Time-frequency analysis is applied to the measured data in order to visualize dispersion relations of the measured waves. The results are compared with the simulated ones in terms of the group velocity and the various wave types are identified. All these experimental results are described in Chapter 6.

To be able to validate the simulated decay rates, it is necessary to carry out a measurement over a longer section of rail. One such experiment is carried out in Chapter 7, on an operational track, to extract decay rates over a long section of rail. Also, from a practical point of view, it is apparent that there is great merit if operational trains can be used as excitation sources for the long range inspection of a rail instead of using external excitation. Hence, to determine whether train excitation can be used or not, its frequency characteristics should be identified in an operational railway. This will show how effectively the high frequency waves are generated by a running train and how they propagate in a rail, particularly between 20 kHz and 40 kHz where the minimum decay rates are found to occur. In this experiment rail vibrations are measured for seven trains at three different positions on the rail cross-section. These measured data will allow visualization of how far waves can travel along a rail and at which frequencies. Finally, the measured decay rates are compared with the simulated ones produced by WFE analysis.

By using waves which propagate furthest in rails as incident waves, it may be achievable to detect rail defects at long distances by monitoring their reflected and/or transmitted powers. In Chapter 8, as a feasibility study, wave reflection and transmission due to cracks in rails are estimated by means of a newly developed numerical method, named the combined spectral super element and finite element (SSE/FE) method. In the literature, a similar method, called the combined spectral element and finite element (SE/FE) method, has been used to investigate local non-

uniformities in beam structures at relatively low frequencies. This SE/FE method is extended here to more complex railway track structures by introducing the SSE method, in place of the SE method. To check the reliability of this method, numerical errors occurring are examined for two limiting cases, i.e., homogeneous and broken rails, in terms of the power conservation. Then, for various cracks of progressively increasing size, power reflection and transmission characteristics are estimated by the combined SSE/FE method. Through this simulation, the relative efficiency of the incident and reflected waves chosen are discussed for detecting defects in rails.

Finally, the conclusions drawn from each chapter are summarized in Chapter 9 and some possible further work is briefly suggested.

1.3 Summary of original contribution

The original contributions of this thesis are:

- prediction of dispersion relations for the waves propagating along the rail at frequencies up to 80 kHz by means of the FE and WFE methods, including the contribution of the rail pad as a continuous foundation (Chapters 3 and 4)
- prediction of the decay rates for each individual wave propagating along the railway track up to 80 kHz by using FE and WFE analyses (Chapters 3 and 4)
- prediction of waves that are measurable on the rail surface by introducing a new metric which quantifies deformation energies at several regions of the rail cross-section (Chapter 4)
- identification of the contribution of the damping in the rail and rail pad to the decay rates of each individual wave (Chapter 4)
- prediction of the effect of foundation stiffness on each wave's decay rate (Chapter 4)
- measurement of damping loss factors of rails as a function of frequency up to 80 kHz (Chapter 5)

- identification of the most effective wave types, decay rates and corresponding frequency ranges for long range wave propagation in rails (Chapters 6 and 7)
- measurement of train-induced rail vibration on an operational track for several running trains up to 80 kHz (Chapter 7)
- development of the SSE for semi-infinite waveguide structures (Chapter 8)
- development of the combined SSE/FE method to investigate wave propagation in rails with local non-uniformities (Chapter 8)

Chapter 2

Literature Review

2.1 Wave Propagation in Railway Tracks

In order to understand the dynamic behaviour of a railway track, above all appropriate track models are required. Various theoretical models for the dynamic behaviour of railway track are outlined in ref. [12]. There are several difficulties in dynamic track modelling. The rail itself has a complex geometry which causes coupling phenomena between the various propagating waves. At low frequency, below 500 Hz, a rail can be considered as an Euler-Bernoulli beam. However such a model is no longer adequate for the response at higher frequencies as the shear deformation of the rail becomes increasingly important. The Timoshenko-beam model, involving shear deformation, expands the reliable frequency range only up to around 2 kHz for the vertical and longitudinal waves. The most important hypothesis of these beam theories is that the cross-section remains undeformed while undergoing vibrational movement. This hypothesis is not valid at higher frequencies. Moreover the presence of supports, i.e., rail pads, sleepers and ballast, etc. (Fig. 2.1) which are also periodically spaced along the track, makes it more difficult to model.

In terms of the generation of noise by a train in the frequency range 100 to 5000 Hz, useful theoretical models are a 'continuously supported beam model' and 'periodically supported beam model', using Timoshenko-beam theory for the rail [13]. The support in these models consists of a resilient layer (the rail pads), a mass layer (the sleepers) and a second resilient layer (the ballast). At higher frequencies, however, the rail cross-section deforms and many higher order wave types exist in the

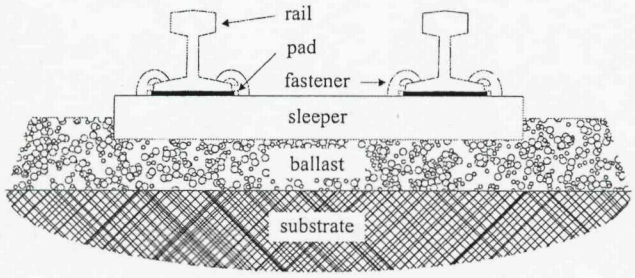

Fig. 2.1. Components of a railway track.

rail. Experimental investigations show that the cross-section deforms significantly above about 1500 Hz [14]. This cross-sectional deformation has to be taken into account for an accurate evaluation of the dispersion properties. A model including cross-sectional deformations was developed by Thompson [14] with the rail standing on a continuous support. Thompson considered an infinite rail as a periodic structure of arbitrary period and introduced the short periodic segment made up from finite elements. The advantages and disadvantages of these three track models were compared in ref. [13].

For the purpose of long range track inspection, Rose *et al.* [7, 11] suggested, based on experimental work, that the frequency range up to 80 kHz should be considered and that the most effective range is between 40 kHz and 80 kHz. Since no exact theoretical model exists for wave propagation in complex cross-sectional profiles, such as a rail, covering the frequency range up to tens of kilohertz, the conventional finite element (FE) method was employed to predict the mode shapes and dispersion relations for a free rail [15]. The simulation results showed that several tens of different wave types are sustained within this frequency range, making the dispersion curves very complicated. Because of that, there has been little work aimed at identifying effective wave types and decay rates of waves propagating along railway tracks.

Although the conventional FE method is a useful tool, it has several drawbacks for dealing with wave propagation in structures. As well recognised already, this FE method requires very large models for high frequency analysis. Hence it costs long computing times and large computing facilities. Furthermore, very considerable manual post-processing has to be performed to build dispersion curves from the FE analysis results. That is required because each natural frequency and the

corresponding mode shape obtained from FE analysis needs to be checked in order to determine their wavenumbers. Another disadvantage is that the group velocities can only be roughly estimated from the discrete dispersion curves by means of the finite difference approximation between two discrete points, which can introduce significant errors, as will be seen in Chapter 3. Due to the difficulties stated above, repeated use of this conventional FE method for any input parameter changes should be avoided because the same time-consuming process would be required for each analysis.

A number of methods to reduce the number of degrees of freedom and increase the computational efficiency have been presented in the past, for example, the spectral finite element method [16–18], the dynamic stiffness method (or spectral element method) [19], spectral super element method [20] and methods using a periodic structure theory [14, 21, 22].

For infinite length waveguide structures, a two-dimensional finite element technique for modelling the wave propagation was introduced first by Aalami [23] as an alternative to the conventional FE method. In this method, an exact wave solution was utilised for the propagating direction instead of making finite element meshes and using shape functions along this direction. Two decades later Gavric [24] applied this method for computing the dispersion curves and mode shapes in undamped rails up to 6 kHz and good agreement was found between the predicted and experimental results. This technique is referred to in the literature as the wavenumber (or waveguide) finite element (WFE) method [25–27][1]. One of its great advantages is that different wave types are readily identified and can be analysed directly in terms of their wavenumbers, enabling a physical interpretation of the wave propagation in the structure under investigation.

For high frequency analysis, this method has been used by several authors for track modelling, because it can compute waves of very short wavelengths. Cawley and Wilcox *et al.* [6, 8, 10] used this method to predict dispersion curves and wave modes up to 50 kHz for the purpose of rail testing. Also, Hayashi *et al.* [28] predicted dispersion relations for a free rail up to 100 kHz. Among multiple propagating

[1] In [28, 29] it is also called the semi-analytical FE (SAFE) method.

waves, they highlighted waves that have large deformations at the rail head when a point load is applied at the top of the rail head. Recently, Finnveden [27] formulated group velocities theoretically for each wave solution obtained by this method. This is a significant step towards application of this method to predict the decay rates because the group velocity is one of the crucial quantities required for it. However, most of the previous work was confined to analysing dispersion relations and group velocities in undamped free rails.

Most recently, Bartoli *et al.* [29] presented decay rates for a damped rail, without considering its foundation, up to 50 kHz using this method. In this prediction, they introduced an energy velocity, rather than the group velocity, to obtain decay rates for damped media because the definition of group velocity is not valid in the damped case. However, since they disregarded the contribution of the rail pad which has a large damping, the predicted decay rates seem to be unrealistic from a practical point of view. Furthermore, they failed to describe the behaviour of each wave with respect to frequency and did not present which type of waves propagate furthest along the rail.

For damped waveguide structures, Nilsson [26] derived damped wavenumbers of individual propagating waves using this WFE method to predict an input power flowing into the structure. In this formulation, damped wavenumbers are easily found from the damping loss factor and group velocity that is obtained from the undamped case. In this thesis, decay rates are evaluated from damped wavenumbers of individual waves, as presented in ref. [26].

2.2 Experimental Analysis of Wave Propagation in Rails

While the various track models and numerical methods exist to predict the vibration propagating in rails, experimental studies are particularly challenging due to the multimodal and dispersive behaviour of the waves at high frequencies.

In terms of wheel-rail rolling noise, Vincent and Thompson [30] have measured accelerances and decay rates on several operating tracks over the range 100 to

5000 Hz by means of impact excitation using an instrumented hammer. These experimental results were compared with the simulation results presented in ref. [13]. This comparison showed that the track model with a continuous support gives a good agreement with measured results at higher frequency. That is because the periodicity effect of a discrete support does not occur strongly at high frequencies. In addition, Thompson [31] developed an experimental analysis technique, based on the Prony method [32], which can produce dispersion curves and decay rates of propagating waves by using measured data taken on track. However, this method is less suitable for the wave propagation extending up to 80 kHz because it requires multiple, equally spaced measurement points along the rail and around the cross-section. Moreover the spacing of the measurement points along the rail and the number of the measurements in the cross-section limit the highest measurable frequency and the maximum number of measurable modes.

As an alternative experimental method for the high frequency region, Lanza di Scalea and McNamara [9, 33] applied an impulse excitation to the rail and measured the direct and echo signals reflected from the opposite end of a 7.3 m long rail section. Comparing the direct and reflected signals, they extracted group velocity curves and the frequency-dependent attenuation up to 50 kHz for a free rail using time-frequency analysis. However, the contribution of the rail fastening, particularly the rail pad, to the decay rates and the possibility of energy loss or mode conversion resulting from the reflecting end of the rail were not considered in this experiment.

Hayashi *et al.* [28] measured phase velocity diagrams up to 100 kHz on a free rail of about 2.4 m length. In this experiment they used a toneburst type contact transducer having a 50 kHz centre frequency as an exciter and a non-contact air-coupled transducer of 60 kHz centre frequency as a receiver. Waveforms were collected at 200 points in 10 mm increments along the rail in order to cover frequencies up to 100 kHz and a two-dimensional Fourier transform technique was applied. However, since the transducers used in this experiment have a narrow operating frequency range, the measured results seem to be less reliable at frequencies away from their centre frequencies. Also this measurement technique is not suitable for practical application because it requires a large number of measurement points. Rose *et al.* [7, 11] suggested, based on their experimental work, that waves can travel more than 2 km along the rail within the frequency range between 40 kHz and 80 kHz.

However, they did not clearly specify the decay rates of the waves in this frequency range. Instead, they measured waveforms at the top of the rail head at various distances along a free rail of length 10.7 m by using 60 kHz EMATs (electromagnetic acoustic transducers) [7]. From this measurement they found a decay rate of about 0.56 dB/m at around 60 kHz. However, detailed information on the wave types measured and the contribution of the rail foundation to decay rates in the high frequency region is lacking in both these previous studies.

Wilcox *et al.* [6] developed equipment using a transducer array mounted along the length of the rail, as well as around the perimeter of the rail cross-section, to excite and detect desired wave modes effectively for rail inspection. Gurvich *et al.* [34] also developed an ultrasonic flaw detector, which has a line array of 12 probes placed along a rail, and is used with a waveguide echo-pulse method to detect rail defects over long distances. Both of them used frequency ranges up to around 50 kHz and 60 kHz for their measurements. However, they did not present clearly what type of waves are most efficient for their purpose and how far they can propagate along the rail.

Rose and Avioli [35] carried out feasibility studies on broken rail detection by using the waves in the tens of kilohertz frequency range. In this experiment, they used waves excited by a train moving down the test track and compared time signals measured on the web close to the rail break. However, they focused only on whether these waves are applicable for broken rail detection and did not investigate the features of the waves.

As described previously, there are several tens of different waves propagating along rails at high frequencies below 80 kHz. Because of this multiplicity of propagating waves, array transducers are used to extract specific wave types from others. From a practical point of view, however, it would be very useful if the waves of interest could be measured by a single sensor attached on the rail surface. To make it possible, their wave types, i.e., deformation shapes, have to be clearly understood. However, the investigations in the literature are too limited for this purpose. In this thesis, therefore, it will be investigated whether waves of interest can be detected by a single sensor attached on the rail surface.

2.3 Wave Reflection and Transmission due to Defects for Long Range Rail Inspection

If an infinite length waveguide structure has a local non-uniformity, like a crack, it will reflect a part of incident power and transmit the rest of it. These reflection and transmission characteristics associated with the presence of the discontinuity may give some indication of both the crack location and depth. In order to be able to investigate these characteristics, it is necessary above all to model wave propagation in finite or semi-infinite length waveguide structures. For these waveguide structures with boundaries, the boundary conditions need to be specified in addition to the homogeneous wave solutions in order to predict the structure's response.

For simple beam structures, Mace [36] estimated the reflection and transmission properties due to a discontinuity in a beam, like a joint or support, theoretically. Doyle *et al.* [37–39] investigated wave propagation in beams by means of a spectral element (SE) method, also called the dynamic stiffness method (DSM). In this method, a single SE is modelled in terms of applied forces and displacements at the boundaries. This method was extended by Gopalakrishnan and Doyle [40] for a beam with local non-uniformities, like cracks and holes, by introducing the FE method to model local regions of the non-uniformities. In this method, they subdivided the beam into a few sub-elements, separating uniform regions from local regions with discontinuities, which are modelled by SEs and FEs, respectively. Then these SEs and FEs were combined by condensing the FE nodes at boundaries connected with the SEs. However, they only considered the forced response of the structure because the SE method requires input forces. Shone *et al.* [41, 42] imposed incident waves within this method to predict wave reflection and transmission due to cracks in infinite beams. Neither of these works is directly suitable for high frequency analysis, in which the higher order cross-sectional deformations have to be taken account, because beam theories are used to make the SEs.

As a numerical method, Finnveden [16] has developed the spectral finite element (SFE) method, using a variational principle for simple beam structures with finite length. In this method, he formulated a dynamic stiffness matrix numerically using wave solutions of the beam as basis functions. Since the element length is

limited only by discontinuities in geometry and in excitation, this method reduces the computational effort considerably, compared with standard FE methods. As described in Section 2.1, for a waveguide structure with a complex cross-section, homogeneous wave solutions can be predicted numerically from the WFE method. Combining it with the SFE method, Birgersson *et al.* [20] developed an improved method to predict the response of coupled rectangular plates. They named it the spectral super element (SSE) method[2]. A great advantage of this method is that the SSEs can be easily connected to neighbouring elements if the same nodes are used at the joints between two substructures. Therefore, it is not necessary in this method to condense the dynamic stiffness matrix of the FE part to connect it to the SSEs, as long as the same cross-sectional models are used.

Birgersson *et al.* [20] utilised the SSE method for finite length plate structures, consisting of thin-walled strip elements [43]. For studying sound transmission in infinite waveguides, Peplow and Finneveden [44] attached very long finite length SSEs, of the order of 10^9 m, with damping at both ends of the finite length SSEs to approximate the infinite waveguide. In this thesis, the SSE for semi-infinite waveguides is developed to model semi-infinite rails. Then the combined SE/FE method is modified by employing the semi-infinite SSEs, instead of the SEs, in order to estimate wave reflection and transmission due to cracks in rails at high frequency. This combined method will be called the SSE/FE method here.

To investigate a relation between rail response and crack depth, Rose *et al.* [7, 11] measured the pulse-echo and through transmission responses to rail cuts of varying depths by using 60 kHz EMATs at the top of the rail head. In this measurement, they acquired the variation of corresponding peak-to-peak amplitudes in time data as a function of the cut depth. However, they did not examine the rail response either at other positions on the rail cross-section or at other frequencies covering wider range. In addition, it was not investigated in their experiment which types of wave are efficient for detecting cracks.

On the other hand, Cawley *et al.* [8, 10] used the reflection matrix, which can

[2]Doyle and Gopalakrishnan [19, 40] also called an element modelled by FEA, which has a local non-uniformity, a 'Spectral Super-element' in their method. However, note that although it has the same name, this approach is different from the present SSEM.

present mode conversions of the incident waves, to identify defects. In the simulation, they used a three-dimensional time-marching FE model to predict reflection coefficients for several defect geometries. This method of quantifying the wave mode conversion seems to be an efficient and advanced technique for crack detection. For practical implementation, however, this requires many transducers to be attached along the rail and around the rail cross-section as well as an associated signal processing to decompose each wave mode separately. Furthermore, this technique would not be applicable to operational tracks on which trains are running.

In this thesis, as a feasibility study, it will be investigated whether measuring rail vibration at a single position on the rail cross-section is applicable for crack detection in rails for frequencies up to 50 kHz by using the combined SSE/FE method.

Chapter 3

Finite Element Analysis of a Railway Track

3.1 Modelling a Railway Track

At low frequencies waves propagate in a rail as bending, extensional or torsional waves. At higher frequencies, however, the rail cross-section deforms and many higher order wave types exist. This cross-section deformation has to be taken into account for an accurate evaluation of the dispersion properties. It has been found that the cross-section deforms significantly above about 1500 Hz [14]. So in this chapter a rail is modelled by means of the finite element method in order to take account of the cross-section deformation. The frequency range of interest will extend up to 80 kHz because it has been suggested in ref. [7] that waves at higher frequencies attenuate less over distance than those at lower frequencies. In this chapter, a UIC60 rail has been modelled using the finite element package, ANSYS. Throughout, x will represent the direction along the rail, y the transverse direction and z the vertical direction.

3.1.1 Modelling a rail cross-section

Firstly, a rail cross-section was modelled with different element sizes in order to determine a relevant mesh size which can depict the deformed shapes of the section properly at the frequencies of interest. Since the UIC60 rail has a symmetric cross-section, only half of the width is included as shown in Fig. 3.1. This has the advantage of separating the possible waves into two groups that are uncoupled from

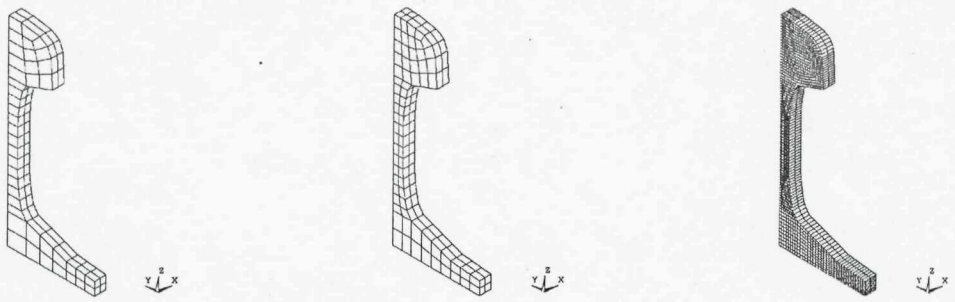

(a) (b) (c)

Fig. 3.1. FE models for rail cross-section. (a) Model 1, (b) model 2, (c) model 3.

each other as well as reducing computational demands. A symmetric boundary condition constrains the deformation of the mid-plane in the y direction (i.e., out of plane) and gives the vertical and symmetric longitudinal modes. An antisymmetric boundary condition constrains the x and z directions (i.e., in plane) in the mid-plane and gives the lateral and torsional modes as well as the antisymmetric longitudinal modes in which opposite sides of the rail move in opposite directions.

Three different cross-sectional FE models are shown in Fig. 3.1. The respective number of elements in the cross-section of these FE models are 42, 70 and 2398, and the length of these models is 10 mm in the x direction. It was supposed in this comparison that model 3 gives precise natural frequencies and mode shapes of the rail cross-section because it has a very fine mesh and can therefore be used as a reference. Each FE model consists of solid elements with 20 nodes, defined in ANSYS as 'solid186', having three translational degrees of freedom per node. The web and the rail foot were modelled with a relatively fine mesh because they are more flexible than other parts of the rail cross-section. To ensure a proper mesh size, a criterion of at least 6 nodes per wavelength is used.

Modal analysis was performed up to 80 kHz and then the natural frequencies and mode shapes of the three models were compared with each other. In this analysis, symmetric boundary conditions were applied at both ends of the FE models (that is, deflections in the x direction were constrained). Since the length of these FE models in the x direction is sufficiently short with respect to the possible wavelengths below 80 kHz, no modes occur along the x direction. For instance, if the shear wave speed is

Table 3.1. Natural frequencies of three FE models in Fig. 3.1 for (a) the vertical modes, (b) lateral and torsional modes.

(a)

mode number	natural frequency (Hz)		
	model 1	model 2	model 3
1	0	0	0
2	5029	5027	5021
3	9490	9489	9484
4	18100	18092	18061
5	22776	22771	22754
6	27255	27243	27217
7	31788	31772	31737
8	36242	36211	36166
9	39206	39166	39100
10	47895	47880	47839
11	52606	52587	52559
12	58064	57918	57799
13	59749	59477	59295
14	63650	63625	63554
15	70042	70038	69953
16	72206	72122	72061
17	77867	77638	77364
18	81764	80317	79751

(b)

mode number	natural frequency (Hz)		
	model 1	model 2	model 3
1	0	0	0
2	0	0	0
3	1275	1274	1273
4	3822	3811	3806
5	9225	9209	9193
6	13113	13080	13055
7	20536	20471	20420
8	27936	27887	27828
9	30661	30628	30585
10	35234	35188	35151
11	37734	37701	37680
12	43660	43554	43458
13	49433	49271	49117
14	52469	52370	52282
15	56496	56451	56433
16	60370	60238	60088
17	60921	60831	60774
18	66715	66417	66127
19	70563	70338	69984
20	70960	70628	70496
21	73086	72895	72748
22	78398	78105	77803

assumed as 3000 m/s, the shortest wavelength would be about 37.5 mm at 80 kHz. Therefore, the boundary conditions used at both ends mean that the FE models are effectively in a plane strain state because the deformation in the longitudinal direction is not allowed by the boundary conditions. Although longitudinal modes are excluded from this analysis it can be expected that a mesh size that is suitable for bending of the cross-section will also be suitable for longitudinal motion.

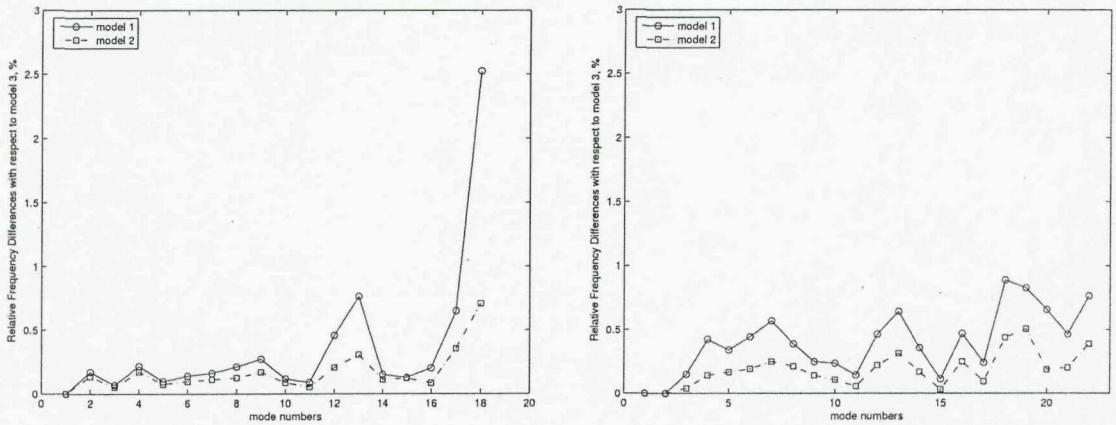

(a) (b)

Fig. 3.2. Relative frequency differences between FE models with respect to model 3 for (a) vertical modes, (b) lateral and torsional modes.

(a) (b)

Fig. 3.3. Comparison of mode shapes at the 16th mode of the vertical modes for (a) model 1 (72.2 kHz), (b) model 3 (72.06 kHz).

(a) (b)

Fig. 3.4. Comparison of mode shapes at the 20th mode of the lateral and torsional modes for (a) model 1 (70.96 kHz), (b) model 3 (70.5 kHz).

The natural frequencies of each mode obtained from the three FE models are listed in Table 3.1 for the vertical, lateral and torsional modes. The corresponding mode shapes were checked visually to ensure that modes are paired correctly. Fig. 3.2(a) shows the relative frequency differences between the FE models with respect to model 3 for vertical modes and Fig. 3.2(b) shows equivalent results for the lateral and torsional modes. This figure indicates that model 1 can predict the natural frequencies to within a 3% error margin in this frequency region; in fact most natural frequencies are predicted to within a 1% margin. So model 1 is applicable as an appropriate cross-sectional model in this analysis. Model 2 gives improved results but the reduction in error margin is not sufficient to justify the large increase in number of degrees of freedom this would entail. Example mode shapes at about 70 kHz for the symmetric and antisymmetric boundary conditions at the mid-plane are represented and compared with those of model 3 in Fig. 3.3 and Fig. 3.4. These two figures also reveal that model 1 describes the deformed shape of the cross-section acceptably with four elements (8 nodes) per wavelength in the web in the mode in Fig. 3.4.

3.1.2 Modelling a length of railway track

In this section, a short length of rail is modelled by using the cross-section model 1 considered in the previous section. Since the contribution of the sleeper and ballast are limited to the low frequency region below 1 kHz [12], only the rail and rail pad are included in this model.

The length of the rail model determines the increment of discrete wavenumbers, $\Delta\kappa$, because the wavenumbers predicted from the rail model are spaced according to the relation

$$\Delta\kappa = \frac{\pi}{2L} , \tag{3.1}$$

where L is the length of the rail model in the x direction. This relation will be discussed later in section 3.2. It is found from Eq.(3.1) that, in order to obtain more precise results in the wavenumber domain from the FE analysis, a longer rail model has to be analysed. To make the rail model longer, two approaches can be used: increasing the size of each element or increasing the number of elements in the x

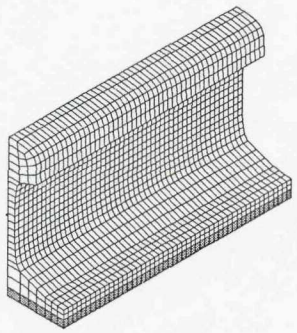

Fig. 3.5. FE model of a rail on a distributed elastic foundation.

direction[1]. However, it may be inappropriate to increase the size of elements in the x direction because the element size determines the upper frequency limit of the FE analysis results. Hence it is more reliable to increase the number of elements in the x direction. The cost, however, is that the storage space required and computational load increase dramatically due to the increased number of degrees of freedoms and this may make the analysis impractical. Moreover, if damping is introduced, the matrices in the FE model will possess complex numbers, requiring yet more space and computational load. Accordingly, it is necessary for the FE analysis to compromise precision in the results with computing requirements.

In this study, the chosen length of the rail model is 0.3 m, which is selected as half of the usual sleeper span in railway track. The same solid elements, 'solid186' in ANSYS, were used as did in section 3.1.1 and the number of elements in the length was 50 as shown in Fig. 3.5. Larger models were found to be impractical. In total there are 2450 elements and 14608 nodes in the FE model in Fig. 3.5. The length of a single element in the x direction is 6 mm giving six elements per wavelength at 80 kHz for a wave speed of 3000 m/s.

As shown in Fig. 3.5, the rail pad is modelled as a continuous foundation in this study. In practice, however, rail pads are placed discretely between the rail and the sleepers. This discrete support induces a strong periodicity effect, so-called "pinned-pinned resonances", at low frequencies where wavelengths are longer than

[1]As an alternative way of increasing the rail length, periodic structure theory could be used [14, 22] but it was not investigated in this thesis.

the rail pad length and spacing. However, the effect of periodicity resulting from the discrete foundation reduces as frequency increases [13, 30]. The discrete foundation can be considered in the FE modelling by simply compensating the stiffnesses of the foundation for the shorter length of it. A discretely supported rail model and FE analysis results of that are described in detail in Appendix A. From this investigation it was determined that if discrete rail pads are applied, they make uneven deformation shapes along the rail. Furthermore, they allow different wavelengths in different regions of the rail at some frequencies. This implies that several wavelengths can exist at a single frequency. It will, therefore, be hard to determine frequency-wavenumber relations because wavelengths are not clearly defined in the deformed rail shapes. Nevertheless, in terms of the long range wave propagation, the discrete foundation model was confirmed to provide similar features to the distributed one, particularly at high frequency. It can be seen in Fig. A.5 that decay rates of each wave obtained from the continuous and discrete foundation models are very similar at frequencies above 20 kHz. The results of Fig. A.5 demonstrate that the distributed foundation model provides a good approximation of the real situation. That is mainly because the stiffness of the rail pad is much less than that of the rail so that reflections of waves at the start and end of each discrete pad will be insignificant. According to this simulation result, the rail pads are modelled as a distributed foundation in the rest of this thesis, as shown in Fig. 3.5.

The low frequency stiffness of the single rail pad placed at 0.6 m spacing is assumed to be 150 MN/m for the vertical direction and 20 MN/m for the lateral and longitudinal directions. These values are chosen to correspond to the relatively soft pad used in the ISVR test track [45]. The stiffnesses of several other types of rail pads are given in ref. [30, 31] as falling in the range 200 MN/m to 1300 MN/m for the vertical direction and 48 MN/m to 200 MN/m for the lateral direction. The effect of the rail pad stiffness on the long range wave propagation will be discussed in Chapter 4. In addition, the damping loss factor of the rail pad is taken as 0.2 for all directions. Practical values vary between about 0.1 and 0.25 [13]. The rail clip is generally much more flexible than the rail pad and is omitted from the model [12].

As a distributed solid layer, the rail pad is modelled by an orthotropic material in this thesis. In the orthotropic material, nine elastic constants are required to define the material's elastic characteristics because there is no interaction between

the normal stresses σ_x, σ_y, σ_z and the shear strains ϵ_{yz}, ϵ_{zx}, ϵ_{xy} [46]. These nine constants are comprised of the three Young's moduli E_x, E_y, E_z, the three Poisson's ratios ν_{yz}, ν_{zx}, ν_{xy}, and the three shear moduli G_{xy}, G_{yz}, G_{zx}. Additionally, it is assumed in the modelling that this orthotropic material has the same physical properties along the directions of each of the axes. This means $E_x = E_y = E_z$, $\nu_{yz} = \nu_{zx} = \nu_{xy}$ and $G_{xy} = G_{yz} = G_{zx}$.

For the vertical direction, the stiffness of the distributed foundation, $k_{p,z}$, can be determined using Hooke's law for a one-dimensional model as

$$k_{p,z} = \frac{E_{p,z}S}{h} , \tag{3.2}$$

where $E_{p,z}$ and h are Young's modulus and the thickness of the foundation, respectively. S is the contact area between the rail and the foundation. Since $k_{p,z} = 75$ MN/m and $S = 0.045$ m^2 for the rail segment of length 0.3 m, the elastic modulus of the foundation for $h = 0.01$ m becomes

$$E_{p,z} = 1.667 \times 10^7 \text{ N/m}^2. \tag{3.3}$$

In the same way, when $h = 0.01$ m the lateral and longitudinal stiffnesses $k_{p,x} = k_{p,y} = 10$ MN/m are achieved if the shear modulus for the lateral and longitudinal directions is chosen as

$$G_{p,xz} = G_{p,yz} = 2.22 \times 10^6 \text{ N/m}^2. \tag{3.4}$$

Therefore, the moduli of the distributed foundation are given as

$$E_{p,x} = E_{p,y} = E_{p,z} = 1.667 \times 10^7 \text{ N/m}^2, \tag{3.5}$$

$$G_{p,xy} = G_{p,yz} = G_{p,xz} = 2.22 \times 10^6 \text{ N/m}^2. \tag{3.6}$$

In an orthotropic material, the normal strains are coupled with three normal stresses and expressed as

$$\begin{aligned} \epsilon_{xx} &= s_{xx}\sigma_{xx} + s_{yx}\sigma_{yy} + s_{zx}\sigma_{zz} , \\ \epsilon_{yy} &= s_{xy}\sigma_{xx} + s_{yy}\sigma_{yy} + s_{zy}\sigma_{zz} , \\ \epsilon_{zz} &= s_{xz}\sigma_{xx} + s_{yz}\sigma_{yy} + s_{zz}\sigma_{zz} , \end{aligned} \tag{3.7}$$

where $s_{xx} = 1/E_x$, $s_{yy} = 1/E_y$, $s_{zz} = 1/E_z$, $s_{xy} = -\nu_{xy}/E_y$ $(= s_{yx})$, $s_{yz} = -\nu_{yz}/E_z$ $(= s_{zy})$ and $s_{zx} = -\nu_{zx}/E_x$ $(= s_{xz})$ [47]. In this study, however, in order to simplify

the model the coupling terms in Eq. (3.7) are removed by setting the three Poisson's ratios of the foundation to zero, i.e.,

$$\nu_{p,xy} = \nu_{p,yz} = \nu_{p,xz} = 0 \ . \tag{3.8}$$

In addition, the density of the foundation material was assumed as

$$\rho_p = 0 \ . \tag{3.9}$$

By introducing this last assumption, the rail pad is regarded as a massless spring component in this model. Consequently this FE model cannot represent internal resonances occurring in the rail pad. Instead, the contribution of the internal resonances of the rail pad will be considered later by using a stiffness increment.

Using a mass of 60 kg/m $\times$ 0.3 m = 18 kg and the required stiffnesses, the natural frequencies of rigid body motions are theoretically predicted as $f_0 = 324.7$ Hz for the vertical direction and $f_0 = 118.6$ Hz for the lateral and longitudinal directions. In the FE analysis, the model in Fig. 3.5 produced these frequencies as 324.4 Hz and 118.2 Hz, respectively, confirming that the desired stiffnesses were achieved.

3.1.3 Dynamic stiffening of the rail pad

At high frequencies, the stiffness of the rail pad usually becomes much higher than the static or low frequency one. This is because the rail pad has mass which leads to internal resonances at high frequencies. Moreover the rubber material itself becomes stiffer at higher frequencies [48]. This stiffness of the rail pad, called the 'dynamic stiffness' here, is one of the important parameters for track modelling. It could be possible to measure this in the laboratory [13] or directly to model the rail pad with fine finite element layers to capture the dynamic stiffness. In this direct FE modelling for the rail pad, however, several tens of finite elements in the vertical direction are required even in 1 cm thickness to be able to express the internal resonance effect. For this reason, the dynamic stiffness was predicted theoretically from a one-dimensional foundation model in the z direction in this study[2] [49].

[2]Note that the rail pad may not be uniform, for example, studs or ribs are often present on its surfaces. However, here a uniform structure is considered for simplicity.

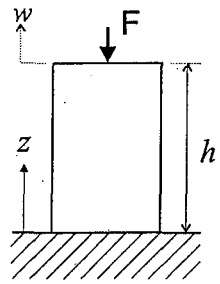

Fig. 3.6. One dimensional model for a continuous foundation.

Considering a one-dimensional foundation with thickness h as shown in Fig. 3.6, the longitudinal wave solution in the z direction can be expressed as

$$w(z) = B_1 e^{j\kappa z} + B_2 e^{-j\kappa z} , \tag{3.10}$$

where κ is the wavenumber given by $\kappa = \omega/c_L$ with the longitudinal wave speed, $c_L = \sqrt{E_{p,z}/\rho_p}$. The two boundary conditions are given as

$$w = 0 \qquad at\ z = 0 , \tag{3.11}$$

$$F = -E_{p,z} S \frac{dw}{dz} \qquad at\ z = h . \tag{3.12}$$

Substituting $w(z)$ from Eq. (3.10) into these two boundary conditions gives

$$w(z) = \frac{-jF}{E_{p,z} S\kappa (e^{j\kappa h} + e^{-j\kappa h})} \left[e^{j\kappa(h-z)} - e^{-j\kappa(h-z)} \right] . \tag{3.13}$$

Hence for a distributed foundation with thickness h, the dynamic stiffness, $k^d_{p,z}$, can be expressed from Eq. (3.13) as

$$k^d_{p,z} = \frac{F}{w(z)}\bigg|_{z=0} = \frac{-jE_{p,z} S\kappa (e^{-j\kappa h} + e^{j\kappa h})}{e^{-j\kappa h} - e^{j\kappa h}} = \frac{E_{p,z} S\kappa \cos \kappa h}{\sin \kappa h} . \tag{3.14}$$

If damping is introduced then the elastic modulus and the wavenumber become complex as

$$E'_{p,z} = E_{p,z}(1 + j\eta_p) , \tag{3.15}$$

$$\kappa_d = \omega \left(\frac{\rho_p}{E'_{p,z}} \right)^{1/2} , \tag{3.16}$$

where η_p is the damping loss factor of the foundation [50] and κ_d is the damped wavenumber. Hence the damped dynamic stiffness is written as

$$k'^d_{p,z} = \frac{E'_{p,z} S\ \kappa_d \cos \kappa_d h}{\sin \kappa_d h} . \tag{3.17}$$

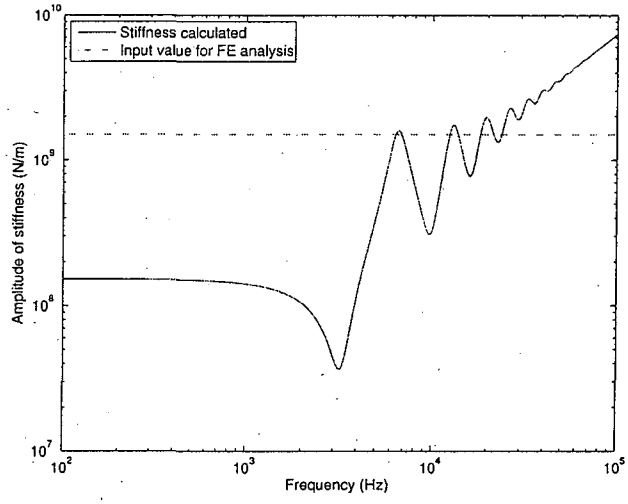

(a)

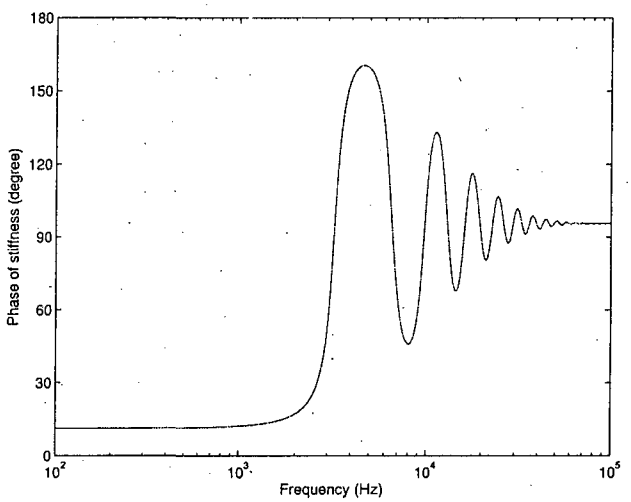

(b)

Fig. 3.7. Rail pad stiffness in Eq. (3.17) as a function of frequency when $\rho_p = 1000$ kg/m^3 and $\eta_p = 0.2$. (a) Magnitude, (b) phase.

Fig. 3.7 illustrates the magnitude and phase of the stiffness, $k'^{d}_{p,z}$, of the foundation in the vertical direction as a function of frequency when $\rho_p = 1000$ kg/m^3 and $\eta_p = 0.2$. As shown in Fig. 3.7(a), the stiffness increases due to the presence of standing waves in the foundation and the maxima occur at frequencies corresponding to $h = n\lambda/2$ with n an integer and λ the wavelength. In addition, it can be seen from this figure that the amplitude of stiffness grows continuously and the phase of it approaches around 90 degrees as frequency increases. This predicted result shows

that the rail pad behaviour tends to that of a damper at frequencies above several kilohertz. Hence, it would be more relevant to model the rail pad as a damper than a spring component for high frequency analysis. Nevertheless, the rail pad is modelled as a spring element with a dynamic stiffness in this thesis because it will not make much difference in the results of identifying the waves propagating furthest along the rail. The contribution of the rail pad to this aspect will be discussed in Section 4.4.

In the ANSYS model it is not feasible to introduce a frequency-dependent stiffness. Therefore, based on this simulated stiffness, the dynamic stiffnesses of the foundation were set to 10 times larger than the low frequency ones as a constant value as shown in Fig. 3.7. That is to say, $E_{p,x} = E_{p,y} = E_{p,z} = 1.667 \times 10^8$ N/m^2 and $G_{p,xy} = G_{p,yz} = G_{p,xz} = 2.23 \times 10^7$ N/m^2. This dynamic stiffness approximation will lead to overestimation of the dissipated energy resulting from the rail pad deformation in the lower frequency region below 5 kHz and will lead to underestimation in the higher frequency region above 20 kHz.

3.2 Prediction of Dispersion Relations

To simulate the waves in an infinite rail, the model was solved with symmetric and/or antisymmetric boundary conditions at both ends of the 0.3 m length. Fig. 3.8 shows the degrees of freedom allowed for three different combinations of symmetric and antisymmetric boundary conditions. As shown in this figure, the symmetric boundary condition allows two translational motions in the y and z directions, and one rotational motion in the x direction. Conversely the antisymmetric condition allows two rotational motions in the y and z directions, and one translational motion in the x direction. For a simple beam these conditions reduce to sliding or pinned boundaries as shown in Fig. 3.8.

Modal analysis will produce natural frequencies and the corresponding mode shapes of the 0.3 m rail section [14]. Each natural frequency and mode shape produced by the modal analysis has a sinusoidal mode shape in the x direction and can be interpreted as the sum of two identical waves which travel in opposite directions and thus form a standing wave in an infinite rail. Each natural frequency and wavelength of these boundary conditions thus corresponds to a point on the

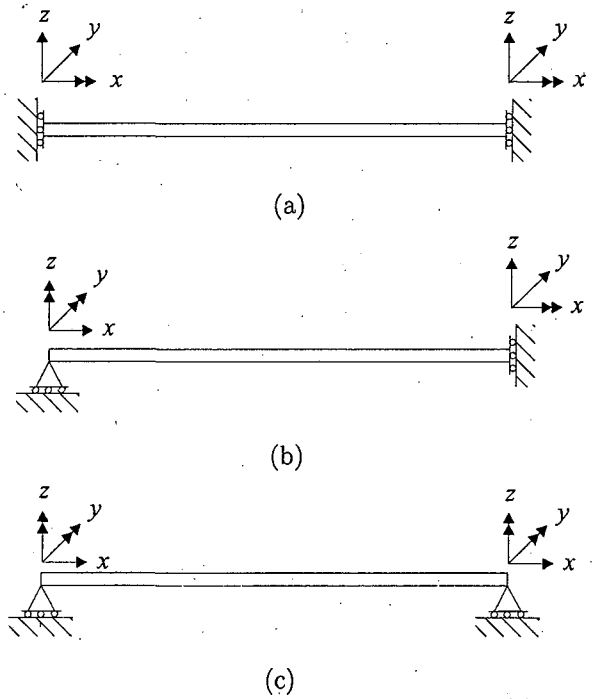

Fig. 3.8. Released degrees of freedom at both ends of the beam for (a) the symmetric-symmetric boundary conditions, (b) the antisymmetric-symmetric boundary conditions, (c) the antisymmetric-antisymmetric boundary conditions.

frequency-wavenumber relation for an infinite rail. For the symmetric-symmetric (or antisymmetric-antisymmetric) boundary conditions, the wavenumbers will be

$$\kappa = n\pi/L \quad , \tag{3.18}$$

and for the symmetric-antisymmetric (or antisymmetric-symmetric) case

$$\kappa = (2n+1)\pi/2L \quad , \tag{3.19}$$

where L is the length of the rail section and n is $0, 1, 2, \ldots$. Therefore, if both conditions are included, $\Delta\kappa$ in the predicted dispersion relation becomes $\pi/2L$ as stated in Eq. (3.1).

Fig. 3.9(a) illustrates the dispersion curves generated by connecting the discrete frequency-wavenumber points produced from the modal analysis for the vertical and symmetric longitudinal waves. Fig. 3.9(b) shows the corresponding results for the lateral, torsional and antisymmetric longitudinal waves. These figures reveal that there are 63 wave types in total in the rail within the frequency range up to 80 kHz. Of these, 40 waves with zero wavenumber were listed in Table 3.1; the remaining waves are longitudinal since this motion was constrained in the cross-section model

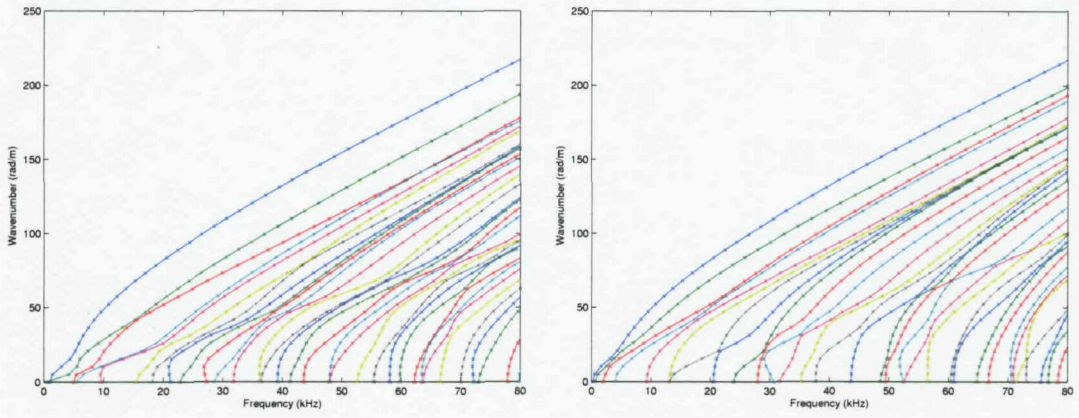

(a) (b)

Fig. 3.9. Predicted dispersion curves for (a) the vertical and symmetric longitudinal waves, (b) the lateral, torsional and antisymmetric longitudinal waves.

used in section 3.3.1. In this thesis, each wave type in this figure is named simply by the order of the wavenumber from top to bottom, for example, the first wave, second wave, etc. in the vertical and symmetric longitudinal waves.

Since the dispersion curves within one of the graphs in Fig. 3.9 (i.e., symmetric or antisymmetric waves with respect to the mid-plane) do not cross each other, these waves exhibit mode coupling and finally swap their mode shapes when they come close to one another. This phenomenon is known as the 'curve veering' which is associated with the coupling between modes [51]. For example, the second (green line) and third (red line) waves in Fig. 3.9(a) approach one another and swap their mode shapes at around 5 kHz and 15 kHz. Fig. 3.9(a) shows a non-dispersive wave increasing to about 100 rad/m by 80 kHz in the frequency-wavenumber plot, formed by consecutive pieces of different waves with a constant slope. These are non-dispersive longitudinal waves in which the head, web and foot move longitudinally in the same or opposing directions to each other. The phase speed is around 5000 m/s, the longitudinal wave speed in a rod of steel. Furthermore, it seems in Fig. 3.9(b) that longitudinal wave motions also take place as a group of waves appear with a phase speed around 5000 m/s. These longitudinal waves will have an antisymmetrically deformed mode shape in the rail with respect to the mid-plane.

Fig. 3.10 and Fig. 3.11 show the respective deformation shapes of a number of waves at about 25 kHz and 50 kHz for the symmetric boundary condition at the

mid plane. Fig. 3.12 and Fig. 3.13 show equivalent results for the antisymmetric boundary condition at about 25 kHz and 50 kHz, respectively. In each case they correspond to the six waves with the highest wavenumbers in Fig. 3.9.

For the vertical and symmetric longitudinal waves around 25 kHz, the first two and fourth ones among the selected six waves are the 1^{st}, 2^{nd} and 3^{rd} order foot bending waves as illustrated in Fig. 3.10(a), (b) and (d). It can be seen from Fig. 3.9(a) that these convert from the global bending wave at about 5 kHz and 15 kHz, and from the longitudinal wave at about 18 kHz, respectively. In other words, the first wave has global bending deformation below 5 kHz, whereas the second wave has the longitudinal deformation below 5 kHz and global bending deformation between 5 kHz and 15 kHz. The third wave is the vertical bending wave in the rail head (Fig. 3.10(c)) and the fifth and sixth waves appear to have global deformation shapes possessing large deformations in the foot (Fig. 3.11(e) and (f)). However, at around 50 kHz, these two were converted to longitudinal type waves in the foot and rail head, as shown in Fig. 3.11(e) and (f), respectively.

For the lateral, torsional and antisymmetric longitudinal waves around 25 kHz, the first and second waves selected are the foot bending wave and the 1^{st} order web bending wave, respectively (Fig. 3.12(a) and (b)). The remaining four from the third to sixth waves show global deformation shapes in the rail head, web and foot (Fig. 3.12(c) to (f)). Meanwhile, the first and second waves around 50 kHz are the same type of waves as those in Fig. 3.12(a) and (b) but have increased wavenumbers. On the other hand, the third and fourth waves selected around 50 kHz are the 2^{nd} order foot bending and web bending waves, respectively, (Fig. 3.13(c) and (d)), which were converted from the waves of global deformation at around 20 kHz. The fifth and sixth waves show mixed motions of the rail head and web (Fig. 3.13(e) and (f)). The other wave modes around 50 kHz, having lower wavenumbers, generally have globally coupled deformation shapes in which head, web and foot all vibrate. These examples of deformation shapes indicate that waves with larger wavenumbers are more likely to propagate through a local region of the rail cross-section.

The dispersion curves predicted from the supported rail model are compared with those for a free rail in Fig. 3.14 for frequencies below 20 kHz. This figure shows that the effect of the elastic foundation appears mainly at frequencies below

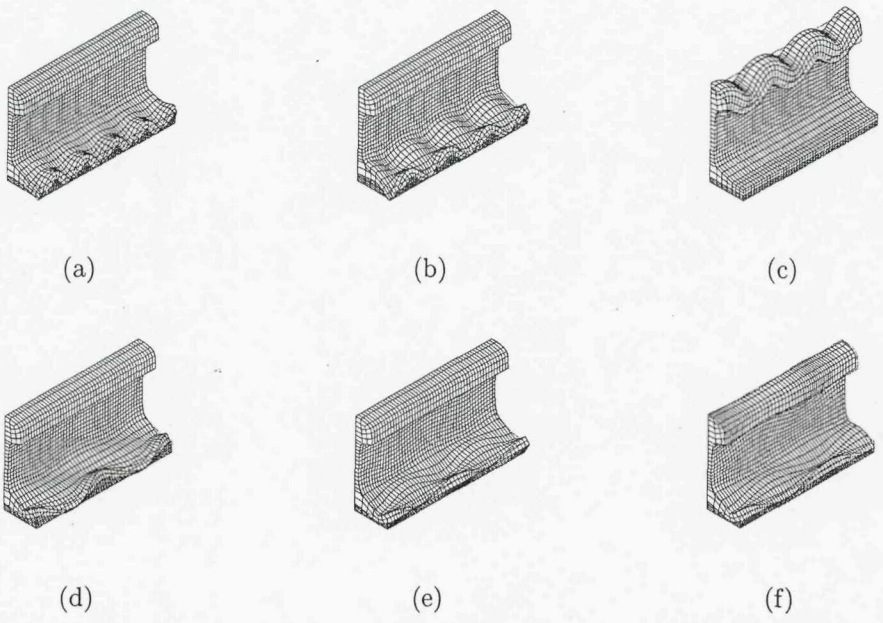

Fig. 3.10. Deformation shapes of the top 6 waves around 25 kHz in Fig. 3.9(a), (a) wave 1 at 24377 Hz, (b) wave 2 at 26348 Hz, (c) wave 3 at 24911 Hz, (d) wave 4 at 23681 Hz, (e) wave 5 at 24915 Hz, (f) wave 6 at 24401 Hz.

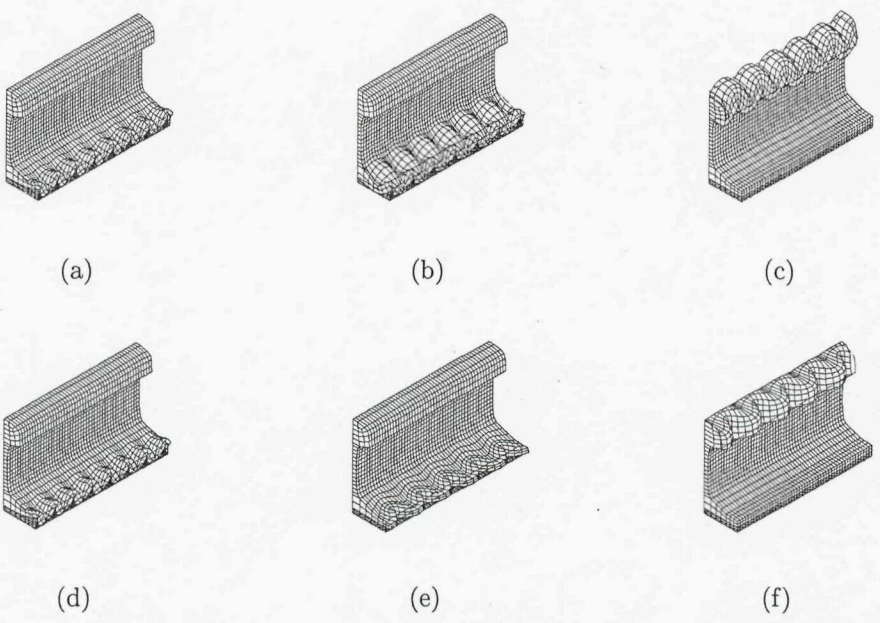

Fig. 3.11. Deformation shapes of the top 6 waves around 50 kHz in Fig. 3.9(a), (a) wave 1 at 48740 Hz, (b) wave 2 at 50719 Hz, (c) wave 3 at 50398 Hz, (d) wave 4 at 49732 Hz, (e) wave 5 at 49870 Hz, (f) wave 6 at 50723 Hz.

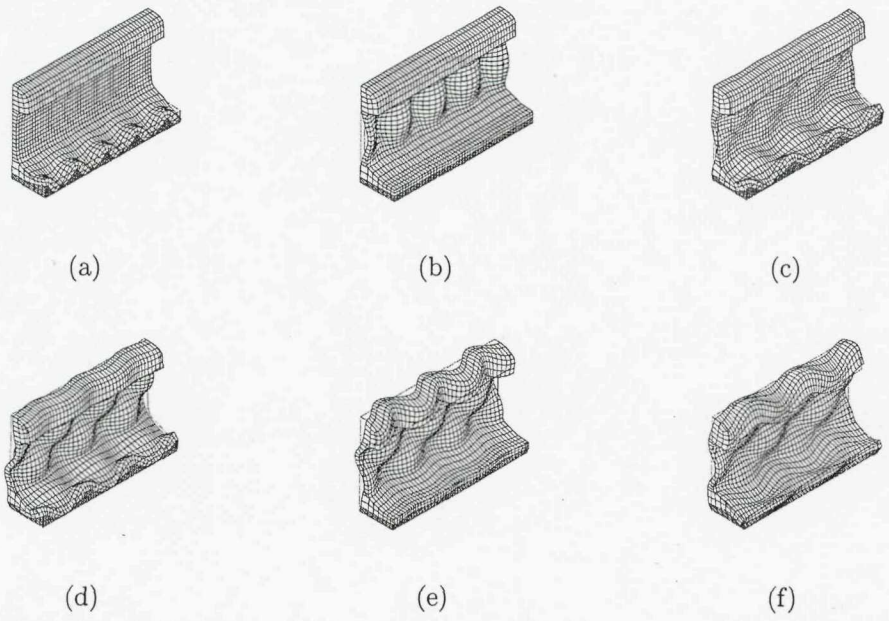

(a) (b) (c)

(d) (e) (f)

Fig. 3.12. Deformation shapes of the top 6 waves around 25 kHz in Fig. 3.9(b), (a) wave 1 at 24387 Hz, (b) wave 2 at 25766 Hz, (c) wave 3 at 23905 Hz, (d) wave 4 at 24631 Hz, (e) wave 5 at 26869 Hz, (f) wave 6 at 24405 Hz.

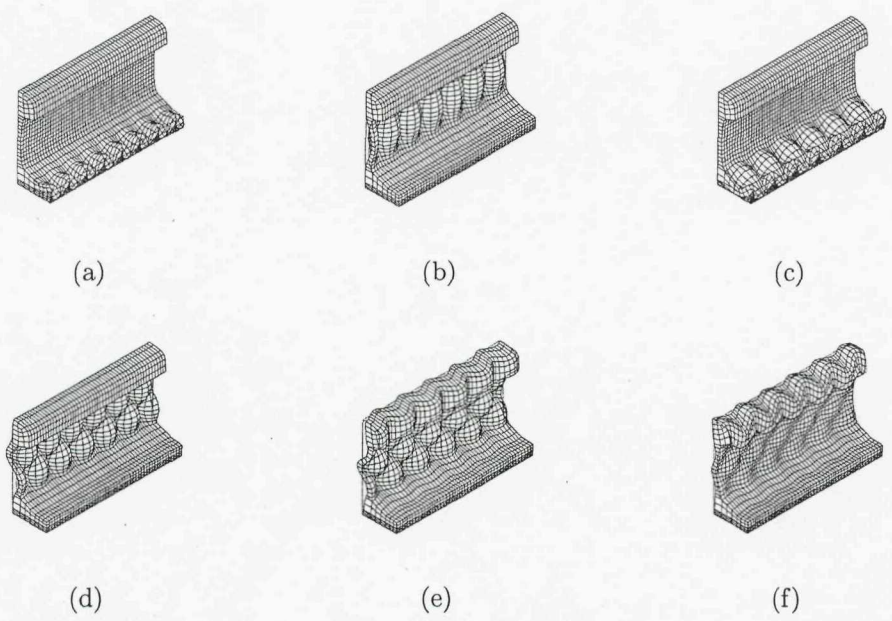

(a) (b) (c)

(d) (e) (f)

Fig. 3.13. Deformation shapes of the top 6 waves around 50 kHz in Fig. 3.9(b), (a) wave 1 at 51139 Hz, (b) wave 2 at 49193 Hz, (c) wave 3 at 48793 Hz, (d) wave 4 at 50192 Hz, (e) wave 5 at 49020 Hz, (f) wave 6 at 50505 Hz.

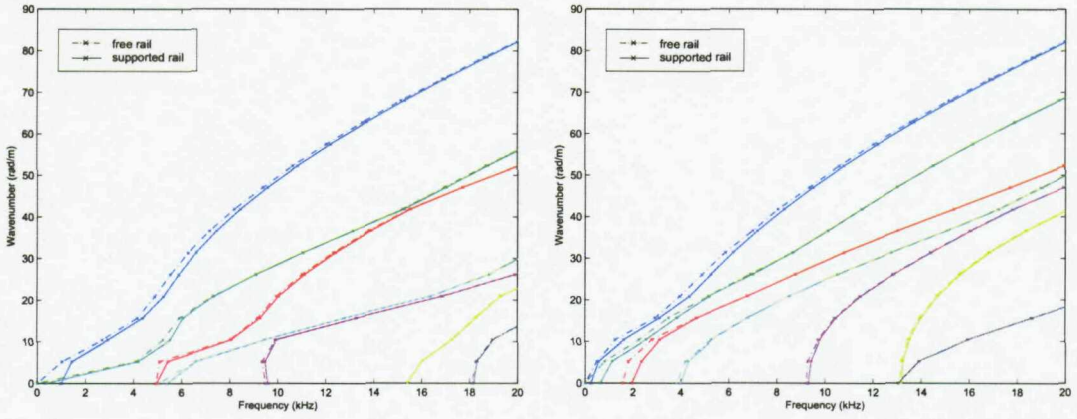

(a) (b)

Fig. 3.14. Comparison of dispersion relations between free and supported rail for (a) the vertical and symmetric longitudinal waves, (b) the lateral, torsional and antisymmetric longitudinal waves.

10 kHz, resulting in the cut-on frequencies being moved slightly higher. The cut-on of the first vertical bending wave is most affected, as shown in Fig. 3.14(a), being increased from 0 to 1 kHz by the presence of the support. It can therefore be said that the presence of the foundation does not result in large changes in the frequency-wavenumber plot at high frequencies. However, the foundation will contribute considerably to the decay rates of each wave because the damping loss factor of a rail pad is generally much higher than that of the rail itself.

3.3 Prediction of Group Velocities

The phase velocities, c, and group velocities, c_g, of each wave can be predicted from the dispersion curves in Fig. 3.9 by use of the relations

$$c = \frac{\omega}{\kappa} , \tag{3.20}$$

$$c_g = \frac{d\omega}{d\kappa} . \tag{3.21}$$

In this calculation, the group velocity of the i^{th} wave at the n^{th} frequency was evaluated approximately by a finite difference scheme

$$(c_g^i)_n \approx \frac{\omega_{n+1}^i - \omega_{n-1}^i}{\kappa_{n+1}^i - \kappa_{n-1}^i} . \tag{3.22}$$

The predicted phase and group velocities are shown in Fig. 3.15 and Fig. 3.16, respectively. At a cut-on frequency, the phase velocity becomes infinite, corresponding to rigid body motion of the rail, because the wavenumber, κ, is zero at that

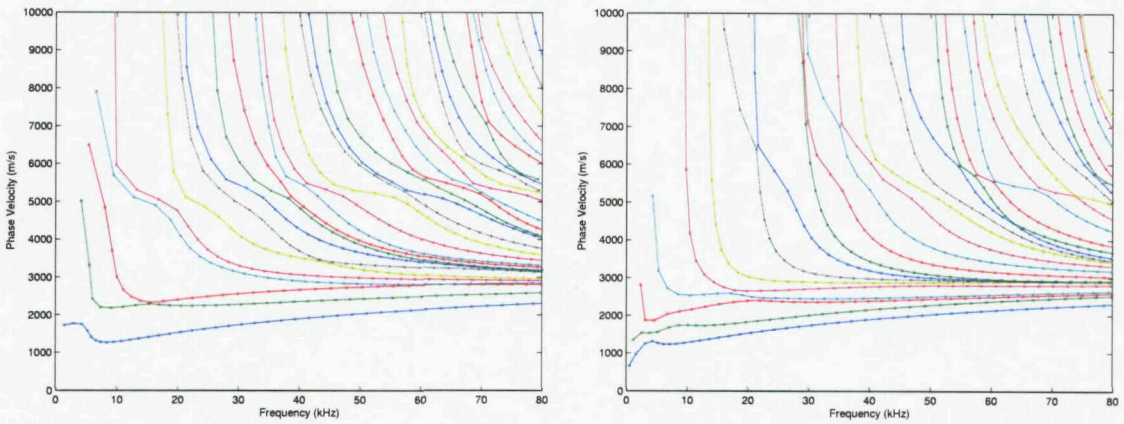

(a) (b)

Fig. 3.15. Predicted phase velocities for (a) the vertical and symmetric longitudinal waves, (b) the lateral, torsional and antisymmetric longitudinal waves. Colours correspond to Fig. 3.9

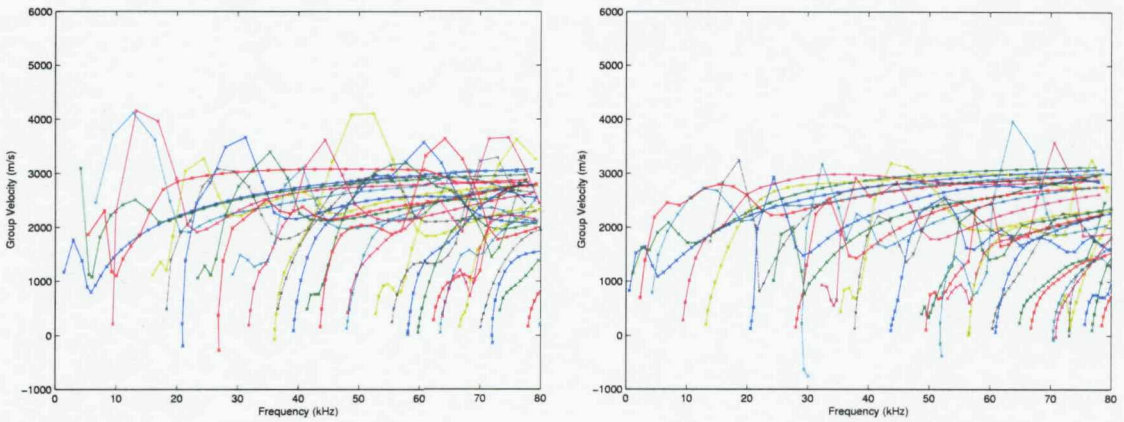

(a) (b)

Fig. 3.16. Predicted group velocities for (a) the vertical and symmetric longitudinal waves, (b) the lateral, torsional and antisymmetric longitudinal waves. Colours correspond to Fig. 3.9

frequency. Conversely the group velocity is zero at the cut-on frequency.

The longitudinal waves are graphically well distinguished in Fig. 3.15 because they have phase velocities approaching 5000 m/s. As depicted in Fig. 3.16, the predicted group velocity curves are not smooth enough, particularly for longitudinal waves, because of the limited resolution $\Delta\kappa$. It seems from these phase and group velocity figures that many of the phase velocities tend to approach a certain value, possibly the shear wave speed, as frequency increases. The shear wave speed is about 3100 m/s for a bulk shear wave and about 2850 m/s for a shear wave in a beam with a

square cross-section. In addition, negative group velocities arise around some cut-on frequencies. This negative group velocity means that for a wave travelling forwards the energy carried by the wave propagates backwards and vice versa [22, 52]. These can be seen as curves in the dispersion plot with a negative slope near cut-on, for example the blue curve just above 20 kHz in Fig. 3.9(a).

3.4 Predictions of Decay Rates

When damping is introduced, waves will decay with distance along the rail and this decay rate, Δ (in dB/m), will determine how far a wave can travel along a rail.

3.4.1 Decay rates

If damping is included in the model by making the elastic modulus complex, $E(1+j\eta)$, with η the material loss factor, waves decay as they propagate. The decay rate, Δ, can be defined from the amplitude reduction over one wavelength as

$$\Delta = -\frac{20}{\lambda}\log_{10}\left(\frac{|u(\lambda)|}{|u(0)|}\right), \tag{3.23}$$

where $u(x)$ is the displacement of the travelling wave along x and λ is the wavelength. For the damped propagating wave i at frequency ω, the energy decaying with time can be expressed as

$$W^i(t) = W_0^i e^{-\omega\eta^i t}, \tag{3.24}$$

where W_0^i is the energy at $t = 0$ and η^i is the loss factor of this wave. Since this energy propagates with the group velocity, by the relation between time and space, $t = x/c_g^i$,

$$W^i(x) = W_0^i e^{-\omega\eta^i x/c_g^i}. \tag{3.25}$$

Since $W^i(x) \propto |u^i(x)|^2$,

$$|u^i(x)| = u_0^i e^{-\omega\eta^i x/2c_g^i}. \tag{3.26}$$

Therefore, for the wave i, the decay rate in Eq.(3.23) is expressed as

$$\Delta^i = -\frac{20}{\lambda}\log_{10} e^{-\omega\eta^i\lambda/2c_g^i} = 27.29\,\frac{f\eta^i}{c_g^i}. \tag{3.27}$$

As expressed in Eq. (3.27), the damping loss factor of a propagating wave, η^i, and its group velocity, c_g^i, have to be identified to predict the decay rates of each wave

in Fig. 3.9. That is, the decay rate of the i^{th} wave at the n^{th} frequency in Fig. 3.9 is

$$\Delta_n^i = 27.29 f_n^i \eta_n^i / c_{g,n}^i \ . \tag{3.28}$$

For the track model in Fig. 3.5, damping is introduced by assigning a material damping loss factor to the rail and another to the rail pad.

In ANSYS, the material damping parameter has to be defined by a constant β, which is related to the material damping loss factor, η, by $\beta = \eta/\omega$. For the given constant β, the modal analysis in ANSYS gives complex natural frequencies due to the presence of the damping term as

$$\omega_{d,n} = j\sigma_n + \omega_n = j\zeta_n\omega_n + \omega_n \ , \tag{3.29}$$

where ζ_n and ω_n are the modal damping ratio and the natural frequency of the n^{th} mode, respectively. Then the damping ratio, ζ_n, of the n^{th} mode can be obtained from the imaginary part of the complex natural frequency. This means that in order to obtain ζ_n at a specific angular frequency ω_n, the input property β has to be given at ω_n without knowing ω_n a priori. This problem can be tackled by introducing a simple approximation, as presented in ref. [53]. If the input parameter β is fixed at some angular frequency, ω_a, as $\beta_a = \eta/\omega_a$, it can be assumed that the correct β_n at the n^{th} mode would be

$$\beta_n = \frac{\omega_a}{\omega_n}\beta_a \ , \tag{3.30}$$

where ω_a/ω_n is a compensating factor. Therefore, the modal damping ratio at ω_n is approximately calculated from β_a by multiplying by the factor ω_a/ω_n,

$$\zeta_n = \frac{\sigma_n}{\omega_n} \cdot \frac{\omega_a}{\omega_n} \tag{3.31}$$

for all modes in a frequency range of interest. This estimation has been tested for a range of values of ω_a and found to give consistent results for all modes in the frequency range of interest. Finally the modal damping loss factor, η_n, used for the decay rate prediction using Eq. (3.28) can be obtained from the modal damping ratio, ζ_n, by the relation $\eta_n = 2\zeta_n$, valid for small values of ζ_n.

3.4.2 Predicted results

Two material damping components are required for this track model, i.e., the material damping loss factor of the rail, η_r and of the rail pad, η_p. In practice

both may be frequency-dependent. In this numerical analysis, however, the material damping loss factors of the rail and rail pad were set to constant values of 0.0002 and 0.2, respectively. η_r was chosen to represent the material damping loss factor of steel. The damping of the rail pad corresponds to typical values [13, 30] and is a thousand times higher than that of the rail, as specified here. In this prediction, the angular frequency ω_a for the input property β is chosen in the middle of the frequency range of interest, corresponding to 40 kHz. For these two material damping loss factors, the input parameters, values of β, for the rail pad and rail at 40 kHz were 7.94×10^{-7} and 7.94×10^{-10}, respectively.

Fig. 3.17 shows the predicted modal damping loss factors, η_n^i, of each wave produced by the modal analysis in ANSYS after applying the correction factor described above. As given in this figure, the input material damping of the rail, η_r, determines the lower limit of η_n^i of all waves. In other words, if there is no damping in the rail pad then all the waves in the structure will have the same damping loss factors as η_r, i.e., $\eta_n^i = \eta_r$, regardless of the wave type. Therefore it reveals that the differences of the predicted modal damping η_n^i from the input material damping η_r directly depend on how much the rail foundation deforms in their modes. For instance, a wave which propagates only through the rail head as shown in Fig. 3.11(c) will be little affected by the damping of the foundation. Hence it can be imagined that waves which have small deformation in the foundation propagate further along the

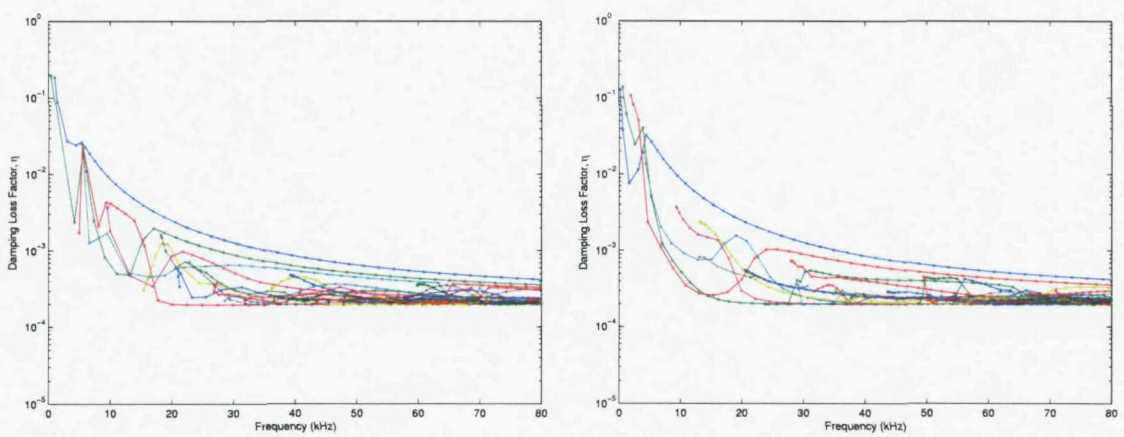

(a) (b)

Fig. 3.17. Predicted damping loss factors for (a) the vertical and symmetric longitudinal waves, (b) the lateral, torsional and antisymmetric longitudinal waves. Colours correspond to Fig. 3.9

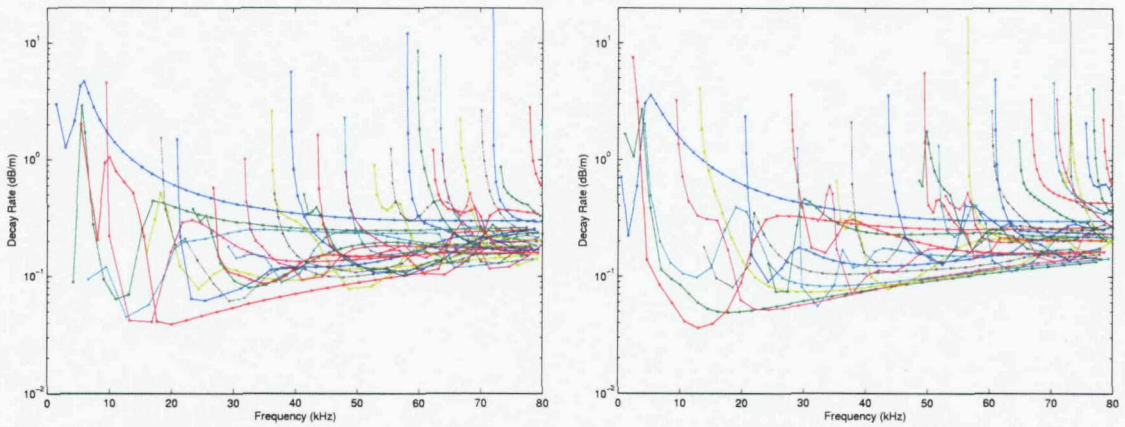

(a) (b)

Fig. 3.18. Predicted decay rates for (a) the vertical and symmetric longitudinal waves, (b) the lateral, torsional and antisymmetric longitudinal waves. Colours correspond to Fig. 3.9

rail since η_p is 1000 times larger than η_r. Conversely the wave shown in Fig. 3.14(a) has a much higher damping loss factor, shown by the upper blue curve in Fig. 3.17.

The decay rates predicted by Eq. (3.28) are illustrated in Fig. 3.18 for all waves in this track model up to 80 kHz. At cut-on frequencies of each wave, the decay rates become infinite because the group velocities are zero at those frequencies. Note that, as described in Section 3.2, the dispersion curves created by a given boundary condition (i.e., symmetric or antisymmetric boundary conditions in the mid-plane) do not cross each other. Instead, they swap their deformation shapes when two dispersion curves approach each other. Hence one has to be aware that when the deformation shapes are exchanged between two waves, their decay rates are also swapped so that two decay rate curves do cross each other. Because the decay rate is directly proportional to the frequency as given Eq. (3.28), the lower limit of the decay rate increases with frequency as shown in Fig. 3.18. Although longitudinal waves possess large group velocities, they do not seem to give lower decay rates than other types of waves. This is because the longitudinal waves normally have global deformations so that their damping loss factors are relatively larger than those of other waves. In other words, considerable deformations of the rail foundation occur when the longitudinal waves propagate. Fig. 3.18 indicates that the minimum decay rate is about 0.04 dB/m and seems to occur between 10 kHz and 20 kHz.

In practice, a range of rail pads with different stiffnesses is used in tracks. So it will be worth investigating the effects of the foundation stiffness (k_p) on decay rates. This will be performed and discussed in Chapter 4 with the wavenumber finite element approach.

3.5 Summary

In this chapter, the conventional FE method was employed to predict dispersion relations and decay rates up to 80 kHz. To do that, an appropriate cross-sectional FE model for UIC60 rail was found and then a 0.3 m long railway track model was established as a rail on a distributed elastic foundation, corresponding to the rail pad. This elastic foundation was modelled as a massless spring and the stiffening of the rail pad due to internal resonances was compensated by introducing a higher dynamic stiffness. Two damping components were considered as constants in this track model: damping for the rail and for the foundation, respectively.

It was found from this simulation that there are more than 60 different types of waves propagating in the rail below 80 kHz. For these multiple waves, their dispersion relations and decay rates were predicted. Deformation shapes of each wave indicated that waves with larger wavenumbers are more likely to propagate through a local region of the rail cross-section. The other wave modes, having lower wavenumbers, normally have globally coupled deformation shapes in which head, web and foot all vibrate.

Through this FE analysis, it was found that the minimum decay rates of about 0.04 dB/m occur between 10 kHz and 20 kHz. Since damping for the foundation is 1000 times larger than that for the rail, it could be said that waves which have small deformation in the foundation propagate further along the rail. This simulation result conflicts with that reported in ref. [11] where it is stated that the most effective frequency range for the long range wave propagation in railway track is 40 kHz to 80 kHz. The validity of the FE results will be verified in the remaining chapters in this thesis.

Since there are several tens of different waves propagating below 80 kHz in the track model, it will be worthwhile identifying which of them are measurable at

various points on the rail surface. That is achievable by quantifying the 'energy' contained in different parts of the rail surface from the displacement predicted by FE analysis. However, this is discussed in the next chapter using another numerical method, called the wavenumber finite element method.

Chapter 4

Wavenumber Finite Element Analysis of a Railway Track

In Chapter 3, the FE method was used to generate dispersion curves and decay rates at frequencies up to 80 kHz. However, it has several drawbacks for practical application. Primarily the FE method requires very large models for high frequency analysis and so imposes a large computational burden. Furthermore, considerable manual post-processing is required to build dispersion and group velocity curves from the results of the FE analysis. For example, in Chapter 3, more than 2000 natural frequencies and mode shapes were checked one by one to specify their wavenumbers. Another disadvantage is that the group velocities are roughly estimated from the discrete dispersion curves by means of the finite difference approximation between two discrete points.

In this chapter, to overcome these difficulties, an improved numerical method called the wavenumber (or waveguide) finite element (WFE) method is employed as an alternative to the conventional FE method. One of its great advantages is that different wave types are readily identified and can be analysed, enabling a physical interpretation of the wave propagation in the structure under investigation. Further information on this approach can be found in refs [20, 25, 26, 54]. For the WFE analysis in this thesis a software program, called 'WAFER (WAveguide Finite Element Resources)', developed at ISVR is used for modelling the wave behaviour in railway tracks numerically. A more recent version, called 'WANDS', includes boundary element analysis and is described in [55, 56].

4.1 Wavenumber Finite Element Method

In this part, the basic equations of the WFE method and how they can be solved to predict dispersion relations and decay rates will be described briefly.

4.1.1 Equation of motion

Suppose that there is an undamped waveguide structure which is infinitely long in one direction, call it the x direction, and its cross-section normal to the x axis is uniform along x. In conventional FE analysis, this structure can be modelled for a finite length with symmetric and/or antisymmetric boundary conditions, as done in Chapter 3. For the assembled FE model, the global equation of motion is expressed in matrix form as

$$\{\mathbf{K}_{fe} + \mathbf{M}_{fe}\frac{\partial^2}{\partial t^2}\}\mathbf{\Phi}_{fe}(x,t) = \mathbf{0} \quad , \tag{4.1}$$

where $\mathbf{K}_{fe}$ and $\mathbf{M}_{fe}$ are stiffness and mass matrices and $\mathbf{\Phi}_{fe}$ denotes the displacement vector of the FE model. $\mathbf{K}_{fe}$ and $\mathbf{M}_{fe}$ are real if damping is not considered. Note that, in this FE formulation, the displacements u, v and w in the x, y and z directions are approximated by the prescribed 'element displacement function' (or shape function) [57].

For this waveguide structure, it is possible to define a wave solution for the x direction instead of making a finite element mesh and using a shape function along this direction. Then time harmonic displacements, (u,v,w), of the element in three directions of (x,y,z) can be expressed with separable variables as

$$\begin{aligned} u(x,y,z,t) &= \chi(y,z)\cdot\tilde{u}e^{-j\kappa x}e^{j\omega t} \\ v(x,y,z,t) &= \psi(y,z)\cdot\tilde{v}e^{-j\kappa x}e^{j\omega t} \\ w(x,y,z,t) &= \xi(y,z)\cdot\tilde{w}e^{-j\kappa x}e^{j\omega t} \end{aligned} \tag{4.2}$$

where t denotes time, y and z denote coordinates of the cross-section, χ, ψ and ξ define the displacements of the cross-section and $\tilde{u}$, $\tilde{v}$ and $\tilde{w}$ are scaling constants. Note that in Eq.(4.2) only the y and z dependence is specified by shape functions.

By using these wave solutions for the x direction in the FE formulation, a two-dimensional FE equation is made over a cross-sectional model, instead of a three-dimensional full structure model. The differential equation for the cross-section

modelled with solid finite elements is given by

$$\{\mathbf{K_2}\frac{\partial^2}{\partial x^2} + \mathbf{K_1}\frac{\partial}{\partial x} + \mathbf{K_0} + \mathbf{M}\frac{\partial^2}{\partial t^2}\}\mathbf{u}(x,t) = \mathbf{0} \tag{4.3}$$

where $\mathbf{K_2}$, $\mathbf{K_1}$ and $\mathbf{K_0}$ are the matrices that come from the stiffeness of the structure[1], $\mathbf{M}$ is the mass matrix and $\mathbf{u}(x,t)$ is the displacement vector of the cross-section[2] [26, 27, 54]. In this equation, the three stiffness matrices $\mathbf{K_2}$, $\mathbf{K_1}$ and $\mathbf{K_0}$ contain derivative components of order $\left(\frac{\partial}{\partial y}, \frac{\partial}{\partial z}\right)^0$, $\left(\frac{\partial}{\partial y}, \frac{\partial}{\partial z}\right)^1$ and $\left(\frac{\partial}{\partial y}, \frac{\partial}{\partial z}\right)^2$, respectively. The matrices $\mathbf{K_2}$, $\mathbf{K_0}$ and $\mathbf{M}$ are symmetric and $\mathbf{K_1}$ is antisymmetric. All of them are independent of x and they are real if there is no damping included.

Since $\mathbf{u}(x,t) = \tilde{\mathbf{\Phi}}e^{j(\omega t - \kappa x)}$ as described in Eq.(4.2), the differential equation in Eq.(4.3) can be simplified to an eigenvalue problem,

$$\{\mathbf{K_2}(-j\kappa)^2 + \mathbf{K_1}(-j\kappa) + \mathbf{K_0} - \omega^2\mathbf{M}\}\tilde{\mathbf{\Phi}} = \mathbf{0} \tag{4.4}$$

where $\tilde{\mathbf{\Phi}}$ contains the displacements (χ, ψ and ξ) of the cross-section which define the deformation shapes of waves. Here κ, ω and $\tilde{\mathbf{\Phi}}$ are the unknown variables to be identified.

As shown in Eq.(4.3) and Eq.(4.4), there are three different stiffness terms. They represent slightly different physical behaviour of the structure induced by waves propagating along the x direction. Since the matrix $\mathbf{K_0}$ is independent of x, it possesses stiffness components which do not vary along the x direction. Thus if only $\mathbf{K_0}$ is present, waves will occur which form cross-sectional modes of the waveguide structure at $\kappa = 0$. That is, $\{\mathbf{K_0} - \omega^2\mathbf{M}\}\tilde{\mathbf{\Phi}} = \mathbf{0}$ will generate cut-on frequencies and the corresponding cross-sectional mode shapes of the structure. On the other hand, the matrix $\mathbf{K_2}$ will have stiffness components which are associated with propagating behaviour along the x direction because it is expressed together with the second derivative of $\mathbf{u}$ with respect to x. Note that, $\mathbf{K_2}$ contains only stiffness components that are uncoupled with the y and z directional strains. Those terms originating from coupled deformations between the x and (y, z) directions are contained in the matrix $\mathbf{K_1}$ which is antisymmetric.

[1] The physical units of $\mathbf{K_2}$, $\mathbf{K_1}$ and $\mathbf{K_0}$ are Nm, N and N/m, respectively.

[2] For beam or plate structures, $\mathbf{K_4}\frac{\partial^4\mathbf{u}(x,t)}{\partial x^4}$ will be added in the left-hand side of Eq.(4.3).

In elastic structures, there are two coupled relations between each directional deformation. The first one is defined by the Poisson's ratio. That is, strains normal to one direction are coupled with the strains in other directions by the Poisson's ratio, ν. The other one comes from the rotation of the element by the shear force applied. That is, a shear stress causes a rotational deformation which is expressed by two strain components as, for example,

$$\tau_{xy} = G\epsilon_{xy} = G\left(\frac{\partial u}{\partial y} + \frac{\partial v}{\partial x}\right) \quad , \tag{4.5}$$

where G denotes the shear modulus of the material. The first term in Eq.(4.5) will be contained in $\mathbf{K_1}$ and the second term will be in $\mathbf{K_2}$ because $\partial\tau_{xy}/\partial x$ is used in the formulation of Eq.(4.3). Since $\mathbf{K_1}$ originates only from the coupling between strains in the x direction with the y or z directions, it would vanish if there is no coupling between them. For instance, if wave propagation in fluids is investigated with this WFE method, the matrix $\mathbf{K_1}$ will disappear because the Poission's ratio ν and the shear modulus G are normally set to zero for fluids. Also, in terms of the strain energy which can be stored by each stiffness term in Eq.(4.4), one has to be aware that the term involving $\mathbf{K_1}$ does not store any energy since it only expresses coupling between the x directional and y or z directional strains. That is,

$$(-j\kappa)\tilde{\mathbf{\Phi}}^H\mathbf{K_1}\tilde{\mathbf{\Phi}} = 0 \quad . \tag{4.6}$$

The mass and stiffness matrices in Eq.(4.4) for the cross-sectional model are produced from the WAFER software in this study. The process of using WAFER is schematically presented in Fig. 4.1. As shown in this chart, the post-processing

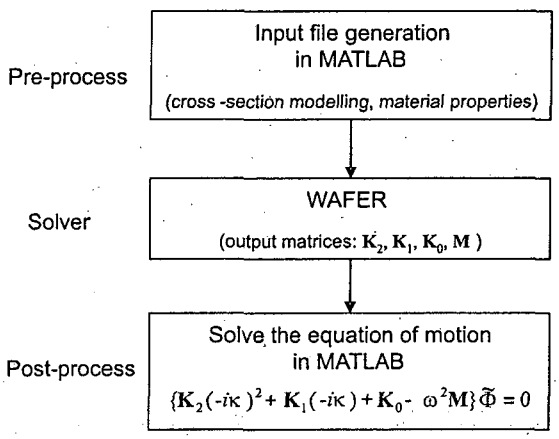

Fig. 4.1. Process for using WAFER.

to solve Eq.(4.4) is performed in MATLAB after assembling each of the matrices, $\mathbf{K_2}$, $\mathbf{K_1}$, $\mathbf{K_0}$ and $\mathbf{M}$. The details of how to obtain κ and ω from Eq.(4.4) will be discussed below.

4.1.2 Dispersion curves

The twin-parameter eigenvalue problem in κ and ω in Eq.(4.4) has to be solved to obtain dispersion relations. Since there are two variables, two solution approaches are available. Firstly, Eq.(4.4) can be solved as a generalized eigenvalue problem for frequency ω if a wavenumber, κ, is given. In this case, the equation can be solved by a MATLAB built-in function, 'eig.m'. If another function, 'eigs.m', is used for sparse matrices instead, a small number of eigenvalues can be obtained more rapidly. This method will give natural frequencies (eigenvalues) and mode shapes (eigenvectors) of propagating waves at given wavenumbers.

Conversely, if a frequency is given instead of a wavenumber, then the equation becomes a polynomial eigenvalue problem in the wavenumber, κ. Then the function 'polyeig.m' in MATLAB can be used to obtain κ at a given frequency ω. This method outputs wavenumbers and mode shapes at each frequency of both propagating and nearfield waves; the latter decay exponentially with distance. This polynomial eigenvalue problem can be transformed to a generalized eigenvalue problem in order to reduce its computational time and improve numerical robustness [43]. Nevertheless, it was reported in [27] that this approach still takes about 100 times longer in computation time than the first solution method.

The choice of how to solve Eq.(4.4) will depend on what response is to be investigated by using the results obtained. In this chapter, it is preferred to solve for ω at a given κ since dispersion relations and decay rates of propagating waves are of interest. The second method, solving for κ at a given frequency ω, is used and discussed in Chapter 8 to investigate wave reflection and transmission characteristics along a rail.

As derived above, the WFE method utilises the exact wave solutions for the x direction instead of making FE meshes which use approximate shape functions. Hence it is anticipated that WFE analysis will yield more accurate natural frequen-

cies than conventional FE analysis for the same cross-sectional model, especially at high frequencies. The dispersion curves predicted by the FE and WFE methods will be compared later.

4.1.3 Group velocities

In WFE analysis, group velocities can be derived theoretically from the equation of motion, Eq.(4.4), using the method given by Finnveden [27]. Since the equation has to be satisfied for any solutions of κ in the dispersion relation, then the derivative of Eq.(4.4) with respect to the wavenumber should always be zero. That is,

$$\frac{\partial}{\partial \kappa}\left\{[\mathbf{K}-\omega^2\mathbf{M}]\tilde{\mathbf{\Phi}}\right\}=\mathbf{0} \quad , \tag{4.7}$$

where $\mathbf{K}=\mathbf{K_2}(-j\kappa)^2+\mathbf{K_1}(-j\kappa)+\mathbf{K_0}$. This derivative can be written as

$$\left[\frac{\partial}{\partial \kappa}\mathbf{K}-2\omega\frac{\partial \omega}{\partial \kappa}\mathbf{M}\right]\tilde{\mathbf{\Phi}}+\left[\mathbf{K}-\omega^2\mathbf{M}\right]\frac{\partial}{\partial \kappa}\tilde{\mathbf{\Phi}}=\mathbf{0} \quad . \tag{4.8}$$

By multiplying the above equation by the left eigenvector, $\tilde{\mathbf{\Phi}}^L$, of $[\mathbf{K}-\omega^2\mathbf{M}]$,

$$\tilde{\mathbf{\Phi}}^{L^T}\left[\frac{\partial}{\partial \kappa}\mathbf{K}-2\omega\frac{\partial \omega}{\partial \kappa}\mathbf{M}\right]\tilde{\mathbf{\Phi}}+\tilde{\mathbf{\Phi}}^{L^T}\left[\mathbf{K}-\omega^2\mathbf{M}\right]\frac{\partial}{\partial \kappa}\tilde{\mathbf{\Phi}}=0 \quad , \tag{4.9}$$

where the superscript ^{T} denotes a matrix transpose. From the definition of the left eigenvector,

$$\tilde{\mathbf{\Phi}}^{L^T}[\mathbf{K}-\omega^2\mathbf{M}]=\mathbf{0} \quad . \tag{4.10}$$

Then Eq.(4.9) simplifies to

$$\tilde{\mathbf{\Phi}}^{L^T}\left[\frac{\partial}{\partial \kappa}\mathbf{K}-2\omega\frac{\partial \omega}{\partial \kappa}\mathbf{M}\right]\tilde{\mathbf{\Phi}}=0 \quad . \tag{4.11}$$

Since $\mathbf{K}$ is Hermitian and $\mathbf{M}$ is real and symmetric, Hermitian transpose of Eq.(4.11) will become

$$\tilde{\mathbf{\Phi}}^{H}\left[\frac{\partial}{\partial \kappa}\mathbf{K}-2\omega\frac{\partial \omega}{\partial \kappa}\mathbf{M}\right]\tilde{\mathbf{\Phi}}^{L^*}=0 \quad , \tag{4.12}$$

where ^{H} denotes Hermitian transpose. From Eq.(4.11) and Eq.(4.12), it is found that the left eigenvector is equal to the complex conjugate of the right eigenvector, $\tilde{\mathbf{\Phi}}^L=\tilde{\mathbf{\Phi}}^*$. Hence, the group velocity, c_g, can be expressed as

$$c_g=\frac{\partial \omega}{\partial \kappa}=\frac{\tilde{\mathbf{\Phi}}^H\mathbf{K}'\tilde{\mathbf{\Phi}}}{2\omega\tilde{\mathbf{\Phi}}^H\mathbf{M}\tilde{\mathbf{\Phi}}} \quad , \tag{4.13}$$

where

$$\mathbf{K}'=\frac{\partial \mathbf{K}}{\partial \kappa}=-2\kappa\mathbf{K_2}-j\mathbf{K_1} \quad . \tag{4.14}$$

From this relation the group velocity can be easily evaluated for each individual solution of the dispersion relations.

4.1.4 Decay rates

So far all the WFE equations were derived for an undamped structure. Now suppose that damping is included in the model by adding an imaginary part to the real valued stiffness matrices as

$$\mathbf{K_d} = \mathbf{K_2}(1+j\eta)(-j\kappa)^2 + \mathbf{K_1}(1+j\eta)(-j\kappa) + \mathbf{K_0}(1+j\eta) = \mathbf{K}(1+j\eta) \quad (4.15)$$

where $\mathbf{K_d}$ indicates the complex stiffness matrix and η is the damping loss factor. For small damping, a damped wavenumber can be expressed approximately using a Taylor series as

$$\kappa_d \approx \kappa + \frac{\partial \kappa_d}{\partial \eta}\Big|_{\eta=0} \eta \quad (4.16)$$

where κ and κ_d denote undamped and damped wavenumbers, respectively [26] .

For a given frequency, the derivative with respect to η at $\eta = 0$, in Eq.(4.16), can be evaluated as follows. Since the equation of motion has to be satisfied even if damping is slightly increased,

$$\frac{\partial}{\partial \eta}\{[\mathbf{K_d} - \omega^2\mathbf{M}]\tilde{\mathbf{\Phi}}\} = \mathbf{0}. \quad (4.17)$$

As the stiffness matrix $\mathbf{K_d}$ is a function of κ, the derivative of this equation can be written as

$$\Big[j\mathbf{K} + \frac{\partial \mathbf{K_d}}{\partial \kappa}\frac{\partial \kappa}{\partial \eta}\Big]\tilde{\mathbf{\Phi}} + \big[\mathbf{K_d} - \omega^2\mathbf{M}\big]\frac{\partial}{\partial \eta}\tilde{\mathbf{\Phi}} = 0 \quad . \quad (4.18)$$

Multiplying by the left eigenvector, $\tilde{\mathbf{\Phi}}^L$,

$$\tilde{\mathbf{\Phi}}^{L^T}\big[\mathbf{K_d} - \omega^2\mathbf{M}\big]\frac{\partial}{\partial \eta}\tilde{\mathbf{\Phi}} = 0 \quad . \quad (4.19)$$

Then the derivative with respect to η at $\eta = 0$ is given by

$$\frac{\partial \kappa}{\partial \eta}\Big|_{\eta=0} = \frac{-j\tilde{\mathbf{\Phi}}^H\mathbf{K}\tilde{\mathbf{\Phi}}}{\tilde{\mathbf{\Phi}}^H\mathbf{K}'\tilde{\mathbf{\Phi}}} \quad . \quad (4.20)$$

Since $\mathbf{K} = \omega^2\mathbf{M}$ when $\eta = 0$, this becomes

$$\frac{\partial \kappa}{\partial \eta}\Big|_{\eta=0} = \frac{-j\omega^2\tilde{\mathbf{\Phi}}^H\mathbf{M}\tilde{\mathbf{\Phi}}}{\tilde{\mathbf{\Phi}}^H\mathbf{K}'\tilde{\mathbf{\Phi}}} \quad . \quad (4.21)$$

Using the group velocity in Eq.(4.13), it follows that

$$\frac{\partial \kappa}{\partial \eta}\Big|_{\eta=0} = \frac{-j\omega}{2c_g} \quad . \quad (4.22)$$

Therefore, a damped wavenumber can be approximated by

$$\kappa_d = \kappa + \frac{\partial \kappa}{\partial \eta}\Big|_{\eta=0} \eta = \kappa - \frac{j\omega}{2c_g}\eta \ . \tag{4.23}$$

Then decay rates can be obtained from the imaginary part of the damped wavenumber as

$$\Delta = -20\log_{10}(e)\ \mathrm{Im}(\kappa_d) = 8.686\left(\frac{\omega\eta}{2c_g}\right) = 27.29\ \frac{f\eta}{c_g} \ . \tag{4.24}$$

This decay rate is exactly the same expression as Eq.(3.27) derived in the previous FE analysis.

As an another way of predicting the decay rate in Eq.(4.24), $\mathrm{Im}(\kappa_d)$ could be directly obtained by solving wavenumbers from $[\mathbf{K_d} - \omega^2\mathbf{M}]\tilde{\mathbf{\Phi}} = \mathbf{0}$ at each frequency ω. However, this approach is not efficient for the prediction of decay rates of propagating waves because it gives all the wavenumber solutions and mode shapes, most of which are nearfield waves. These nearfield waves are not of interest in this section. Moreover it will require very long computation time. Therefore, this approach has not been used in the decay rate prediction.

4.2 Modelling a Railway Track

In this section, the WFE method is applied to the railway track which was used in the FE analysis in Chapter 3. Although the cross-sectional track model appropriate for the previous FE analysis was already established, it is necessary to check the suitability of the cross-sectional model for this WFE method. The physical properties of the rail and foundation are exactly the same as those specified in Chapter 3.

4.2.1 Modelling a rail cross-section

Firstly, in order to check the proper mesh size for this WFE method, two cross-sectional models of the UIC60 rail were constructed with two different element sizes. These models are shown in Fig. 4.2. Model 1 in Fig. 4.2 is the same model as used in Chapter 3 and model 2 has a finer mesh. Each model consists of quadrilateral solid elements which possess 8 nodes each having three translational degrees of freedom. The corresponding numbers of elements are 42 and 70, respectively.

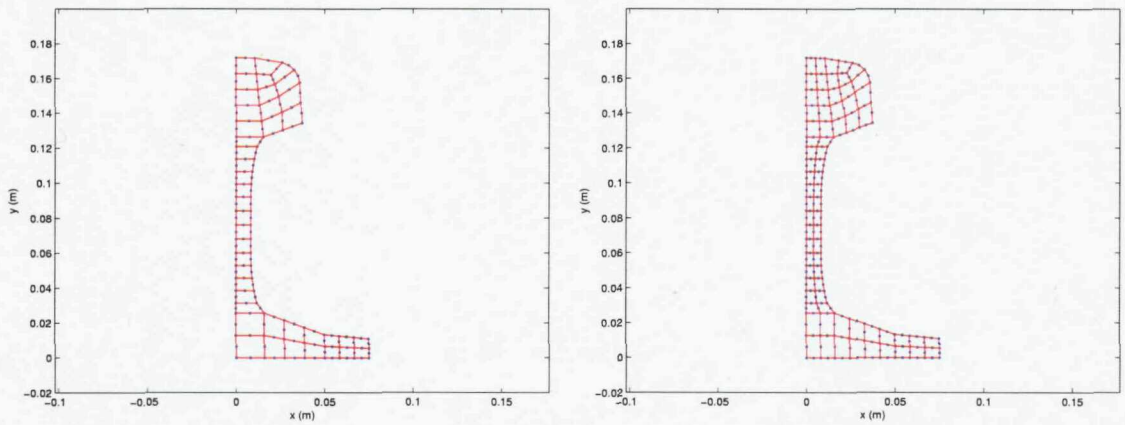

(a) (b)

Fig. 4.2. FE models for rail cross-section. (a) Model 1 as used in FE analysis in Chapter 3, (b) model 2.

As in the previous FE analysis, symmetric and anti-symmetric boundary conditions were applied at the vertical centreline of the cross-section. The symmetric boundary condition gives the vertical and symmetric longitudinal modes; the antisymmetric boundary condition gives the lateral, torsional and the antisymmetric longitudinal modes.

The dispersion curves predicted by the WFE method are shown in Fig. 4.3 for the two cross-sectional models of Fig. 4.2. As stated earlier, the WFE method utilises the exact wave solutions for the x direction. Hence it is anticipated that WFE analysis will yield more accurate natural frequencies than a conventional FE analysis for the same cross-sectional model, especially at high frequencies. For comparison the dispersion curves produced by the previous FE method are also illustrated in Fig. 4.3 for the same discrete wavenumbers.

From Fig. 4.3, it is found that the conventional FE analysis gives slightly lower frequencies for given wavenumbers than does the WFE analysis at high frequency. Referring to Table 3.1 in Chapter 3, which listed the natural frequencies for three different cross-sectional models having different mesh sizes, it can be seen that the natural frequencies predicted from the finer model become slightly lower than those created from the coarser model. Therefore, it is apparent that the FE method has generated more accurate natural frequencies than the WFE method for the same cross-sectional model, contrary to expectation. The reason for this result is that

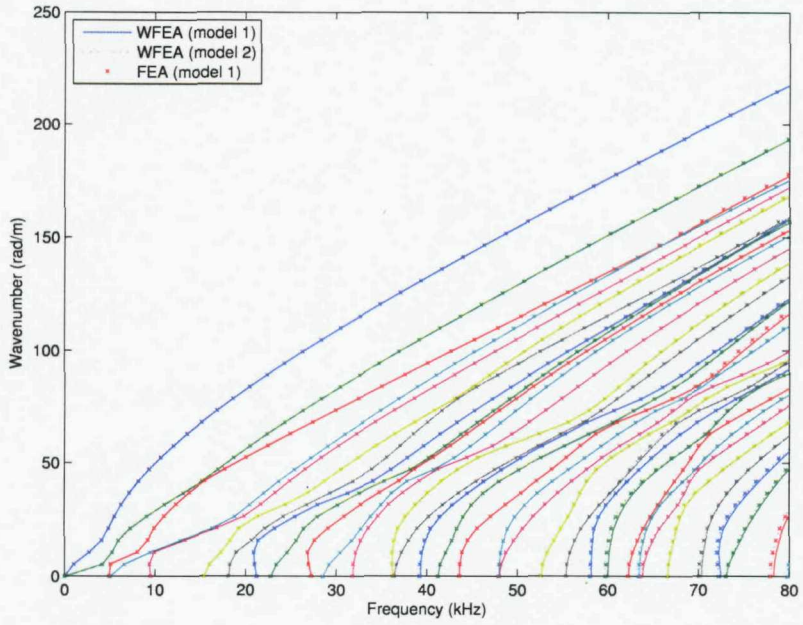

(a)

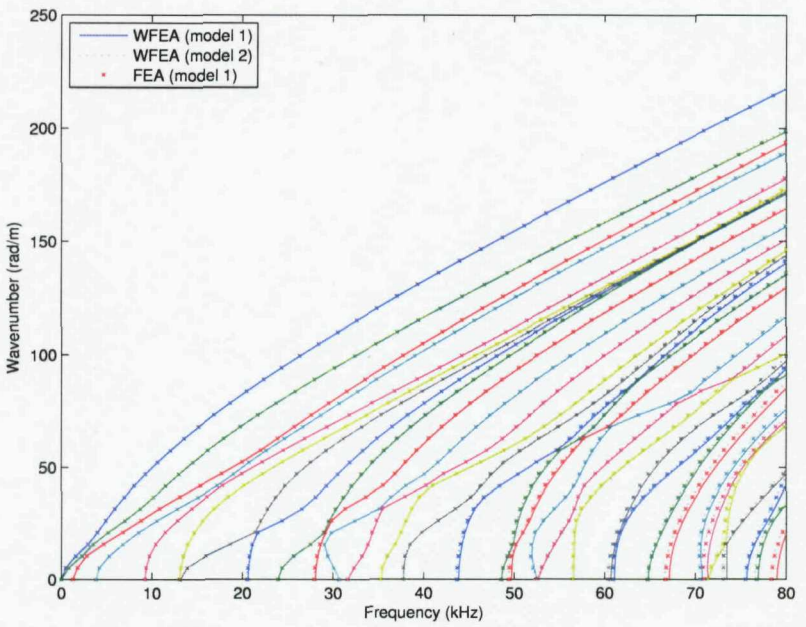

(b)

Fig. 4.3. Comparison of dispersion curves predicted by FE and WFE analyses for (a) the vertical and symmetric longitudinal waves, (b) the lateral, torsional and antisymmetric longitudinal waves.

the commercial FE software, ANSYS, used in the FE simulation, is making use of more sophisticated techniques to create mass and stiffness matrices than the WFE software.

Fig. 4.3 also indicates that the dispersion curves produced from model 2 by WFE analysis coincide very well with those obtained by FE analysis from model 1. Based on these comparison results, model 2 will be used as an appropriate cross-sectional model for WFE analysis from now on.

4.2.2 Modelling a rail on a foundation

Having established a suitable rail cross-sectional model, in this section, a foundation for the rail appropriate for the WFE method will be specified. As in Chapter 3, only the rail pad will be included in the foundation in this model as the contributions of the sleepers and ballast are limited to the low frequency region below 1 kHz [12].

In Chapter 3, the rail pad was considered as a massless single layer elastic foundation having a constant 'dynamic stiffness' approximated from a simple one-dimensional model. This was because it was impractical in the FE analysis to model it with a finer mesh and also not feasible to introduce a frequency-dependent dynamic stiffness in the ANSYS. However, it might be possible in this WFE analysis to model the rail pad with more layers of elements. If so, it would not be necessary to regard the dynamic stiffness separately because this model would be able to express the internal resonance effects properly by itself. WFE analysis makes this attempt substantially possible as it can create dispersion curves very quickly and easily, getting rid of the large manual post-processing which was inevitable with the FE analysis. Note, however, that it is not possible simply to specify a frequency-dependent stiffness even in the present WFE analysis due to the form of eigensolution used in which κ is specified and the system solved for ω.

To find an appropriate foundation model, three different models were considered with the two different cross-sectional FE meshes shown in Fig. 4.4. Foundation model A is the same as used in the previous FE analysis, having the constant dynamic stiffness of 10 times the nominal value. Model B has the same FE meshes

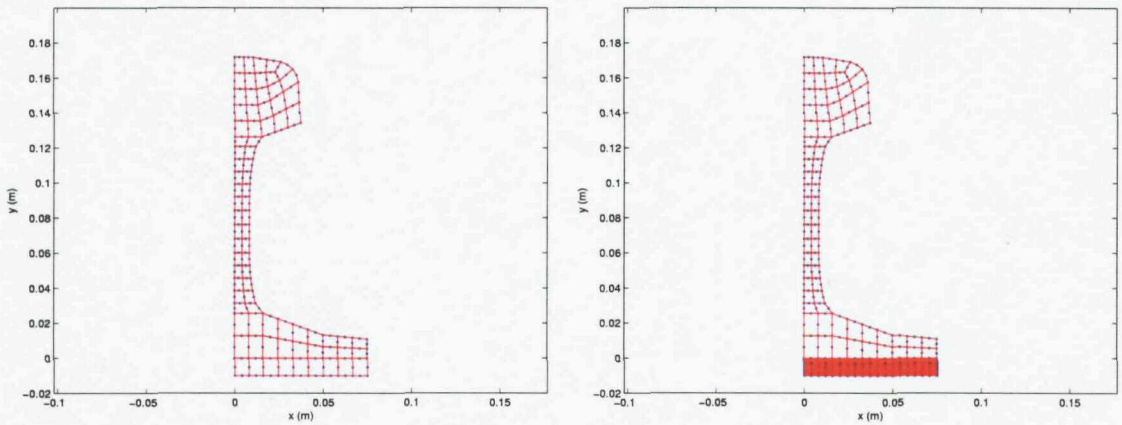

(a) (b)

Fig. 4.4. Cross-sectional FE models of a rail on foundation. (a) Model A and B, (b) model C.

Table 4.1. Details on foundation models.

Properties	Model A	Model B	Model C
Number of layers of elements	1	1	20
Density (ρ_p)	0 kg/m^3	1000 kg/m^3	1000 kg/m^3
Young's Moduli ($E_{p,x}$, $E_{p,y}$, $E_{p,z}$)	166.7 MN/m^2	16.7 MN/m^2	16.7 MN/m^2
Shear Moduli ($G_{p,xy}$, $G_{p,yz}$, $G_{p,zx}$)	22.3 MN/m^2	2.2 MN/m^2	2.2 MN/m^2

as model A but has a density of 1000 kg/m^3 for the foundation and does not have the higher dynamic stiffness. Model B was considered in order to investigate what happens if mass is included in the foundation in model A. As the final model, model C was generated with 20 layers in the vertical direction as well as the density of 1000 kg/m^3. The properties specified for each foundation model are listed in Table 4.1.

All dispersion curves evaluated from the three track models are shown in Fig. 4.5 for the vertical and symmetric longitudinal waves. Comparing Fig. 4.5(a) with Fig. 4.5(b), it can be seen that the dispersion curves obtained from model B possess several additional waves which propagate slowly along the track. These are internal waves propagating through the foundation only. The result shown in Fig. 4.5(b) indicates that if the density of the foundation is introduced, waves propagating through the rail foundation occur in the numerical simulation. Also it is clear that the number of waves travelling in the foundation is dependent on the number of de-

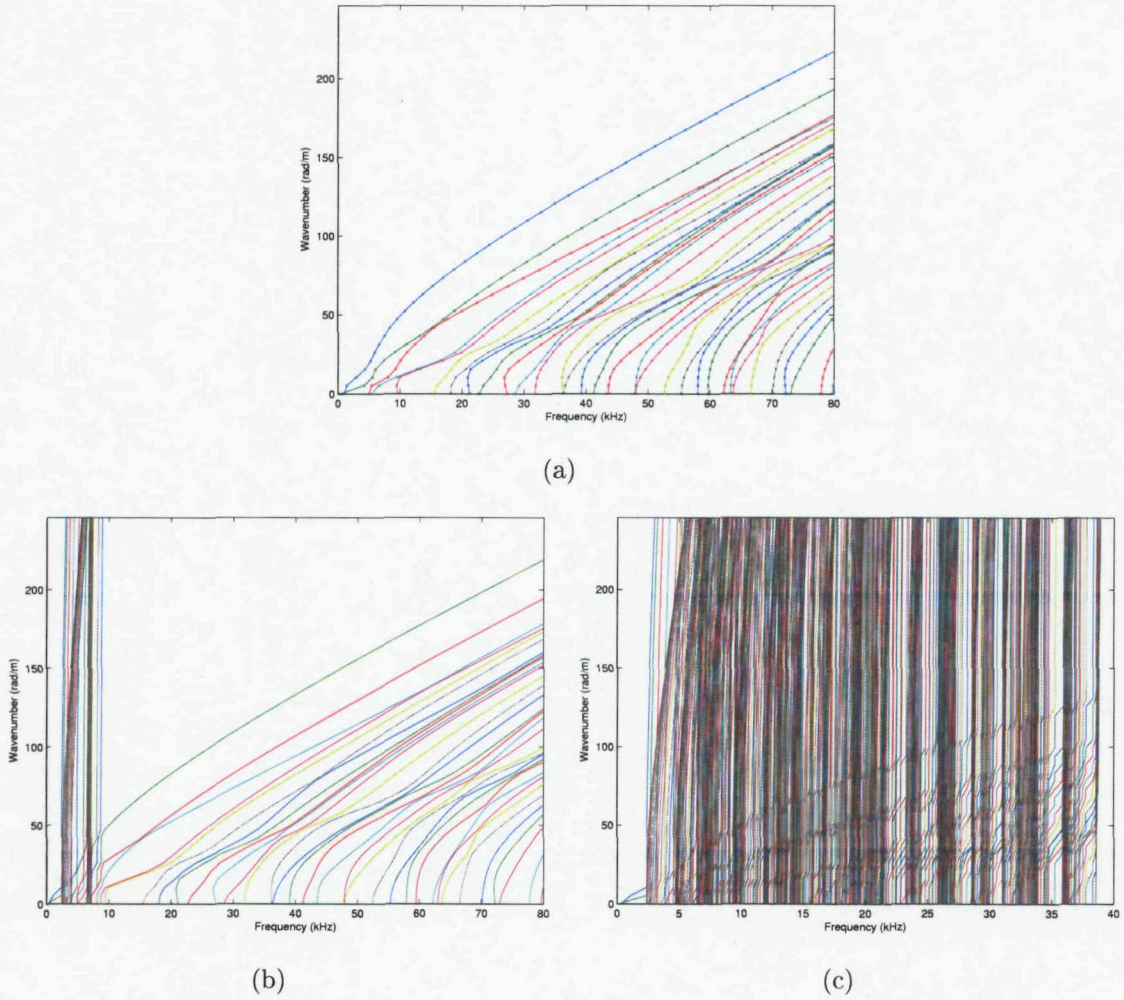

Fig. 4.5. Dispersion curves for the vertical and symmetric longitudinal waves created from (a) model A, (b) model B, (c) model C.

grees of freedom in the foundation model. This is demonstrated in Fig. 4.5(c) which shown results for model C up to 40 kHz. Here, most of the solutions correspond to internal waves in the foundation. Therefore, it is very difficult to identify the waves of interest propagating along the rail, rather than along the foundation, from these complicated curves. Note that the waves propagating along the foundation layer occur when the rail pad is modelled as a continuous foundation with mass. So, these internal waves would not appear if the rail pad is modelled as a discrete rail foundation.

As discussed in section 4.1.1, the stiffness terms which make wave behaviour along the x direction are contained in the matrices $\mathbf{K}_2$ and $\mathbf{K}_1$. So it was examined what happens to the dispersion relations if the stiffness components for the rail

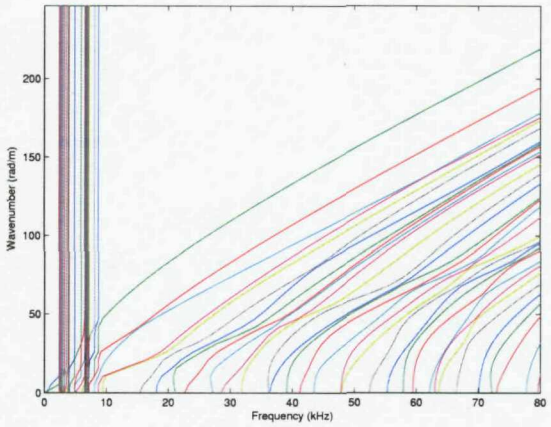

Fig. 4.6. Dispersion curves for the vertical and symmetric longitudinal waves created from model B with $\mathbf{K}_2$ and $\mathbf{K}_1$ corresponding to the rail foundation set to zero.

pad in $\mathbf{K}_2$ and $\mathbf{K}_1$ are set to zero. The dispersion curves obtained are shown in Fig. 4.6 for model B. This figure reveals that the dispersion curves corresponding to the waves in the foundation are still present but become straight vertical lines, implying that they are not propagating waves. From this figure, it was found that this method is not useful to remove the internal waves in the foundation from the dispersion curves in Fig. 4.5(b), particularly in Fig. 4.5(c).

It turned out from Fig. 4.5 that although the WFE method can deal even with the complicated model C, the solutions are not suitable for this study. In other words, most of the dispersion relations generated from model C depict the waves propagating along the foundation, not along the rail. Also because there are many solutions for a given wavenumber, longer computation time is required unnecessarily to create dispersion curves. Consequently, model A, which has zero density and constant dynamic stiffness in the foundation, will be used again as a suitable foundation model in this WFE analysis.

4.3 Prediction of Dispersion Relations and Group Velocities

The track model appropriate to this WFE analysis was identified in the previous section. For this track model, the predicted dispersion curves are shown in Fig. 4.7. In FE analysis, the increment of discrete wavenumber, $\Delta\kappa$, was inversely proportional to the length of the FE model. In this WFE method, however, the

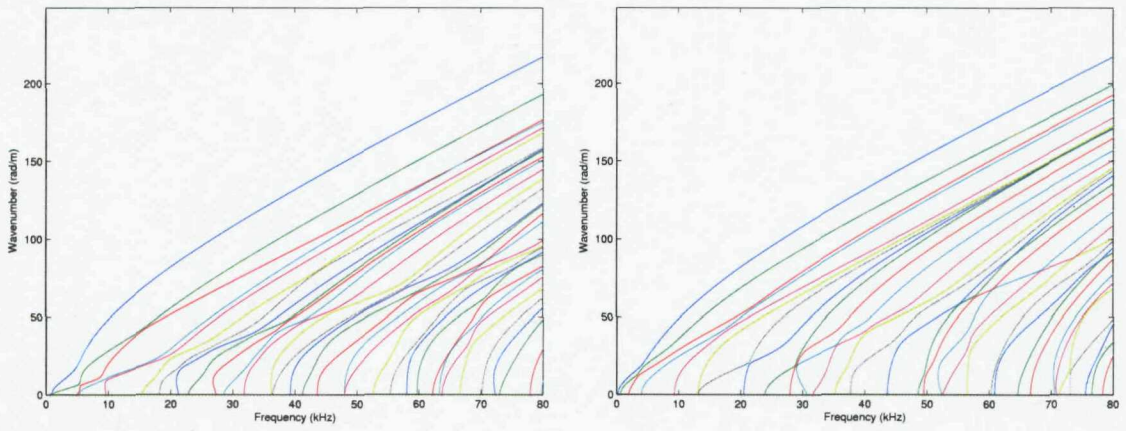

(a) (b)

Fig. 4.7. Predicted dispersion curves for (a) the vertical and symmetric longitudinal waves, (b) for the lateral, torsional and antisymmetric longitudinal waves.

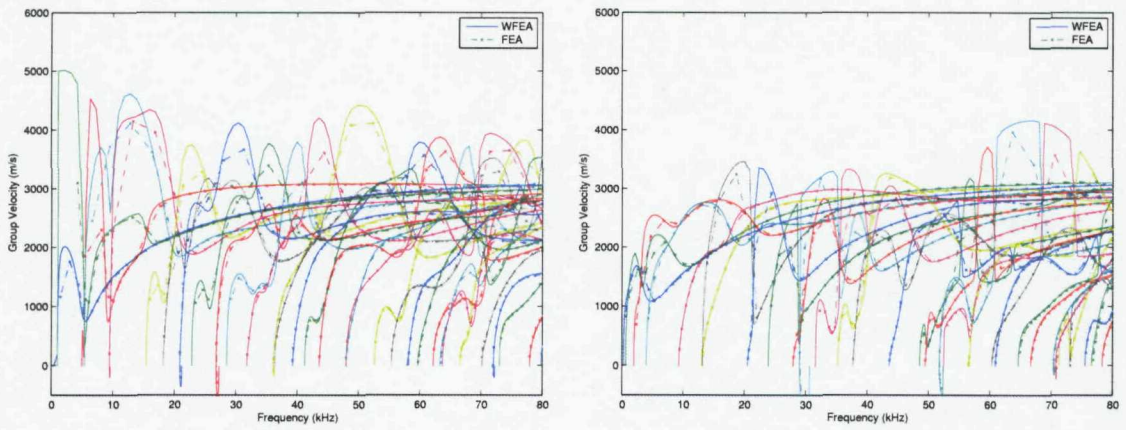

(a) (b)

Fig. 4.8. Comparison of group velocities predicted by the WFE and FE methods for (a) the vertical and symmetric longitudinal waves, (b) the lateral, torsional and antisymmetric longitudinal waves.

discrete wavenumbers can be selected arbitrarily allowing a finer resolution. In this prediction, the wavenumber increment used was 1.3 rad/m, which is a quarter of that specified in FE analysis in Chapter 3, so that smoother curves were generated as illustrated in Fig. 4.7.

As stated above, the group velocities can be readily predicted by Eq.(4.14) for each wave. The group velocities obtained by the WFE method are presented in Fig. 4.8. They are also compared with the previous FE analysis results from Fig. 3.16. The FE and WFE methods yield generally similar results but the WFE

method produces more accurate and smoother curves than the FE method. Now it becomes much easier to recognize each line's behaviour, particularly for the longitudinal waves which have the highest group velocities.

The improved graphical result obtained by the WFE method mainly results from the finer wavenumber resolution. That is, if a finer wavenumber resolution were used by extending the length of the model in FE analysis, similarly smooth curves should be obtained. However, to achieve comparable results to those obtained by the WFE method in Fig. 4.8, an FE model of length 1.2 m needs to be used, which would dramatically increase computational requirements. Moreover the finite difference approach requires an even finer wavenumber resolution than the direct approach used with the WFE method.

4.4 Prediction of Decay Rates

So far the track model has been analysed without considering any damping in the structure. From now on damping will be included in the track model to predict decay rates of the propagating waves.

There are two damping components in the track model: the damping in the rail, η_r, and in the foundation, η_p. The stiffness matrix of this damped track model can be separated into two parts

$$\mathbf{K_d} = (1 + j\eta_r)\mathbf{K_r} + (1 + j\eta_p)\mathbf{K_p} \tag{4.25}$$

where $\mathbf{K_r}$ and $\mathbf{K_p}$ denote the stiffness matrices for the rail and foundation, respectively. These stiffness matrices possess separate material properties for the rail and foundation as specified in Table 4.2. Because of the different dampings in the rail

Table 4.2. Elastic moduli of the rail and foundation for the generation of stiffness matrices in WAFER.

Elastic Modulus	$\mathbf{K_r}$	$\mathbf{K_p}$
Young's Modulus of rail (E_r)	200 GPa	0 GPa
Young's Modulus of foundation (E_p)	0 MPa	166.7 MPa
Shear Modulus of foundation (G_p)	0 MPa	22.7 MPa

and foundation, the damped wavenumber of this track model has to be slightly modified from Eq.(4.23).

For this track model a damped wavenumber, κ_d, can be expressed as

$$\kappa_d = \kappa + \frac{\partial \kappa_d}{\partial \eta_r}\Big|_{\eta_r=0} \eta_r + \frac{\partial \kappa_d}{\partial \eta_p}\Big|_{\eta_p=0} \eta_p \quad . \tag{4.26}$$

Since the equation of motion has to be satisfied for the derivatives with respect to η_r and η_p,

$$\frac{\partial}{\partial \eta_r}\left\{[(1+j\eta_r)\mathbf{K_r} + (1+j\eta_p)\mathbf{K_p} - \omega^2\mathbf{M}]\tilde{\mathbf{\Phi}}\right\} = \mathbf{0} \quad , \tag{4.27}$$

$$\frac{\partial}{\partial \eta_p}\left\{[(1+j\eta_r)\mathbf{K_r} + (1+j\eta_p)\mathbf{K_p} - \omega^2\mathbf{M}]\tilde{\mathbf{\Phi}}\right\} = \mathbf{0} \quad . \tag{4.28}$$

By following the same process as described in section 4.1.4, the two derivative terms in Eq.(4.26) become

$$\frac{\partial \kappa_d}{\partial \eta_r}\Big|_{\eta_r=0} = \frac{-j\tilde{\mathbf{\Phi}}^H \mathbf{K_r} \tilde{\mathbf{\Phi}}}{\tilde{\mathbf{\Phi}}^H \mathbf{K}' \tilde{\mathbf{\Phi}}} \quad , \quad \frac{\partial \kappa_d}{\partial \eta_p}\Big|_{\eta_p=0} = \frac{-j\tilde{\mathbf{\Phi}}^H \mathbf{K_p} \tilde{\mathbf{\Phi}}}{\tilde{\mathbf{\Phi}}^H \mathbf{K}' \tilde{\mathbf{\Phi}}}. \tag{4.29}$$

where $\mathbf{K} = \mathbf{K_r} + \mathbf{K_p}$. Therefore, the damped wavenumber is obtained as

$$\kappa_d = \kappa - j\frac{\tilde{\mathbf{\Phi}}^H(\mathbf{K_r}\eta_r + \mathbf{K_p}\eta_p)\tilde{\mathbf{\Phi}}}{\tilde{\mathbf{\Phi}}^H \mathbf{K}' \tilde{\mathbf{\Phi}}} \tag{4.30}$$

Finally the decay rates of waves propagating along the track can be evaluated from the imaginary part of κ_d as

$$\Delta = 8.686 \ \frac{\tilde{\mathbf{\Phi}}^H(\mathbf{K_r}\eta_r + \mathbf{K_p}\eta_p)\tilde{\mathbf{\Phi}}}{\tilde{\mathbf{\Phi}}^H \mathbf{K}' \tilde{\mathbf{\Phi}}} \quad . \tag{4.31}$$

As presented above, the damping loss factors of the rail and rail pad are required for this track model. The material damping loss factors of the rail and rail pad are set to constant values of 0.0002 and 0.2, respectively, as specified in Chapter 3. The predicted decay rates are shown in Fig. 4.9, along with the previous FE analysis results. As revealed in Fig. 4.9, the decay rates predicted from the WFE and FE methods are almost the same but again the WFE method creates smoother curves than the FE method.

In practice, a range of rail pads with different stiffnesses is used in track. This difference in stiffness will bring a change in $\mathbf{K_p}$ in Eq.(4.30) which will affect the

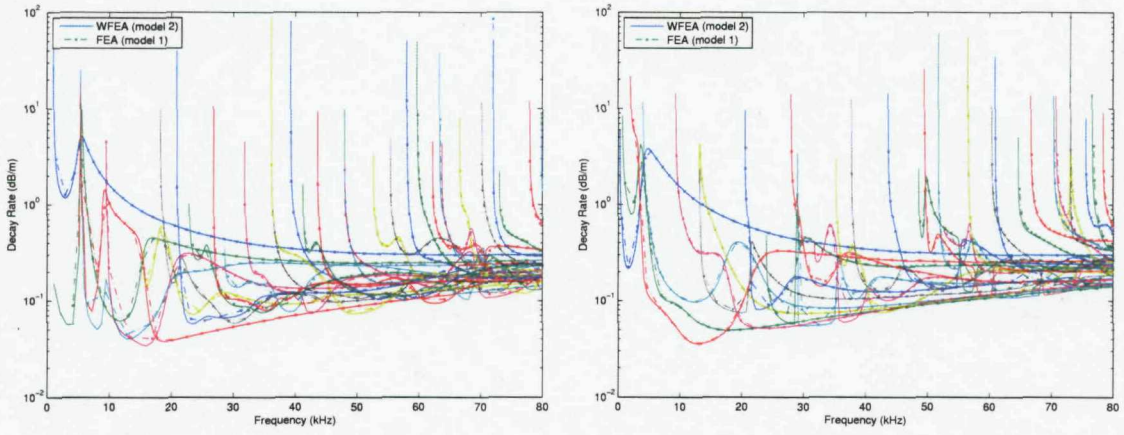

(a) (b)

Fig. 4.9. Comparison of decay rates predicted by the WFE and FE methods for (a) the vertical and symmetric longitudinal waves, (b) the lateral, torsional and antisymmetric longitudinal waves.

imaginary part of the damped wavenumber. In order to investigate the effects of the foundation stiffness on decay rates, different values of stiffness are applied here. The values chosen aim to represent the soft and stiff ends of the stiffness range of rail pads. In this prediction, the respective stiffnesses of the soft and stiff rail pads are considered as 80 MN/m and 1500 MN/m in the vertical direction and 11 MN/m and 200 MN/m in the lateral direction, respectively [12, 30]. (The chosen stiffnesses of the rail pad for the decay rate calculation shown in Fig. 4.9 are 150 MN/m and 20 MN/m in the vertical and lateral directions, respectively.) In each case a factor of 10 is applied to the stated values to represent the dynamic stiffening.

The predicted decay rates are presented in Fig. 4.10 and Fig. 4.11 for these soft and stiff foundation models. These figures show that with the soft pad there are more waves with low decay rates, whereas with the stiff pad most of the waves have higher decay rates. However, it turns out that the lowest decay rates for frequencies greater than around 20 kHz are not significantly affected by whether the rail pads are soft or stiff. This behaviour can be explained from the wave deformation shapes. Waves inducing large deformations in the rail foot are mainly affected by the stiffness changes in the foundation. In other words, the most slowly decaying waves propagate only through localized regions, such as the rail head and the web. Consequently, the decay rates of these localized waves are primarily dependent on the damping of the rail, not the rail pad. It is apparent from this sensitivity check that the lower

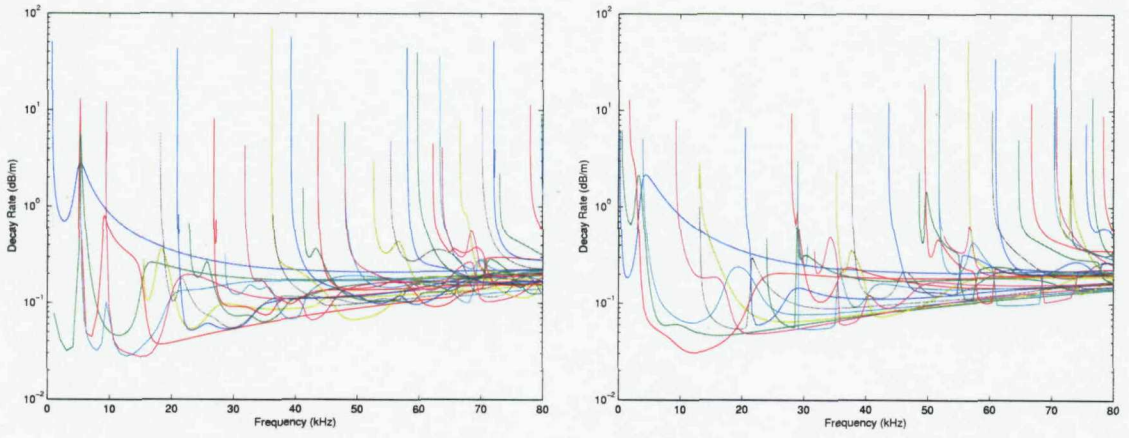

(a) (b)

Fig. 4.10. Predicted decay rates with the soft rail pad of 80 MN/m for (a) the vertical and symmetric longitudinal waves, (b) the lateral, torsional and antisymmetric longitudinal waves.

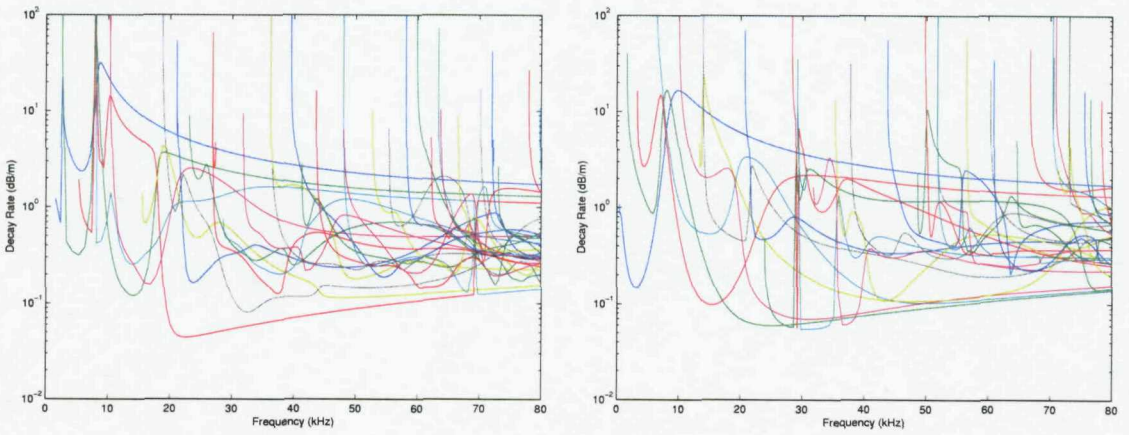

(a) (b)

Fig. 4.11. Predicted decay rates with the stiff rail pad of 1500 MN/m for (a) the vertical and symmetric longitudinal waves, (b) the lateral, torsional and antisymmetric longitudinal waves.

limits of the decay rates at frequencies above 20 kHz are directly associated only with the structural damping of the rail. Therefore, the structural damping of the rail is a principal factor in determining long range wave propagation, even when the rail pad is quite stiff. This result implies that the lower limits of the decay rates will be little changed although the rail pad is modelled as a damper, which was discussed in Section 3.1.3. Structural damping loss factors of rails will be measured and discussed in Chapter 5.

4.5 Prediction of Measurable Waves on the Rail Surface

As described previously, there are 63 different waves propagating below 80 kHz in the track model. It will, therefore, be worthwhile identifying which waves among them belong to which regions of the rail cross-section and also which ones are measurable on the rail surface at different locations. Since dynamic responses are usually measured normal to the rail surface, the energy distributions around the rail surface can provide useful information on which waves are detectable in a specific region. For instance, the deformation energies of waves shown in Fig. 3.11 which have local deformations are concentrated in local regions. To quantify this feature, the 'energy' associated with different parts of the rail surface has been calculated from the predicted displacement of the track model produced by the WFE (or FE) method.

For this purpose, four separate regions have been specified on the rail surface as shown in Fig. 4.12. These are the top of the rail head, the side of the rail head, the middle of the web and the top of the foot. In this figure, y and z denote lateral and vertical directions, respectively. Then the normalized energies for each region and each direction were predicted using

$$Q_{j,z} = \frac{\frac{1}{n_j}\sum_{n_j} |\tilde{\Phi}_{z,j}|^2}{\frac{1}{N_s}\sum_{N_s} \|\tilde{\Phi}_s\|^2}, \tag{4.32}$$

where $\tilde{\Phi}_s$ denotes displacements in all directions at all nodes on the rail surface,

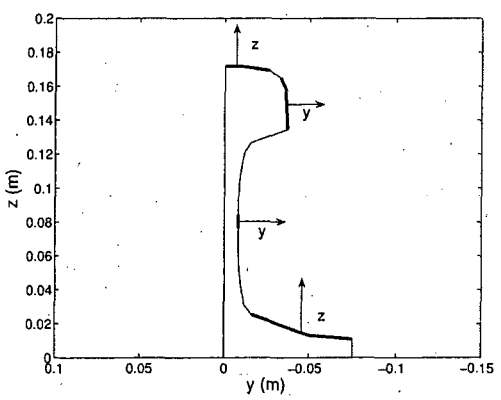

Fig. 4.12. Four regions specified for the prediction of energy distribution on the rail surface.

$\| \ \|$ is the vector norm, $\tilde{\Phi}_{z,j}$ is displacement in the z direction (and similarly for the x and y directions) at nodes belonging to the region j, n_j is the number of nodes in the region j and N_s is the total number of nodes on the rail surface. Therefore, this quantity would depict implicitly which waves are measurable in region j among all the waves in the system. In this calculation, no information on the input force or modal participation factor is included so that all the modes are treated equally. These measurable waves predicted by Eq.(4.32) will be used in comparison to the measured results in subsequent chapters of this thesis.

4.5.1 Measurable waves in the vertical and lateral directions

The predicted dispersion curves at each region are illustrated in Fig. 4.13 in terms of the energy ratio given in Eq.(4.32). In these figures, all curves from Fig. 4.7 are present but the strength of the line colour depicts the level of the normalized energy at each frequency. In other words, the darker curves correspond to waves that are the more detectable. Fig. 4.13(a) reveals that only a single type of wave, i.e., the head bending wave, is predominantly measurable at the top of the rail head below 32 kHz. This is the wave shown in Fig. 3.11(c). The changes of colours along this line indicate that the rail head bending wave is maintained through the wave mode conversions as stated before. Other vertical waves that are significant tend to cut-on at around 32 kHz. A similar phenomenon is obtained at the side of the rail head for the lateral direction (Fig. 4.13(b)) where the wave seen in Fig. 3.11(e) is most important. Conversely, at the middle of the web a large number of waves are present throughout the whole frequency range, but the 1^{st} order web bending wave (Fig. 3.11(b)), i.e., the green line in Fig. 4.13(c), is prominent above 10 kHz. At the top of the foot, foot bending waves will possess most deformation energy.

In the same manner, the group velocities of waves that are detectable at each region can be presented in terms of the energy ratio. These measurable group velocities predicted at each region will be shown in Chapter 6 together with the measured ones.

The predicted decay rates at each region are shown in Fig. 4.14 also in terms of the energy ratio. Again, all lines from Fig. 4.9 are plotted, but the strength of line colour depicts the level of normalized energy at each frequency. Fig. 4.14(a)

shows that the minimum decay rate of 0.04 dB/m would appear around 20 kHz if it is measured at the top of the rail head. It has to be noted from Fig. 4.14(a) that the decay rates grow when the wave modes are swapped with each other. For example, around 15 kHz, the green coloured and red coloured waves are exchanging their deformation shapes. At this point, the low decay rate wave becomes the higher decay rate wave and vice versa. Hence the decay rate increases when the two lines cross. The deformation shape of the wave having the minimum decay rate at the top of the rail head is illustrated in Fig. 4.15(a) which was obtained from the previous

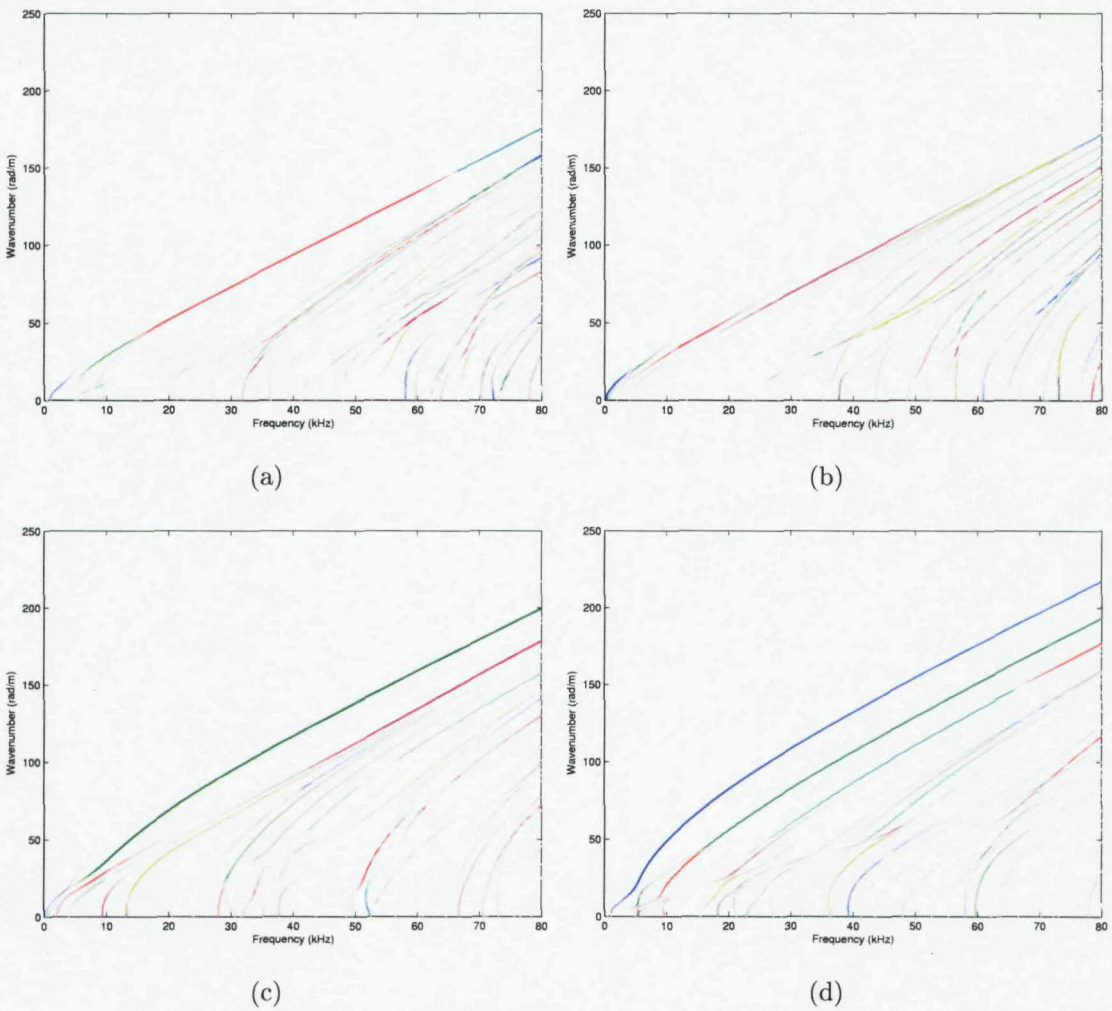

Fig. 4.13. Predicted dispersion curves in terms of the energy ratio for the vertical and lateral directions. (a) At the top of the rail head for the vertical and symmetric longitudinal waves, (b) at the side of the rail head for the lateral, torsional and antisymmetric longitudinal waves, (c) at the middle of the web for the lateral, torsional and antisymmetric longitudinal waves, (d) at the top of the foot for the vertical and symmetric longitudinal waves.

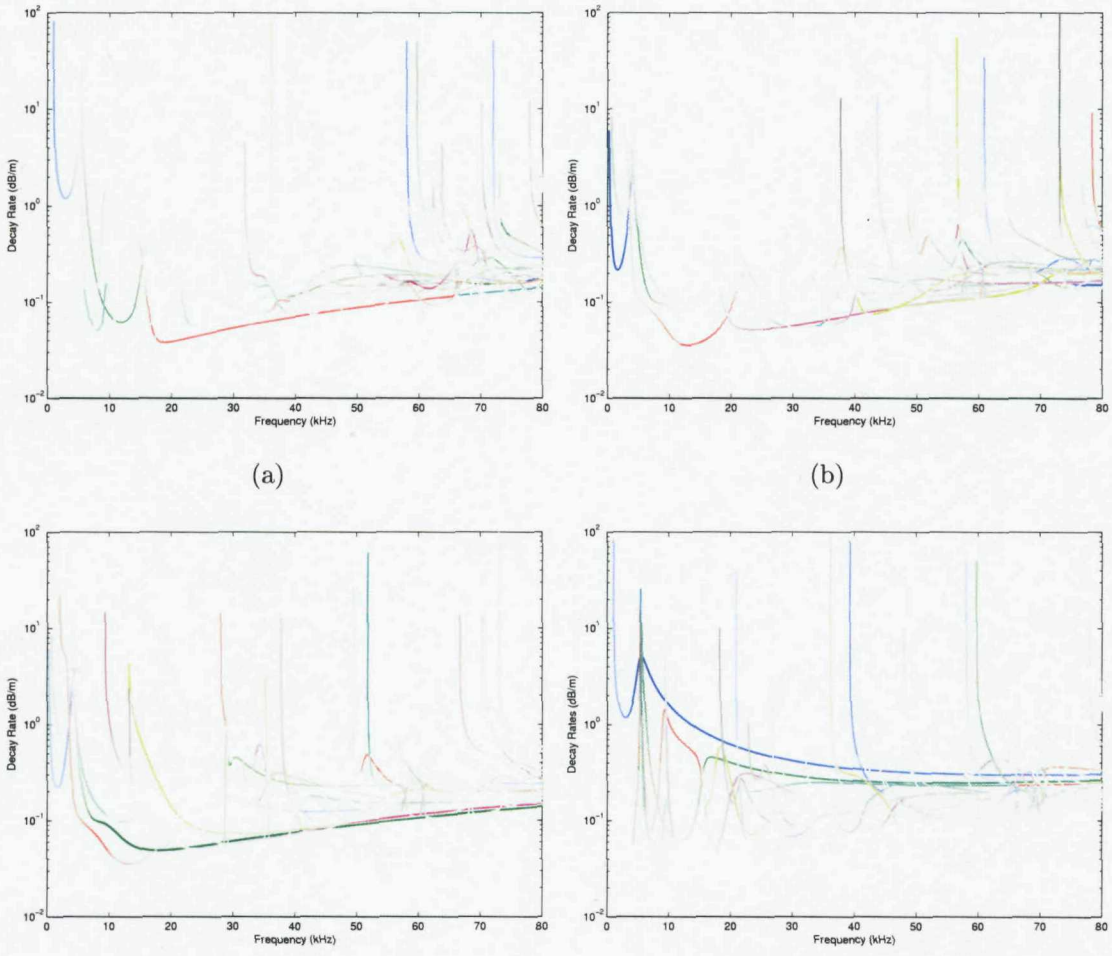

Fig. 4.14. Predicted decay rates in terms of the energy ratio in the vertical and lateral directions. (a) At the top of the rail head for the vertical and symmetric longitudinal waves, (b) at the side of the rail head for the lateral, torsional and antisymmetric longitudinal waves, (c) at the middle of the web for the lateral, torsional and antisymmetric longitudinal waves, (d) at the top of the foot for the vertical and symmetric longitudinal waves.

Fig. 4.15. Simulated deformation shapes of waves which have the minimum decay rates (a) at 20045 Hz in Fig. 4.14(a), (b) at 13028 Hz in Fig. 4.14(b).

FE analysis. For the case of the lateral response of the rail head, it was determined in the simulations that the minimum decay rate of about 0.04 dB/m would occur around 15 kHz and its deformation shape is shown in Fig. 4.15(b). At the middle of the web the most measurable wave is the 1^{st} order web bending wave and its decay rate has a minimum at around 20 kHz of about 0.05 dB/m. In the case of the foot, much larger decay rates are inevitable because of the greater contribution of the rail pad.

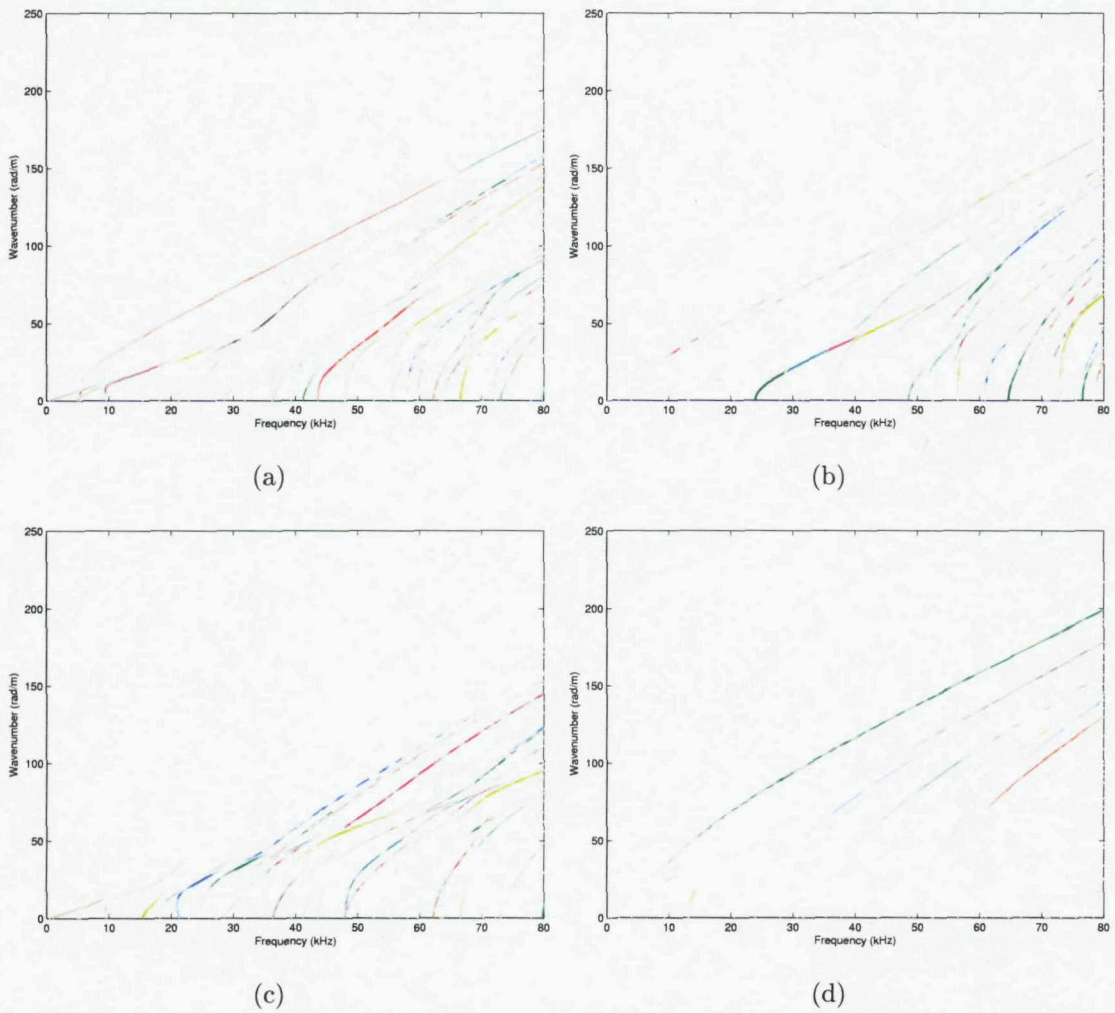

Fig. 4.16. Predicted dispersion curves of measurable waves in the longitudinal direction (a) at the top of the rail head for the vertical and symmetric longitudinal waves, (b) at the side of the rail head for the lateral, torsional and antisymmetric longitudinal waves, (c) at the middle of the web for the vertical and symmetric longitudinal waves, (d) at the middle of the web for the lateral, torsional and antisymmetric longitudinal waves.

4.5.2 Measurable waves in the longitudinal direction

For the longitudinal direction, the predicted dispersion curves measurable at the top of the rail head, at the side of the rail head and at the middle of the web, are illustrated in Fig. 4.16 in terms of the energy ratio. In this figure, any types of waves having large deformations in the longitudinal direction will appear with relatively strong line colours, not just purely longitudinal waves. This includes the vertical and lateral bending waves in the rail head which appear in Fig. 4.16(a) and (b) with considerable strength. It is found from Fig. 4.16(a) that the symmetric longitudinal waves appear to have large deformation between 10 kHz and 35 kHz at the top of the rail head. On the other hand, Fig. 4.16(b) shows that the antisymmetric longitudinal waves appear to be measurable above 23 kHz at the side of the rail head. Figs. 4.16(c) and (d) indicate that the symmetric longitudinal waves are present at the middle of the web but no antisymmetric longitudinal waves are found there. (The green line in Fig. 4.16(d) is the 1^{st} order web bending wave). That is because the web is too narrow in the y direction to reveal considerable antisymmetric deformation in the longitudinal direction.

The predicted decay rates at these three regions for the waves which have large deformations in the longitudinal direction are illustrated in Fig. 4.17 in terms of the energy ratio. Fig. 4.17(a) illustrates that at the top of the rail head the minimum decay rate of the longitudinal waves is about 0.04 dB/m at around 15 kHz. (The wave coloured purple in Fig. 4.17(a)). At the side of the rail head and at the middle of the web, they are about 0.05 dB/m at around 32 kHz and 0.06 dB/m at around 24 kHz, respectively. The mode shapes of these longitudinal waves having the minimum decay rates are illustrated in Fig. 4.18; these were obtained from the previous FE analysis. From this simulation, it was confirmed that the longitudinal waves do not have significantly lower decay rates than other types of waves despite having a higher group velocity. This is because they normally induce considerable deformations of the rail foundation which has a large damping loss factor.

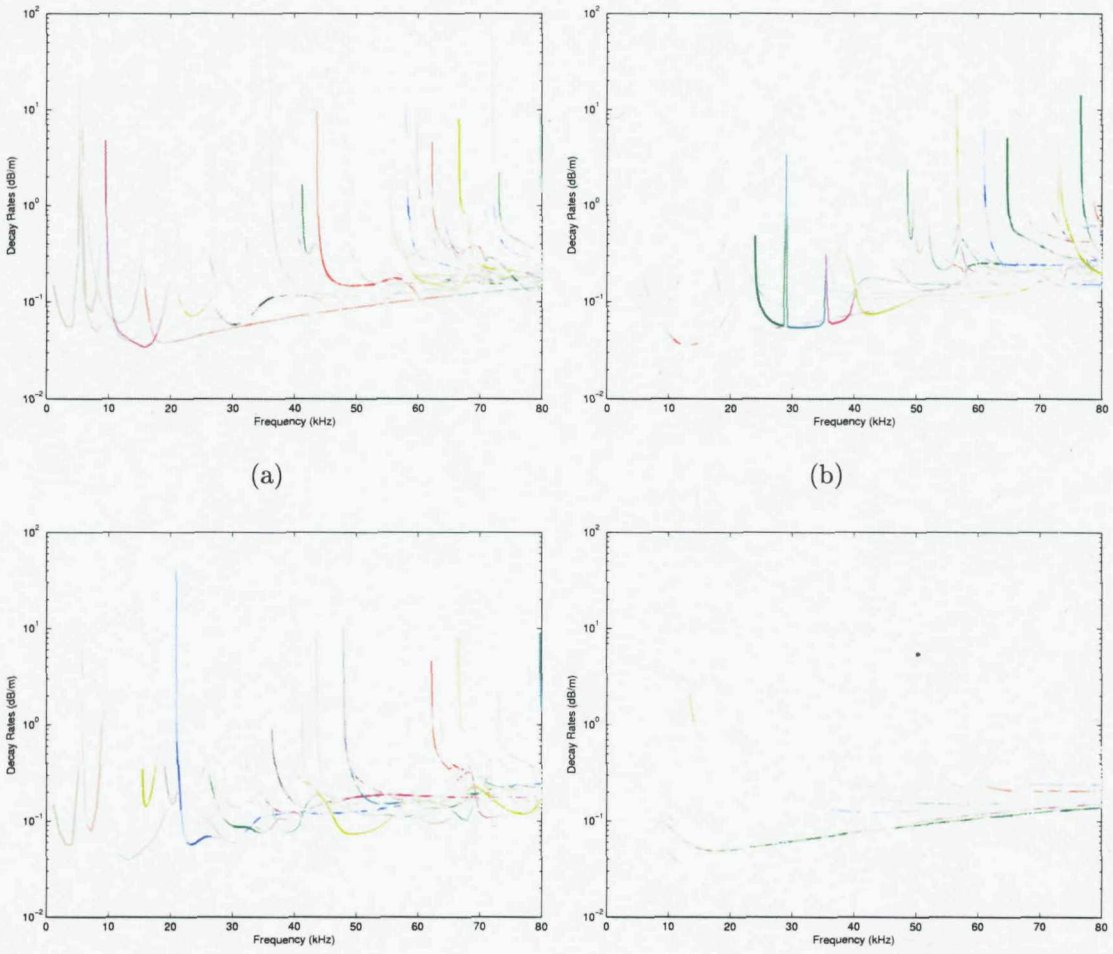

Fig. 4.17. Predicted decay rates of measurable waves in the longitudinal direction (a) at the top of the rail head for the vertical and symmetric longitudinal waves, (b) at the side of the rail head for the lateral, torsional and antisymmetric longitudinal waves, (c) at the middle of the web for the vertical and symmetric longitudinal waves, (d) at the middle of the web for the lateral, torsional and antisymmetric longitudinal waves.

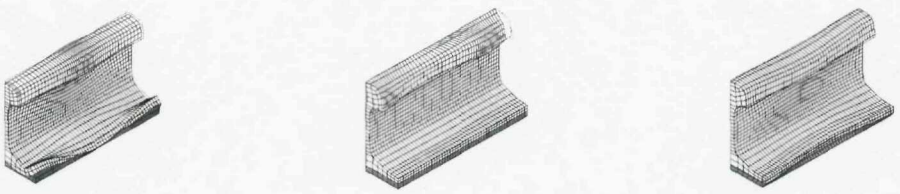

Fig. 4.18. Deformation shapes of the longitudinal waves which have the minimum decay rates in Fig. 4.17. (a) At 16867 Hz in Fig. 4.17(a), (b) at 32365 Hz in Fig. 4.17(b), (c) at 23223 Hz in Fig. 4.17(d).

4.6 Summary

In this chapter, the WFE method was employed as an alternative and more advanced approach instead of the conventional FE method. This method requires only a cross-sectional model by using wave solutions for the direction in which waves propagate, which makes it very efficient.

An appropriate cross-sectional track model was created as a rail on a distributed elastic foundation. A cross-sectional model that had twice as many elements as that used in the FE analysis was chosen as a suitable one in this method. The same foundation model was used as specified in Chapter 3, which was a massless elastic layer with the stiffness increased by a factor of 10 to represent dynamic stiffening.

In this WFE method, the group velocity and decay rates are readily formulated for each individual wave. Comparing the results produced from the FE and WFE methods, it was observed that both methods produce almost the same dispersion relations and decay rates but the WFE method creates smoother curves more efficiently, particularly for the group velocities. Consequently it was confirmed that the WFE method is more relevant for the work presented in this thesis because it is much faster and more efficient than the ordinary FE method.

In this chapter, waves measurable on the rail surface were also predicted by quantifying deformation energies in several regions of the rail cross-section. The most measurable waves which have the lowest decay rates were

- the vertical bending wave which has a local deformation in the rail head
- the lateral bending wave which has deformation in both the rail head and web
- the 1^{st} order web bending wave in the web.

The reason why a wave can travel furthest through the rail head is shown to be because the wave makes little deformation of the rail foundation which has a large damping loss factor. Furthermore, it was predicted that the longitudinal waves do not propagate further than other types of waves. This is because they induce considerable deformations of the rail foundation.

Finally, a parameter study was performed on the effect of foundation stiffness on decay rates and it was revealed that the minimum decay rates are directly related to the damping of the rail, not of the foundation. The structural damping loss factors of rails will be investigated in Chapter 5 based on experiments.

Chapter 5

Damping Loss Factors of Rails

In Chapter 4, the decay rates of waves propagating along a railway track were predicted by WFE analysis. It was identified from this simulation that the minimum decay rates are directly determined by the structural damping of the rail, particularly for the waves with the lowest decay rates at frequencies above 20 kHz. Therefore, it can be said that structural damping of a rail is a primary input parameter in the decay rate prediction. However, in those predictions, the structural damping loss factor of the rail was assumed simply as a constant value of 0.0002 for the entire frequency range. In this chapter, in order to check this assumption and determine the value as a function of frequency, structural damping loss factors have been measured for frequencies up to 80 kHz from impact hammer tests on samples of three different types of rail. Then the decay rates are improved using the measured damping factors for rails.

5.1 Measurement for Damping Loss Factors of Rails

For well separated modes of a structure, the damping ratio, ζ_n, and damping loss factor, η_n, of the n^{th} resonance mode can be estimated from its resonance peak and half power bandwidth using

$$\zeta_n = \frac{\omega_b - \omega_a}{2\omega_n} \quad , \tag{5.1}$$

$$\eta_n = 2\zeta_n \quad , \tag{5.2}$$

where ω_n is the resonance frequency of the n^{th} mode, ω_a and ω_b denote its half power frequencies, i.e., the frequencies at which the response is 3 dB lower than the resonance peak value [32].

Measurements have been carried out on three short sections of rail. The rail types used for this measurement are UIC60, 56E1 (both conventional rail steel) and MHT (Mill Heat Treated) which has the same cross-section as that of 56E1. The lengths of the samples used are 0.6 m, 0.45 m and 0.31 m, respectively. Among these rail samples, the MHT rail is more brittle than the others due to the additional heat treatment applied to it.

In order to excite the rails, a miniature impact hammer, PCB 086D80, was used to generate a broadband signal. According to the manufacturer's specification sheet, the excitation frequency range of this impact hammer is limited to 20 kHz. Lanza di Scalea *et al.* [9], however, reported that they were able to excite frequencies up to between 40 kHz and 50 kHz with this type of hammer. Piezoelectric accelerometers, PCB 352C22, attached by beeswax, were used to measure the response. Again the specification sheet indicates that this accelerometer has a limited measurement range of up to 20 kHz and the mounting resonance frequency of the accelerometer is specified as around 90 kHz. Since the extraction of damping using Eq.(5.1) does not require a calibrated frequency response amplitude, however, this will not adversely affect the measurement.

The same experiment was carried out twice for the low and high frequency regions separately with different data acquisition units. For the region below 20 kHz, the measurement was performed using an 8 channel data acquisition unit which works with its own exclusive signal analyser. With this equipment, the frequency resolution is automatically determined by setting the frequency bandwidth. That is, the frequency resolution, Δf, becomes wider as the overall bandwidth broadens. If the frequency span is set to 42 kHz as its maximum, the frequency resolution would be acceptable at the higher frequency region but would be insufficient at lower frequencies where the resonance peaks are relatively sharp. So, in order to maintain sufficient frequency resolution at low frequencies, the measurements were carried out using several different bandwidths, namely, from 0 to 5 kHz, 0 to 10 kHz and 0 to 20 kHz. The corresponding frequency resolutions were about 0.2 Hz,

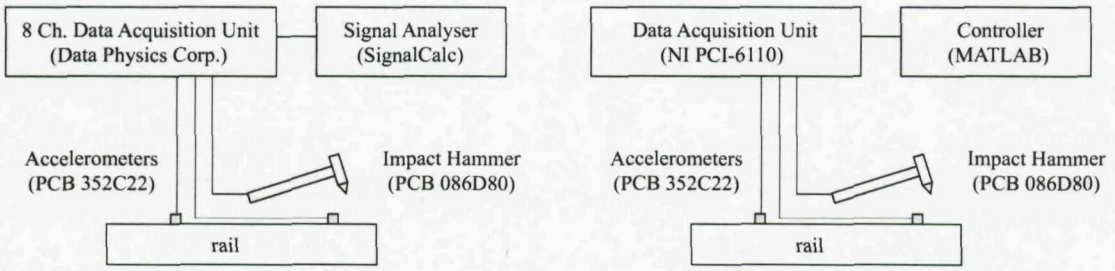

Fig. 5.1. Experimental setups for damping loss factor measurement for (a) low frequencies up to 20 kHz, (b) high frequencies up to 80 kHz.

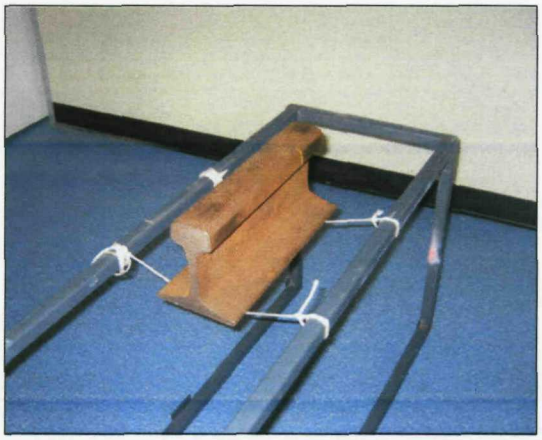

Fig. 5.2. A rail sample supported on rope.

0.39 Hz and 0.78 Hz, respectively. Damping values were then determined for modes in limited frequency bands of 0 to 5 kHz, 5 kHz to 10 kHz, 10 kHz to 20 kHz from each measurement. For the high frequency range between 20 kHz and 80 kHz, an NI data acquisition board, PCI 6110, was used with a sampling rate of 200 kHz and the resulting frequency interval was 1 Hz. (The measurement range was 0 to 80 kHz but only data above 20 kHz were used.) Regardless of the frequency ranges and acquisition units, the same impact hammer and accelerometer were used as exciter and sensor. The measurement setup is shown in Fig. 5.1. In these experiments, the rail samples were supported on soft ropes as illustrated in Fig. 5.2. It was found from the measurement that the resonance frequencies of this mounting system are below 50 Hz and are therefore unlikely to affect measurements of damping above 1 kHz.

The rail specimens were excited at the end of the sample at the top and side of the railhead and the responses were measured at two points on the top and side of

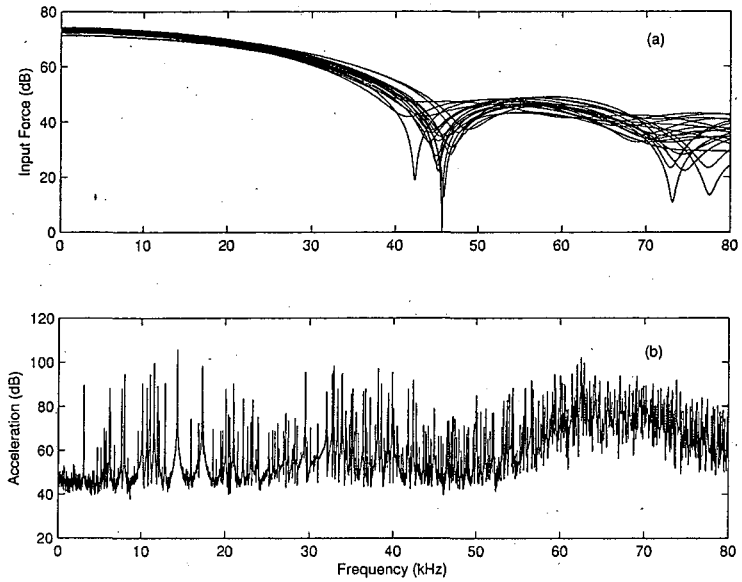

Fig. 5.3. An example of measured response. (a) Frequency spectrum of an input force, (b) averaged response spectrum of 56E1 rail at the top of the railhead.

the railhead for each excitation as shown in Fig. 5.1. (The UIC60 rail section was only measured up to 40 kHz).

As an example, Fig. 5.3 shows the frequency spectra of the input force and the averaged output acceleration levels measured from the 56E1 rail up to 80 kHz. As shown in Fig. 5.3(a), the impact hammer does not provide a uniform force spectrum over the whole frequency span. This unevenness came from the duration of the input impulse excited by the impact hammer, which was not sufficiently short to generate frequencies above 20 kHz. However, there is still sufficient energy, even at high frequencies, to excite the resonances of the structure. It is observed from the response spectrum in Fig. 5.3(b) that the sensor's mounting resonance appears to be located between around 60 and 70 kHz, causing relatively large responses despite a small input force. Despite these effects the force and overall response level around the mounting resonance vary slowly with frequency so that the response spectrum can be used to extract the half power bandwidths of the structural resonances because only resonances with large amplitude are of interest. Also it can be seen from the response spectrum that there is a noise floor but that there are many resonances with peaks that are 30 to 50 dB above the noise floor.

Damping loss factors were extracted from the resonance peaks and their half

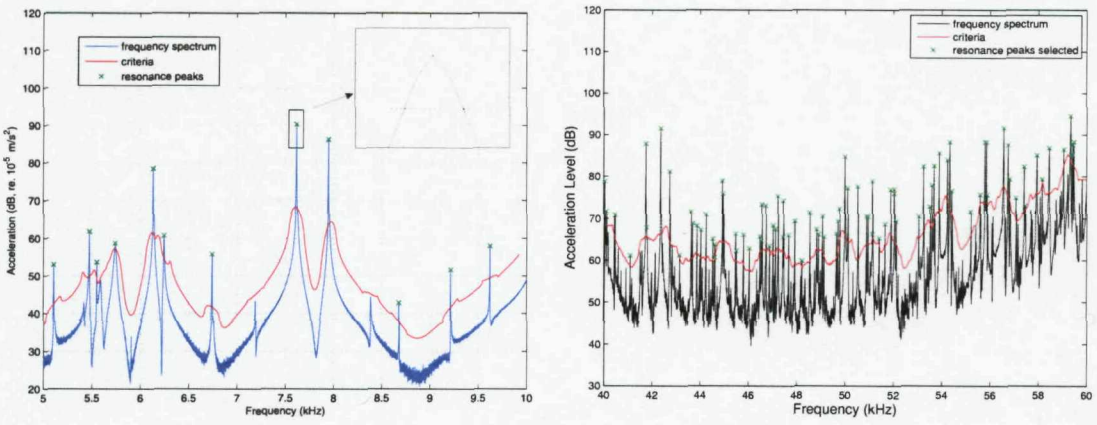

(a) (b)

Fig. 5.4. Examples of measured frequency responses of 56E1 rail at the top of the railhead (a) between 5 kHz and 10 kHz, (b) between 40 kHz and 60 kHz.

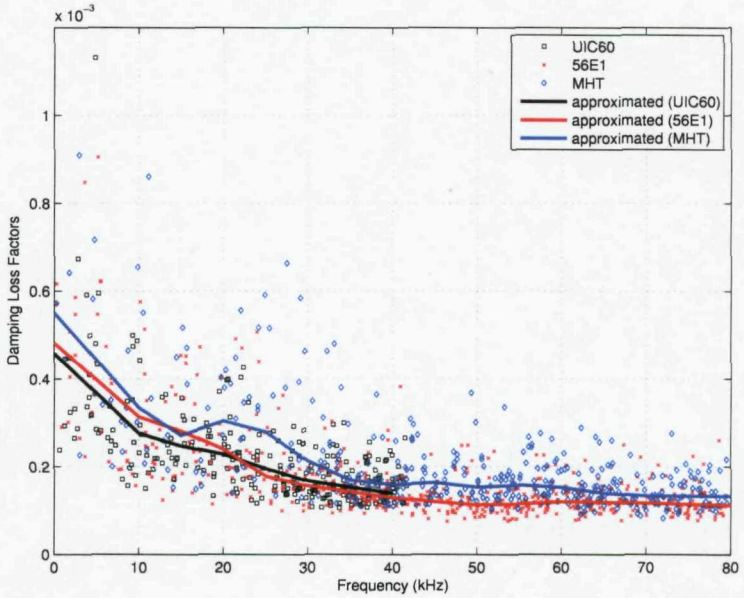

Fig. 5.5. Measured and approximated damping loss factors of three different rail samples.

power bandwidth for all relatively large amplitude resonance peaks as illustrated in Fig. 5.4 as an example. For this calculation, a criterion line was created as presented in Fig. 5.4 by using moving average of the response over 600 Hz bands in order to select relatively large amplitude resonance peaks, specifically those more than 10 dB above the moving average. For these selected resonances, the measured damping loss factors for all the rail samples are illustrated in Fig. 5.5. As shown in this figure, the extracted damping loss factors vary greatly from mode to mode at lower frequencies. Despite these variations, the experimental results reveal that the

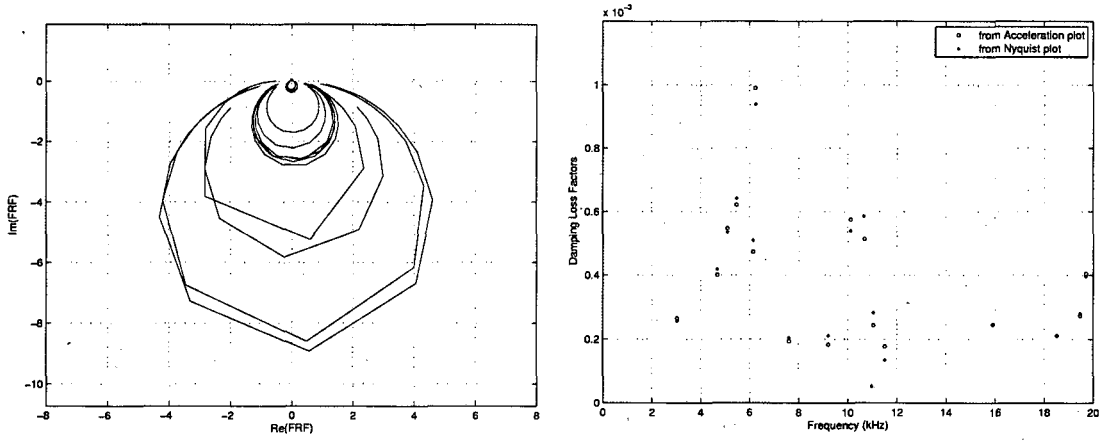

(a) (b)

Fig. 5.6. (a) Nyquist plot for resonances below 20 kHz, measured at the top of the railhead of 56E1 rail, (b) comparison of damping loss factors obtained from the amplitude and Nyquist plots of output response below 20 kHz.

damping loss factors of the rails tend to decrease quite rapidly until about 30 kHz and then more slowly at higher frequencies.

Since there are large fluctuations in the extracted damping loss factors, particularly at lower frequencies, the validity of these estimates has been confirmed. It is known that the accuracy of the estimates of loss factors can be improved using modal circle fitting, referred to as Nyquist plot [32]. However, this method is much harder to automate for a large number of modes. So damping loss factors were estimated from the Nyquist plots only for a small number of resonances below 20 kHz for comparison with estimates obtained from the amplitude plot. For these resonances, the Nyquist diagrams are shown in Fig. 5.6(a) and the estimated damping loss factors are compared in Fig. 5.6(b). Fig. 5.6(b) provides evidence that the scattering of damping loss factors is more likely associated with structure's physical behaviour rather than any error in the estimate.

Nyquist plots for the modes used in Fig. 5.5 between 40 kHz and 80 kHz are shown in Fig. 5.7 as examples, although these have not been used to extract damping values. From these Nyquist plots for the resonances included in Fig. 5.5, it was observed that most of the modes were sufficiently separated even at high frequencies.

Based on the measured results shown in Fig. 5.5, average damping loss factors

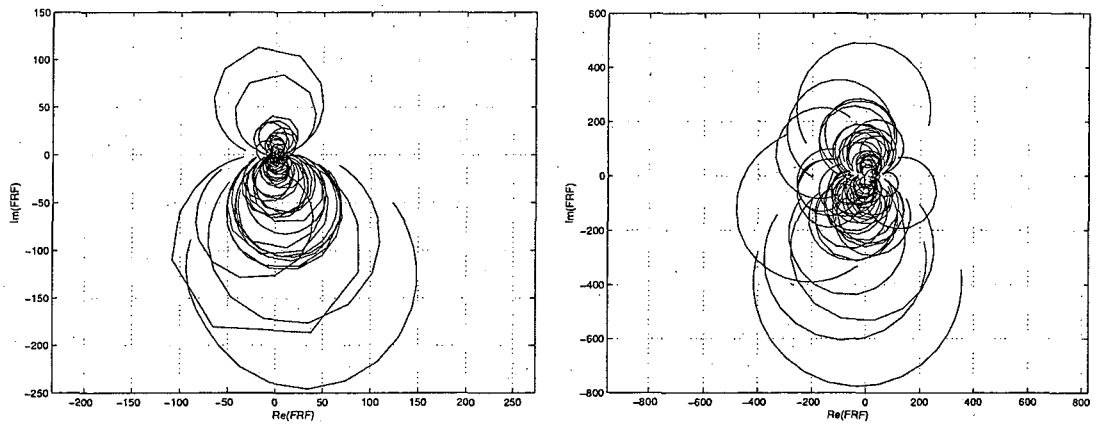

(a) (b)

Fig. 5.7. Nyquist plots for the modes of the 56E1 rail used in Fig. 5.5 (a) between 40 kHz and 60 kHz, (b) between 60 kHz and 80 kHz.

of each rail sample were found taking averages over 10 kHz bands which were chosen to be overlapping to create a result at each 5 kHz. In this estimate, for frequencies above 20 kHz, the average was taken of $1/\eta$ within the band and then inverted to give η. This reduces the influence of a small number outlying estimates. The approximated damping loss factors are shown in Fig. 5.5 for each rail sample. The linear interpolation was used between the results obtained at each 5 kHz.

It was identified from this experiment that the three rail samples have very similar damping loss factors regardless of differences in their shapes and heat treatments. So it seems that the damping loss factor is governed by the material of the rail itself. In addition, it turned out from this experiment that the measured results did not differ greatly from the estimated damping loss factor of 0.0002, used for the previous decay rate prediction. For the rest of the work reported in this thesis, the moving average curve representing the approximate damping loss factor of the 56E1 rail is used to improve the accuracy of the simulated decay rates.

5.2 Decay Rate Recalculation

In this section, the decay rates are recalculated by using the damping loss factor which was approximated from the measured results for the 56E1 rail, as shown in Fig. 5.5.

In the FE analysis in Chapter 3, the decay rate, Δ, was evaluated by Eq.(3.27) as a function of η. For the track model, η is specified by the two damping components: η_r for the rail and η_p for the rail pad. Since η_r was given as a constant in Chapter 3, the loss factor of the i^{th} wave, η^i, can be expressed as

$$\eta^i = \eta_r + F^i(\eta_p) \quad , \tag{5.3}$$

where $F^i(\eta_p)$ denotes a function of η_p. By using the measured damping loss factor for the 56E1 rail, as shown in Fig. 5.5, decay rates can be recalculated. Since η_r was given as a constant of 0.0002 in the previous FE simulation, the decay rates can be recalculated simply by replacing 0.0002 with the averaged damping of the rail. That is, the improved decay rates are created by subtracting the structural damping of 0.0002 from η^i in Eq.(5.3) and then adding the measured one instead. This recalculation was performed to obtain improved decay rates for each wave predicted from the FE analysis [58]. However, since the decay rates predicted by the WFE method are more accurate, as validated in Fig. 4.9, only those obtained from the WFE method will be presented in this section.

In WFE analysis, the improved decay rates is predicted from Eq.(4.31) by using the measured η_r, instead of using the constant value. The revised decay rates are illustrated in Fig. 5.8 by using the measured damping loss factor of the 56E1 rail. Comparing these revised decay rates in Fig. 5.8 with the previous ones shown in Fig. 4.9, it can be seen that using the measured damping loss factor of the rail

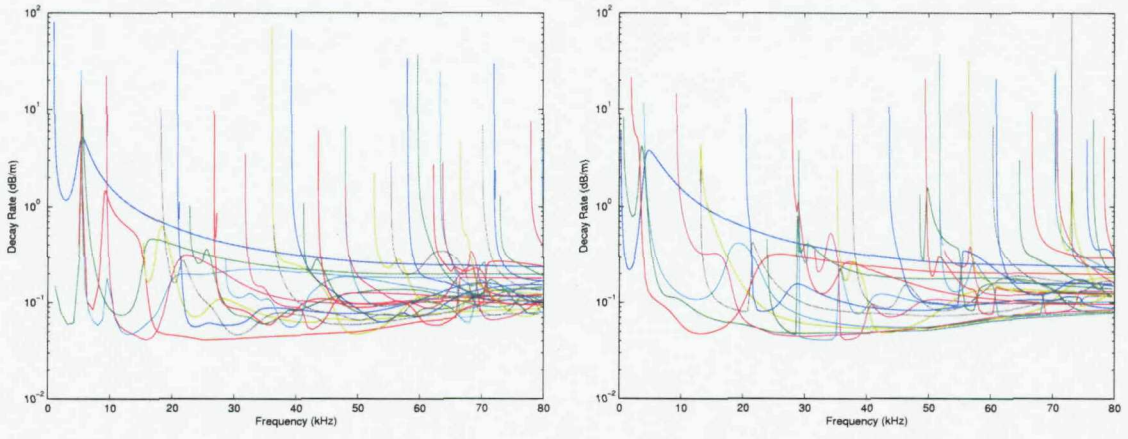

(a) (b)

Fig. 5.8. Decay rates predicted by using the measured structural damping of the 56E1 rail for (a) the vertical and symmetric longitudinal waves, (b) the lateral, torsional and antisymmetric longitudinal waves.

causes the curves with low decay rates to increase at frequencies below 25 kHz and to reduce above 25 kHz. Particularly, the lowest decay rate curves were mainly modified because they are most strongly affected by the structural damping of the rail. From this decay rate recalculation, it was found that the minimum values of decay rate are little changed but the frequency range where the minimum decay rates occur becomes somewhat broader, moving to the range between 20 kHz and 40 kHz.

Finally, the decay rates of the waves measurable at the top/side of the rail head, at the middle of the web and at the top of the foot are obtained as shown in

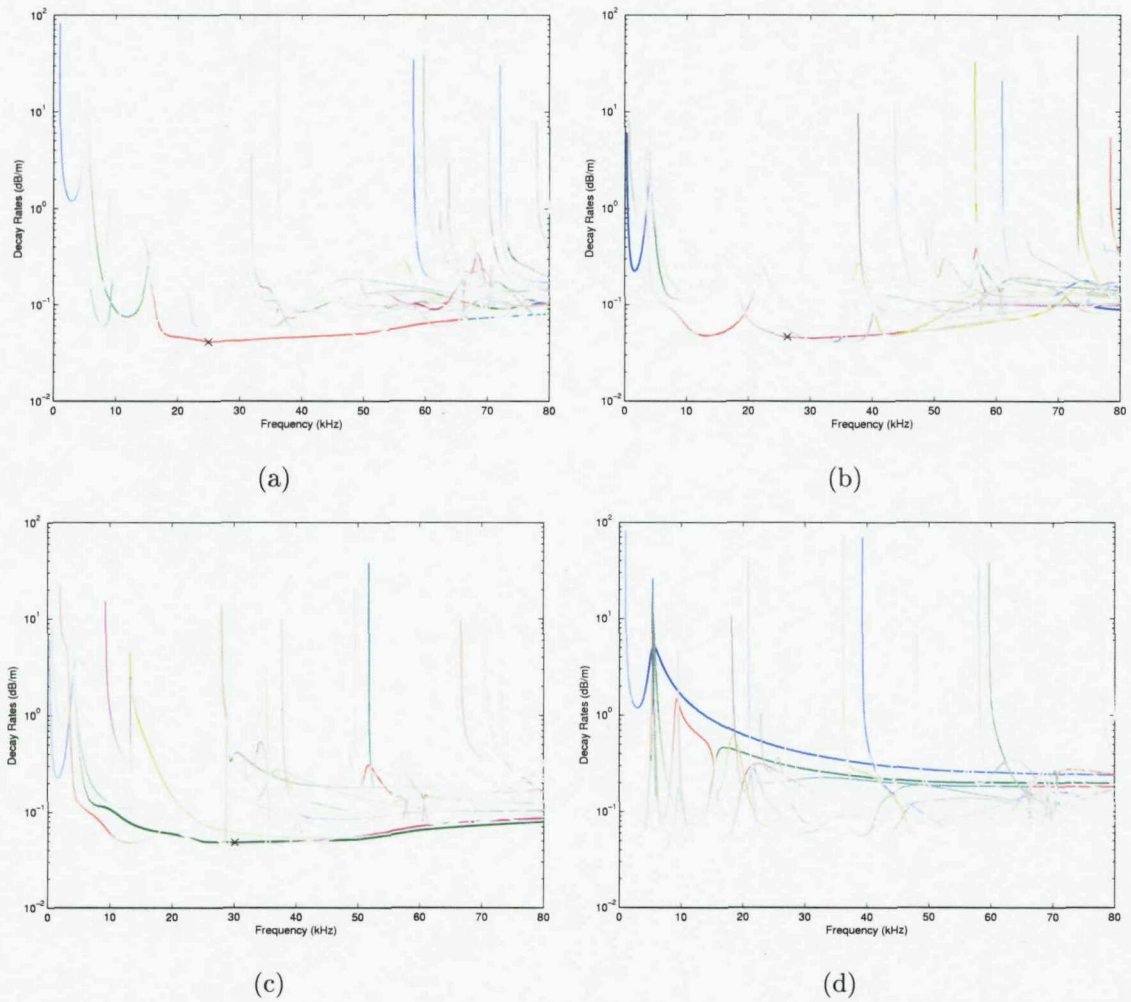

Fig. 5.9. Decay rates of the measurable waves predicted (a) at the top of the rail head in the vertical direction, (b) at the side of the rail head in the lateral direction, (c) at the middle of the web in the lateral direction, (d) at the top of the foot in the vertical direction.

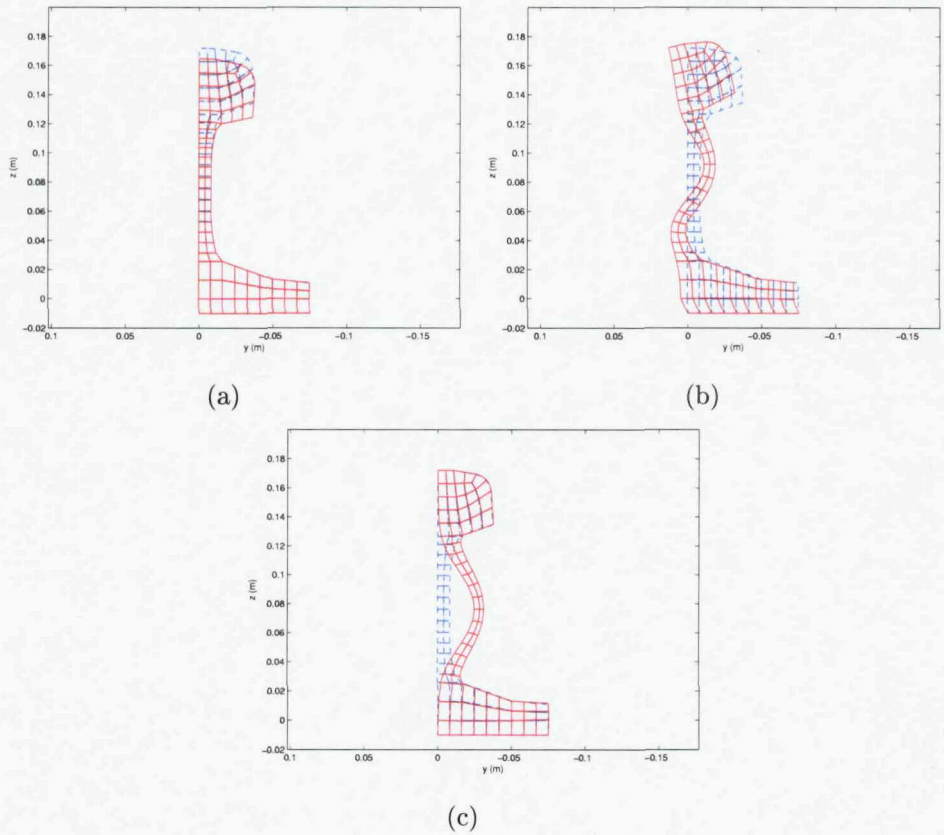

Fig. 5.10. Simulated deformation shapes of the waves (a) marked '×' in Fig. 5.9(a), (b) marked '×' in Fig. 5.9(b), (c) marked '×' in Fig. 5.9(c).

Fig. 5.9. The minimum decay rates measurable on the rail surface tend to be about 0.04 dB/m at the top and side of the rail head and about 0.05 dB/m at the middle of the web, respectively. The wave types that possess the minimum decay rates are marked '×' in Fig. 5.9 and their deformation shapes are illustrated in Fig. 5.10. This figure verifies that the respective types of these waves are the vertical bending wave localized in the rail head, the lateral bending wave of the rail head with a global deformation of the web and the 1^{st} order web bending wave, as presented in Chapter 3. The simulated decay rates in Fig. 5.9 will be compared with field test results in Chapter 7.

5.3 Summary

Since it was revealed in Chapter 4 that minimum decay rates are directly related to the damping of the rail, structural damping loss factors were measured up to 80 kHz from impact hammer tests for three different rail samples.

From this experiment, it was found that the measured damping loss factor reduces as frequency increases although it does not deviate much from the estimated value of 0.0002, used for the previous numerical simulations. In addition it was revealed that the damping loss factors tend not to be significantly dependent on the different rail geometries and heat treatments. Accordingly, it seems that the damping loss factor is governed by the material of the rail itself.

Using the measured damping of rails, decay rates of measurable waves were recalculated. This caused some changes in the predicted decay rates, particularly the lowest decay rate curves. From the recalculated decay rates, it was identified that the minimum decay rates are about 0.04 to 0.05 dB/m which were little changed by using the measured damping but the frequency range where they occur was moved to between 20 kHz and 40 kHz.

Chapter 6

Group Velocity Measurements on ISVR Test Track

In the previous chapters, numerical analyses for railway track have been performed up to 80 kHz. To validate these simulation results, two experiments were implemented on a short test track. These experiments use an impact hammer to excite frequencies up to 42 kHz and piezoceramic transducers for frequencies up to 80 kHz. Accelerometers were used as receivers. The experiments have been performed on the ISVR test track located at Chilworth (Fig. 6.1) which is equipped with UIC60 rail of about 32 m in length. The rail is mounted with Pandrol Fastclips and 10 mm studded rubber rail pads on concrete sleepers surrounded by ballast. It has been used previously by de France [45]. Time-frequency analysis has been applied to the measured data in order to extract dispersion relations. Then the measured

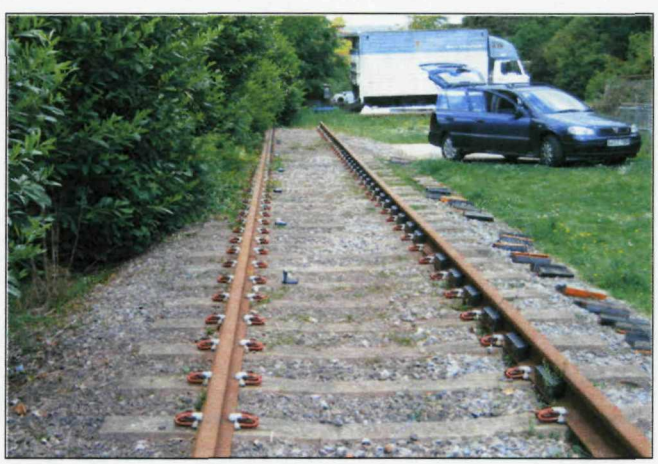

Fig. 6.1. ISVR test track at Chilworth.

results are compared with the simulated ones obtained by WFE analysis.

6.1 Measurement Using an Impact Hammer for Frequencies below 42 kHz

6.1.1 Measurement setup

The same miniature impact hammer used in the measurement of damping loss factor in Chapter 5 was employed to generate a broadband signal at one end of the rail. The same model of accelerometer, as used in Chapter 5, was utilised to detect propagating waves along the rail. As stated before, since the mounting resonance frequency of the accelerometer is specified as around 90 kHz, they can be used well beyond the sensor's quoted measurement range of 20 kHz for measuring dispersion characteristics of propagating waves, as long as the measurements do not need to be calibrated.

Six accelerometers were set up along the rail, spaced at a distance of five sleeper spans (about 3 m). They were each placed at the mid span between two sleepers and attached by means of beeswax. Also, to avoid the near-field effects that take place around both ends of the rail and to diminish the contributions of the rapidly decaying waves, the sensors were located in the central portion of the rail. As a data acquisition unit, an 8 channel SignalCalc Mobilyzer (Data Physics Corp.) was used. The maximum frequency range of this unit was limited up to 42 kHz, and the corresponding sampling rate was 107.52 kHz. The measurement setup is shown in Fig. 6.2.

In the experiment, the excitations and measurements were implemented for the three different directions, that is, in the vertical, lateral and longitudinal directions. For each location, 10 excitations were recorded and analysed. Data were recorded as time domain signals. For the vertical and lateral directions, four excitation and receiver points on the rail cross-section are indicated in Fig. 6.3(a): the top and side of the rail head, middle of the web and top of the foot, respectively. The excitation points were less than about 10 mm away from the adjacent end of the rail. Since the frequency range was limited up to 42 kHz, the shortest wavelengths in the rail

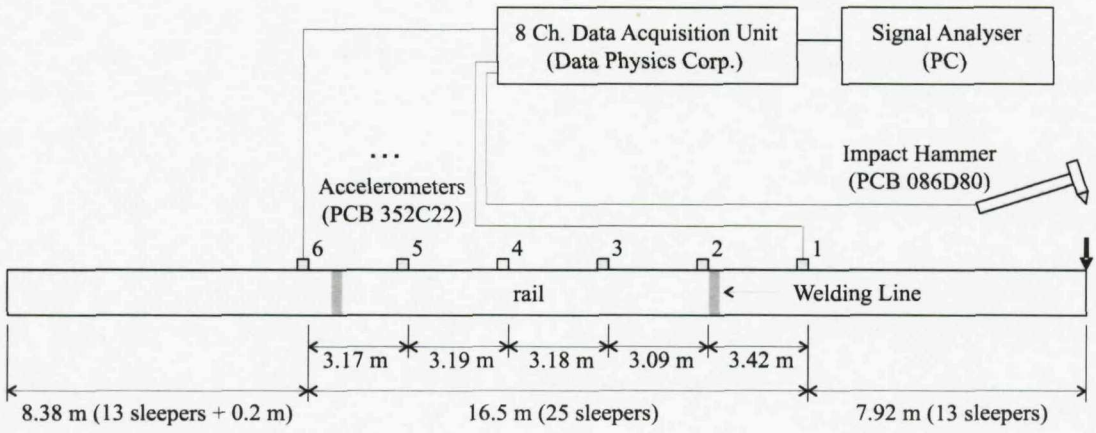

Fig. 6.2. Experimental setup using an impact hammer as an exciter.

(a) (b) (c)

Fig. 6.3. Excitation and measuring points for the decay rate measurement. (a) The four excitation and measurement points on the rail cross-section in the vertical and lateral directions, (b) the three excitation points on the rail cross-section in the longitudinal direction, (c) measurement points on the rail cross-section in the longitudinal direction.

are about 63 mm at the rail head, 48 mm at the web and 42 mm at the rail foot, respectively (from Fig. 4.13). So, the phase cancellation due to the waves reflected from the adjacent end of the rail will be negligible.

At all four positions on the rail cross-section, the excitation was applied and the responses along the rail were measured at the corresponding position on the cross-section normal to the rail surface. In the calculation of the energy ratio in Eq.(4.32), it was assumed that all the modes are excited equally. In practice, however, the rail response will depend on the position of the excitation which determines the excited modes. In order to make similar condition to that used in Eq.(4.32) in the measurement, the rail responses were acquired at the same positions on the rail

cross-section as the excitation is applied. If the excitation and receiving positions are different, the rail response would appear as a combination of the energy metric in Eq.(4.32) for the excitation and receiving positions on the cross-section.

For the longitudinal direction, small blocks were attached on the corresponding rail surfaces as shown in Fig. 6.3(b) and Fig. 6.3(c) to create and measure the propagating waves in the longitudinal direction. (In the experiment for the longitudinal direction, the foot was not used as an excitation and receiving point). The arrows in Fig. 6.3(b) depict the excited direction for the longitudinal wave generation. In this measurement for the longitudinal direction, the web was also used as an excitation and receiving point at shown in Fig. 6.3(b) and (c). However, it was found from the measured data that the excitation on the block creates bending waves much more efficiently than longitudinal waves, because of the flexibility of the web. So the results measured on the middle of the web in the longitudinal direction are omitted in this section.

It should be noted that there are two welds in the rail of this test track as marked in Fig. 6.2 and one of them is illustrated in Fig. 6.4. These welds may lead to wave reflections, particularly at the web and foot of the rail because there is considerable thickness change, as seen in Fig. 6.4.

Fig. 6.4. A welded region located between 1st and 2nd measurement positions. An accelerometer can be seen attached at the 2nd measurement position on the web.

6.1.2 Time-frequency analysis

Since it is anticipated from the simulation results that several propagating waves will coexist in the measured time signals and the frequency content of the signal will vary with time, the simple one-dimensional frequency domain results, such as Fourier spectra, are not sufficient to separate and identify them. Therefore a two-dimensional time-frequency analysis has been applied to the measured responses. There are several methods which can be used to generate time-frequency diagrams from the time signals, for example, spectrogram, Wigner-Ville distribution, wavelet transform, etc [59]. However, if multiple waves are present in a time signal, the Wigner-Ville distribution does not create a clear time-frequency diagram due to the occurrence of their cross-terms. The scalogram produced by using the wavelet transform has poor time resolution at low frequency and poor frequency resolution at high frequency according to the uncertainty principle. So it does not seem to be suitable for this study because the goal is to distinguish several waves at low and high frequencies evenly. Alternatively, the spectrogram has uniform time-frequency resolution throughout the whole range of the diagram, although it is still limited by the uncertainty principle. In this thesis, therefore, the spectrogram, using the Short Time Fourier Transform, was used for time-frequency analysis of the measured signals.

In order to make a two-dimensional diagram, a 1024 $\times$ 1024 data matrix was created from the measured time signal by using a weighting function. The data structure of this two-dimensional matrix is illustrated in Fig. 6.5. The Hanning window function was used in this analysis. As shown in this figure, each column of this 2-D matrix corresponds to each discrete time of the signal and each row is composed of measured data in a short time length extended with zeros. The data points in the Hanning window function were given as $M = 129$ and $m = (M+1)/2 = 65$ in Fig. 6.5. The Fourier transform of every column of this 2-D matrix creates a time-frequency matrix which can be plotted as a time-frequency diagram. Due to the limited length of 1024 points, the frequency increment Δf of the frequency axis becomes 105 Hz by the relation of $\Delta f = f_s/N = 107520/1024 = 105$ Hz, where f_s denotes the sampling frequency.

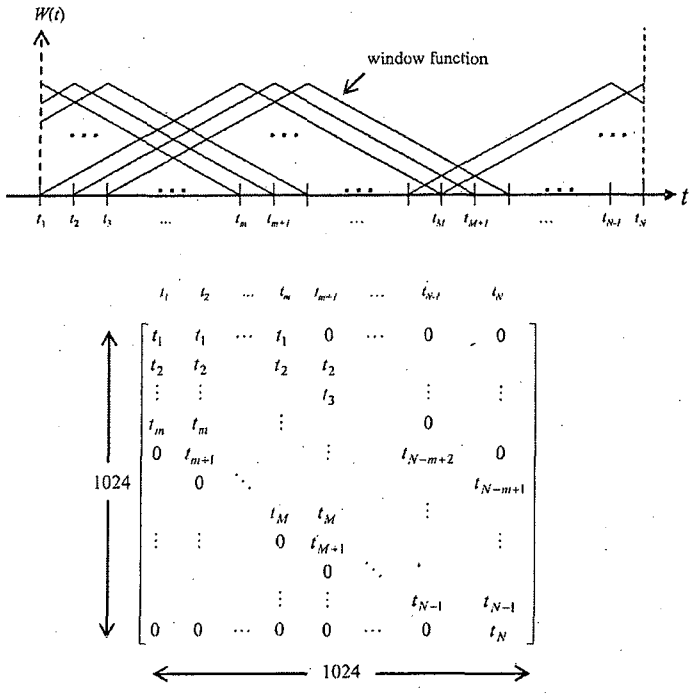

Fig. 6.5. Data structure of the two-dimensional matrix for creating a spectrogram.

6.1.3 Measured results at the top of the rail head in the vertical direction

As described above, the reliable frequency range of the impact hammer and the accelerometer are specified as up to 20 kHz by the manufacturer. However, in the signal analysis it was possible to detect frequencies above 40 kHz. Fig. 6.6(a)

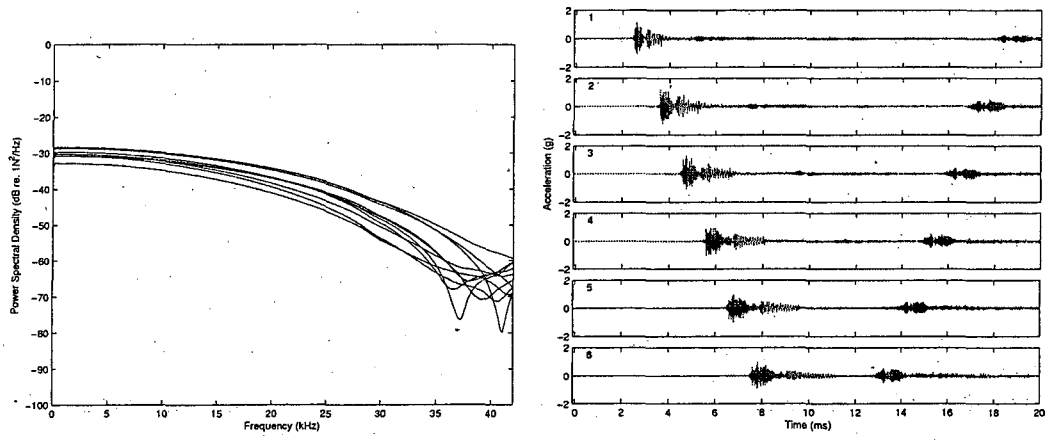

(a) (b)

Fig. 6.6. (a) Power spectra of input forces, (b) an example of the measured time signals at the top of the rail head along the rail.

shows the power spectra of the 10 input forces measured at the top of the rail head. Although the spectra are not flat above 20 kHz, there is still a reasonable signal over the frequency range considered. In addition, examples of the time signals measured at the top of the rail head at the various positions along the rail are shown in Fig. 6.6(b) for excitation at one end of the rail. Excellent waveforms of direct waves and echoes reflected from the far end of the rail were obtained at various distances. Further examples of the measured time signals at each receiving position are illustrated in Appendix B.

The time signals measured at positions 2 and 4 at the top of the rail head are shown in Fig. 6.7 for the case when the excitation was applied at the end of rail. The origin of the time axis was determined by triggering on the input excitations. At the 4^{th} sensor, the echo signal reflected from the other end of the rail also appears from 15 msec. in this figure. The measured time signals at the top of the rail head appear only slightly dispersive because their waveforms were little changed along the rail. The section of data indicated in red in Fig. 6.7, which has 1024 data points and a duration of 9.5 msec., was analysed to construct the spectrograms.

As an example, two spectrograms obtained from measurements using the 2^{nd} and 4^{th} sensors are shown in Fig. 6.8. The spectrograms were averaged across measurements. These spectrograms present well the dispersive characteristics of the propagating waves and indicate that the waves in the range 7 kHz to 32 kHz dominate the propagating energy. Conversely the waves around 35 kHz propagate

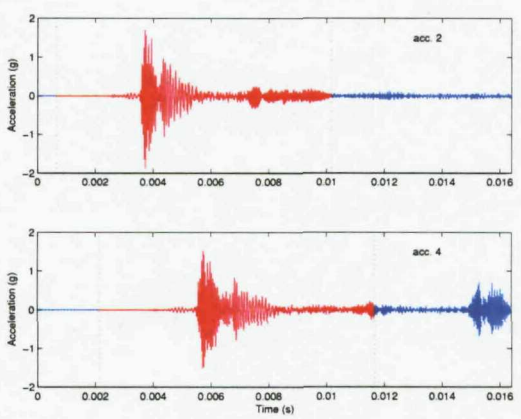

Fig. 6.7. Time signals measured at positions 2 and 4 at the top of the rail head in the vertical direction.

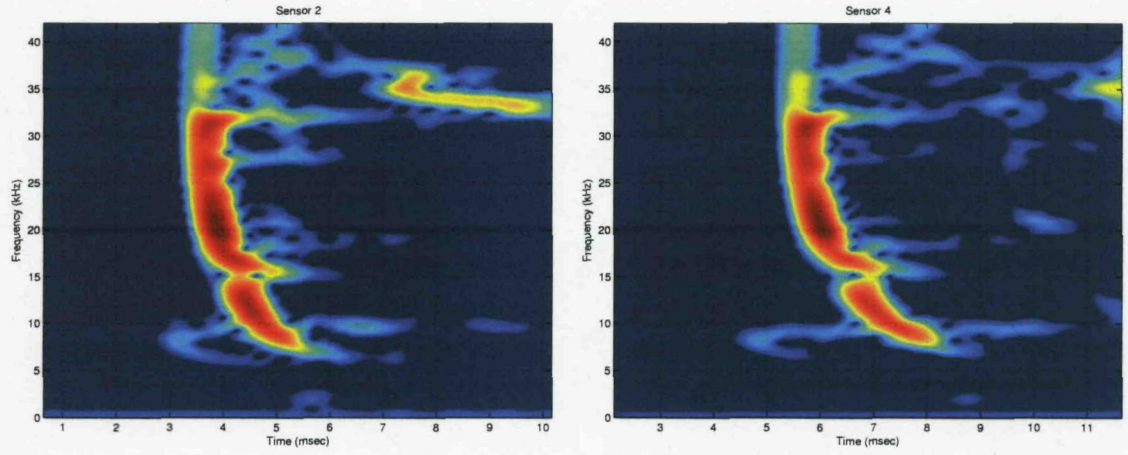

(a) (b)

Fig. 6.8. Spectrograms measured at positions 2 and 4 at the top of the rail head in the vertical direction.

more slowly and decay more rapidly with several wave types present. Below 7 kHz there is relatively little energy in the signal. The spectrograms measured at the six positions along the rail are illustrated in Appendix B.

Since the distances between the excitation point and the receiving positions are known, the time axis of the spectrograms can be easily converted to a velocity axis using *velocity = distance/time*. Hence the time-frequency diagrams can be replotted to show velocity versus frequency. In this diagram, the velocity represents the group velocity because the energy carried by waves travels with the group velocity. The group velocity-frequency diagram at position 3 is illustrated in Fig. 6.9 and compared to the simulation output of measurable waves obtained by WFE analysis. Note that the scale of the velocity axis in Fig. 6.9(a) is nonlinear, because it is inversely proportional to the linear time scale. The simulated results in Fig. 6.9(b) are therefore shown on the same scale.

From this comparison, it is clear that the simulated group velocity curves correspond very well to the measured ones. Therefore, the deformation shapes of the principal waves that are measured can be inferred from the simulation results. The wave dominantly measured at the top of the rail head, which was marked '×' in Fig. 6.9(b), was identified as a vertical bending wave propagating along the rail head as illustrated in Fig. 6.10, which was produced by FE analysis. It should be noted that the dip in the group velocity at 15 kHz in Fig. 6.9(a) and (b) results from

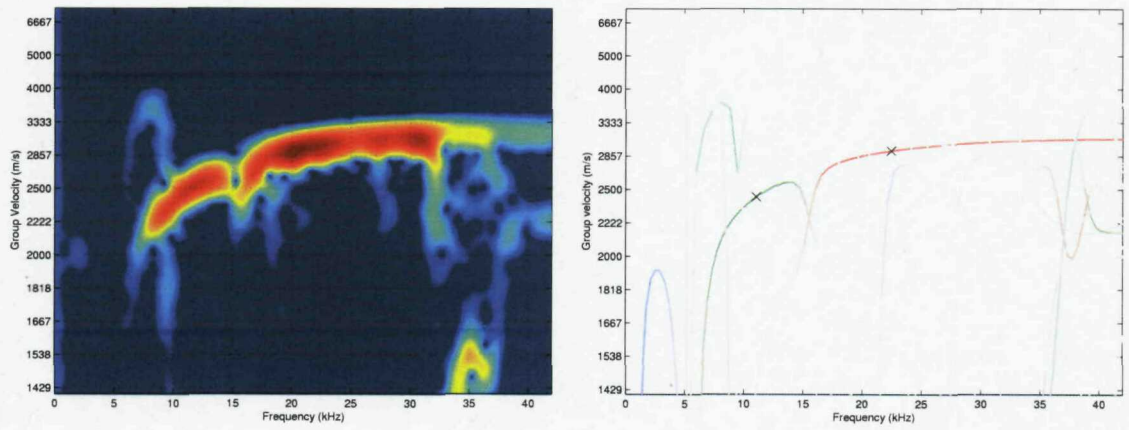

(a) (b)

Fig. 6.9. Group velocities at the top of the rail head in the vertical direction. (a) Measured at position 3, (b) predicted by the WFE method.

(a) (b)

Fig. 6.10. Deformation shapes of the rail, simulated by the FE method, at two points marked '×' in Fig. 6.9(b). (a) 11,065 Hz, (b) 22,456 Hz.

the wave mode conversion which occurs between the second and third waves, see Fig. 4.7(a). In addition, Fig. 6.9(b) exhibits several waves that coexist above 32 kHz so that the input energy transmitted from the impact hammer is shared amongst them. That might be one reason why the energy levels of the waves above 32 kHz in Fig. 6.9(a) suddenly become lower. Another reason would be that the input force is reduced, as shown in Fig. 6.6.

6.1.4 Measured results at the underside of the rail head

From a practical point of view, the top of the rail head is not suitable as a measuring point on an operational track even if it could give better responses in terms of the long range wave propagation. As an alternative, the underside of the rail head could be used as a measuring point to acquire the vertical bending wave

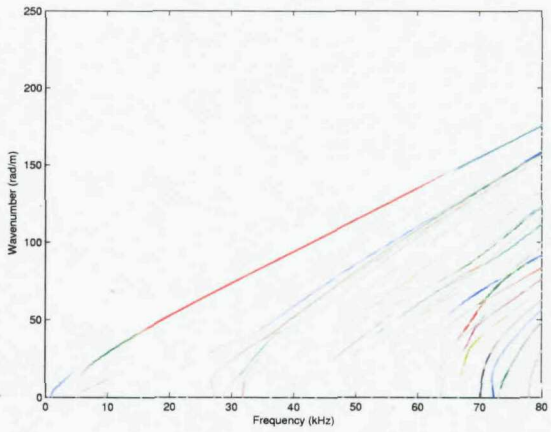

Fig. 6.11. Dispersion curves for waves measurable at the underside of the rail head in the vertical direction, predicted by the WFE method.

which travels through the rail head. So, the responses at the underside of the rail head were also measured when the vertical excitation was applied at the top of the rail head. In this measurement, the excitation was applied at a point about 30 mm away from the end of the rail. The response point was inclined at an angle to the vertical due to the slope on the underside of the rail head.

The dispersion curves measurable at the underside of the rail head in the vertical direction are illustrated in Fig. 6.11, predicted by WFE analysis. Fig. 6.11 shows similar intensities of the measurable dispersion curves to those predicted at the top of the rail head, illustrated in Fig. 4.13(a). Therefore, it is expected from the simulation results that the underside of the rail head could be an appropriate alternative measuring point to detect vertical bending waves which propagate through the rail head.

The spectrograms measured at the underside of the rail head using the 2^{nd} and 4^{th} sensors are shown in Fig. 6.12. Comparing them with those in Fig. 6.8, it is validated that dispersion relations measured at the underside of the rail head are very similar to those measured at the top of the rail head. However, Fig. 6.12 shows somewhat different energy level distributions from those in Fig. 6.8. That is, the energy measured at the underside of the rail head is concentrated between 15 kHz and 25 kHz. The exact reason for that is not clear but it appears nevertheless that the underside of the rail head can be used as an appropriate alternative measuring point to the top of the rail head.

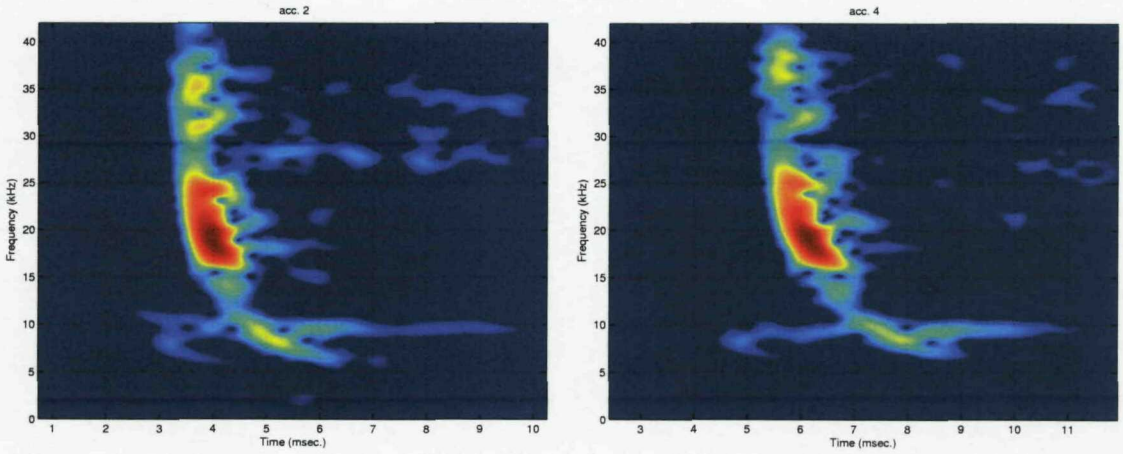

(a) (b)

Fig. 6.12. Spectrograms measured at positions 2 and 4 at the underside of the rail head.

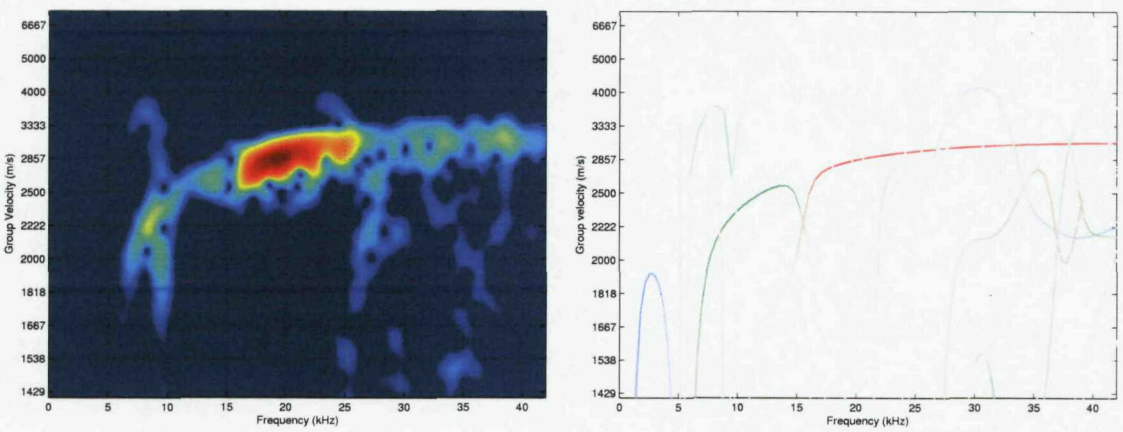

(a) (b)

Fig. 6.13. Group velocities at the underside of the rail head in the vertical direction. (a) Measured at position 3, (b) predicted by the WFE method.

The group velocity diagram measured at position 3 is compared with the simulated one for measurable waves in Fig. 6.13. In this figure, it is observed again that the measured group velocity curves correspond very well to the simulated ones. From this measurement, it was confirmed that the underside of the rail head can be used as an alternative measuring point to the top of the rail head.

6.1.5 Measured results at the side of the rail head in the lateral direction

The time signals measured laterally at positions 2 and 4 at the side of the rail head are shown in Fig. 6.14. (Further examples of the measured time signals at each receiving position are illustrated in Appendix B). The section of data coloured red in Fig. 6.14, which has a duration of 9.5 msec., was analysed to make the spectrograms, as before.

The spectrograms for the 2^{nd} and 4^{th} sensors are presented in Fig. 6.15. These diagrams give more complicated dispersion relations than those measured vertically at the top of the rail head. The spectrograms in Fig. 6.15 indicate that the waves below 20 kHz propagate dominantly with large energy. Meanwhile above 25 kHz several waves are mixed and create intricate diagrams. For this reason the energy levels of the waves seem to be spread above 25 kHz. Unlike the measured result at the top of the rail head, these spectrograms illustrate two changes of the propagating wave modes taking place around 8 kHz and 20 kHz, respectively. This also corresponds to the WFE analysis results shown in Fig. 4.7(b), i.e., changes from green to red line and from red to magenta line.

The group velocity is plotted as a function of frequency for position 3 in Fig. 6.16(a) and compared with the simulated result obtained by WFE analysis. At the side of the rail head, the waves measured mainly have a group velocity around 2850 m/s. The measured group velocity diagram gives excellent agreement with the

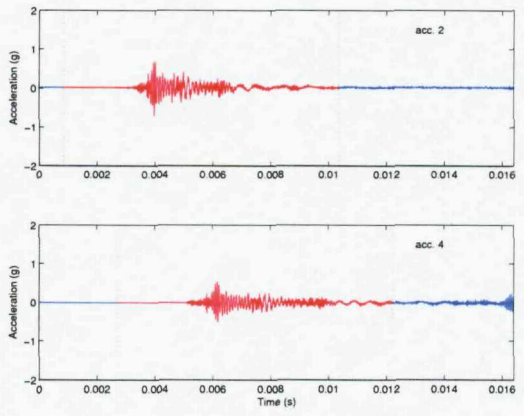

Fig. 6.14. Time signals measured at positions 2 and 4 at the side of the rail head in the lateral direction.

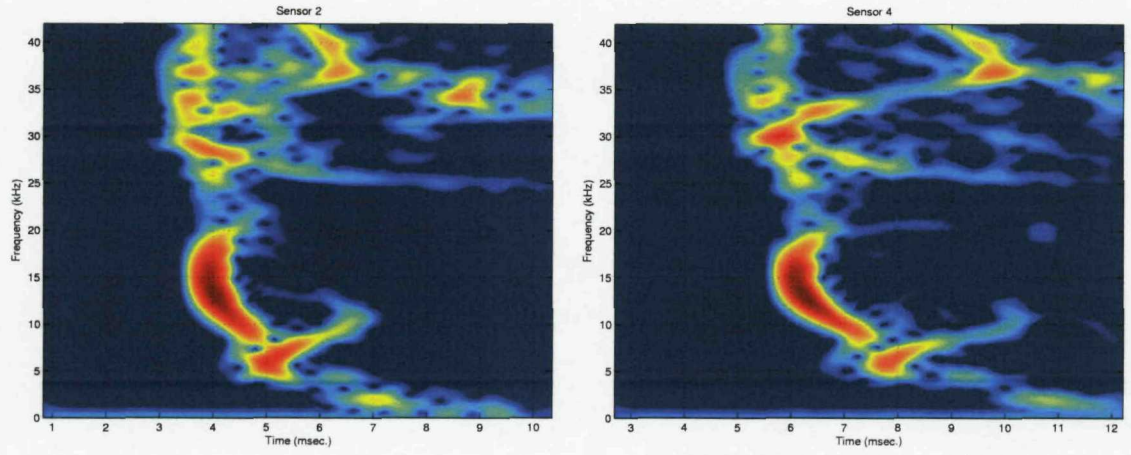

(a) (b)

Fig. 6.15. Spectrograms measured at positions 2 and 4 at the side of the rail head in the lateral direction.

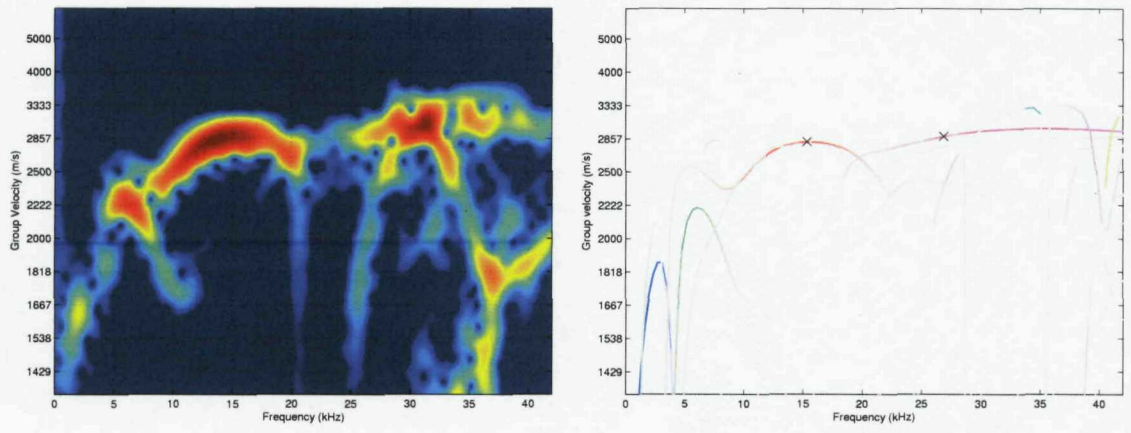

(a) (b)

Fig. 6.16. Group velocities at the side of the rail head in the lateral direction. (a) Measured at position 3, (b) predicted by the WFE method.

(a) (b)

Fig. 6.17. Deformation shapes of the rail, simulated by the FE method, at two points marked '×' in Fig. 6.16(b). (a) 15,359 Hz, (b) 26,869 Hz.

predicted one. The deformation shapes of the waves marked by '×' in Fig. 6.16(b) are illustrated in Fig. 6.17 at two frequencies. This figure shows that the lateral bending waves have global deformation in both the rail head and web at the selected frequencies.

6.1.6 Measured results at the middle of the web in the lateral direction

The time signals measured at positions 2 and 4 at the middle of the web are shown in Fig. 6.18. These measured time signals exhibit completely different behaviour from those obtained at the rail head. The flexibility of the web allows relatively large deformation as shown by the magnitude of the time signals. In addition, at the 2^{nd} sensor, an additional waveform following the direct wave was recorded around 13 msec., which did not appear at the rail head. This occurs too soon to be a wave reflected from the far end of the rail. It will be discussed further below.

From these time data, the time-frequency diagrams were generated as shown in Fig. 6.19. These spectrograms exhibit fairly simple and clear dispersion curves. Fig. 6.19 shows that the waves in the range 8 kHz to 30 kHz carry large energy and do not seem to make any wave mode changes in this range. At the web of the rail, it is expected that the welds will cause considerable energy reflection and that is indeed observed Fig. 6.19(b). That is to say, the wave reflected from the weld located between positions 5 and 6 appears in the spectrogram at position 4 between 10 and

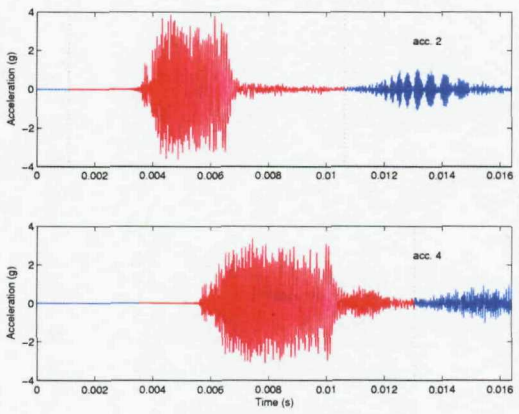

Fig. 6.18. Time signals measured at positions 2 and 4 at the middle of the web in the lateral direction.

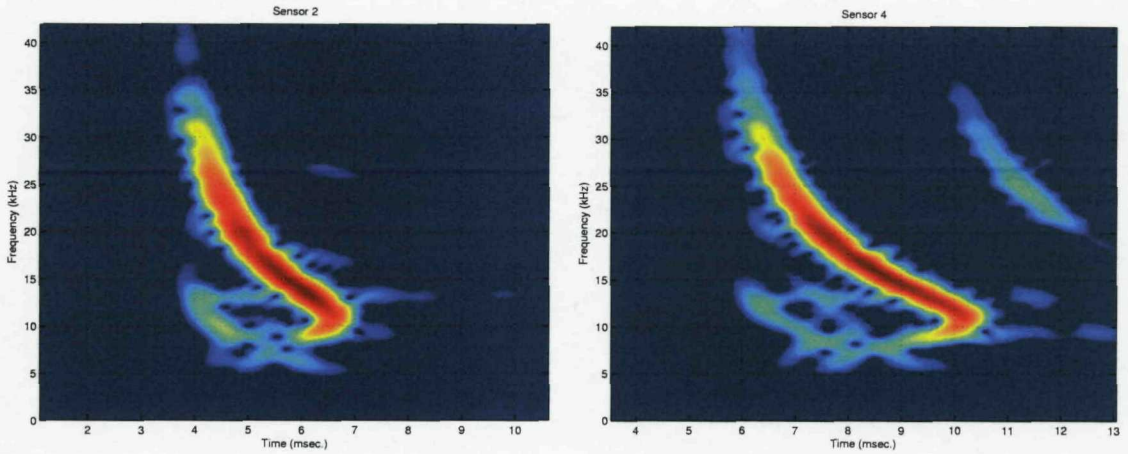

(a) (b)

Fig. 6.19. Spectrograms measured at positions 2 and 4 at the middle of the web in the lateral direction.

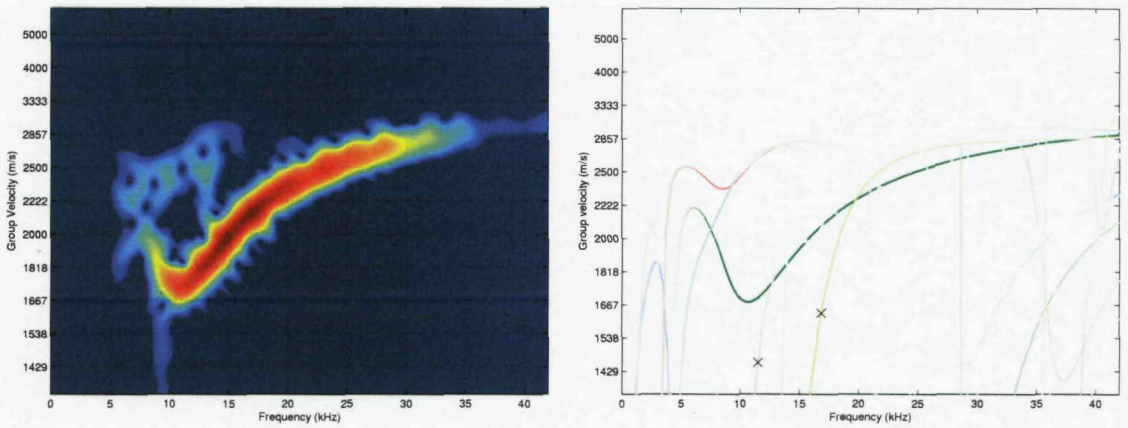

(a) (b)

Fig. 6.20. Group velocities at the middle of the web in the lateral direction. (a) Measured at position 3, (b) predicted by the WFE method.

12 msec. Therefore it appears that the waveform around 13 msec. shown in Fig. 6.18 at position 2 was also created by waves reflected from the weld located between positions 5 and 6. Similar wave reflections can also be seen in other spectrograms shown in Fig. B.10 in Appendix B, especially for positions 1 and 5.

The group velocity diagram measured at the middle of the web is illustrated in Fig. 6.20(a) and compared with the simulated result. It is clear that these measured group velocity curves correspond well to the predicted ones, in particular, to the green line in Fig. 6.20(b). This green line corresponds to the 1^{st} order web bending

(a) (b)

Fig. 6.21. Deformation shapes of the rail, simulated by the FE method, at two points marked '×' in Fig. 6.20(b). (a) 11,497 Hz, (b) 16,864 Hz.

wave. However, there is an apparent discrepancy between these two results. That is, several curves presented in Fig. 6.20(b), for example, the two wave modes marked with an '×', do not appear in the measured result. The deformation shapes of these two waves are illustrated in Fig. 6.21 and possess global deformation of the rail. The main reason that these are not observed in the measurement seems to be associated with the rapid decay due to the high damping in the rail pad and the influence of the clip which makes waves with global deformation disappear quickly.

6.1.7 Measured results at the top of the foot in the vertical direction

The time signals measured at positions 2 and 4 at the top of the foot are given in Fig. 6.22. These two measured time signals show how rapidly waves decay along the rail foot. This clearly occurs due to the energy dissipation by the rail pads and

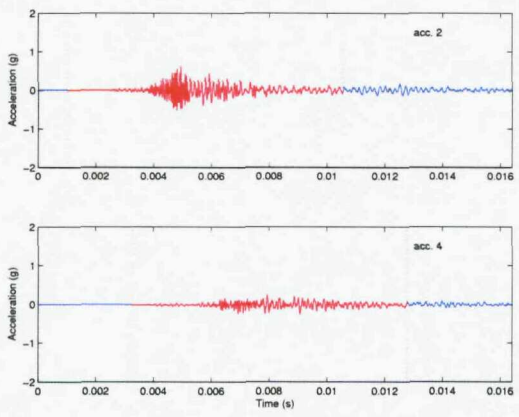

Fig. 6.22. Time signals measured at positions 2 and 4 at the top of the foot in the vertical direction.

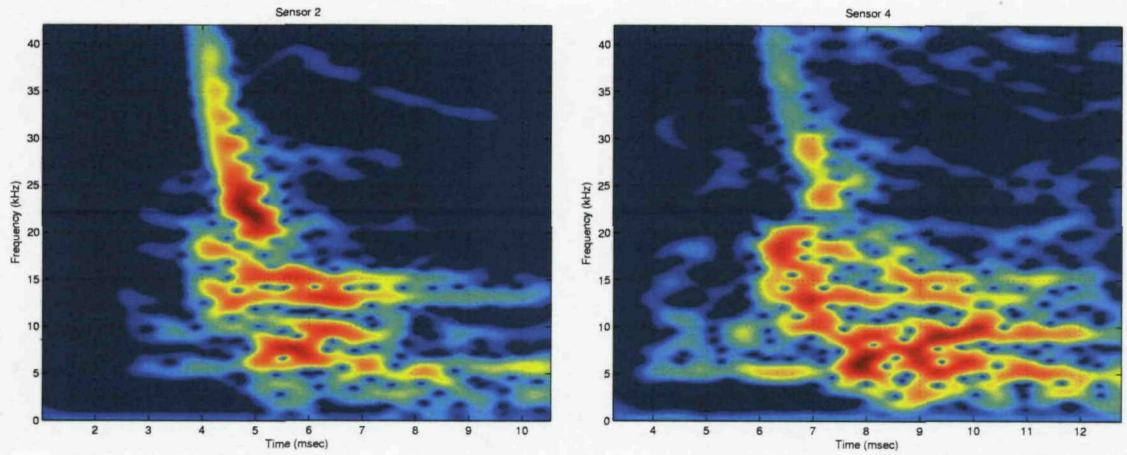

(a) (b)

Fig. 6.23. Spectrograms measured at positions 2 and 4 at the top of the foot in the vertical direction.

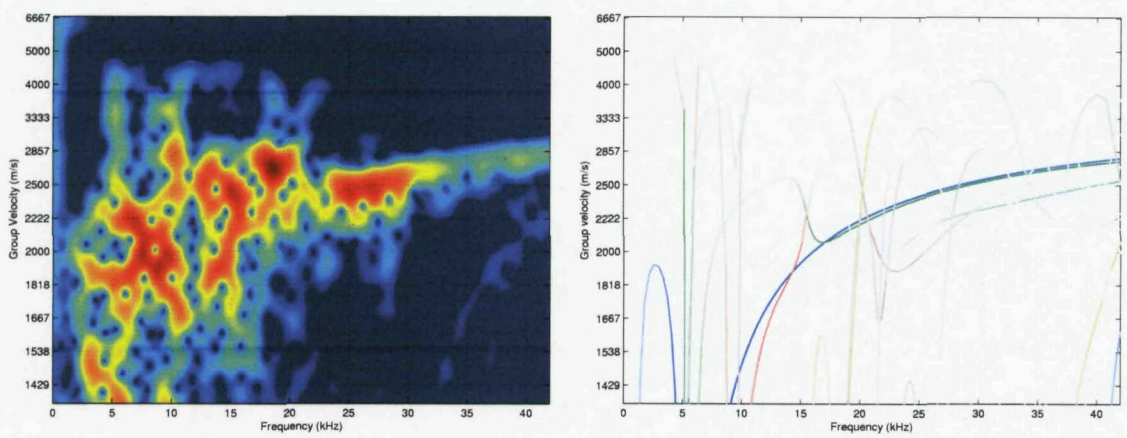

(a) (b)

Fig. 6.24. Group velocities at the top of the foot in the vertical direction. (a) Measured at position 3, (b) predicted by the WFE method.

clips.

The time-frequency diagrams measured at the top of the foot are shown in Fig. 6.23. It is hard to define any characteristics of propagating waves, especially below 20 kHz because of noise contamination. This noise appears because the waves travelling along the rail foot decay very rapidly into the noise floor, due to the energy dissipation by the rail pads. In addition, there would be multiple wave reflections arising from the fasteners. These spectrograms demonstrate that waves cannot propagate over a long range along the rail foot. Although the dispersion curves do

not clearly appear in the spectrograms, the measured and predicted group velocities are compared and illustrated in Fig. 6.24. Despite noise contamination, this shows that the measured group velocity curves correspond well to the predicted ones above 20 kHz, and the dominant wave type is the 1^{st} order foot bending wave, shown in Fig. 3.11(a).

6.1.8 Measured results at the top of the rail head in the longitudinal direction

The time signals measured at positions 2 and 4 at the top of the rail head are shown in Fig. 6.25 when the excitation was applied at the block attached on the end of rail in the longitudinal direction. The section of data coloured red in Fig. 6.25 was analysed to make the spectrograms as before. The measured wave form in Fig. 6.25 reveals that the amplitude of the measured response in the longitudinal direction is much larger than those measured in the vertical and lateral directions. The reason for this and the wave type occurring in this large amplitude signal will be discussed later with the aid of the spectrograms.

The spectrograms for the 2^{nd} and 4^{th} sensors are shown in Fig. 6.26 for the longitudinal direction. Comparing these diagrams to those measured in the vertical direction (Fig. 6.8), Fig. 6.26 shows that the vertical bending waves in the rail head were primarily found in this measurement. The longitudinal waves which travel faster than the bending waves occur between 4 and 5.5 msec. in Fig. 6.26(b) with small amplitudes. Therefore, it is clear from these spectrograms that the

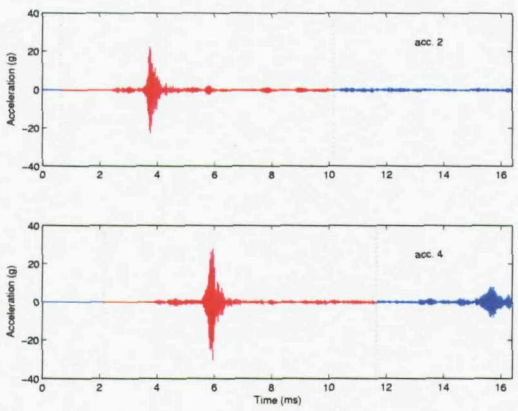

Fig. 6.25. Time signals measured at positions 2 and 4 at the top of the rail head in the longitudinal direction.

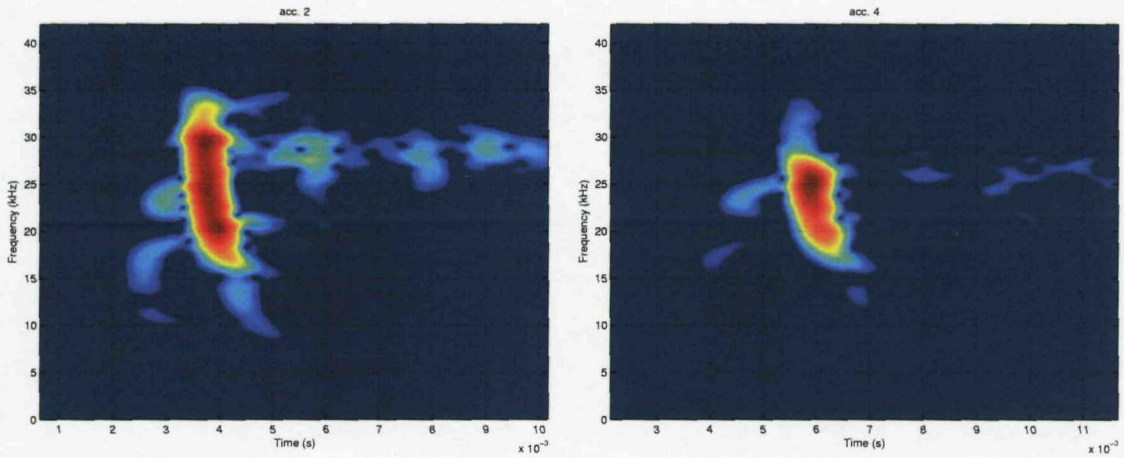

(a) (b)

Fig. 6.26. Spectrograms measured at positions 2 and 4 at the top of the rail head in the longitudinal direction.

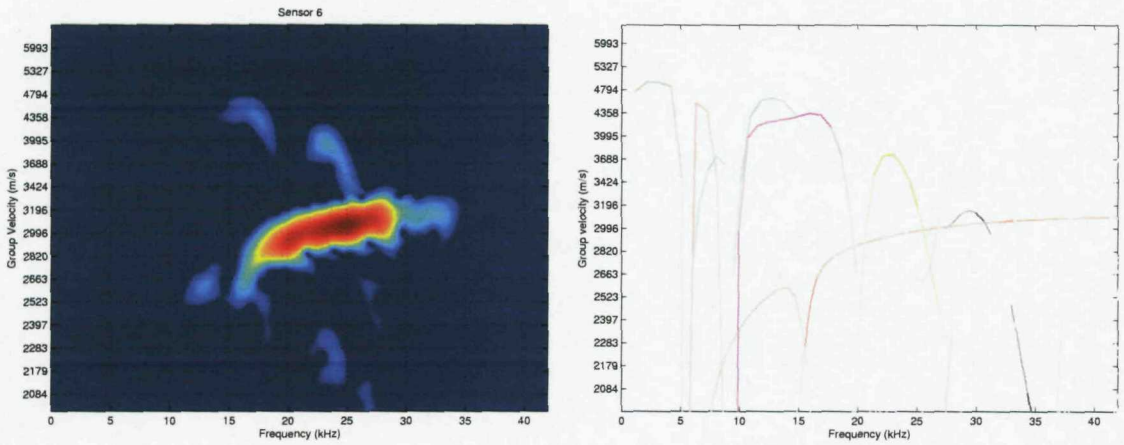

(a) (b)

Fig. 6.27. Group velocities at the top of the rail head in the longitudinal direction. (a) Measured at position 3, (b) predicted by the WFE method.

longitudinal excitation at the top of the rail head creates the vertical bending waves more effectively between 10 kHz and 35 kHz than the longitudinal waves. This is because the longitudinal excitation at the top of the rail head induces a large rotational moment with respect to the y axis. These time-frequency analysis results indicate that the measurable longitudinal waves are contained only in the initial part of the measured time signals, for instance, between 4 msec. and 5 msec. of the measured response at the 4^{th} sensor (Fig. 6.25).

The group velocity diagram measured at the top of the rail head is illustrated in

Fig. 6.27(a) and compared with the simulated result for the longitudinal direction. Although the longitudinal waves are not clearly highlighted in the measured group velocity diagram, it is clear that the measured waves correspond well to the predicted ones between 10 kHz and 25 kHz for the longitudinal direction.

6.1.9 Measured results at the side of the rail head in the longitudinal direction

In this measurement, the excitation was applied at the side of the rail head in the longitudinal direction, which is expected to create the antisymmetric longitudinal waves effectively. However, the measured propagating waves at positions 2 and 4 at the side of the rail head shown in Fig. 6.28 have similar initial time signals to those shown in Fig. 6.25 and also have a similar wave form to the measured ones shown in Fig. 6.14 for the lateral excitation. So it is anticipated that not only longitudinal waves but also lateral bending waves in the rail head were excited and captured in this experiment.

The spectrograms for the 2^{nd} and 4^{th} sensors were created from the data coloured red in Fig. 6.28 and are shown in Fig. 6.29 for the longitudinal direction. Compared with Fig. 6.15, the diagrams in Fig. 6.29 validate the presence of longitudinal waves and also bending waves in this measurement. The group velocity diagram measured at the side of the rail head is shown in Fig. 6.30(a) and the simulated result for the longitudinal direction is illustrated in Fig. 6.30(b). The antisymmetric longitudinal waves appear strongly in the simulated group velocity graph. Fig. 6.30(b) reveals

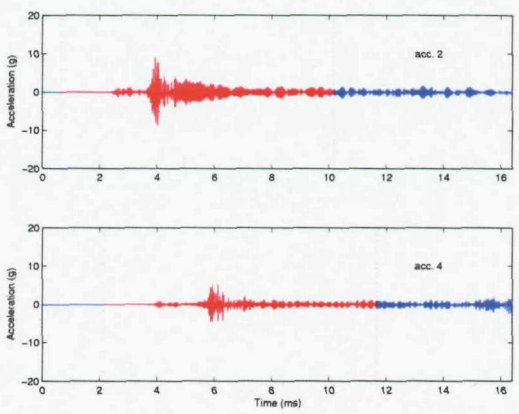

Fig. 6.28. Time signals measured at positions 2 and 4 at the side of the rail head in the longitudinal direction.

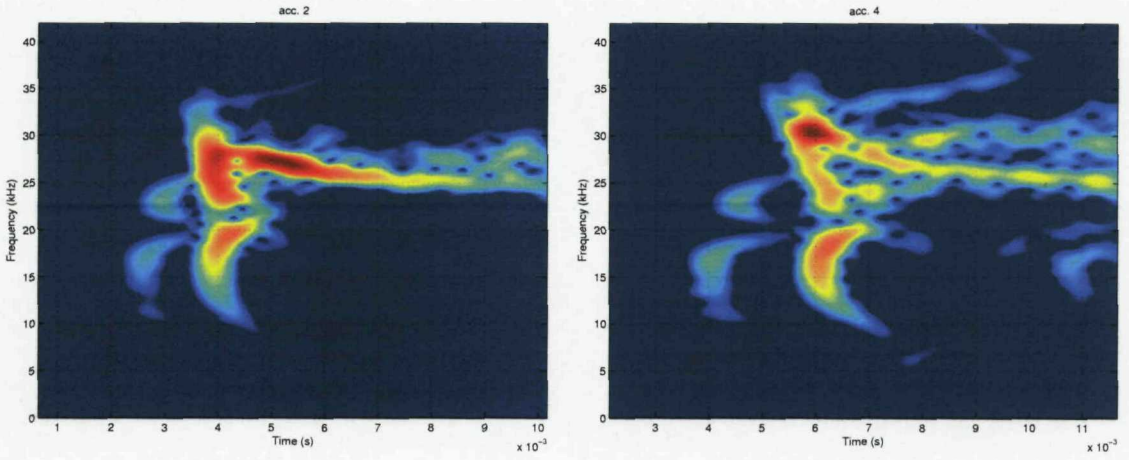

(a) (b)

Fig. 6.29. Spectrograms measured at positions 2 and 4 at the side of the rail head in the longitudinal direction.

that the first antisymmetric longitudinal wave occurs around 30 kHz. However, these measured and predicted group velocity diagrams provide completely different patterns. That is to say, the prominently measured longitudinal waves are not the antisymmetric ones, but the symmetric ones. The simulated group velocity at the side of the rail head predicted for the vertical and symmetric longitudinal waves is displayed again in Fig. 6.30(c). It can be easily recognized that a similar group velocity diagram to the measured one can be created if Fig. 6.30(b) and Fig. 6.30(c) are superimposed. So it is clear that the measured longitudinal waves between 3.5 msec. and 5.5 msec. in Fig. 6.29(b) at the side of the rail head are the same symmetric longitudinal waves as those shown in Fig. 6.26. The reason for this result is that the longitudinal excitation at the side of the rail head creates symmetric longitudinal waves effectively as well as antisymmetric ones.

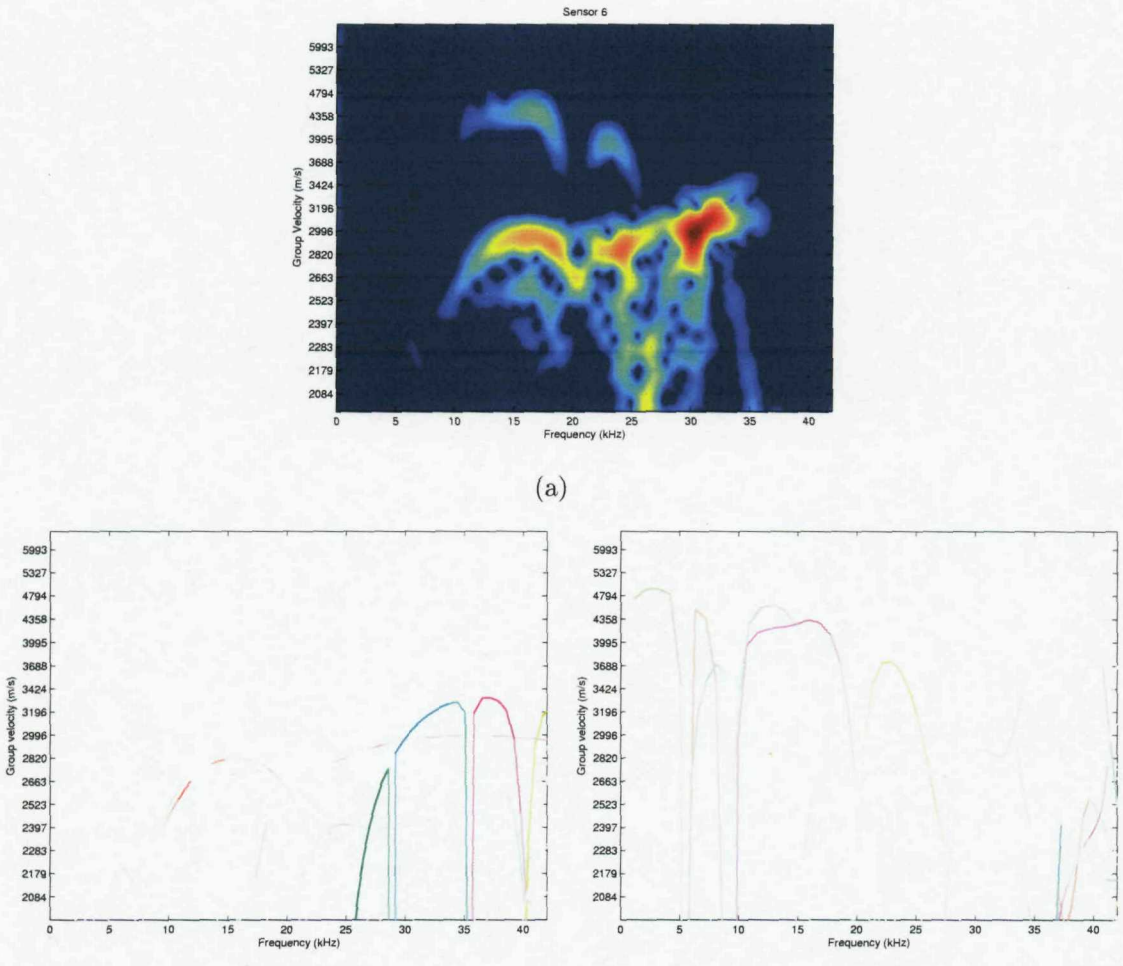

Fig. 6.30. Group velocities at the side of the rail head in the longitudinal direction. (a) The measured group velocities, (b) predicted ones for the vertical and symmetric longitudinal waves, (c) predicted one for the lateral, torsional and antisymmetric longitudinal waves.

6.2 Measurement Using Piezoceramic Transducers for Frequencies up to 80 kHz

In section 6.1, measurements were carried out only up to 42 kHz. That was because the data acquisition unit used had a frequency limit of 42 kHz and also because the impact hammer did not seem to be suitable for the excitation of waves in the whole frequency range up to 80 kHz. So a further experiment which can cover the high frequency region between 40 kHz and 80 kHz was required to validate the FE and WFE analysis results for whole frequency range from 0 to 80 kHz.

This additional experiment was conducted using piezoceramic transducers (PZTs)

for excitation instead of an impact hammer. In addition, an NI data acquisition board was used to achieve the higher rate of sampling required. The same processing as used for the previous measurement in section 6.1 was applied to extract dispersion relations. The measured results were then compared with the simulated ones obtained by WFE analysis.

6.2.1 Piezoceramic transducer

In this second experiment, PZTs were used for excitation because they can create a sharp impulse which is capable of exciting the structure up to 80 kHz. The PZT transfers electrical energy into mechanical energy when an electrical field is applied and vice versa. That is, applying an A.C. voltage to a PZT will cause it to vibrate, and thus generate mechanical vibration with the same frequency as the electrical voltage.

The type of PZT used in this experiment was Pz27 plate, manufactured by Ferroperm Piezoceramics A/S [60]. This PZT has a height of 1 mm and a square area of 12.7 mm $\times$ 12.7 mm. The working mechanism of this transducer is schematically shown in Fig. 6.31. When a voltage is applied it expands or contracts primarily in the length and width directions. The magnitude of these changes depends on the strength of the electrical field. As shown in Fig. 6.31, this causes a moment to be applied at the edges of the element due to the constraint applied by the structure, which in this case is the rail.

In terms of the structural response, the effectiveness of the excitation by PZT will be associated with how well the transducer's deformation is coupled to the

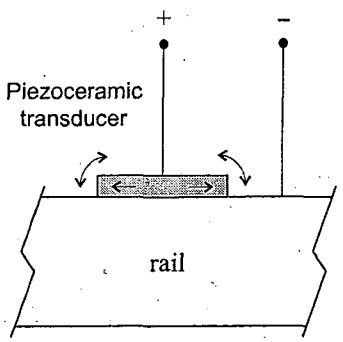

Fig. 6.31. Working mechanism of a piezoceramic transducer attached on a rail.

structural behaviour. For example, suppose that a PZT is attached on a thick plate. If an excited wave in the plate has much longer wavelength than the attached transducer's length, then this transducer would be inefficient in generating this wave. So the transducer used here will be inefficient at creating low wavenumber (long wavelength) waves because of its small size. On the other hand, the shortest wavelengths calculated at 80 kHz in the rail are about 35 mm at the rail head, 31 mm at the web and 29 mm at the rail foot, respectively, which are two or three times longer than the length of the PZT used in the experiment. So it will not exhibit nulls at frequencies below 80 kHz.

6.2.2 Measurement setup

The same accelerometers, PCB 352C22, as used before were utilised again in this high frequency measurement. Note that, according to the manufacturer's data sheet, their mounting resonances are located at about 90 kHz. Before carrying out the main experiment, a pretest was carried out in a laboratory with two different types of accelerometer having different mounting resonance frequencies. These two accelerometers are B&K Type 4344 and PCB 352C22 and their weights are 2.7 and 0.5 grams, respectively. It was reported from the manufacturers that usable frequency ranges for calibrated measurements using these sensors are up to 16.5 kHz and 20 kHz and also their resonances are located around 50 kHz and 90 kHz, respectively. This pretest was conducted to check the effect of the sensor's mounting resonance. In this pretest, the same plate type PZT was attached with glue on a short rail segment of length 15 cm. The accelerometers were attached using beeswax. For the same input excitations, the responses were measured from both sensors at the same location at the top of the rail head in turn.

It was found from this pretest that the B&K Type 4344 accelerometer had its mounting resonance around 30 to 40 kHz while for the PCB 352C22 it was around 60 to 70 kHz. Consequently the accelerometer, PCB 352C22, gave a larger signal than B&K Type 4344 at high frequencies above 40 kHz. It may be mentioned that these measured mounting resonances are a bit lower than those presented in the manufacturer's data sheets because both sensors were attached with beeswax. Although beeswax is known as a soft adhesive, it seems to be usable to mount sensors on the rail for this high frequency experiment because it gives a mounting

Fig. 6.32. Piezoceramic transducers attached at the top and side of the rail head and the middle of the web.

resonance which yields large output in the frequency range of interest. Based on this pretest result, it is anticipated that the accelerometer's resonances will occur between around 60 and 70 kHz in the test track measurement. It should be recalled that the measurements in the test are not required to be calibrated.

The Pz27 plate transducers, attached on the rail head and middle of the web are shown in Fig. 6.32. As a data acquisition unit, a four channel data acquisition board, PCI 6110 (National Instruments), was used. It was controlled with the MATLAB data acquisition toolbox. Of the four channels in the acquisition unit, one was allocated to the exciter delivering the impulse signal. The rest were connected to the sensors capturing the responses. A sampling rate of 200 kHz would be sufficient for capturing the rail responses but not enough for the generation of a suitable half sine input impulse with a short duration. Therefore, the sampling frequency of the acquisition unit was set to 400 kHz.

Like the previous measurement using an impact hammer, six accelerometers were set up along the rail, spaced at a distance of five sleeper spans apart. They were each placed at the mid span between two sleepers and attached by means of beeswax. However, since only three input channels in the data acquisition unit were available for each excitation, the same experiment was conducted twice with different sets of three sensors, simply changing sensor connections to the signal conditioner. That is, sensors 1, 3 and 5 or 2, 4 and 6 were used alternately for each excitation.

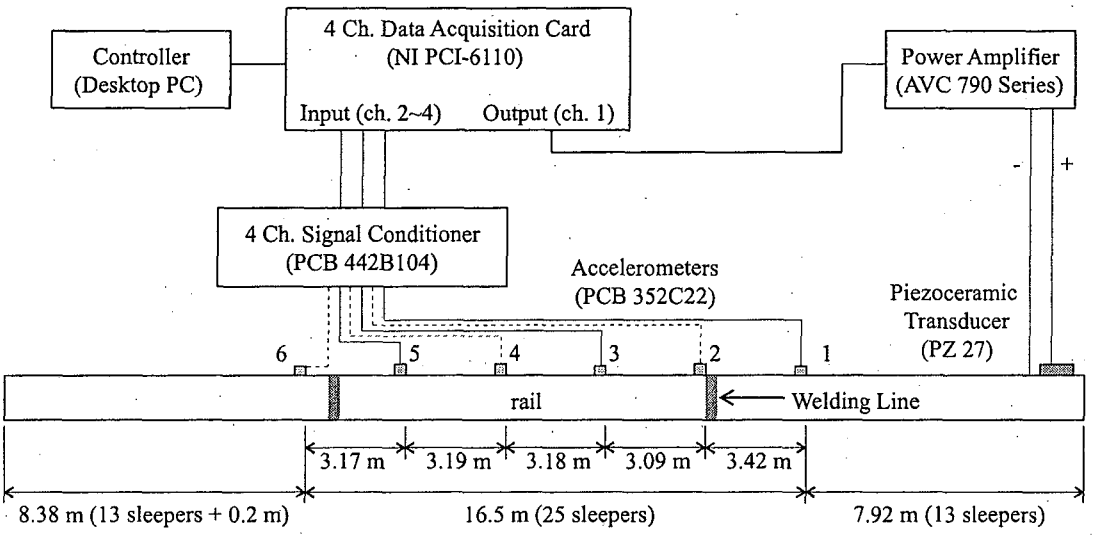

Fig. 6.33. Experimental setup using piezoceramic transducers as an exciter.

The measurement setup is shown in Fig. 6.33.

The excitations and measurements were implemented at three locations on the rail cross-section, i.e., at the top and side of the rail head and at the middle of the web as shown in Fig. 6.32. (Measurements on the foot were excluded in this experiment because it was found from the previous experiment that waves do not travel long distances along the rail foot). For each location, 10 excitations were applied and the responses along the rail were measured at the corresponding positions on the cross-section normal to the rail surface. A single half sine pulse with a duration of 12.5 μsec. was applied as an excitation signal and was supplied through the power amplifier set to an output of 200 volts which was its maximum output. In this measurement, the PZTs were attached about 5 mm away from the adjacent end of the rail. Since the shortest wavelengths in the rail below 80 kHz are around 30 mm as stated above, the phase cancellation due to the waves reflected from the adjacent end of the rail will not be significant for frequencies below 80 kHz.

6.2.3 Measured results at the top of the rail head in the vertical direction

As described above, the time signals were measured with a 400 kHz sampling rate. However, since the frequency band of interest in this analysis is limited to below 80 kHz, the original time data were decimated to a 200 kHz sampling rate by

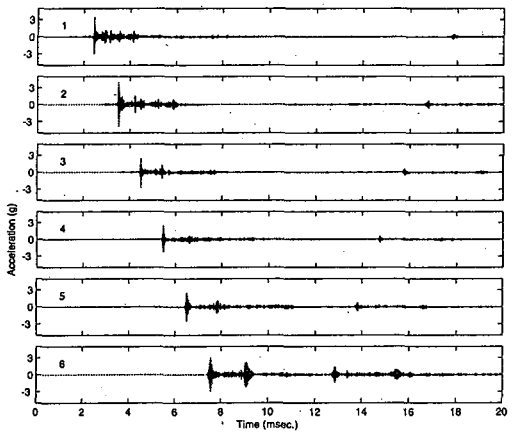

Fig. 6.34. An example of the measured time signals at the top of the rail head along the rail.

a factor of 2 in order to reduce the data size and computing load. In the decimation process the original data is filtered with a lowpass filter to avoid aliasing and then resampled at the lower rate.

Examples of the time signals measured at the top of the rail head at each position along the rail are shown in Fig. 6.34. These time signals display excellent waveforms of direct waves and echoes reflected from the end of the rail. It should be recalled that the responses at positions 1, 3 and 5 and positions 2, 4 and 6 in Fig. 6.34 were measured separately because the data acquisition unit had only three input channels. In addition, the measured time signals were not exactly synchronised with the instant of excitation because of a time delay internally in MATLAB while controlling the data acquisition board. Further examples of the measured time signals at each receiving position are illustrated in Appendix B.

The time signals measured at positions 2 and 4 at the top of the rail head are shown in Fig. 6.35 when the excitation was applied at the end of rail. At the 4^{th} sensor, the echo signal reflected from the far end of the rail also appears from 15 msec. in this figure. The section of data indicated in red in Fig. 6.35, which has 2048 data points and a duration of 10.24 msec., was analysed to construct the spectrograms. Therefore, the frequency increment Δf of the frequency axis will be 98 Hz since $\Delta f = (10.24 \times 10^{-3})^{-1} = 98$ Hz.

The spectrograms for the 2^{nd} and 4^{th} sensors are presented in Fig. 6.36. These

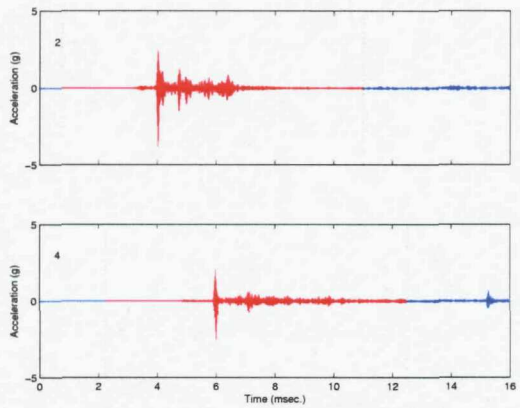

Fig. 6.35. Time signals measured at positions 2 and 4 at the top of the rail head in the vertical direction.

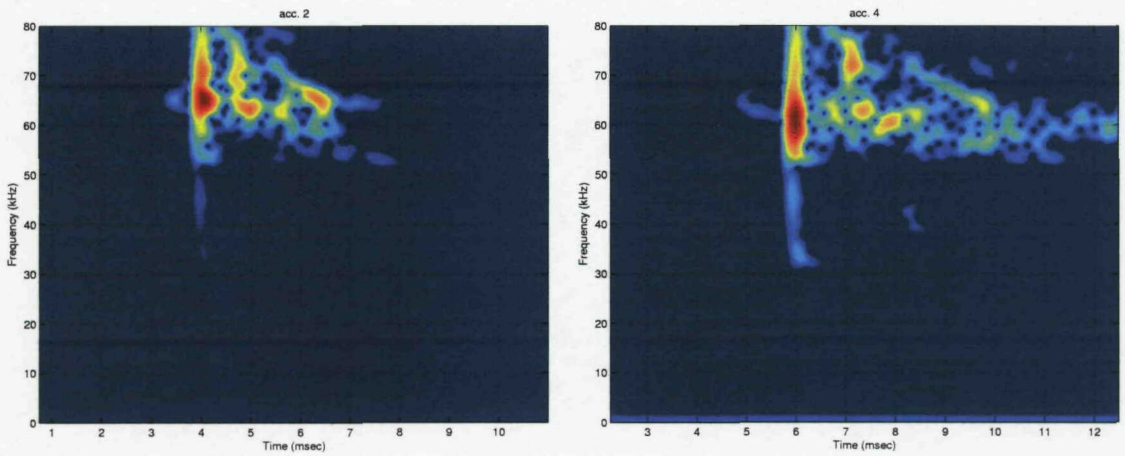

(a) (b)

Fig. 6.36. Spectrograms measured at positions 2 and 4 at the top of the rail head in the vertical direction.

spectrograms reveal that the waves in the range 50 kHz to 80 kHz were dominant in the measured signal with large energy. This is mainly because the mounting resonances of the sensors are located in this frequency range. Another considerable reason for it is that the piezoceramic transducer is not an efficient exciter for low wavenumber waves. These diagrams show which wave is dominant at high frequency.

The group velocity-frequency diagram at position 3 is illustrated in Fig. 6.37(a). As stated above, the time axis in Fig. 6.36 was not exactly synchronized with the moment of excitation. This probably causes a small bias in the conversion to a velocity axis in the frequency-velocity diagram but it will be neglected. A normalized version of Fig. 6.37(a) is shown in Fig. 6.37(b). This was formed by dividing each

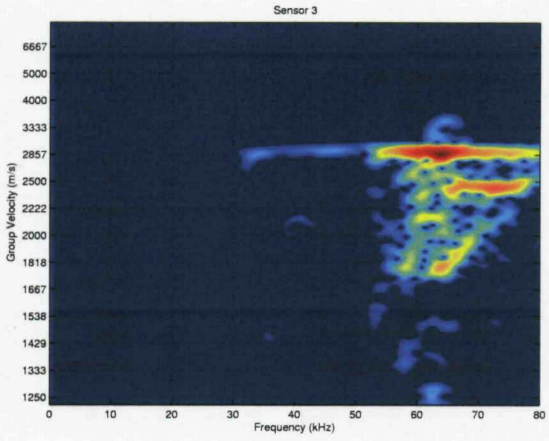

(a)

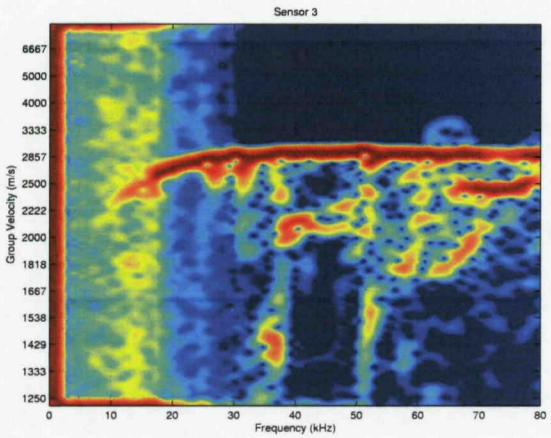

(b)

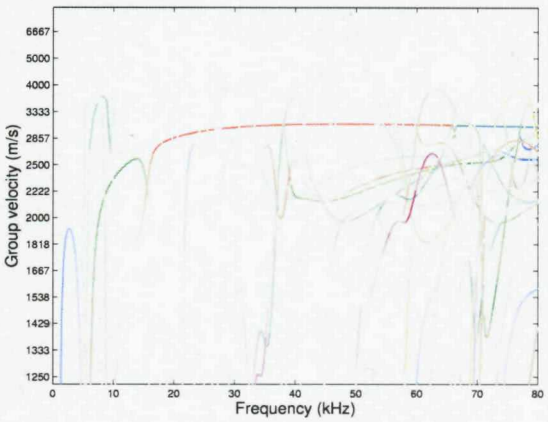

(c)

Fig. 6.37. Group velocities at the top of the rail head in the vertical direction. (a) Measured at position 3, (b) normalized version of (a), (c) predicted by the WFE method.

frequency column by its maximum value so as to improve the graphical visibility of the group velocity diagram at frequencies below 50 kHz. It is clearly observable from Fig. 6.37(b) that the exciter generated waves down to 20 kHz although they had much smaller amplitudes there. Also it can be seen that the low frequency region below 20 kHz is severely contaminated by noise. From the comparison with the simulated group velocities in Fig. 6.37(c), it is clear that the measured group velocity curves correspond very well to the simulated ones. This measured result indicates that the most measurable wave at the top of the rail head is still the vertical bending wave in the rail head at high frequencies.

6.2.4 Measured results at the side of the rail head in the lateral direction

The time signals measured at positions 2 and 4 at the side of the rail head are shown in Fig. 6.38. The section of data coloured red in Fig. 6.38, which has a duration of 10.24 msec., was analysed to make the spectrograms as before.

The spectrograms for the 2^{nd} and 4^{th} sensors are presented in Fig. 6.39. As shown in Fig. 6.39, most of the measured energy is concentrated at frequencies above 40 kHz. By comparing all the spectrograms obtained from six accelerometers, shown in Appendix B, it can be easily seen which wave propagates mainly along the rail.

Fig. 6.40(a) and (b) show the group velocity vs frequency diagram for position 3 and its normalized version. This normalized diagram clearly displays which waves are more effectively generated by the exciter than others. This effectiveness is thought to be related to the deformation shapes of the waves in the rail. Furthermore, not all possible waves will be excited by the PZT on the side of the rail head. However, it was not easy to identify the exact type of the wave measured primarily at high frequencies. Nevertheless, it could be said from Fig. 6.40(b) and (c) that the measured group velocity diagram agrees well with the predicted one. Again the results below 20 kHz are severely contaminated by noise.

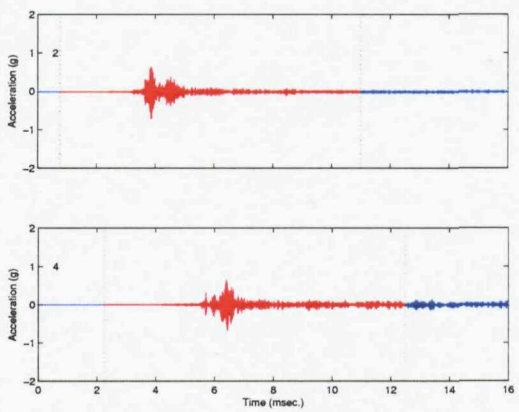

Fig. 6.38. Time signals measured at positions 2 and 4 at the side of the rail head in the lateral direction.

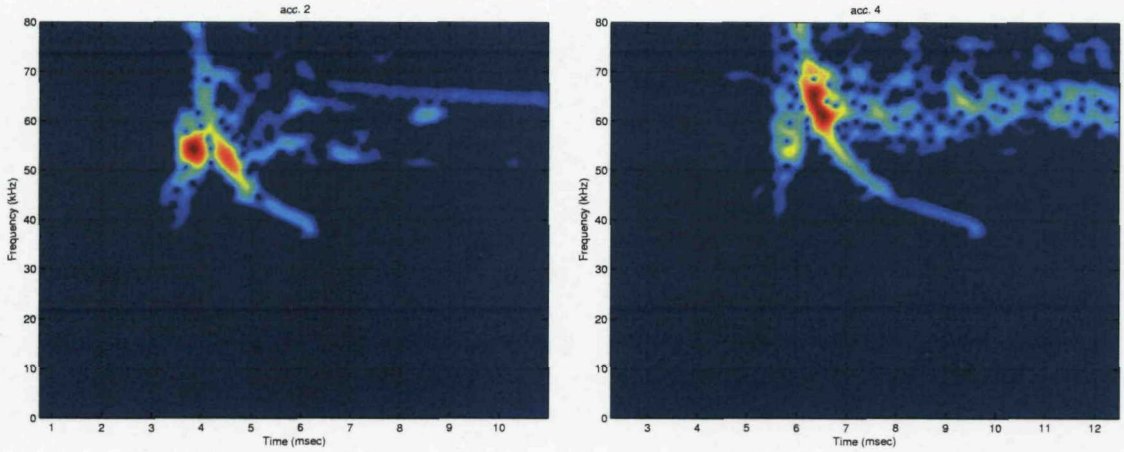

(a) (b)

Fig. 6.39. Spectrograms measured at positions 2 and 4 at the side of the rail head in the lateral direction.

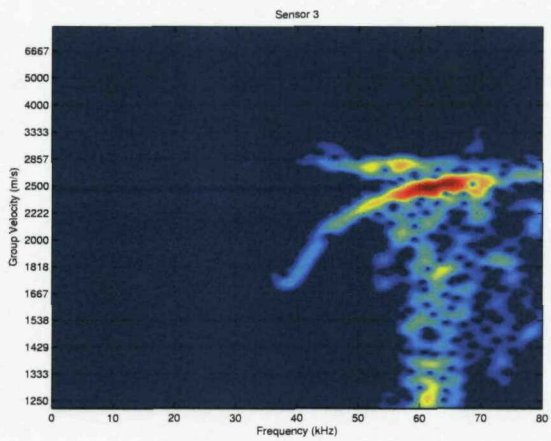

(a)

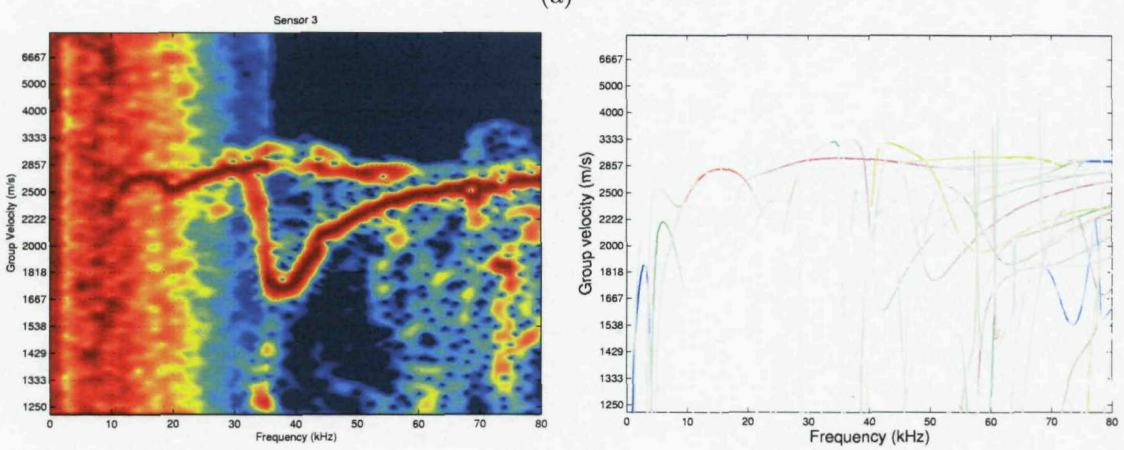

(b) (c)

Fig. 6.40. Group velocities at the side of the rail head in the lateral direction. (a) Measured at position 3, (b) normalized version of (a), (c) predicted by the WFE method.

6.2.5 Measured results at the middle of the web in the lateral direction

The time signals measured at positions 2 and 4 at the middle of the web are shown in Fig. 6.41. The flexibility of the web allows relatively large deformation as shown by the magnitude of the time signals. In addition, at the 4^{th} sensor, a waveform was recorded around 10 msec. that was created by the reflection due to the weld located between positions 5 and 6.

From these time data, the time-frequency diagrams were generated as shown in Fig. 6.42. These spectrograms exhibit fairly simple and clear dispersion curves. It turns out from Fig. 6.42 that only one wave is primarily measurable through almost the entire frequency range with a secondary one visible just above 50 kHz. Also, the wave reflected from the weld located between positions 5 and 6 appears in the spectrogram at position 4 around 10 msec. The wave reflections can also be seen clearly in the other spectrograms shown in Appendix B.

The group velocity diagram measured at the middle of the web is shown in Fig. 6.43(a) and its normalized version shown in Fig. 6.43(b). This normalization improves the graphical visibility in the low frequency region and demonstrates that only a single wave is primarily measurable through almost the entire frequency range with a secondary one visible just above 50 kHz. It is clear that the measured group velocity curves correspond to the green and purple lines in Fig. 6.43(c), which are the 1^{st} and 3^{rd} order web bending waves. Also, the wave reflected from the welding

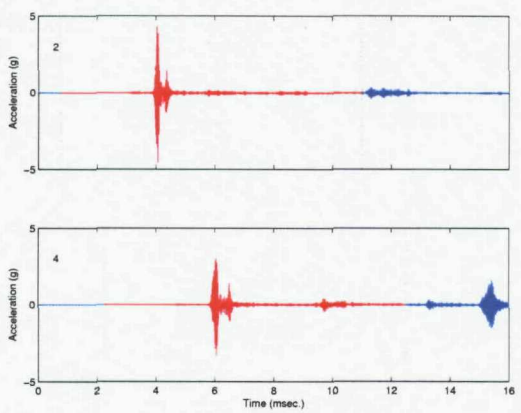

Fig. 6.41. Time signals measured at positions 2 and 4 at the middle of the web in the lateral direction.

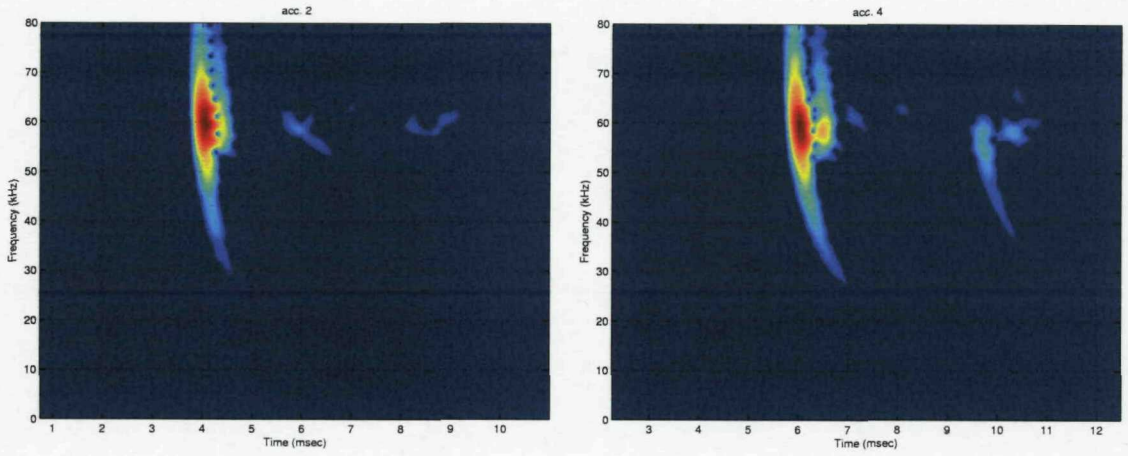

(a) (b)

Fig. 6.42. Spectrograms measured at positions 2 and 4 at the middle of the web in the lateral direction.

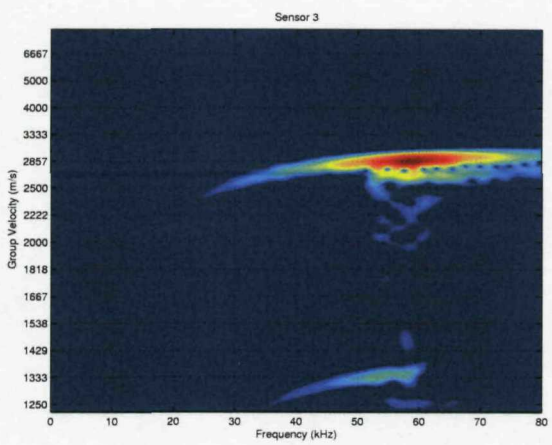

(a)

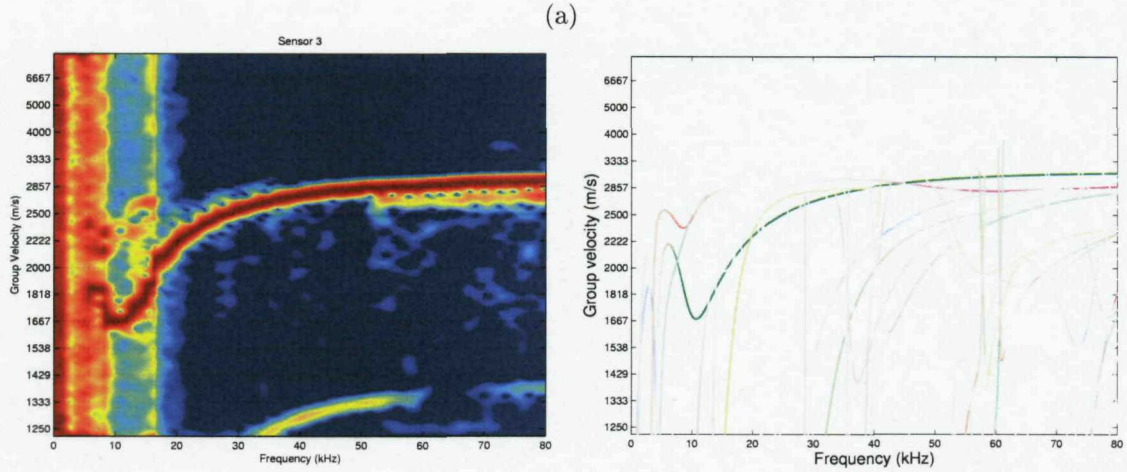

(b) (c)

Fig. 6.43. Group velocities at the middle of the web in the lateral direction. (a) Measured at position 3, (b) normalized version of (a), (c) predicted by the WFE method.

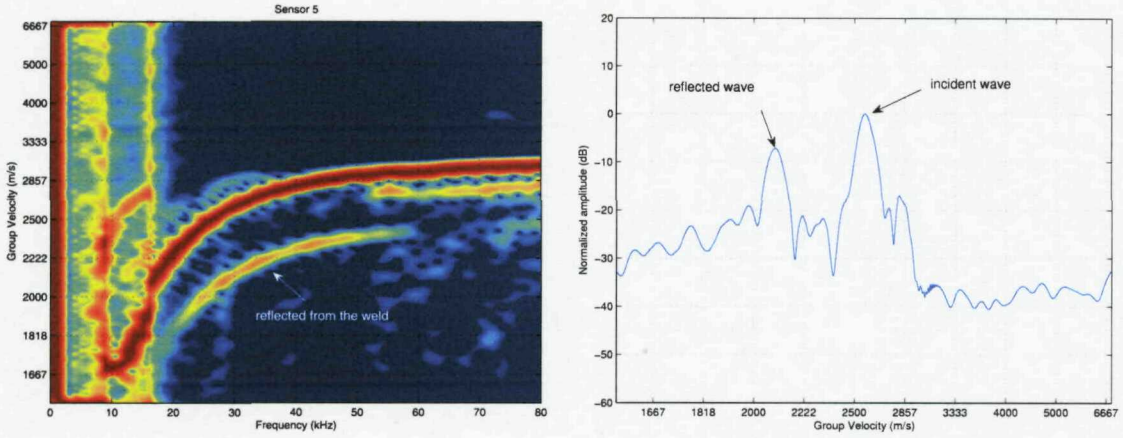

(a) (b)

Fig. 6.44. Normalized group velocity diagram measured at position 5 in the middle of the web in the lateral direction.

line located just after position 2 appears in the bottom of the measured diagram.

In order to quantify the rate of energy reflection caused by the weld in the rail, the group velocity diagram measured at the position 5 was investigated. The normalized diagram is shown in Fig. 6.44(a) and the wave reflected from the weld located between positions 5 and 6 is well presented. This figure shows that the reflection occurs primarily between 20 kHz and 60 kHz by the weld. For example, the normalized amplitudes of the incident and reflected energy at 28.3 kHz are compared in Fig. 6.44(b). As shown in Fig. 6.44(b), the reflected wave has about -7.3 dB which means that about 20 % of the incident power is reflected by the weld

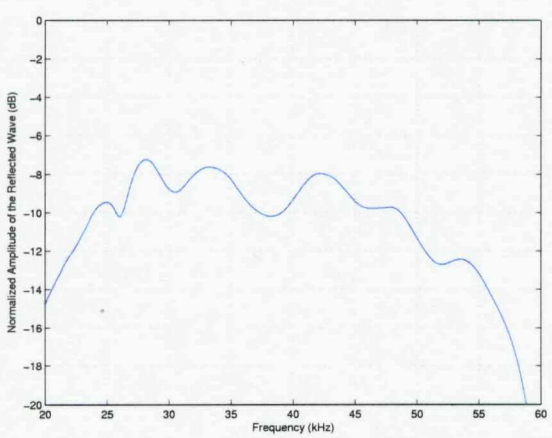

Fig. 6.45. Normalized amplitude of the energy reflected by the weld, measured at the middle of the web in the lateral direction.

at 28.3 kHz. The normalized amplitude of the reflected energy is shown in Fig. 6.45 for frequencies between 20 kHz and 60 kHz. It was found that about 10 to 20 % of the incident energy tends to be reflected by the weld between 25 kHz and 50 kHz.

6.3 Summary

In this chapter, experiments carried out on the ISVR test track of length about 32 m were reported in order to validate which wave types can propagate furthest along the rail. In these experiments group velocities were measured along the test track using an impact hammer and PZTs as exciters. A miniature impact hammer was used for frequencies below 42 kHz while PZTs were utilised for higher frequencies up to 80 kHz.

From the group velocity versus frequency diagrams measured at four different regions on the rail cross-section, it was validated that the measured group velocities give an excellent agreement with those of the measurable waves simulated in almost the entire frequency range. Therefore, by comparing the measured and simulated diagrams, the deformation shapes of the measured waves were inferred from the simulated results. These wave types found were to be identical to those specified in section 4.6.

From the signals measured on the foot, it was verified that waves do not travel long distances in that region of the rail. Also it was confirmed that the underside of the rail head can be used as an alternative measuring point to the top of the rail head. Meanwhile, in the signals measured at the middle of the web, it was observed that considerable reflections occur at the web due to welds. From the measured diagram, it was found that about 10 to 20 % of the incident energy carried by the web bending wave is reflected by a single weld between 25 kHz and 50 kHz. These could affect the long range propagation of a wave by reflecting a proportion of travelling energy. This rate of reflection may vary in other types of weld.

Since the waves propagating primarily were measured at six positions along the rail in the test track measurement, attempts were made to extract their decay rates. However, it has to be noted that the 32 m length track is not long enough to measure low decay rates of the order of about 10^{-2} dB/m precisely. Also sensor calibration

was an issue because multiple sensors were used and also the beeswax applied to attach them gives less reliable responses at high frequencies. Nevertheless, it was attempted to extract decay rates from the measured data by exciting at both ends of the rail. Details of this attempt are given in Appendix B.3.

Chapter 7

Decay Rate Measurements on an Operational Track

In Chapter 6, the simulated group velocities were validated from measurements made on the ISVR test track and the types of main propagating waves are identified in the various regions of the rail cross-section. However, the ISVR test track is too short to allow low decay rates to be determined precisely from the measured data, as presented in Appendix B.3.

In order to validate the simulated decay rates over a longer section of rail, it is necessary to carry out a field measurement on an operational railway track. Also it is apparent that there is great merit if operational trains can be used as excitation sources for the long range inspection of a rail instead of using external excitation. Hence, to determine whether train excitation is applicable or not, it is required to identify its frequency characteristics in an operational railway. This will show how effectively the high frequency waves are generated by a running train and the extent to which they propagate in a rail, particularly between 20 kHz and 40 kHz where the minimum decay rates are expected to occur. So in this chapter, the train-induced rail vibrations measured on an operational railway track are presented. These experiments were carried out with assistance from Balfour Beatty. Measurements were made for several running trains. The decay rates have been extracted from the measured signals and are then compared with those simulated by WFE analysis.

7.1 Test Site

The field measurement has been performed on the Up Slow track of the West Coast Main Line at Cattle Arch bridge in Dudswell north of Berkhamsted, UK in August 2006. This site has four tracks as shown in Fig. 7.1(a) and the first one from the right in the picture is the track on which the measurement was carried out. This track was selected to satisfy the following requirements for the measurement: a continuously welded rail and at least 500 m of plain line before and after the test site with no expansion joints, insulated rail joints or switches and crossings. This track had concrete sleepers but detailed information on the track components, such as rail geometry, support type, etc., was not available.

During the measurement, an observer located on a footbridge which is 924 m in advance of the test site gave a radio signal to warn of approaching trains so that the instrumentation recording could be switched on. The test site, Cattle Arch bridge, is shown in Fig. 7.1(b).

(a) (b)

Fig. 7.1. Pictures of test site. (a) Tracks near the test site looking North, (b) Cattle Arch bridge in Dudswell.

7.2 Measurement Setup

Four accelerometers, PCB 352C22, were used to measure the vibration at different locations on the rail cross-section as shown in Fig. 7.2 and Fig. 7.3. Two accelerometers were attached to the underside of the railhead (ch.2 and 4), one to the field side of the railhead (ch.1) and one to the middle of the rail web (ch.3).

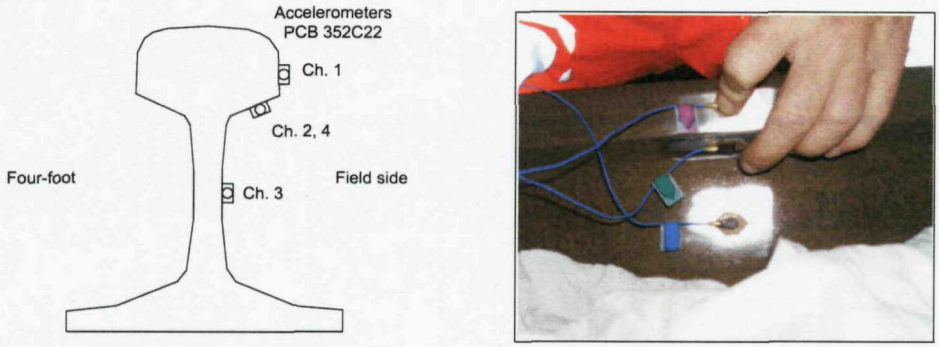

(a) (b)

Fig. 7.2. (a) Locations of accelerometers, (b) sensor attachment.

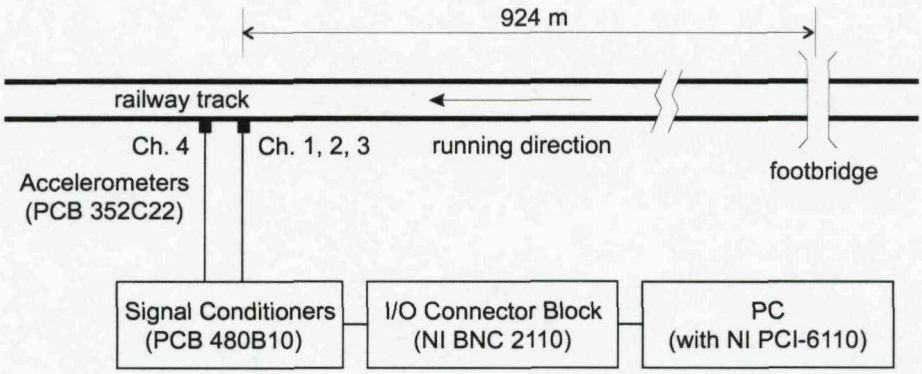

Fig. 7.3. Experimental setup for the field test.

The underside of the rail head was shown in numerical simulations to give very similar responses to the top of the rail head and this was validated from a test track measurement (see Section 6.1.3). Accelerometer 4 was applied with the intention of being able to detect train speeds from the signals measured by accelerometers 2 and 4. The distance between them was 3.25 m. All accelerometers were mounted at a position midway between sleepers using glue. To provide electrical isolation (both for traction return currents and any signalling issues) a nonconductive laminate material of thickness 0.4 mm was attached between the accelerometer and the rail. This can be seen in Fig. 7.2(b). The level of isolation provided by this wafer has been tested at ISVR to greater than 1000 MΩ at 1000 Volts DC. The equipment setup for this experiment is shown in Fig. 7.3.

The accelerometers were attached to the rail by Balfour Beatty staff during a routine night-time track possession and the cables run to the lineside for later connection to the instrumentation. The measurements took place the next day and

the instrumentation was removed during the following night. During the measurement, the data acquisition unit and controller (PC) were powered by a portable petrol-driven generator but the signal conditioners were battery powered. All the instrumentation was located under the bridge shown in Fig. 7.1(b).

Rail vibration was recorded for seven service trains. The input range of the data acquisition board and gains of the signal conditioners were varied in order to maximise the dynamic range of data obtained. The data acquisition unit digitized the input analogue signals with 12 bits of resolution. Although this range is limited, this data acquisition system was chosen because of its ability to acquire long time samples at a high enough sampling rate. The details on the measured data are listed in Table 7.1. For each train, two minutes of data were captured with a sampling rate of 200 kHz. The trains measured were all electric multiple units (EMUs) of either 4 or 8 coaches.

The train speeds listed in Table 7.1 were evaluated by two slightly different methods. The average speeds in Table 7.1 were calculated from the elapsed time between passing the footbridge shown in Fig. 7.3 and passing the site. On the other hand, the instantaneous speeds were found by using carriage lengths of each train and the elapsed time for a single carriage passage. The carriage lengths for Class 321 and Class 350 were considered as 19.95 m and 20.5 m, respectively. The elapsed time for a single carriage passage was identified by means of the autocorrelation of the vibration measured at the middle of the web. In setting up the measurement, it was intended to use the signals captured by accelerometers 2 and 4 to measure train speeds. However, it was observed from the post-processing of the measured data that the crosscorrelation between them does not present clear information on the time delay between the two signals. So the autocorrelation of the signal measured at the middle of the web, which identified well the time delay for a single carriage passage, was employed to determine train speeds.

For train 3, as an example, the vibration measured at the middle of the web and its autocorrelation are shown in Fig. 7.4. The passage of 8 bogies can be clearly seen in the time signal. Also from the autocorrelation of this time signal shown in Fig. 7.4, it can be found that the time elapsed during a single carriage passage is about 0.62 second. (Other peaks correspond to the distance between various pairs

Table 7.1. Details of data measured from the field test.

File name	Train type	Input range (V)	Speed (km/h)	
		× Amp. gain	Average	Instantaneous
train 1	8-car Class 321	± 5 × 1	-	156
train 2	4-car Class 321	± 1 × 1	109	119
train 3	4-car Class 321	± 0.2 × 1	111	116
train 4	8-car Class 350	± 0.2 × 1	166	162
train 5	4-car Class 321	± 0.5 × 1	111	119
train 6	4-car Class 321	± 0.5 × 1	123	132
train 7	4-car Class 321	± 1 × 10	115	124
ambient noise 1	-	± 1 × 10	-	-
ambient noise 2	-	± 0.2 × 1	-	-

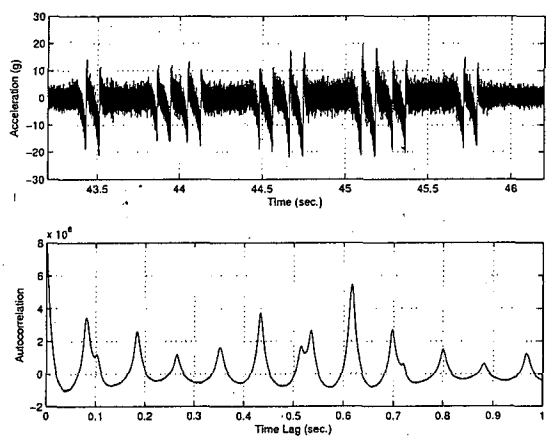

Fig. 7.4. Low pass filtered time signal measured at the middle of the web and its autocorrelation for train 3.

of wheels.) Hence the instantaneous speed is determined as 116 km/h. In this computation the time signals were low pass filtered with a 20 kHz cut-off frequency in order to enhance the autocorrelation.

It can be seen from Table 7.1 that the instantaneous speeds are slightly higher than the averaged ones in general. Based on these results, it is likely that trains were accelerating slightly as they approached the test site. However, since the speed profiles of the individual trains were not measured, the train's running distances have been estimated by using the instantaneous train speeds in the decay rate calculation. The effect of the acceleration of trains on measured results will be discussed further

below.

7.3 Measurement Results

As examples of the measured time signals, captured time histories for trains 2 and 3 are shown in Fig. 7.5 and Fig. 7.6. According to the input ranges given in Table 7.1 above, the measurable acceleration ranges for these two trains were about $\pm$ 100 g and $\pm$ 20 g, respectively, where g denotes the acceleration of gravity. All

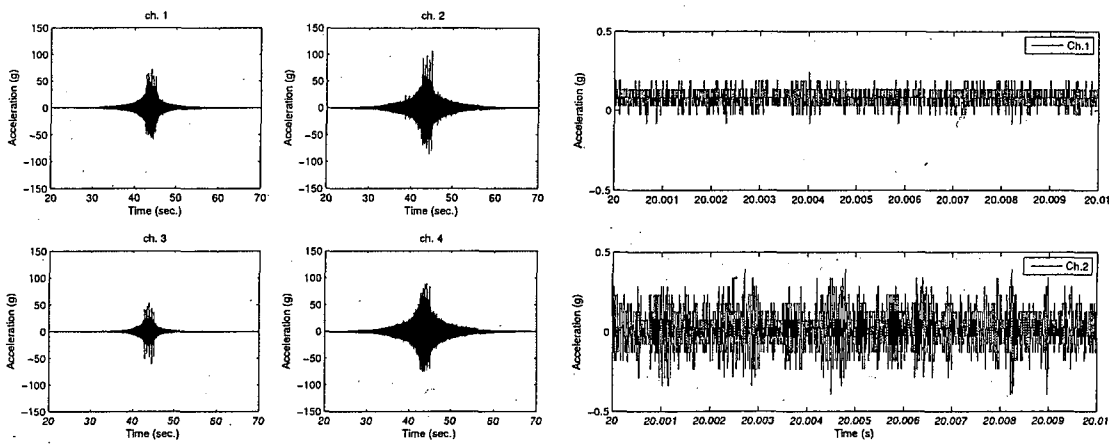

(a) (b)

Fig. 7.5. Time signals measured for train 2. (a) From 20 to 70 seconds for each channel, (b) around 20 seconds for channels 1 and 2.

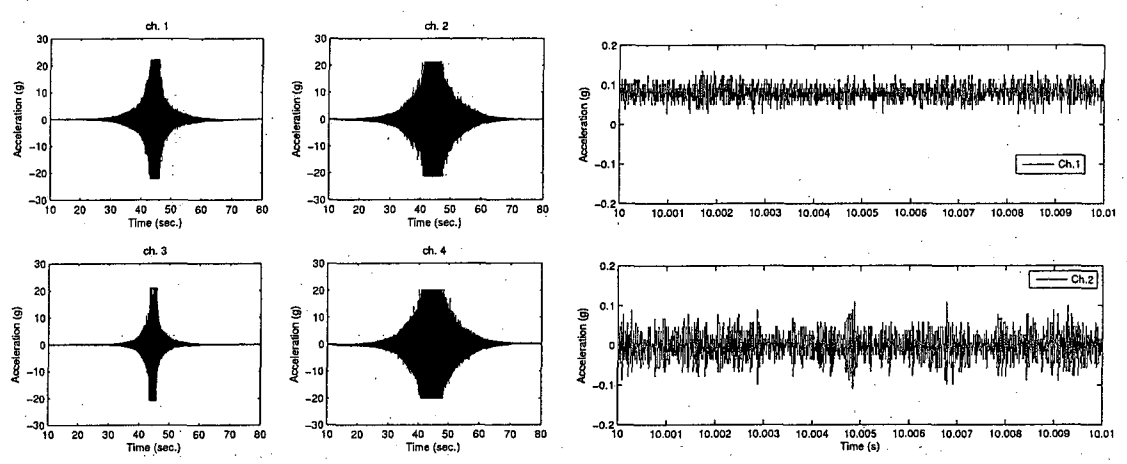

(a) (b)

Fig. 7.6. Time signals measured for train 3. (a) From 10 to 80 seconds for each channel, (b) around 10 seconds for channels 1 and 2.

the measured time signals are illustrated in Appendix C.1.

From the time signal for train 2 in Fig. 7.5(a), it was seen that all the data were captured without any saturation with the ± 1 V input range. Unfortunately, however, it is found that the low amplitude signals were poorly quantized as revealed in Fig. 7.5(b). So the sampled low amplitude signals will be less reliable in this case. On the other hand, the signals captured for train 3 show that saturation occurred when the train was just passing the test site. However, as depicted in Fig. 7.6(b), the low amplitude signals were quantized more reliably than those in Fig. 7.5(b) at the cost of this saturation. So the data for train 3 would be more useful for the purpose of determining long range propagation than those obtained for train 2. More detail on the measured signals will be analysed and discussed later.

In this chapter, the analysed results are described only for trains 2, 3, 4 and 7 because trains 5 and 6 produce similar results to trains 2 and 3. The measured data for train 1 was excluded in this analysis because the ± 5 volts input range used was too broad to capture the signals accurately. In addition, analysis of the measured ambient noise will be described later. All the analysed results for all the measured data are attached in Appendix C.2.

7.3.1 Analysis results for train 2

For train 2, the measured time signals during the train passage were shown in Fig. 7.5(a). These signals indicate that the train is passing the test site at between 42 and 45 seconds, inducing large rail vibrations at that time. According to these measured time signals, the response at the underside of the rail head is larger than the others, whereas the signal obtained from the middle of the web has the lowest amplitude. In addition, this figure shows that ±1 volt input range setting enabled the signals to be captured without clipping. As discussed already, it is apparent from Fig. 7.5(b) that the low amplitude signals were poorly quantized.

Above all, the responses acquired while a train is passing the measurement point need to be investigated in order to clarify the frequency characteristics of excitation which is generated by the wheel/rail rolling contact. The spectrograms obtained between 42 and 48 seconds are illustrated in Fig. 7.7. It should be noted that the

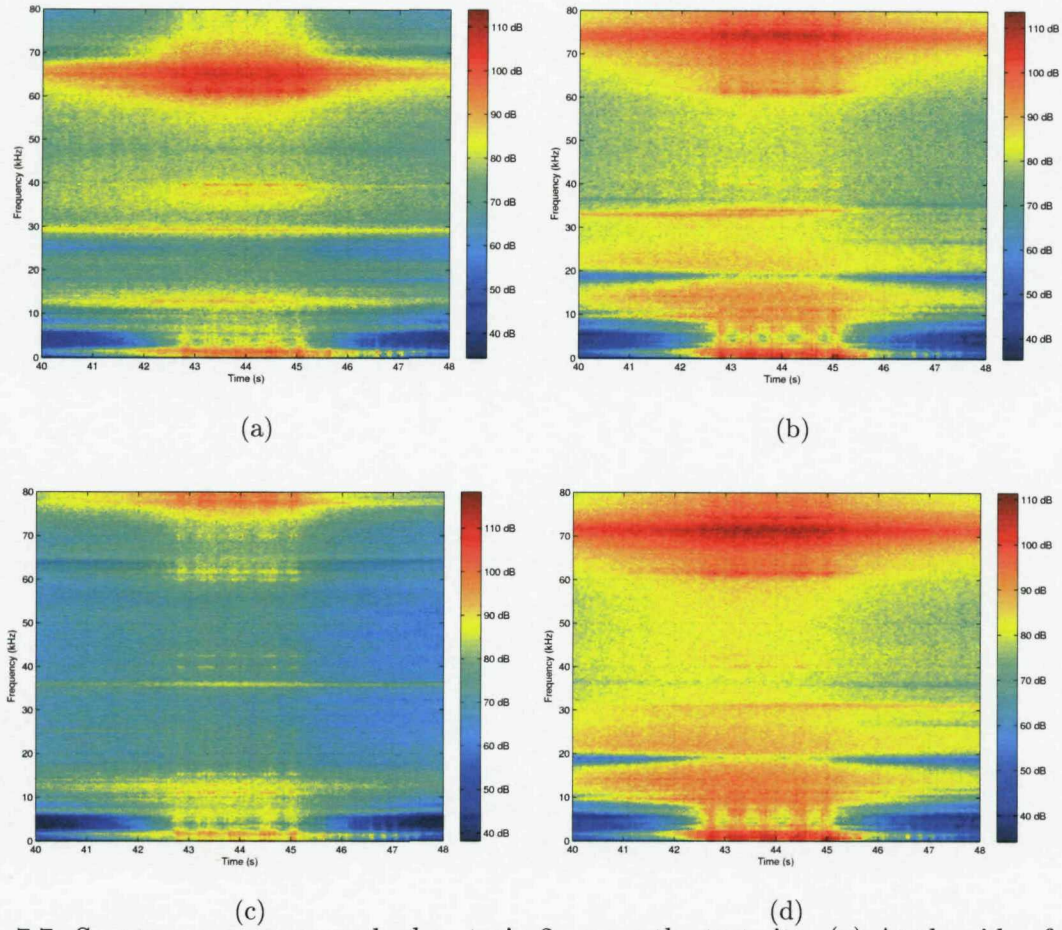

Fig. 7.7. Spectrograms measured when train 2 passes the test site. (a) At the side of the rail head (ch. 1), (b) at the underside of the rail head (ch. 2), (c) at the middle of the web (ch. 3) and (d) at the underside of the rail head (ch. 4).

large responses around 60 kHz and 80 kHz for each channel resulted not from the physical responses of the rail itself but from the sensor's mounting resonances.

It turned out from Fig. 7.7 that each part of the rail is excited in a different manner. The number of coaches of this train is detectable from these graphs. There are four cars in train 2 and thus five groups of wheels. The two responses measured at the underside of the rail head, that is, ch. 2 and ch. 4, were expected to be almost identical. As depicted in Fig. 7.7(b) and (d), they look similar in general but a large difference is found around 34 kHz and 31 kHz. The reason for this has not been identified. Also the rail responds well at 29 kHz at the side of the rail head and 36 kHz at the middle of the web although the reason for it is not understood.

The frequency spectra of the rail acceleration during the passage of the first

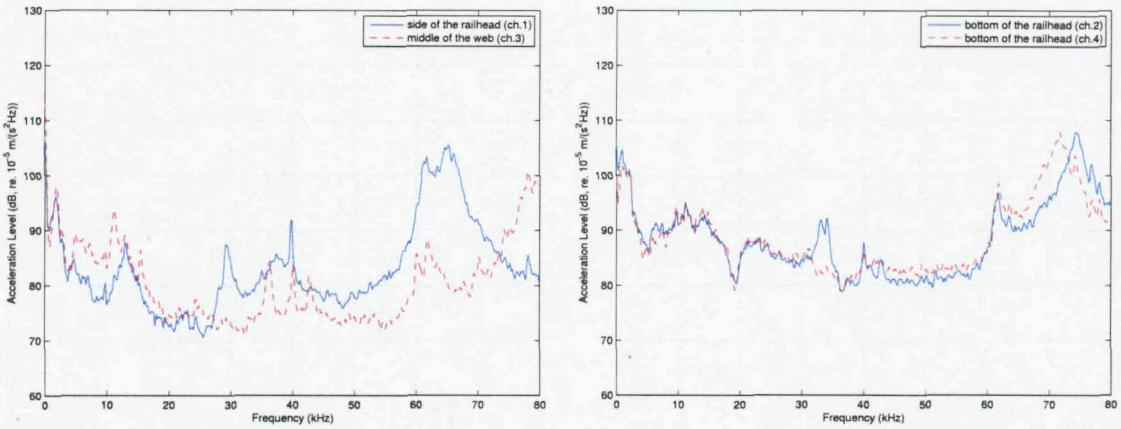

(a) (b)

Fig. 7.8. Acceleration levels created by the wheel/rail rolling contact. (a) At the side of the rail head (ch. 1) and middle of the web (ch. 3), (b) at the underside of the rail head (ch. 2 and 4).

bogie of train 1 past the measurement location are shown in Fig. 7.8. These were produced from the time signals between 42.7 and 42.9 seconds in Fig. 7.5. It is seen from this figure that the train induces a considerable rail vibration at frequencies below 5 kHz. This behaviour coincides very well with the published results in literature [61] which present the contact filtering effect between wheel and rail surface. What is more interesting in the present context is that running trains are found to be capable of exciting the rails quite well even at higher frequencies between 20 kHz and 50 kHz. The mechanism for this high frequency excitation was not identified yet.

7.3.2 Analysis results for train 3

For train 3, the measured time signals are illustrated above in Fig. 7.6(a). This figure showed that the ± 0.2 volt input range was too narrow so that the signals between 40 and 50 seconds were clipped. Conversely, however, this setting gives better quantization for small amplitude signals, as shown in Fig. 7.6(b). So this measured signal for train 3 is more reliable for studying the low amplitude response.

The spectrograms created for 0-90 seconds for each channel are presented in Fig. 7.9. Each column of the spectrograms was produced from 0.1 second of data and the frequency increment, Δf, of the frequency axis is 195 Hz. From these spectrograms it is clear that the waves below 20 kHz decay very rapidly, particularly at

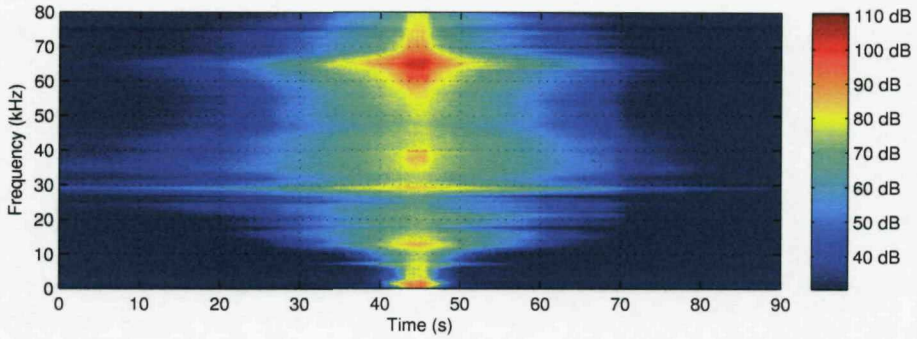

(a)

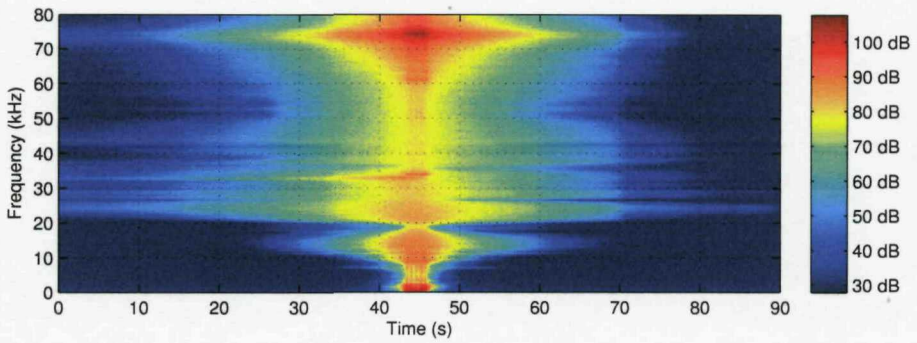

(b)

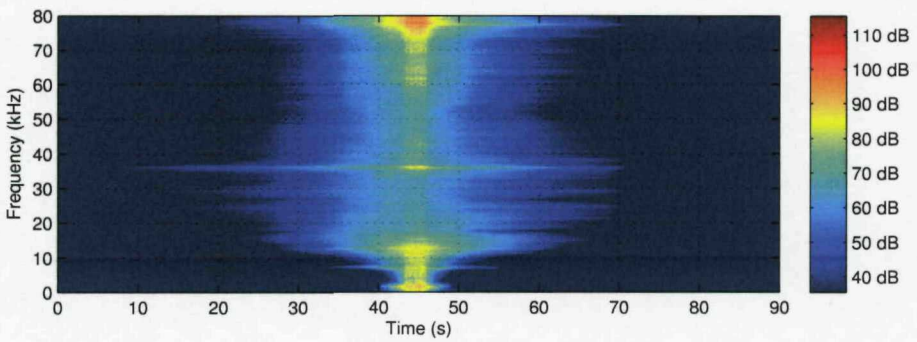

(c)

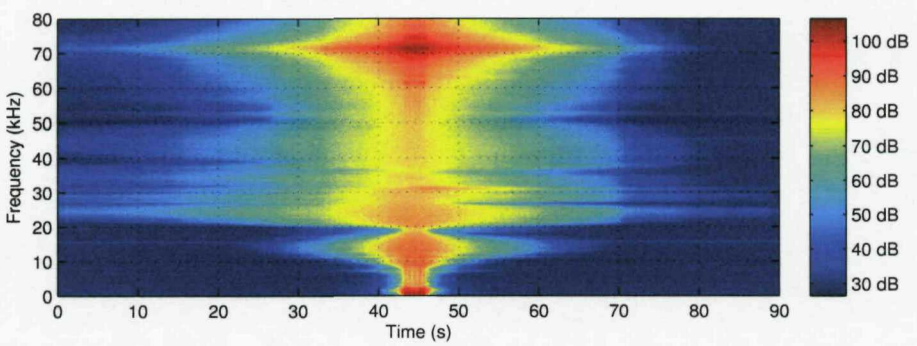

(d)

Fig. 7.9. Spectrograms measured for train 3. (a) At the side of the rail head (ch. 1), (b) at the underside of the rail head (ch. 2), (c) at the middle of the web (ch. 3) and (d) at the underside of the rail head (ch. 4).

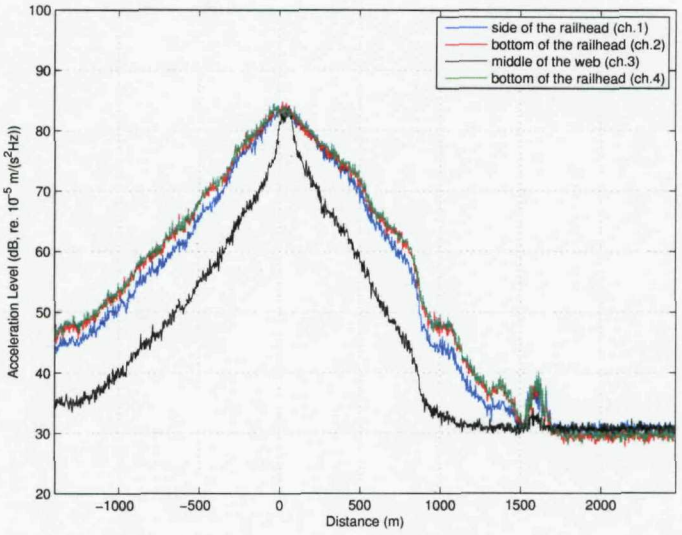

Fig. 7.10. Variations of acceleration levels along distance at each measuring point for train 3 in the frequency bands of about 29 kHz (ch.1), about 24 kHz (ch.2 and ch.4) and about 36 kHz (ch.3).

the underside of the rail head. Conversely, at this location, some energy between 20 kHz and 30 kHz is still measurable even about 40 seconds in advance of the train arrival. The frequency ranges which seem to be particularly useful in a practical application are about 29 kHz at the side of the rail head (ch.1), 24 kHz at the underside of the rail head (ch.2 and 4) and 36 kHz at the web (ch.3).

In terms of the propagating distance of a wave, the acceleration levels in these interesting frequency bands are shown in Fig. 7.10 for each measuring point with the bandwidth of 975 Hz. The train's running distance was converted from the time axis in Fig. 7.9 by using the instantaneous train speed of 116 km/h. As presented in Fig. 7.10, the approaching train is likely to be detectable at the underside of the rail head much more than a kilometre away. Even at the middle of the web, the detection range of the approaching train seems to be greater than a kilometre. In addition, this graph implies that it will be necessary to reduce the background noise level in the measured data in order to increase the detection range.

As displayed in Fig. 7.10, the measured acceleration levels did not vary linearly with distance. That is, the rate of change increases as the train approaches and increases further as the train recedes. This is very likely to be related to the acceleration of the running train as anticipated from the difference between average and

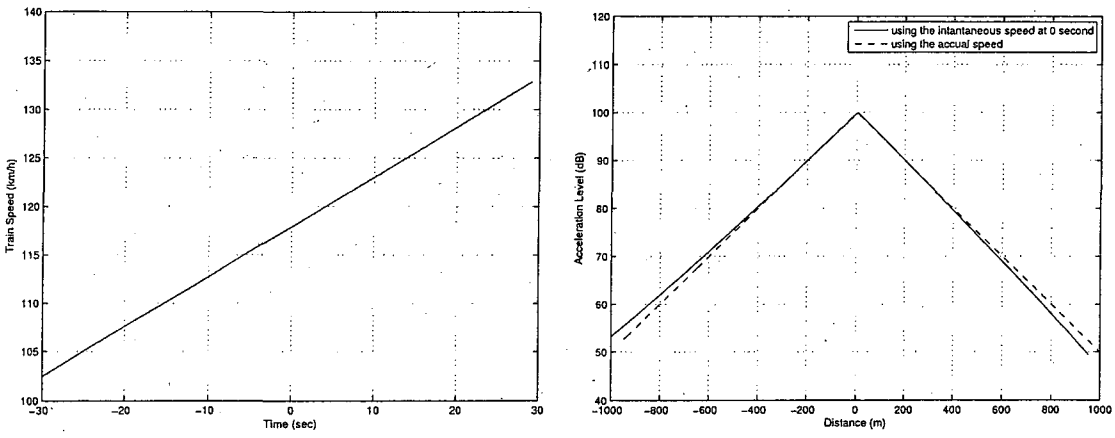

(a) (b)

Fig. 7.11. Simulation of acceleration level of a rail as a function of distance. (a) train speed, (b) simulated acceleration level.

instantaneous speeds shown in Table 7.1.

To investigate the effect of an accelerating train on the acceleration level as a function of distance, a simple simulation was performed assuming linearly increasing train speed with time as shown in Fig. 7.11(a). In this figure, zero seconds corresponds to the instant when the train is passing. This imaginary train's average speed between -30 and 0 seconds becomes about 111 km/h and the instantaneous speed at about 0 second is about 118 km/h. Also, in this simulation, it was assumed that the source level of the train is 100 dB and the decay rate of a propagating wave in the rail is 0.05 dB/m. The simulated acceleration level due to this train is illustrated in Fig. 7.11(b) as a function of distance, which was obtained from the instantaneous speed of 118 km/h. As illustrated in this figure, the simulated acceleration level gives a similar trend to the measured ones in Fig. 7.10. It was therefore plausible from this simulation result that the train was accelerating during the measurement and this acceleration caused the curved shape of variation shown in Fig. 7.10.

Also, as depicted in Fig. 7.10, the acceleration level measured at the middle of the web changes more rapidly near the time of the train passage than the others measured at the rail head. This may be due to a greater contribution from rapidly decaying waves propagating through the web, but this could not be clearly identified yet.

From the spectrograms in Fig. 7.9, it appeared that the level of energy drops suddenly at around 70 seconds. This event is more apparent in Fig. 7.10 around 830 m. Note that if the acceleration of the train is considered, the location of this event is actually about 900 m. Balfour Beatty Rail Technologies arranged for a track walk along the rail to look whether a discontinuity of some sort is present there in the rail but they did not find anything of note. Alternatively the excitation level may be less for a while around this location because the rate of level change seems to be consistent between 500 and 1400 m except around the energy drop between 900 and 1250 m. Furthermore, an abrupt surge of energy appears around 1600 m away from the test site. At approximately this distance the train reaches a tunnel, where it is

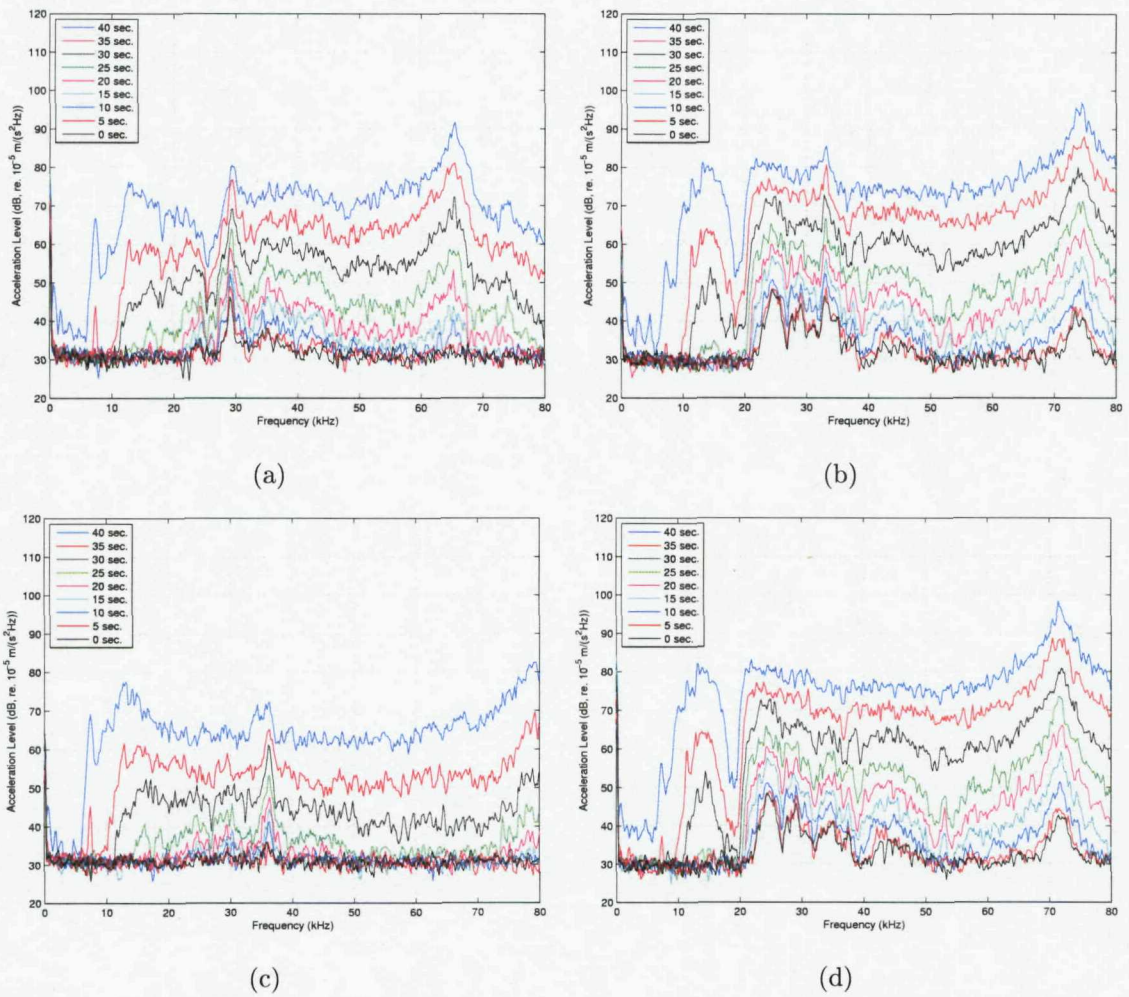

Fig. 7.12. Acceleration levels before the passage of train 3 at different times with the same time interval of 10 seconds. (a) At the side of the rail head (ch. 1), (b) at the underside of the rail head (ch. 2), (c) at the middle of the web (ch. 3) and (d) at the underside of the rail head (ch. 4).

possible that there are some rail joints, but this could not be confirmed.

While a train is approaching or receding, the acceleration levels of the rail at a given frequency will increase or reduce with time. So, decay rates can be obtained from the level difference between two train positions by dividing it by the train's running distance between them. The acceleration spectra of the rail at different times are compared in Fig. 7.12. This shows results before the train passed, spaced at 5 second intervals. Each line in Fig. 7.12 was produced from the time signals of about 3 msec. duration with a frequency resolution of 195 Hz. In these figures, it can be confirmed that the signals in the region 20 kHz to 40 kHz decay more

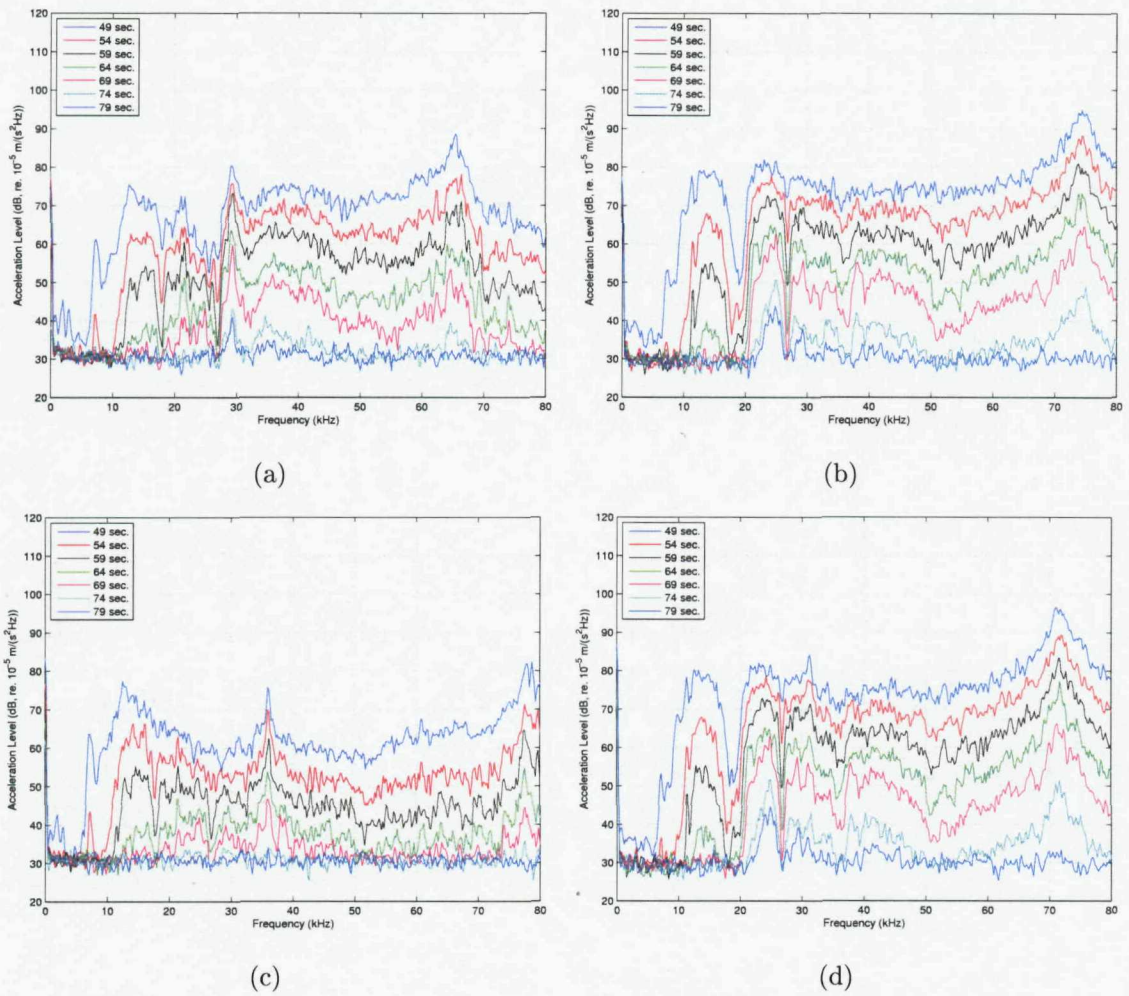

Fig. 7.13. Acceleration levels after the passage of train 3 at different times with the same time interval of 10 seconds. (a) At the side of the rail head (ch. 1), (b) at the underside of the rail head (ch. 2), (c) at the middle of the web (ch. 3) and (d) at the underside of the rail head (ch. 4).

slowly than others. Fig. 7.12 indicates that the acceleration levels from 20 to 40 seconds tend to have consistent level increments and also they seem to be less affected by the background noise. So the acceleration levels from 20 to 40 seconds in Fig. 7.12 will be used for the decay rate calculation. In the case of the web, only the signals at 40, 35 and 30 seconds will be included in the calculation because the signal at 20 seconds was severely contaminated by noise as shown in Fig. 7.12(c).

The measured acceleration spectra after the train passed the measurement location are presented in Fig. 7.13 with the same time interval. As described above, it is clear that there are relatively large level drops between 69 and 74 seconds. From the acceleration levels shown in Fig. 7.13, the levels from 49 to 64 seconds were used for the decay rates calculation. In the case of the web, only the signals at 49, 54 and 59 seconds were included, in order to avoid the contribution of noise. The decay rates produced from this field test will be presented later in Section 7.3.5, comparing them with the simulated results obtained by WFE analysis.

7.3.3 Analysis results for train 4

For train 4 the measured time signals between 0 and 60 seconds are shown in Fig. 7.14. Since this train had 8 coaches and travelled faster, at about 160 km/h, the measured time histories look like a compressed version of the previous one. Also this train seems to induce more rail vibration than the previous one. The signals are clipped for the length of the train (about 8 seconds) on ch. 1 and 3, but for about 16 seconds for ch. 2 and 4.

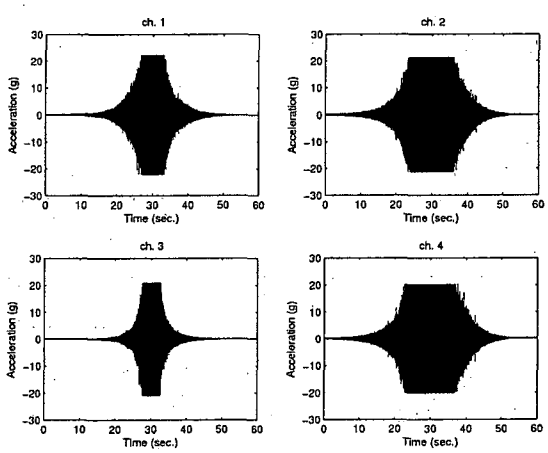

Fig. 7.14. Time signals for train 4 measured from 0 to 60 seconds at each channel.

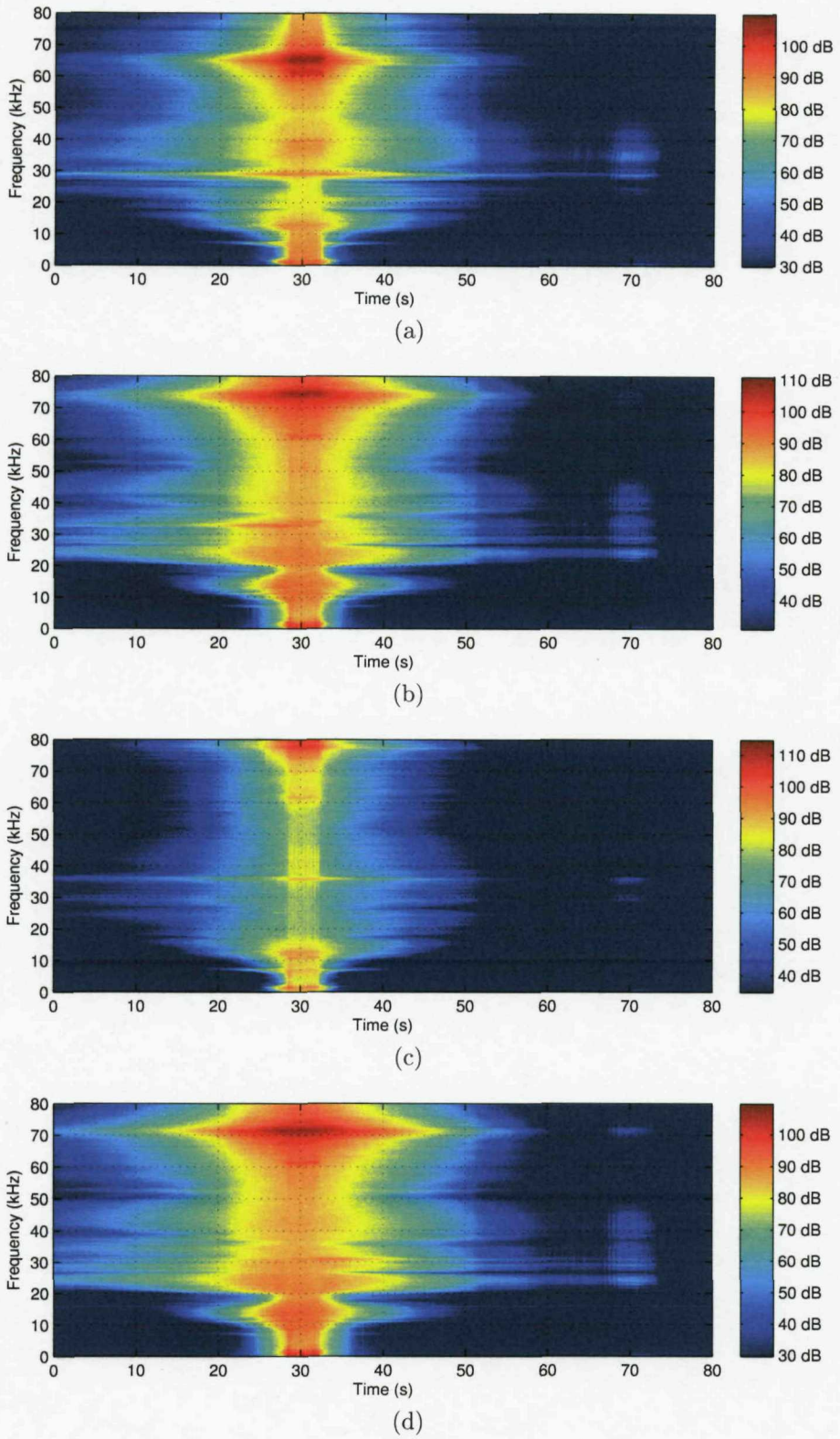

Fig. 7.15. Spectrograms measured for train 4. (a) At the side of the rail head (ch. 1), (b) at the underside of the rail head (ch. 2), (c) at the middle of the web (ch. 3) and (d) at the underside of the rail head (ch. 4).

The spectrograms measured at each transducer location are presented in Fig. 7.15. They look similar to those in Fig. 7.9 for train 3 but compressed in the time axis due to the higher train speed. These spectrograms present almost the same frequency characteristics as the previous ones although train 4 is of a different type and has a higher running speed than train 3. Also, despite the saturation of the measured time data around 30 seconds, the spectrograms clearly indicate how many carriages are in this train. Meanwhile, a distinctive feature in these spectrograms is that a comparatively large amount of vibration energy is seen at 70 seconds, at which the train is about 1650 m away from the measurement point. The reason for this increase in energy remains unexplained.

The variations of acceleration levels with distance are shown in Fig. 7.16 for each channel. The frequency bands used for this plot were centred around 29 kHz at the side of the rail head (ch. 1), around 24 kHz at the underside of the rail head (ch. 2 and 4) and around 36 kHz at the web (ch. 3) with the bandwidth of 975 Hz as used previously. The measured acceleration levels for this train indicate the same behaviour as shown in Fig. 7.10 for train 3. As discussed for train 3, this curved shape level variation possibly results from the acceleration of the train. Compared

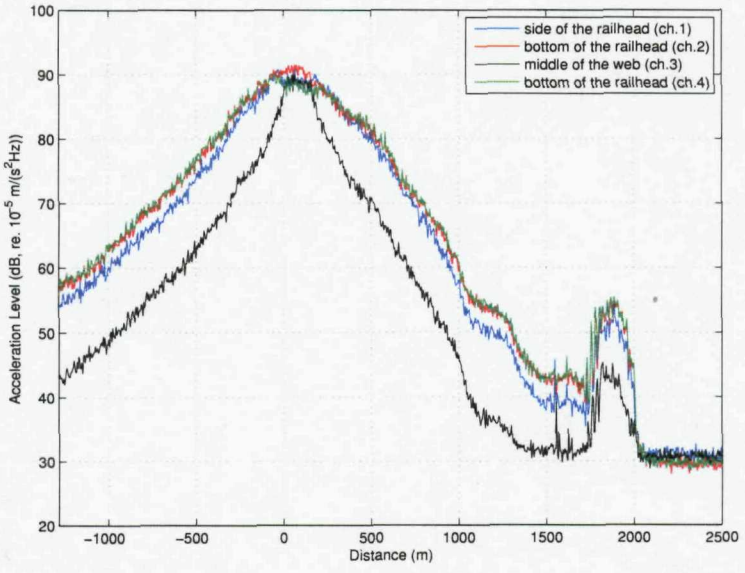

Fig. 7.16. Variations of acceleration levels along distance at each measuring point for train 4 in the frequency bands of about 29 kHz (ch.1), about 24 kHz (ch.2 and ch.4) and about 36 kHz (ch.3).

with Fig. 7.10, it is clear that this train creates rail vibration between 5 and 10 dB larger than the previous one which is unsurprising since it contains twice as many coaches and also is much faster than train 3. Therefore, this approaching train will be detected much more than a kilometre before the train arrival, even at the middle of the web.

The acceleration spectra of the track at different times are compared in Fig. 7.17 and Fig. 7.18 before and after the train passage. It can be confirmed once again from these figures that the frequency spectra of trains 3 and 4 are very similar despite the different train types and running speeds. As before, the decay rates were calculated

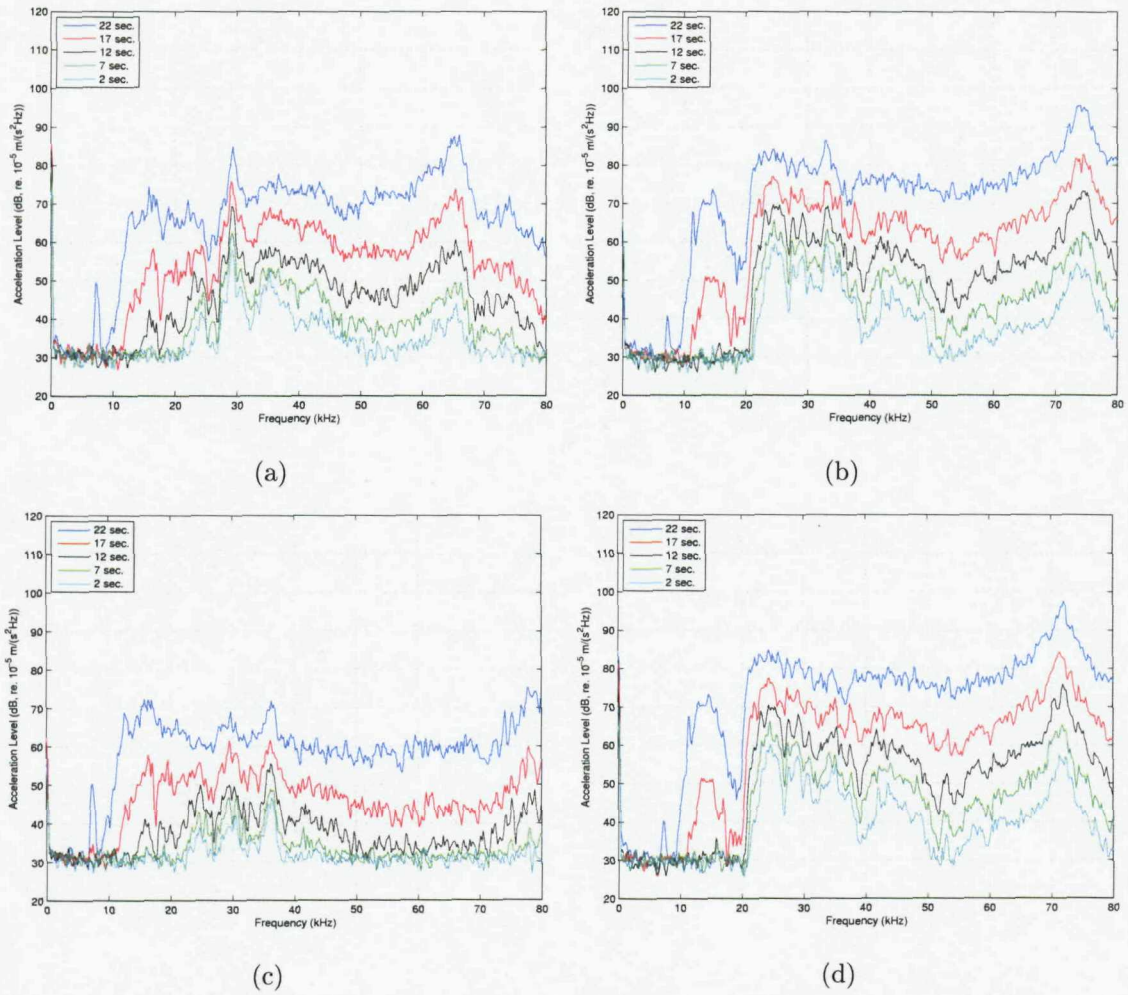

Fig. 7.17. Acceleration levels before the passage of train 4 at different times with the time interval of 5 seconds. (a) At the side of the rail head (ch. 1), (b) at the underside of the rail head (ch. 2), (c) at the middle of the web (ch. 3) and (d) at the underside of the rail head (ch. 4).

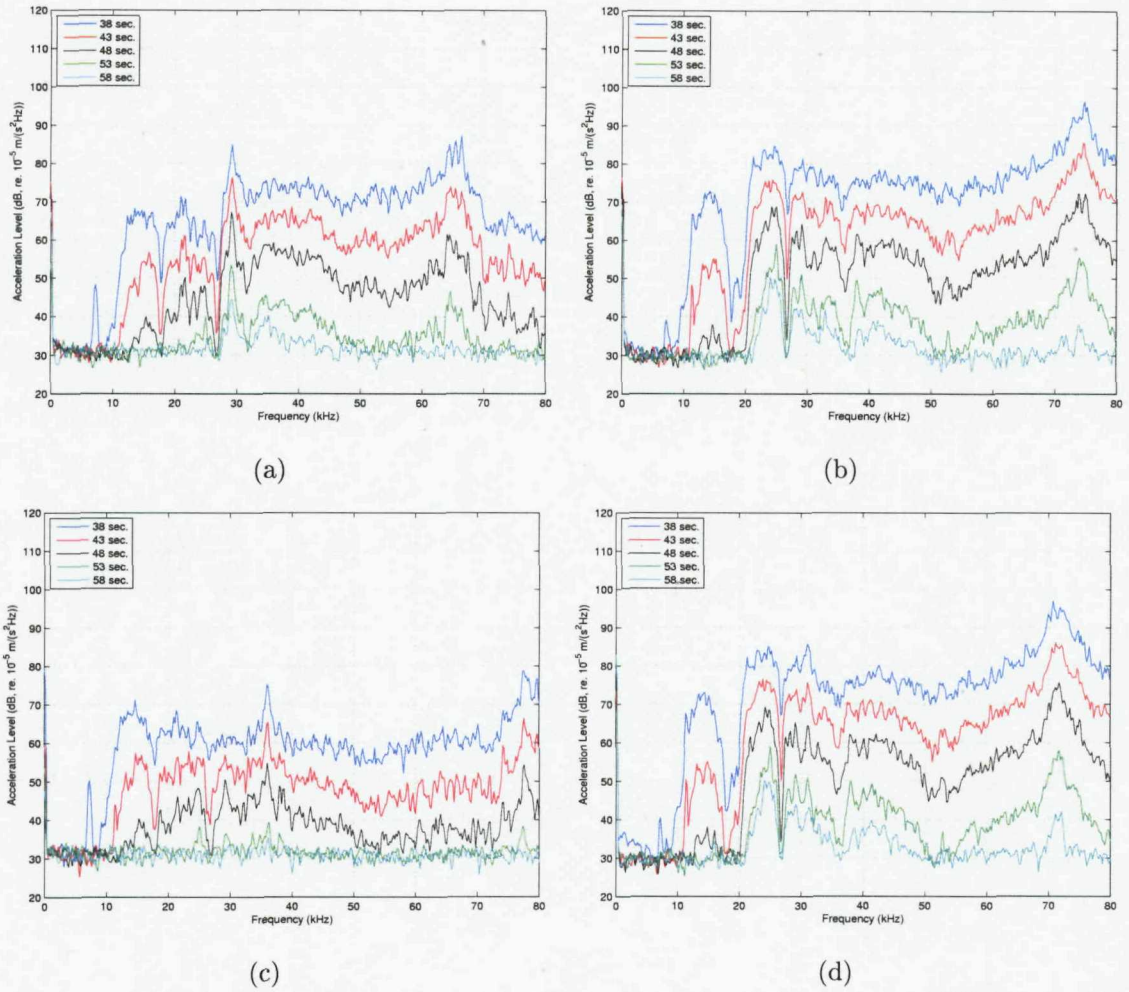

Fig. 7.18. Acceleration levels after the passage of train 4 at different times with the time interval of 5 seconds. (a) At the side of the rail head (ch. 1), (b) at the underside of the rail head (ch. 2), (c) at the middle of the web (ch. 3) and (d) at the underside of the rail head (ch. 4).

from the acceleration levels measured at 22, 17 and 12 seconds in Fig. 7.17 and at 38, 43 and 48 seconds in Fig. 7.18 for all channels. The decay rates produced from this field test will be discussed in Section 7.3.5.

7.3.4 Analysis results for train 7

As listed in Table 7.1, train 7 was measured with instrumentation set to the highest gain, equivalent to $\pm$ 0.1 volt input range, so the area around the train passage will be most overloaded. However, the measured data are expected to have the lowest noise level and should give the furthest detection range without running

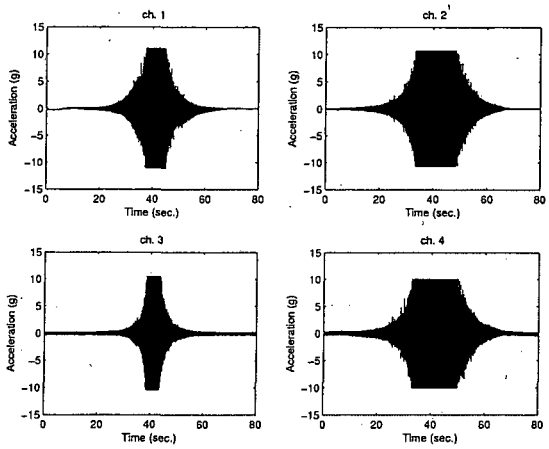

Fig. 7.19. Time signals for train 7 measured from 0 to 80 seconds at each channel.

into the noise. The measured time signals between 0 and 80 seconds are shown in Fig. 7.19 for train 7. Unfortunately, the signals in channels 3 and 4 have relatively large contributions of noise as shown in Fig. 7.19. It is suspected that the signal conditioners, PCB 480B10, connected to channels 3 and 4 introduced this additional noise when their amplification gains were set to 10 but this has not been clearly demonstrated.

The spectrograms are presented for channels 1 and 2 only in Fig. 7.20. The same abrupt level changes appear once again at around 66 seconds and between 85 and 90 seconds in these diagrams. The diagrams for channels 3 and 4 were neglected due to the poor signal to noise ratio for the low amplitude signals.

The levels in the frequency bands specified above are shown in Fig. 7.21 as a function of distance for each sensor. The noise which corrupts channels 3 and 4 is clearly illustrated in Fig. 7.21. The data have a noise floor about 25 dB higher than those in the other channels. On the other hand, the noise levels in channels 1 and 2 become about 4 or 5 dB lower than those in Fig. 7.10 and Fig. 7.16 for trains 3 and 4, as expected. This is because the narrower input range has been used, as stated earlier. According to Fig. 7.21, the rail responses at the side and underside of the rail head are likely to give an early warning of the approaching train at least 1.5 km or even 2 km before it arrives. Also if the problem of additional noise contamination in channel 3 could be overcome, it might be possible to detect an approaching train about 1.5 km before its arrival from the web vibration.

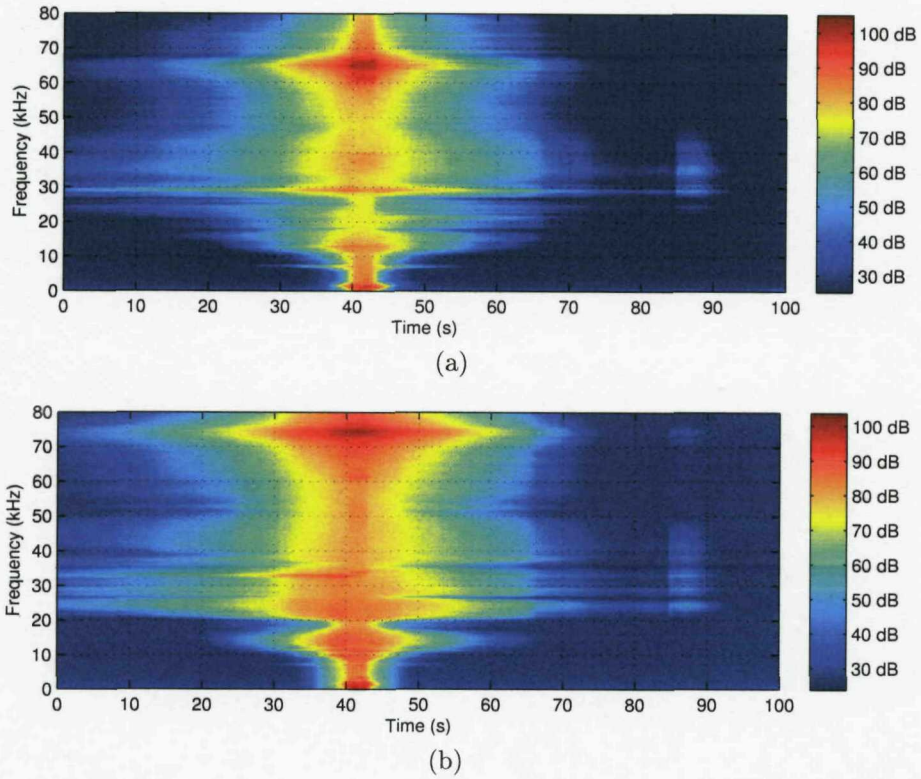

Fig. 7.20. Spectrograms measured for train 7. (a) At the side of the rail head (ch. 1), (b) at the underside of the rail head (ch. 2).

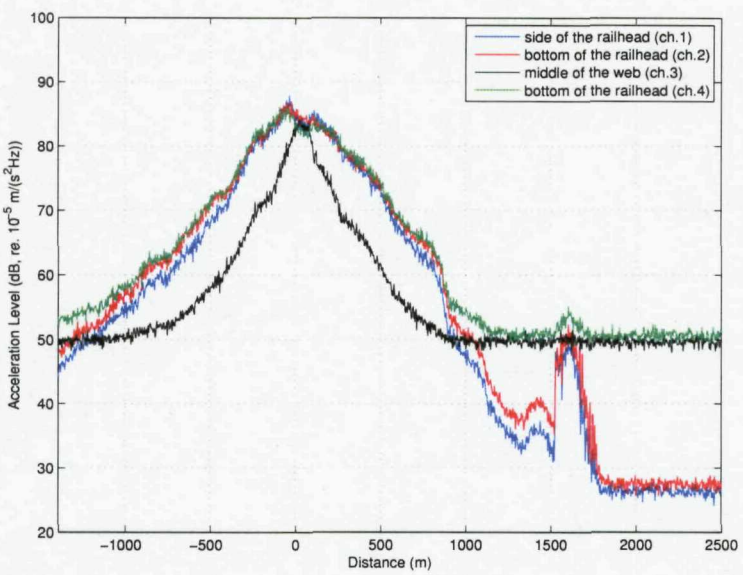

Fig. 7.21. Variations of acceleration levels versus distance at each measuring point for train 7.

The changes in acceleration spectra with time obtained from train 7 were almost the same as described before so will not be presented here. Instead, averaged decay rates created from all the individual decay rates obtained from each train will be presented later and compared with the simulated ones.

7.3.5 Averaged decay rates obtained from the field test

For each train, decay rates were extracted from the acceleration level differences at 5 second intervals. The decay rates obtained from the signals for trains 3 to 7 are compared in Fig. 7.22 for each train. The measured decay rates below 10 kHz were disregarded in Fig. 7.22 because the waves decay too rapidly in this frequency band, leaving just the background noise. It was found from Fig. 7.22 that the measured decay rates are not significantly affected by different train types and running speeds.

The averaged decay rates were calculated from the results shown in Fig. 7.22, simply finding mean values. These are shown in Fig. 7.23 together with the previous simulated ones in Chapter 5. As presented in the previous spectrograms, the waves below 20 kHz decay very quickly. Hence in order to obtain accurate decay rates in this low frequency region, it is necessary to extract them from the acceleration levels in the vicinity of the train passage. For this reason, the decay rates between 10 kHz and 20 kHz in Fig. 7.23 were produced from the signals of train 2 because they were not overloaded at all during the train passage.

It is revealed in Fig. 7.23 that the field test results agree very well with the simulated ones for all frequencies above 10 kHz. The comparison at the underside of the rail head in Fig. 7.23(b) suggests that the measured decay rate between 10 kHz and 20 kHz corresponds to the simulated one but is shifted to slightly higher frequencies. This slight difference between the measured and simulated results may be associated with the rail geometry or the stiffness of the rail pad. The exact types of the rail and rail pads in the operational track or the extent to which the rail head is worn are not known. Nevertheless, the measured decay rates show considerable agreement with the predicted ones particularly between 20 kHz and 50 kHz.

In terms of the long range wave propagation, interesting frequencies at each

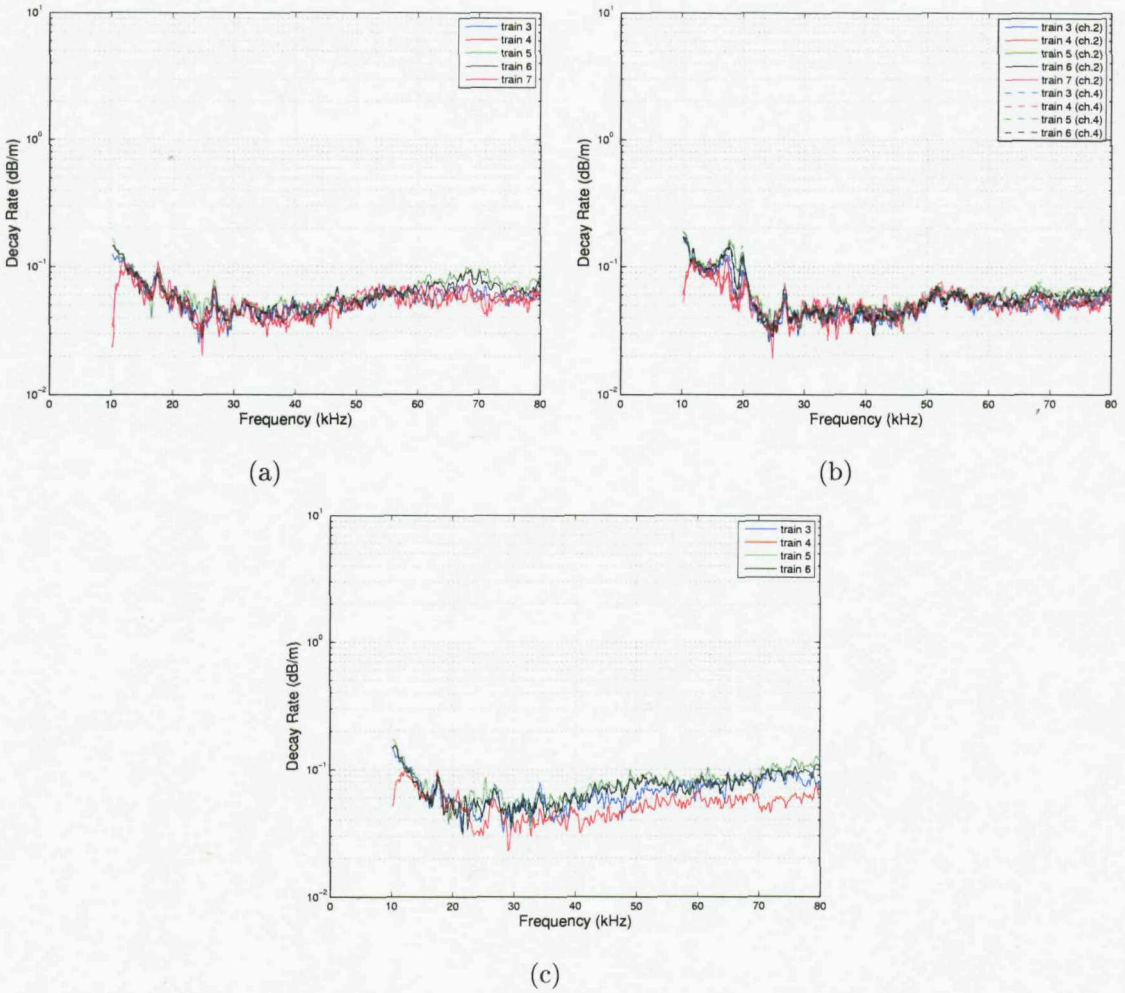

Fig. 7.22. Decay rates obtained from the field test for each train. (a) At the side of the rail head (ch. 1), (b) at the underside of the rail head (ch. 2 and ch. 4), (c) at the middle of the web (ch. 3)

channel were specified as around 29 kHz at the side of the rail head, around 24 kHz at the underside of the rail head and around 36 kHz at the middle of the web. At these frequencies relatively large amplitudes were excited at this test site. The measured decay rates at these frequencies are about 0.04, 0.035 and 0.05 dB/m, respectively, but are not much different from results at other frequencies around them. Also it was confirmed from this field measurement that a dynamic range of more than 50 dB is measurable in the rail vibration. So, if a 50 dB level reduction is assumed, then the maximum propagating distances at each sensing location will be about 1.2 km, 1.4 km and 1.0 km, respectively.

As compared in Fig. 7.23, the measured decay rates at the side and underside

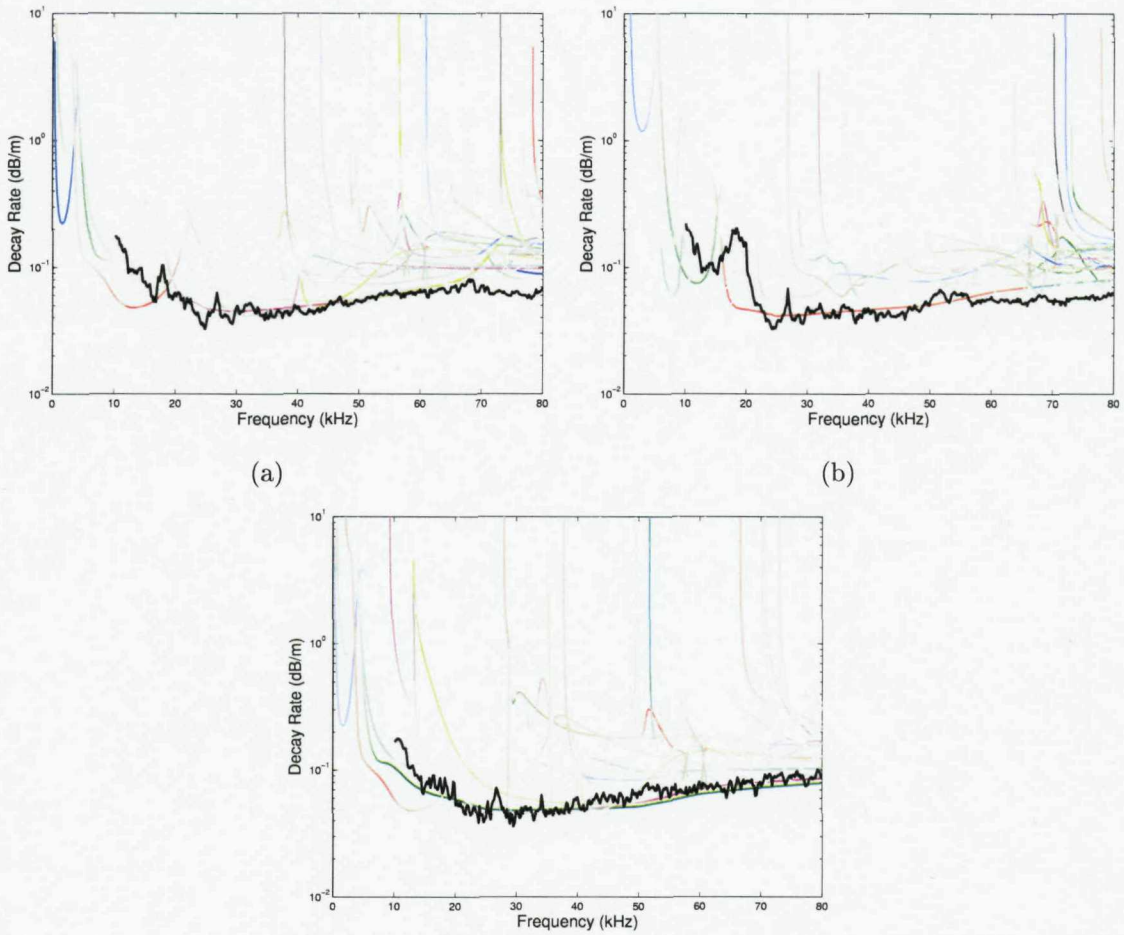

Fig. 7.23. Decay rates obtained from the field test, presented with those predicted by the WFE method. (a) At the side of the rail head (ch. 1), (b) at the underside of the rail head (ch. 2), (c) at the middle of the web (ch. 3)

of the rail head are slightly less than the predicted ones above 40 kHz. On the other hand, the decay rate measured at the middle of the web looks slightly higher than the simulated one. This increase in the measured decay rate at the middle of the web is likely to be related to the presence of the welds which reflect energy primarily in the web, as discussed in Section 6.2.5.

7.3.6 Analysis of the background vibration signal

The background vibration signal was acquired in the field measurement and investigated here. This measurement was carried out with the same input range and gain as set for train 7, i.e., $\pm$ 0.1 volt. It can be clearly seen in Fig. 7.24 how large the electrical noise was in channels 3 and 4. During this measurement, a train

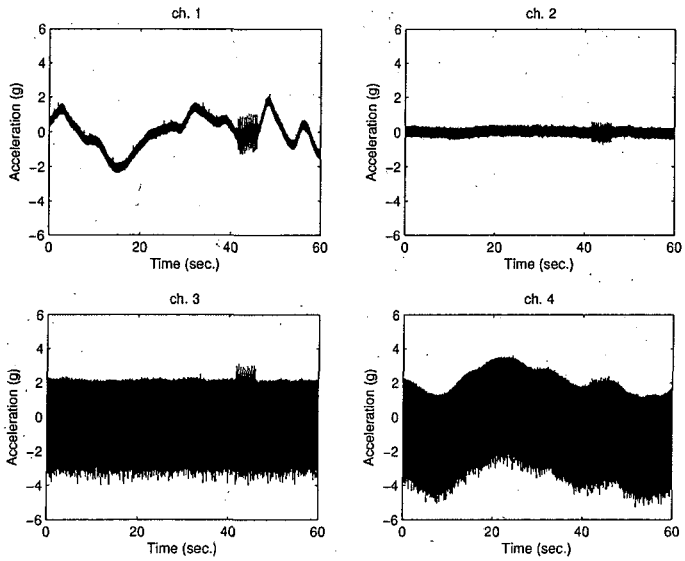

Fig. 7.24. Measured background vibration signals.

passed on an adjacent track. This can be seen in the time signal between 40 and 45 seconds in Fig. 7.24. Analysis of this event will inform how much interference will arise from adjacent tracks.

Since the data acquisition board used in this measurement has a 12 bit quantizer for A/D conversion, the step size, δ, of the quantizer becomes

$$\delta = \frac{X_m}{2^{11}} \quad , \tag{7.1}$$

where X_m denotes the full-scale level of the A/D converter [62]. For instance, X_m for this background vibration measurement is about $11g$ and δ is about $0.005g$. The smallest quantization levels are then $\pm\delta$.

As shown previously in spectrograms and plots of acceleration levels versus distance, such as Fig. 7.10, Fig. 7.16 and Fig. 7.21, the latter parts of the measured signals for each train seem to consist of noise. The time signals measured with various input ranges are compared in Fig. 7.25 for a short time duration around 120 seconds in each case. From this comparison, it is clear that the measured signals in Fig. 7.25(a) and (b) were severely distorted by the poor quantization and the error associated with the quantization decreases as δ becomes smaller.

In terms of spectra of the vibration, the level is directly dependent on the power contained in its time signal. Therefore, it is obvious that the levels of the

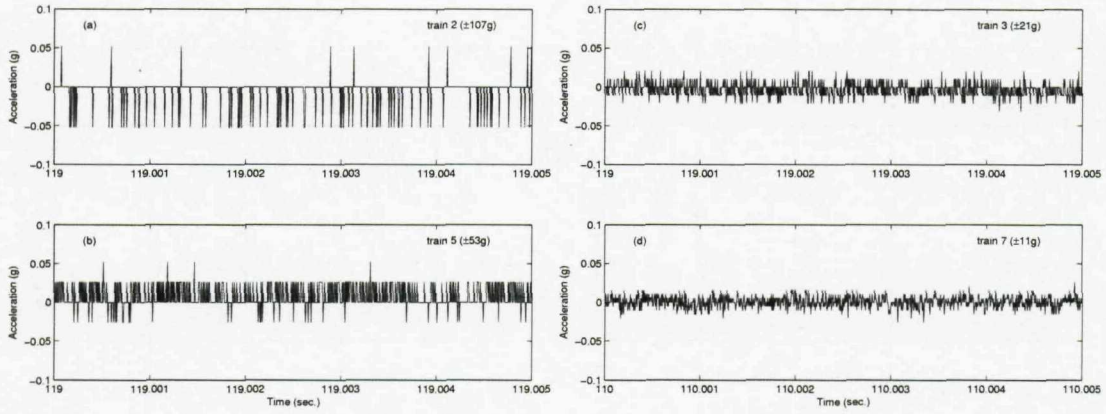

Fig. 7.25. Signals measured at channel 2 for (a) trains 2, (b) train 5, (c) train 3, (d) train 7 with different input ranges as stated in the figure.

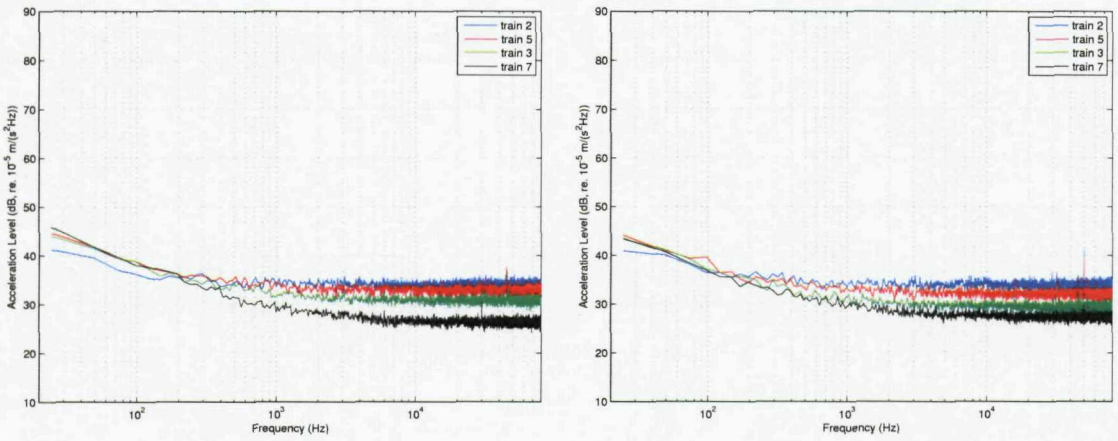

(a) (b)

Fig. 7.26. Comparison of acceleration levels for trains 2, 5, 3 and 7, having different input ranges, measured in (a) channel 1, (b) channel 2.

frequency spectra of the signals shown in Fig. 7.25 will drop gradually as δ reduces until they reach a background level which may be caused by ambient vibration or by electrical noise in the instrumentation chain. This kind of behaviour is observed in Fig. 7.26 which compares frequency spectra of the signals for trains 2, 5, 3 and 7 around 120 seconds. This figure also identifies that any significant background vibration is mainly concentrated at low frequencies below 1 kHz and decreases as frequency increases. Based on this result, it is expected that if a greater resolution or a narrower input range are used for the background vibration measurement, it would reduce the level further only at high frequencies above 1 kHz.

Finally, the contribution of a train running on a neighbouring track was inves-

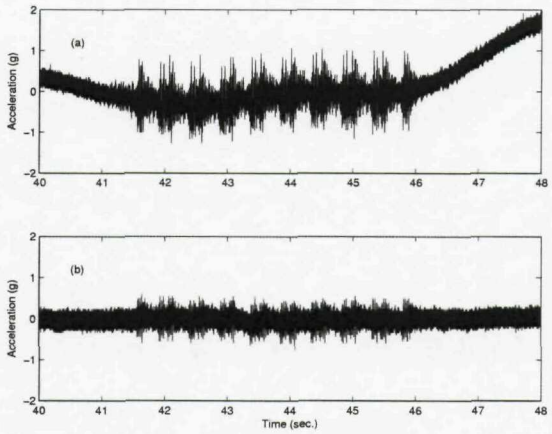

Fig. 7.27. Time histories measured during the train passage on the Up Fast track in (a) ch. 1, (b) ch. 2.

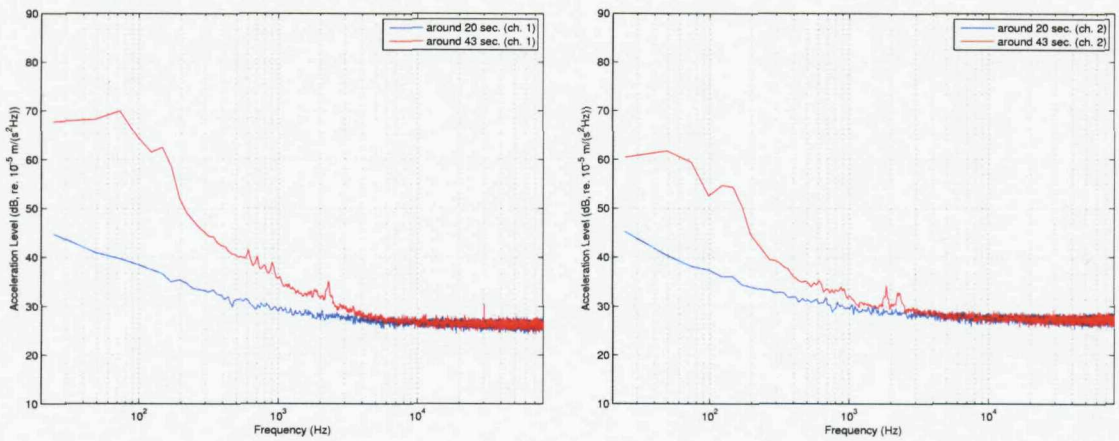

(a) (b)

Fig. 7.28. Power spectra of the background vibration at around 20 and 43 seconds in (a) ch. 1, (b) ch. 2.

tigated by analysing the data obtained before and during the train passage on an adjacent track. The measured time histories during the train passage on the neighbouring track are shown in Fig. 7.27, indicating that the train, a Pendolino, had 9 coaches. The frequency spectra corresponding to the train passage on the neighbouring track are shown in Fig. 7.28 along with the background levels for channels 1 and 2. The spectra in Fig. 7.28 were obtained from the time signals of about 2 seconds duration. From this comparison, it is clear that the train passing on the adjacent track does not have any significant effect, except in the low frequency region below 3 kHz. This is as expected because the resilience of the track support will tend to isolate it at high frequencies.

7.4 Summary

In order to validate the simulated decay rates over a longer rail section, a field measurement was performed on an operational railway track. In this experiment, train-induced rail vibration was measured up to 80 kHz for several service trains at the side and underside of the rail head and at the middle of the web.

From these measurements, it was revealed that running trains are very effective in exciting rails even at high frequencies between 20 kHz and 50 kHz and each part of the rail is excited in a different manner. Spectrograms were plotted for each train passage and it was found that waves can propagate more than a kilometre at some frequencies between 20 kHz and 40 kHz even at the middle of the web. Finally decay rates were extracted from the measured data and compared with the predictions.

This field test validated that the measured decay rates coincide very well with the simulated ones in almost the entire frequency range up to 80 kHz. The measured minimum decay rates and the frequencies at which they occur are

- about 0.035 dB/m at the underside of the rail head around 25 kHz
- about 0.035 dB/m at the side of the railhead around 25 kHz
- about 0.04 dB/m at the middle of the web around 29 kHz.

From the field measurement, particularly strong signals were found at 24 kHz under the rail head, at 29 kHz on the side of the head and at 36 kHz on the web. These frequencies might be different at other sites and with different trains. Also it was found that a train passing on an adjacent track does not have any significant contribution to the measured results at frequencies above 3 kHz.

The characteristics of rail vibration induced by the different trains measured were almost the same, despite differences in running speeds and train type. This may be because the trains measured were all EMUs, mainly of the same class. Nevertheless, this is a very desirable result in terms of the practical application.

A diagram such as the acceleration level versus distance could be used in order to monitor and detect defects in a railway track because abrupt level changes due

to rail defects could be indicated in this diagram from each train passage on the track. To detect waves at greater distances, it is essential to minimize the level of electrical noise in the measurement and to reduce the quantization error in the data acquisition by using an A/D converter with a wider range.

Chapter 8

Wave Reflection and Transmission at Cracks in Rails

So far in this thesis wave propagation has been investigated for homogeneous infinite rails. However, if a rail has a local non-uniformity, like a crack, it will reflect a part of the incident power and transmit the rest of it. These reflection and transmission characteristics associated with the presence of the discontinuity may give some indication of both the crack location and depth. In particular, if the waves that propagate furthest in rails are employed as incident waves, it may be achievable to inspect a long section of rail with every train passage. For example, the diagram of acceleration level versus distance (or time) as shown in Chapter 7 will present an abrupt level drop or surge when a train is passing over a discontinuity in rail. This

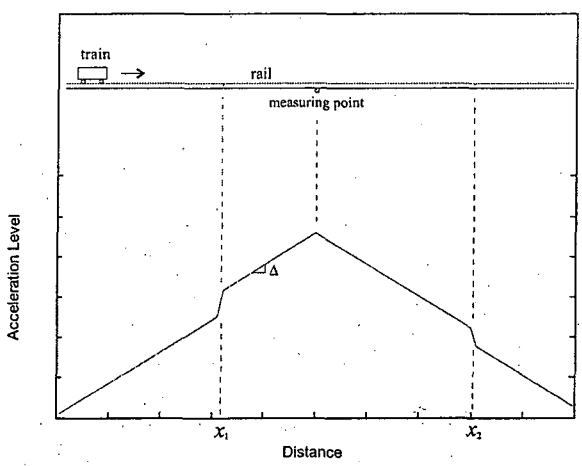

Fig. 8.1. Scheme of acceleration level versus distance diagram for a rail with two different rail defects at x_1 and x_2. (Δ denotes decay rates).

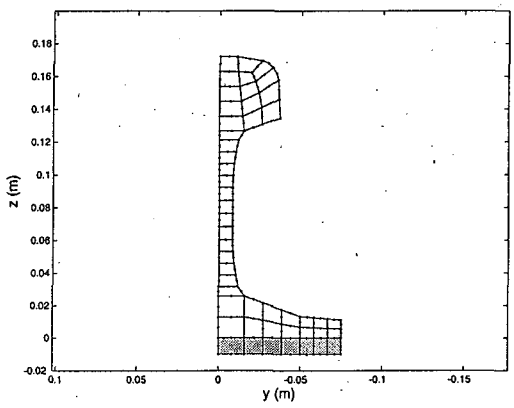

Fig. 8.2. Cross-sectional model of a rail on foundation. The shaded elements represents the rail pad.

is described schematically in Fig. 8.1 for a case where a rail has two different rail defects at x_1 and x_2. The level of this abrupt change will depend predominantly on the transmission characteristics of the rail defect. The reflected waves will be masked by the waves directly produced by the train. So in terms of practical application on an operational track, the transmission coefficients would be more useful than the reflection coefficients for crack detection. On the other hand, if artificial excitation is used instead of relying on excitation by trains, the reflected waves could also be utilised.

In this chapter, to check the feasibility of this application, wave reflection and transmission are investigated for cracks in rails by means of numerical simulations. The waves which propagate furthest along rails, found in the previous chapters, are used as incident waves. Since these fall in the frequency range between 20 kHz and 40 kHz, it is not possible to use simple beam models as in ref. [41, 42]. Therefore, in order to do that, the spectral super element method (SSEM) [20] is introduced and combined with the conventional FE method to estimate power reflection and transmission coefficients associated with cracks in rails. The cross-sectional model used in this study is shown in Fig. 8.2, which is the same cross-section used for the previous FE analysis presented in Chapter 3. A finer cross-sectional model was created and used in the previous WFE analysis in Chapter 4 to improve accuracy in the results. In this chapter, however, that finer model was not suitable because the resulting FE model has too many dofs to handle.

In practice, a crack would induce damping as well as reflection. However, to

make matters simpler, it is assumed in this chapter that the crack itself does not introduce any additional damping effects to the structure. Also it is supposed that the damping of the structure contributes only to the decay of propagating waves, not to the reflection and transmission of waves induced by cracks. Based on these assumptions, the simulation for wave reflection and transmission is performed for undamped rails in this feasibility study.

8.1 Spectral Super Element Method

The spectral super element (SSE) method was developed by Birgersson *et al.* [20] and used to predict the dynamic responses of vibrating finite length plate structures. This method is described briefly in this section, applying it to the rail which is modelled with solid elements. Since this method is a combination of the WFE method with the spectral finite element (SFE) method [16], it will be stated how these two methods are combined in the SSE method. Then the SSE for semi-infinite waveguide structures is newly developed modifying the original formulation in this section.

8.1.1 Homogeneous wave solutions

For an infinite waveguide structure, homogeneous wave solutions can be obtained from the WFE method. This method was already employed to create dispersion relations and decay rates of propagating waves, as presented in Chapter 4.

In this WFE analysis, the equation of motion of a cross-section is given as

$$[\mathbf{K_2}(-j\kappa)^2 + \mathbf{K_1}(-j\kappa) + \mathbf{K_0} - \omega^2\mathbf{M}]\tilde{\mathbf{\Phi}} = \mathbf{0} \tag{8.1}$$

where $\mathbf{K_2}$, $\mathbf{K_1}$ and $\mathbf{K_0}$ are matrices associated with the stiffness of the structure, $\mathbf{M}$ is the mass matrix of the cross-section and $\tilde{\mathbf{\Phi}}$ contains the displacements of the cross-section defining the wave shape. Since damping is not included here, all the stiffness and mass matrices are real. Here the wavenumber κ and frequency ω are the unknown variables to be identified; once they are found $\tilde{\mathbf{\Phi}}$ can also be obtained.

In Chapter 4, the WFE equation given in Eq.(8.1) was solved as a generalized eigenvalue problem to obtain frequency ω at a given wavenumber κ, because only

propagating waves were of interest there. In the SSE method, however, all the wave solutions, including nearfield waves, are required to predict the displacement of the structure. Hence, Eq.(8.1) has to be solved as a polynomial eigenvalue problem to obtain all wavenumbers and mode shapes at a given frequency ω. Note that Eq.(8.1) will have paired wavenumber solutions, representing the positive- and negative-going waves at each frequency. For example, for a cross-sectional model with N dofs, $2N$ wavenumbers and mode shapes will be obtained at each ω.

It was reported in ref. [43, 63] that transforming the polynomial eigenvalue problem to a generalized eigenvalue problem reduces the computational load required and increases its numerical stability. To do this, a new variable $\tilde{\mathbf{\Psi}}$ was introduced as $\tilde{\mathbf{\Psi}} = -j\kappa\tilde{\mathbf{\Phi}}$. Then Eq.(8.1) can be rewritten as

$$\begin{bmatrix} -j\kappa\mathbf{K_1} + \mathbf{K_0} - \omega^2\mathbf{M} & -j\kappa\mathbf{K_2} \\ j\kappa & \mathbf{I} \end{bmatrix} \begin{Bmatrix} \tilde{\mathbf{\Phi}} \\ \tilde{\mathbf{\Psi}} \end{Bmatrix} = \mathbf{0} \quad , \tag{8.2}$$

and expressed in standard eigenvalue form as

$$\left(\begin{bmatrix} \omega^2\mathbf{M} - \mathbf{K_0} & \mathbf{0} \\ \mathbf{0} & \mathbf{I} \end{bmatrix} - (-j\kappa) \begin{bmatrix} \mathbf{K_1} & \mathbf{K_2} \\ \mathbf{I} & \mathbf{0} \end{bmatrix} \right) \begin{Bmatrix} \tilde{\mathbf{\Phi}} \\ \tilde{\mathbf{\Psi}} \end{Bmatrix} = \mathbf{0} \quad . \tag{8.3}$$

Wavenumbers κ and mode shapes $\tilde{\mathbf{\Phi}}$ are obtained by solving this transformed eigenvalue problem at each frequency ω.

Theoretically, at a given frequency ω, all the wavenumber solutions have to be placed symmetrically about the origin in the complex wavenumber plane. Half of them are for waves propagating and decaying in the positive x direction and the rest are for those travelling and decaying in the negative x direction. That is,

$$\kappa_- = -\kappa_+ \quad , \tag{8.4}$$

where κ_+ and κ_- denote the wavenumbers travelling in the positive and negative x directions, respectively. For wavenumbers κ_+, Eq.(8.1) can be written as

$$[-\kappa_+^2\mathbf{K_2} - j\kappa_+\mathbf{K_1} + \mathbf{K_0} - \omega^2\mathbf{M}]\tilde{\mathbf{\Phi}}_+ = \mathbf{0} \quad , \tag{8.5}$$

then by the relation in Eq.(8.4),

$$[-\kappa_-^2\mathbf{K_2} + j\kappa_-\mathbf{K_1} + \mathbf{K_0} - \omega^2\mathbf{M}]\tilde{\mathbf{\Phi}}_+ = \mathbf{0} \quad . \tag{8.6}$$

Since the matrices $\mathbf{K_2}$, $\mathbf{K_0}$ and $\mathbf{M}$ are symmetric and $\mathbf{K_1}$ is anti-symmetric, the transpose of Eq.(8.6) is given by

$$\tilde{\mathbf{\Phi}}_+^T[-\kappa_-^2\mathbf{K_2} - j\kappa_-\mathbf{K_1} + \mathbf{K_0} - \omega^2\mathbf{M}] = \mathbf{0}^T \quad . \tag{8.7}$$

By the definition of a left eigenvector, $\tilde{\mathbf{\Phi}}_+$ in this transposed equation becomes the left eigenvector for κ_-, whereas its right eigenvector $\tilde{\mathbf{\Phi}}_-$ satisfies

$$[-\kappa_-^2\mathbf{K_2} - j\kappa_-\mathbf{K_1} + \mathbf{K_0} - \omega^2\mathbf{M}]\tilde{\mathbf{\Phi}}_- = \mathbf{0} \quad . \tag{8.8}$$

From Eq.(8.7) and Eq.(8.8), it is obtained that $\tilde{\mathbf{\Phi}}_-$ and $\tilde{\mathbf{\Phi}}_+$ are respectively the right and left eigenvectors of $\mathbf{K}(\kappa_-) = [-\kappa_-^2\mathbf{K_2} - j\kappa_-\mathbf{K_1} + \mathbf{K_0} - \omega^2\mathbf{M}]$ (or the left and right eigenvectors of $\mathbf{K}(\kappa_+) = [-\kappa_+^2\mathbf{K_2} - j\kappa_+\mathbf{K_1} + \mathbf{K_0} - \omega^2\mathbf{M}]$). This relation between $\tilde{\mathbf{\Phi}}_-$ and $\tilde{\mathbf{\Phi}}_+$ is valid for damped structures with proportional damping, in which a stiffness matrix is specified as $\mathbf{K}(1 + i\eta)$, because the condition described in Eq.(8.4) will be satisfied even for damped cases.

As an example, some wavenumbers obtained from the rail model shown in Fig. 8.2 at 21 kHz are illustrated in Fig. 8.3. The wavenumbers for the positive- and negative-going waves are coloured blue and red, respectively. That is, the blue ones are κ_+ and the red ones are κ_-. In fact, for undamped systems, symmetry exists between wavenumbers in all four quadrants of the complex plane as can be recognised from Fig. 8.3. The relations between the eigenvectors for four such wavenumbers were described in ref. [26]. However, this contains some typing errors. The corrected ones are listed in Table 8.1.

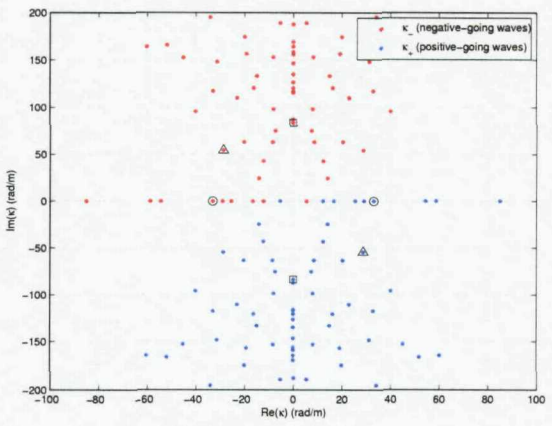

Fig. 8.3. Wave solutions around the origin obtained at 21 kHz from the WFEM. The pairs marked with 'O', '□' and '△' shapes are wavenumbers selected for mode shape comparison.

Table 8.1. Relations between eigenvectors for wavenumbers symmetric in different quadrants for undamped structures.

Quadrant	Wavenumber	Right eigenvector	Left eigenvector
1st	κ	$\tilde{\mathbf{\Phi}}_R$	$\tilde{\mathbf{\Phi}}_L$
2nd	$-\kappa^*$	$\tilde{\mathbf{\Phi}}_R^*$	$\tilde{\mathbf{\Phi}}_L^*$
3rd	$-\kappa$	$\tilde{\mathbf{\Phi}}_L$	$\tilde{\mathbf{\Phi}}_R$
4th	κ^*	$\tilde{\mathbf{\Phi}}_L^*$	$\tilde{\mathbf{\Phi}}_R^*$

In Fig. 8.3, the wavenumbers located on the real axis correspond to positive- and negative-propagating waves which do not decay along the x direction because there is no imaginary part. Note that two wavenumbers located at around ± 5 rad/m on the real axis were swapped because they both have negative group velocities. The remaining wavenumbers indicate nearfield waves exhibiting exponential decay with distance in x. More strictly, the waves on the imaginary axis decay exponentially without any oscillation with distance, while those with complex wavenumbers are decaying exponentially along with some sinusoidal oscillation with distance. Note that since waves exist as nearfield waves until they are cut-on, these complex wavenumbers are created even though there is no damping in this system.

In order to observe what sort of relation occurs between the mode shapes for κ_+ and κ_-, the eigenvectors are compared below for the three wavenumber pairs, marked with symbols in Fig. 8.3. The mode shapes of positive- and negative-propagating waves, marked with '○' in Fig. 8.3, are shown in Fig. 8.4. Since these are purely real

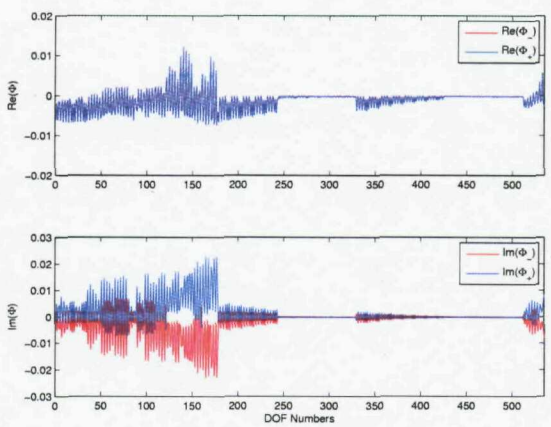

Fig. 8.4. Comparison of mode shapes for the purely real wavenumbers marked '○' in Fig. 8.3.

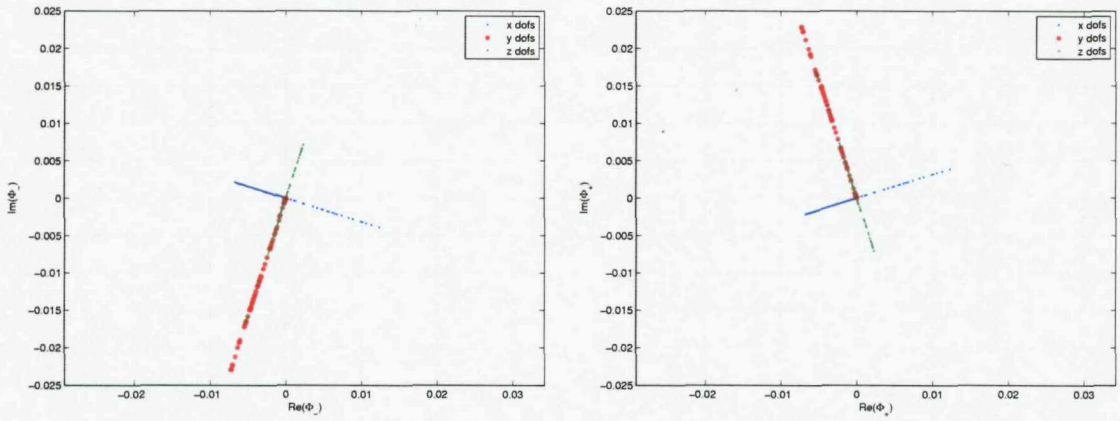

(a) (b)

Fig. 8.5. Mode shapes in complex domain for the wavenumbers, marked 'O' in Fig. 8.3, for each directional dofs. (a) $\tilde{\mathbf{\Phi}}_-$, (b) $\tilde{\mathbf{\Phi}}_+$.

wavenumbers, $\mathbf{K}(\kappa_-)$ and $\mathbf{K}(\kappa_+)$ become Hermitian matrices. Their eigenvectors are, therefore, complex conjugate pairs, i.e., $\tilde{\mathbf{\Phi}}_- = \tilde{\mathbf{\Phi}}_+^*$ as illustrated in Fig. 8.4 for all dofs. The mode shapes in this figure indicate that the two waves chosen are identical but travel in opposite directions. The eigenvectors shown in Fig. 8.4 are plotted in the complex domain for the x, y and z direction dofs separately and compared in Fig. 8.5. It can be identified from this figure that the mode shapes in the x and (y,z) directions have a 90° phase difference between them. This phase difference occurs in the opposite direction for $\tilde{\mathbf{\Phi}}_-$ and $\tilde{\mathbf{\Phi}}_+$.

Meanwhile, for wavenumbers which are purely imaginary, $\mathbf{K}(\kappa_-)$ and $\mathbf{K}(\kappa_+)$ become real and asymmetric so that their eigenvectors are real. For each direction of dofs, the eigenvectors for the wavenumber pairs, marked with '□', are plotted and compared in Fig. 8.6. It is found from Fig. 8.6 that the eigenvectors in the y and z directions are the same but those in the x direction have opposite signs. These results indicate that the mode shapes obtained when κ_+ and κ_- are on the imaginary wavenumber axis are the same but out of phase in the x direction.

The eigenvectors for the complex wavenumber pairs, marked with '△' in Fig. 8.3, are illustrated in Fig. 8.7 for the dofs in the x, y and z directions. It is difficult to identify the relation between $\tilde{\mathbf{\Phi}}_-$ and $\tilde{\mathbf{\Phi}}_+$ in this figure. To present it more clearly, the eigenvectors are replotted in the complex domain and compared in Fig. 8.8. It can be seen from this figure that for each direction the mode shape of $\tilde{\mathbf{\Phi}}_+$ shown in

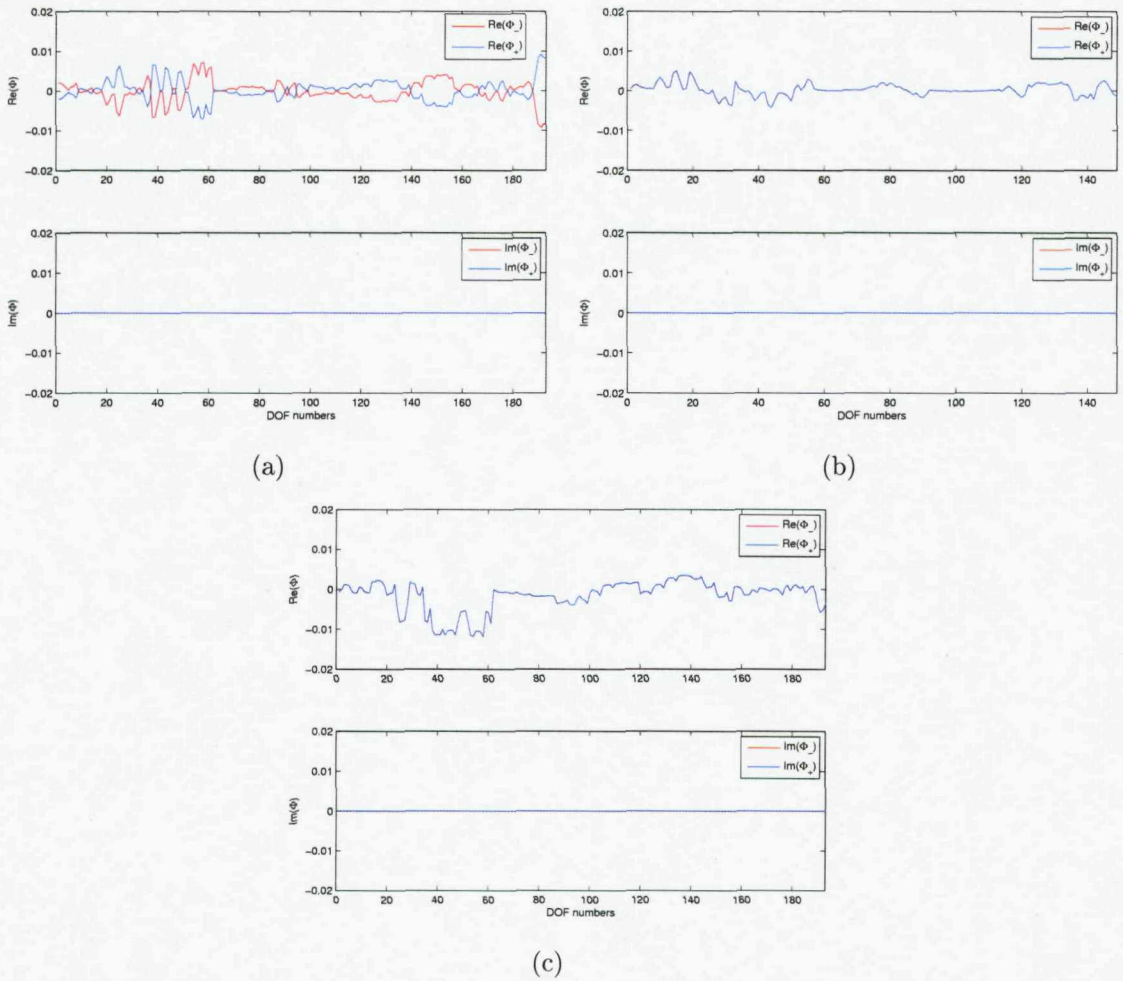

Fig. 8.6. Comparison of mode shapes for the purely imaginary wavenumbers marked '□' in Fig. 8.4(a), (a) in the x direction, (b) in the y direction, (c) in the z direction.

Fig. 8.8(b) is the rotated version of $\tilde{\mathbf{\Phi}}_-$ in Fig. 8.8(a). The phase differences found are 107.75° for the dofs in the x direction and -72.24° for the y and z directions. These differences in phase between mode shapes will vary for different wavenumber pairs. However, it is not clear how they are related to the phase of κ_+ or κ_-. Also Fig. 8.8 shows that $\tilde{\mathbf{\Phi}}_+$ has a slightly larger magnitude than $\tilde{\mathbf{\Phi}}_-$. This difference in amplitude will be compensated in the wave amplitude vector in the calculation of displacement.

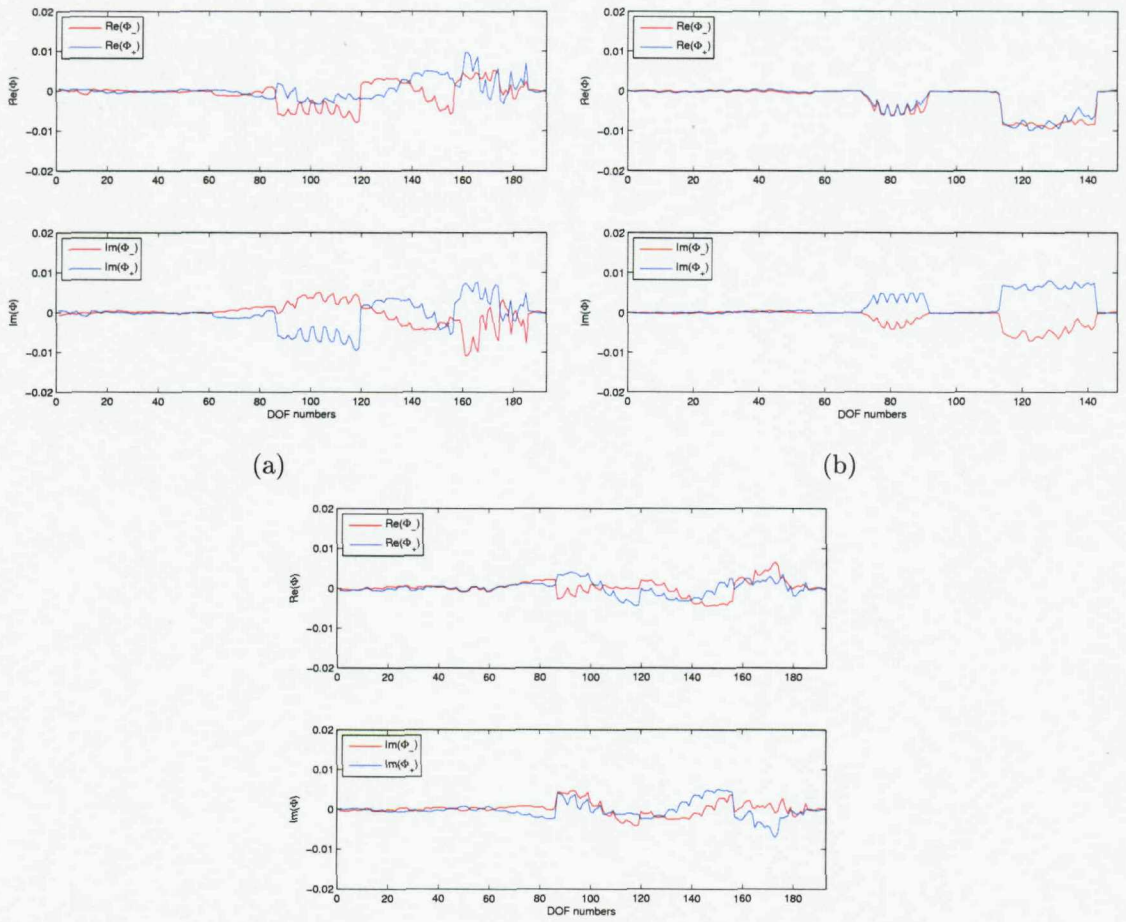

(a) (b)

(c)

Fig. 8.7. Comparison of mode shapes for the complex wavenumbers, marked '△' in Fig. 8.4(a), (a) in the x direction, (b) in the y direction, (c) in the z direction.

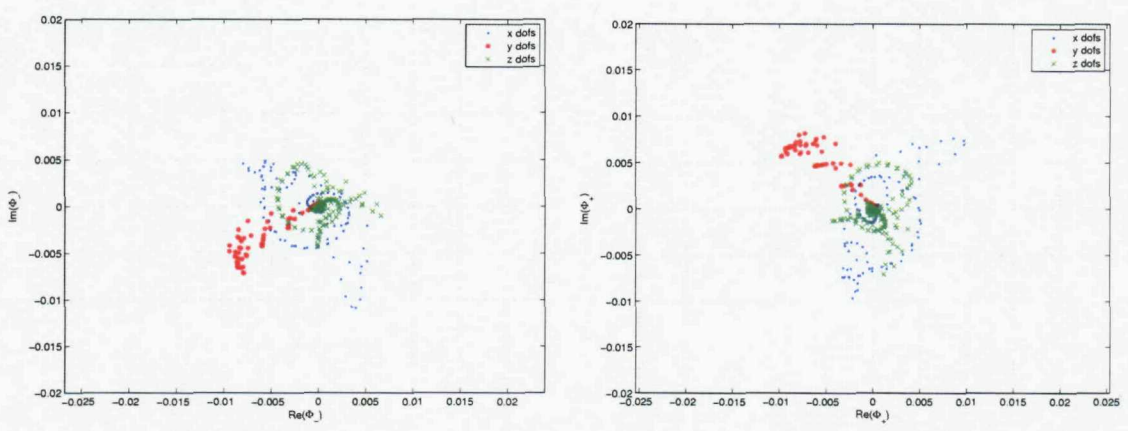

(a) (b)

Fig. 8.8. Mode shapes in complex domain for the wavenumbers, marked '△' in Fig. 8.3, for each directional dofs. (a) $\tilde{\mathbf{\Phi}}_-$, (b) $\tilde{\mathbf{\Phi}}_+$.

8.1.2 Displacement functions

For finite length waveguide structures, the displacement $\mathbf{V}(x)$ can be written as a superposition of each wave solution obtained from Eq.(8.3) [20]. For example, for a finite length structure in $-l_x \leq x \leq l_x$, the $N\times1$ vector $\mathbf{V}(x)$ at a frequency ω can be written as

$$\mathbf{V}(x) = \sum_{m=1}^{2N} a_m \tilde{\mathbf{\Phi}}_m e^{-j\kappa_m x} = \mathbf{\Phi}\mathbf{E}(x)\mathbf{a} \quad , \tag{8.9}$$

where N is the number of dofs in the cross-sectional model, $\tilde{\mathbf{\Phi}}_m$ is the mode shape vector for κ_m, $\mathbf{\Phi}$ is an $N\times2N$ matrix containing each wave's mode shapes, $\mathbf{a}$ is the $2N\times1$ wave amplitude vector and $\mathbf{E}(x)$ is a $2N\times2N$ diagonal matrix containing the exponential terms for x. To avoid numerical instability that is caused by large amplitudes of near field waves at boundaries, $\mathbf{E}(x)$ is scaled by factors of $e^{\pm j\kappa_m l_x}$ [16, 20] as

$$\mathbf{E}_{mm} = e^{-j\kappa_m(x-l_x)} \qquad \text{for } \mathrm{Im}(\kappa_m) > 0 \quad , \tag{8.10}$$

$$\mathbf{E}_{mm} = e^{-j\kappa_m(x+l_x)} \qquad \text{for } \mathrm{Im}(\kappa_m) < 0 \quad . \tag{8.11}$$

In Eq.(8.9), the only unknown variable is the wave amplitude, $\mathbf{a}$, and it can be determined from the boundary conditions of the structure. For example, suppose that the finite length waveguide structure has boundaries at $x = -l_x$ and l_x and the boundary conditions are defined by the displacements $\mathbf{W}_1$ and $\mathbf{W}_2$, respectively, at these locations. The displacements, $\mathbf{V}(x)$, at the boundaries are described using Eq.(8.9) as

$$\mathbf{V}(-l_x) = \mathbf{\Phi}\mathbf{E}(-l_x)\mathbf{a} = \mathbf{W}_1 \quad , \tag{8.12}$$

$$\mathbf{V}(+l_x) = \mathbf{\Phi}\mathbf{E}(+l_x)\mathbf{a} = \mathbf{W}_2 \quad . \tag{8.13}$$

Then $\mathbf{a}$ can be expressed as a function of the nodal displacements at boundaries,

$$\mathbf{a} = \begin{bmatrix} \mathbf{\Phi}\mathbf{E}(-l_x) \\ \mathbf{\Phi}\mathbf{E}(+l_x) \end{bmatrix}^{-1} \begin{Bmatrix} \mathbf{W}_1 \\ \mathbf{W}_2 \end{Bmatrix} = \mathbf{A}\mathbf{W} \quad , \tag{8.14}$$

and the displacement $\mathbf{V}(x)$ is expressed by

$$\mathbf{V}(x) = \mathbf{\Phi}\mathbf{E}(x)\mathbf{A}\mathbf{W} \quad . \tag{8.15}$$

Now, the only unknown parameter in this equation is $\mathbf{W}$.

Birgersson *et al.* [20] suggested to scale all eigenvectors with $\left(\|\tilde{\mathbf{\Phi}}_m\||\kappa_m|^2\right)^{-1}$, where κ_m is the wavenumber corresponding to the eigenvector $\tilde{\mathbf{\Phi}}_m$, in order to reduce the numerical error which is caused by rapidly decaying waves at low frequencies where most waves in the structure are non-propagating. This weighting of the eigenvectors was used initially in the present study but it was found that it does not significantly reduce the error at the frequencies of interest between 20 kHz and 40 kHz. So, the weighting of the eigenvectors has not been implemented in the results presented.

For semi-infinite waveguide structures, only half of the wavenumbers and mode shapes, which propagate and decay in the positive or negative x direction, are present as stated in the previous section. For instance, for a semi-infinite waveguide that extends to infinity in the positive x direction ($0 \leq x < \infty$), the displacement vector $\mathbf{V}(x)$ is expressed as a superposition of wave solutions only for positive-going waves as

$$\mathbf{V}(x) = \sum_{m=1}^{N} (a_{+,m})(\tilde{\mathbf{\Phi}}_{+,m}) e^{-j(\kappa_{+,m})x} = \mathbf{\Phi}_+ \mathbf{E}_+(x)\mathbf{a}_+ \quad , \tag{8.16}$$

where the subscript '+' represents variables for the positive-going waves, $\mathbf{\Phi}_+$ and $\mathbf{E}_+(x)$ are the matrices of size $N \times N$ and $\mathbf{a}_+$ is the $N \times 1$ wave amplitude vector. If the boundary condition is defined by the displacements $\mathbf{W}_0$ at $x = 0$, $\mathbf{a}_+$ can be expressed as

$$\mathbf{a}_+ = [\mathbf{\Phi}_+ \mathbf{E}_+(0)]^{-1} \mathbf{W}_0 = \mathbf{A}_+ \mathbf{W}_0 \quad . \tag{8.17}$$

8.1.3 Dynamic stiffness matrix

If an input force vector, $\mathbf{F}$, is specified at the boundaries of finite length structures, the displacement vector $\mathbf{W}$ can be obtained using a dynamic stiffness matrix of the structure, as developed by Birgersson *et al.* [20]. The dynamic stiffness matrix, $\mathbf{D}_S$, of the finite length waveguide structure is given by

$$\mathbf{D}_S = \mathbf{A}^T (\mathbf{\Theta} \otimes \mathbf{E}_\mathbf{I}) \mathbf{A} \quad , \tag{8.18}$$

where $\otimes$ denotes the Hadamard product, an element-wise multiplication of two matrices, and

$$\Theta = \Big(\sum_{m=0}^{1} \sum_{n=0}^{1} (\boldsymbol{\kappa}^m (\boldsymbol{\Phi}^T \boldsymbol{\varepsilon}_{mn} \boldsymbol{\Phi}) \boldsymbol{\kappa}^n) - \omega^2 (\boldsymbol{\Phi}^T \mathbf{M} \boldsymbol{\Phi}) \Big) \quad , \tag{8.19}$$

$$\mathbf{E_I} = \int_{-l_x}^{l_x} \mathrm{diag}(\mathbf{E}(x)) \mathrm{diag}(\mathbf{E}(x))^T dx \quad . \tag{8.20}$$

Here $\boldsymbol{\varepsilon}_{mn}$ is a $N \times N$ matrix containing strain components used to form the stiffness matrices $\mathbf{K_2}$, $\mathbf{K_1}$ and $\mathbf{K_0}$ in the WFE analysis [20] and the operator diag( ) produces a column vector from the diagonal terms of its argument. For finite length structures, all the wavenumbers and mode shapes are used to calculate the dynamic stiffness in Eq.(8.18) and the displacement vector $\mathbf{V}(x)$. So, $\boldsymbol{\kappa}$ in Eq.(8.19) becomes a $2N \times 2N$ diagonal matrix of wavenumbers, $\mathbf{E_I}$ is also the $2N \times 2N$ matrix and its entries are given by

$$(\mathbf{E_I})_{mn} = \frac{1}{-j(\kappa_m + \kappa_n)} \left[e^{-j(\kappa_m + \kappa_n) l_x} - e^{-j(\kappa_m + \kappa_n)(-l_x)} \right] e^{-j(\pm\kappa_m \pm \kappa_n) l_x} \tag{8.21}$$

where '$\pm$' signs are dependent on the signs of the imaginary parts of κ_m and κ_n. Finally, if an input force $\mathbf{F}$ is specified, the nodal displacement $\mathbf{W}$ can be found by solving

$$\mathbf{D}_S \mathbf{W} = \mathbf{F} \quad , \tag{8.22}$$

and from Eq.(8.15) the displacement of the finite length structure can be obtained at any position.

In the case of semi-infinite structures, only half of the wavenumbers and mode shapes are used in the calculation and then Θ and $\mathbf{E_I}$ in Eq.(8.19) and Eq.(8.20) need to be modified. Since Θ has to be specified for the positive and negative semi-infinite structures separately,

$$\Theta_{\pm} = \Big(\sum_{m=0}^{1} \sum_{n=0}^{1} (\boldsymbol{\kappa}_{\pm}^m (\boldsymbol{\Phi}_{\pm}^T \boldsymbol{\varepsilon}_{mn} \boldsymbol{\Phi}_{\pm}) \boldsymbol{\kappa}_{\pm}^n) - \omega^2 (\boldsymbol{\Phi}_{\pm}^T \mathbf{M} \boldsymbol{\Phi}_{\pm}) \Big) \quad , \tag{8.23}$$

where '$\pm$' signs in the subscript are dependent on the direction that extends to infinity in the semi-infinite structure and $\boldsymbol{\kappa}_{\pm}$ are $N \times N$ diagonal matrices of wavenumbers for the positive- or negative-going waves, respectively. Also,

$$(\mathbf{E_{I-}})_{mn} = \frac{-1}{j(\kappa_m + \kappa_n)} \quad \text{for} \quad -\infty < x \leq 0 \quad , \tag{8.24}$$

$$(\mathbf{E_{I+}})_{mn} = \frac{1}{j(\kappa_m + \kappa_n)} \quad \text{for} \quad 0 \leq x < \infty \quad . \tag{8.25}$$

Then the dynamic stiffness matrices $\mathbf{D}_{S,\pm}$ for semi-infinite structures are given by

$$\mathbf{D}_{S,\pm} = \mathbf{A}_{\pm}^{T}(\mathbf{\Theta}_{\pm} \otimes \mathbf{E}_{\mathrm{I}\pm})\mathbf{A}_{\pm} \quad , \tag{8.26}$$

and if an input force $\mathbf{F}_0$ is specified at $x = 0$, the nodal displacement $\mathbf{W}_0$ will be found by

$$\mathbf{W}_0 = (\mathbf{D}_{S,\pm})^{-1}\mathbf{F}_0 \quad . \tag{8.27}$$

8.2 Combined SSE/FE Method

In the above section, SSEs for semi-infinite waveguide structures were developed. If homogeneous structures are investigated, they can be modelled by connecting these SSEs with finite length SSEs consecutively. If there are local discontinuities, like holes or cracks, in an infinite structure, regions containing these local non-uniformities can be modelled using FE and then the combined SSE/FE method is required to investigate wave propagation in the structure. In this section, the combined SSE/FE method is developed using semi-infinite SSEs to analyse wave propagation in the structure with local non-uniformities.

In this combined SSE/FE method, the whole structure with a local discontinuity is subdivided into three regions: two semi-infinite elements and a finite region containing the local discontinuity. The two semi-infinite regions can be modelled using the SSE method and the finite part with the local discontinuity is modelled by the FE method. These three parts can be connected easily if their nodes at the boundaries are the same. This is one of the great advantages of using SSEs in this combined method. The modelling scheme in the combined SSE/FE method is illustrated in Fig. 8.9.

Fig. 8.9. Combined SSE/FE model with a local non-uniformity.

8.2.1 Coupling between SSE and FE

To couple the SSE with the conventional FE, the dynamic stiffness matrix of the FE part needs to be transformed so that it is described only by the nodal dofs at the boundaries. The dynamic stiffness matrix $\mathbf{D}_f$ of the FE part is defined as

$$\mathbf{D}_f = \mathbf{K}_{fe} - \omega^2 \mathbf{M}_{fe} \quad , \tag{8.28}$$

where $\mathbf{K}_{fe}$ and $\mathbf{M}_{fe}$ are the stiffness and mass matrices of the FE part, respectively. If external forces are applied only to the nodes on boundaries, the dynamic stiffness matrix in Eq.(8.28) can be partitioned as

$$\begin{Bmatrix} \mathbf{F}_b \\ \mathbf{0} \end{Bmatrix} = \begin{bmatrix} \mathbf{D}_{f,bb} & \mathbf{D}_{f,bi} \\ \mathbf{D}_{f,ib} & \mathbf{D}_{f,ii} \end{bmatrix} \begin{Bmatrix} \mathbf{W}_b \\ \mathbf{W}_i \end{Bmatrix} \quad , \tag{8.29}$$

where the subscripts b and i denote boundary and internal dofs, respectively. Then a condensed dynamic stiffness matrix, $\mathbf{D}_F$, is obtained by solving Eq.(8.29) as

$$\mathbf{D}_F = \mathbf{D}_{f,bb} - \mathbf{D}_{f,bi} \mathbf{D}_{f,ii}^{-1} \mathbf{D}_{f,ib} \quad . \tag{8.30}$$

Note that, unlike Guyan reduction [57] which uses only the static stiffness matrix in the condensation process, this does not result in any approximation.

For the combined model shown in Fig. 8.9, dynamic stiffness matrices of the three substructures can be assembled by the same process as for conventional finite elements. The nodal displacements $\mathbf{W}$ at the two coupled interfaces are found by

$$\left(\begin{bmatrix} \mathbf{D}_{S,-} & \mathbf{0} \\ \mathbf{0} & \mathbf{0} \end{bmatrix} + \mathbf{D}_F + \begin{bmatrix} \mathbf{0} & \mathbf{0} \\ \mathbf{0} & \mathbf{D}_{S,+} \end{bmatrix} \right) \begin{Bmatrix} \mathbf{W}_1 \\ \mathbf{W}_2 \end{Bmatrix} = \mathbf{D}_C \mathbf{W} = \mathbf{F} \quad , \tag{8.31}$$

where $\mathbf{W}_1$ and $\mathbf{W}_2$ are displacements at the left- and right-hand boundaries, $\mathbf{D}_{S,-}$ and $\mathbf{D}_{S,+}$ are the dynamic stiffness matrices of the left- and right-hand side semi-infinite SSEs, and $\mathbf{F}$ is the generalized force vector acting on the nodes of the coupled boundaries. Finally, if $\mathbf{F}$ is given at the boundaries, the displacement $\mathbf{V}(x)$ in the SSE parts of the combined model is evaluated by solving Eq.(8.31) and then Eq.(8.15). The response of the FE part can be found from the lower part of Eq.(8.29).

8.2.2 Modelling for incident wave generation

In order to estimate reflected and transmitted waves in rails with a local non-uniformity, waves incident on it are required. However, it is not possible to specify

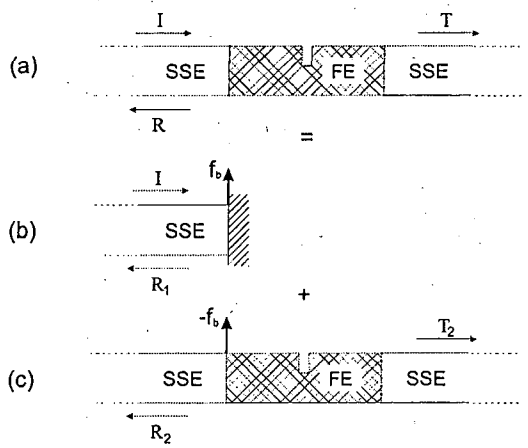

Fig. 8.10. An equivalent model to predict wave reflection and transmission for an infinite rail with a local non-uniformity.

them directly in the semi-infinite SSEs. So a technique to add incident waves to the combined SSE/FE model is necessary. To impose incident waves on the combined SSE/FE model, a method used by Shone *et al.* [41, 42] is employed here, considering an equivalent system with positive and negative blocked forces cancelled out by superposition.

The proposed procedure for imposing an incident wave on the combined SSE/FE model is illustrated in Fig. 8.10. The desired model, shown in Fig. 8.10(a), needs to have incident (I), reflected (R) and transmitted (T) waves along the two semi-infinite SSEs with no external forces acting on the connecting nodes. This desired model is achieved by superposing the blocked case, which gives a blocked force vector due to an incident wave (Fig. 8.10(b)), and the combined SSE/FE model excited by this blocked force vector but with the opposite sign (Fig. 8.10(c)). By summation of these two, the forces are cancelled out so that the desired model containing incident, reflected and transmitted waves is obtained. In the blocked case shown in Fig. 8.10(b), the FE and right-hand side SSE parts are assumed to have zero response and therefore may be omitted from the model.

The blocked force, $\mathbf{f}_b$, shown in Fig. 8.10(b) is determined using two connected semi-infinite SSEs as shown in Fig. 8.11. Suppose that a displacement $\mathbf{W}_0$ is created at x_0 by a single incident wave, I, in an infinite homogeneous structure (Fig. 8.11(b)). Then, the force, $\mathbf{f}_b$, which makes $-\mathbf{W}_0$ at x_0 in the infinite system can be calculated from the dynamic stiffnesses of the connected semi-infinite SSEs as shown in

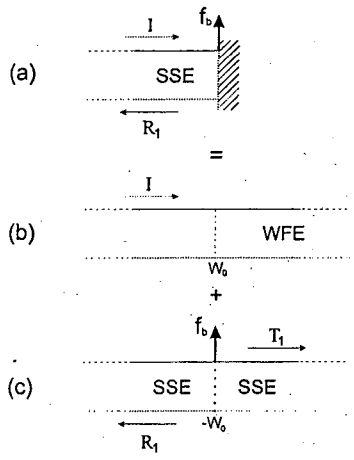

Fig. 8.11. An equivalent model to predict blocked force and wave reflection in a blocked rail.

Fig. 8.11(c),

$$\mathbf{f}_b = -(\mathbf{D}_{S,-} + \mathbf{D}_{S,+})\mathbf{W}_0 \quad . \tag{8.32}$$

This force vector $\mathbf{f}_b$ is the same as the blocked force in Fig. 8.11(a).

8.3 Analysis of numerical error

For the combined SSE/FE model, it is worth checking the level of numerical error associated with this method because artificial separations/connections are introduced and differences exist in element types between the SSE and FE. These may both potentially cause considerable errors. So prior to introducing cracks in the combined SSE/FE model, numerical errors are evaluated for a homogeneous railway track with the cross-section shown in Fig. 8.2. For this track, the dispersion curves of propagating waves created by WFE analysis are shown in Fig. 8.12 up to 50 kHz.

In this investigation into numerical error, two limit cases of a local non-uniformity are considered: homogeneous and broken rails. The broken rail can be treated as a single semi-infinite rail with a free boundary condition at the end. In practice, two parts of a broken rail may be held together in track by the compressive stress and in this case it will not be easy to specify their boundary conditions mathematically. In this thesis, however, it is assumed that they are separated from each other, giving a free end boundary condition.

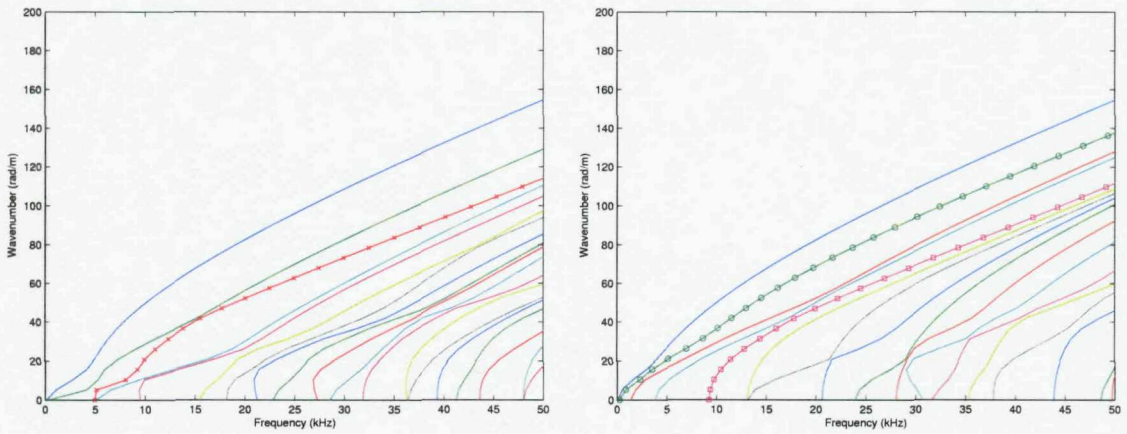

(a) (b)

Fig. 8.12. Dispersion curves for the rail shown in Fig 8.2 (a) for the vertical and symmetric longitudinal waves, (b) for the lateral, torsional and antisymmetric longitudinal waves.

In this analysis, potential errors are investigated in terms of the conservation of incident power. Note that there is no damping in this track model so that the incident power has to be conserved. Since there are multiple propagating waves in the rail, as indicated in Fig. 8.12, the total power contained in the reflected and in the transmitted waves are compared to check the conservation of incident power. The waves propagating furthest along the rail, which were identified in the previous chapters, are chosen as incident waves. They are the vertical bending wave localized in the rail head, the lateral bending wave which has global deformation including the web and rail head, and the 1^{st} order web bending wave, respectively. The waves chosen are shown in Fig. 8.12 with different marks: the wave marked '$\times$' in Fig. 8.12(a) is for the vertical bending wave in the rail head, two waves with '$\square$' and '$\circ$' in Fig. 8.12(b) are for the lateral bending wave in the web and rail head and the 1^{st} order web bending wave, respectively. Using these three waves as incident waves, presented in Fig. 8.12 with the marks, conservation of incident power is examined up to 50 kHz. Note that, at frequencies below 10 or 20 kHz, the waves chosen are not the desired types of incident waves as discussed previously in Chapter 4.

In the case of the homogeneous rail, the power carried by an incident wave has to be conserved giving complete transmission and no reflection. That is, for an incident wave, j, the reflected and transmitted waves should satisfy the conditions

$$\sum_i r_{ij} = 0 \quad , \quad \sum_i t_{ij} = 1 \quad , \tag{8.33}$$

where r and t denote power reflection and transmission coefficients, respectively, and the subscript i corresponds to the reflected and transmitted waves propagating at a given frequency. Conversely, for the broken rail, complete reflection will occur, giving

$$\sum_i r_{ij} = 1 \quad . \tag{8.34}$$

The power reflection and transmission coefficients of the reflected and transmitted wave i for an incident wave j are defined as

$$r_{ij} = \frac{\Pi^i_{ref}}{\Pi^j_{inc}} \quad , \quad t_{ij} = \frac{\Pi^i_{trn}}{\Pi^j_{inc}} \quad . \tag{8.35}$$

The respective powers in Eq.(8.35) are evaluated using the displacement vector $\mathbf{V}(x)$ as,

$$\Pi^j_{inc} = \frac{1}{2N}\rho A\omega^2 c^j_{g,inc} \sum_A |\mathbf{V}(x)^j_{inc}|^2 \quad , \tag{8.36}$$

$$\Pi^i_{ref} = \frac{1}{2N}\rho A\omega^2 c^i_{g,ref} \sum_A |\mathbf{V}(x)^i_{ref}|^2 \quad , \tag{8.37}$$

$$\Pi^i_{trn} = \frac{1}{2N}\rho A\omega^2 c^i_{g,trn} \sum_A |\mathbf{V}(x)^i_{trn}|^2 \quad , \tag{8.38}$$

where ρA is the mass per unit length of the cross-section and $\sum_A$ means summation over the cross-section. Since only waves with purely real wavenumbers carry power along the structure, only these propagating waves are included in power calculation. In this case, $|\mathbf{V}(x)^j_{inc}|$, $|\mathbf{V}(x)^i_{ref}|$ and $|\mathbf{V}(x)^i_{trn}|$ are independent of x.

8.3.1 Numerical error in combined SSE/SSE models

In order to check the error that comes from the SSEs, the homogeneous and broken rails are modelled first with SSEs throughout as shown in Fig. 8.13. The lengths of the finite SSEs in these two models are set to 150 mm and 72 mm, respectively.

As shown in Fig. 8.13(a), the potential error of the homogeneous rail consists of two components: one from determining the blocked case and another from the model with the negative blocked force, $-\mathbf{f}_b$. For the blocked case, the reflected power carried by reflected waves R_1 has to be the same as the incident power. For the model

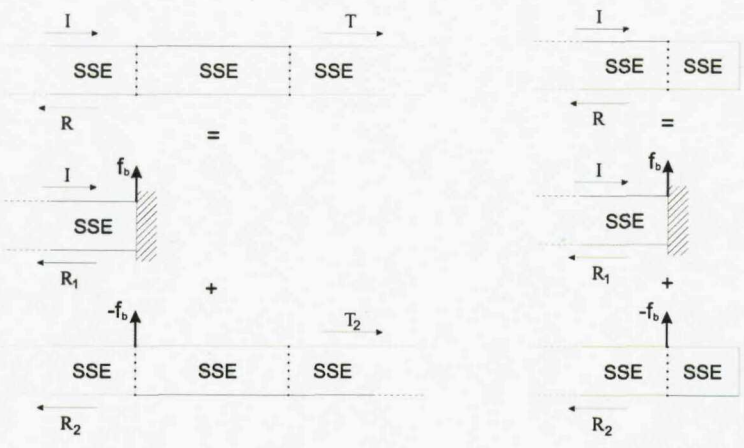

Fig. 8.13. Two combined SSE/SSE models to predict errors associated with the SSEs. (a) A homogeneous infinite rail, (b) a semi-infinite rail with free end.

with the negative blocked force, the displacement created by negative-propagating waves R_2 should be equal to that of $-R_1$ to give zero reflection in the superposed system. Also the transmitted power, carried by waves T_2, has to be the same as the power incident in the wave I.

The errors predicted from the homogeneous rail are shown in Fig. 8.14 for the three incident waves specified. Fig. 8.14(a) shows the error contained in the reflected power which was predicted from reflected waves, $R_1 + R_2$. This is of the order of 10^{-28}. The error in the transmitted waves T_2 is illustrated in Fig. 8.14(b) and is

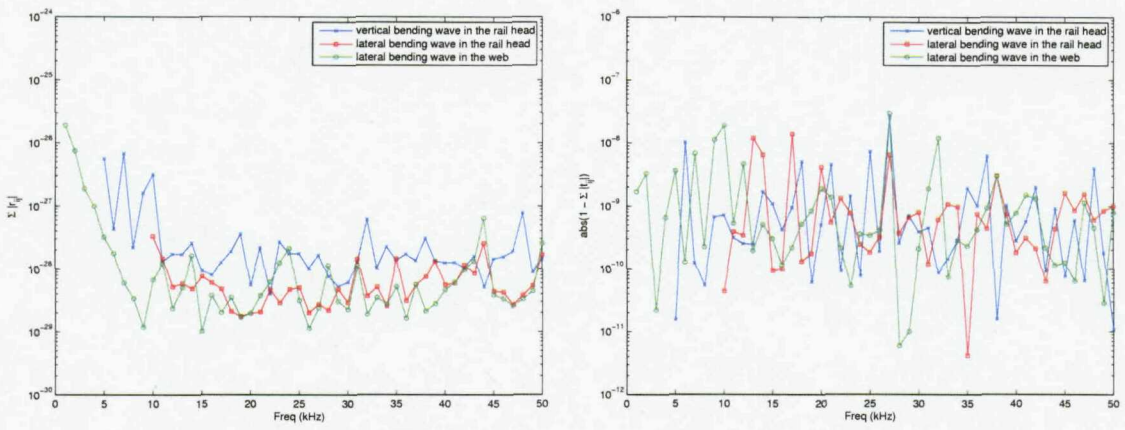

Fig. 8.14. Errors predicted from the connected SSE/SSE homogeneous rail, contained in (a) reflected waves, (b) transmitted waves.

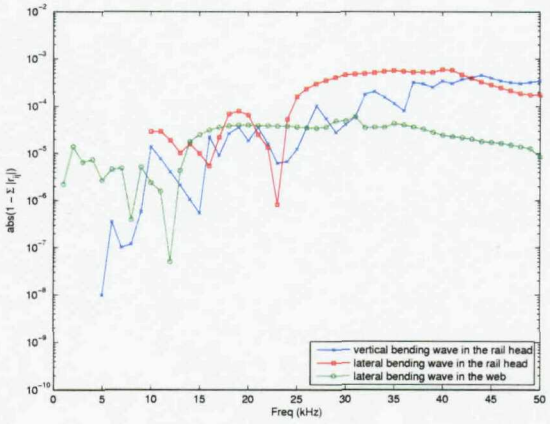

Fig. 8.15. Error created from the blocked semi-infinite rail shown in Fig. 8.13(a).

between 10^{-8} and 10^{-10}. As indicated in Fig. 8.14, the transmitted waves create larger errors than the reflected ones but both of them are very small. However, it should be noted that the very small error in the reflected power seen in Fig. 8.14(a) does not mean both R_1 and R_2 individually have such small errors, because the errors in R_1 and R_2 are cancelled out by adding them. The error contained only in R_1 is presented in Fig. 8.15. From Fig. 8.15, it is clear that the error in R_1 is much larger than those in Fig. 8.14, as high as 10^{-5} to 10^{-3} above 25 kHz.

In the case of the broken rail shown in Fig. 8.13(b), the errors predicted from the reflected waves R, obtained by $R_1 + R_2$, are illustrated in Fig. 8.16. Note that the error contained in R_1 in Fig. 8.13(b) is the same as shown in Fig. 8.15. In addition, it was found that the error in the combined reflected waves R is little affected by

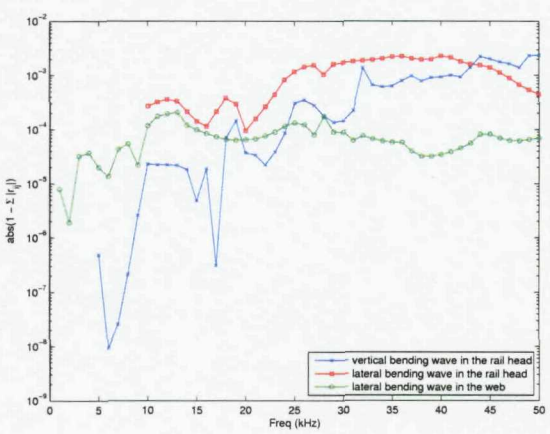

Fig. 8.16. Error created from the combined SSE/SSE semi-infinite rail with free end, shown in Fig. 8.13(b).

the presence of the finite SSE, attached to the semi-infinite one. Therefore, it was identified from Fig. 8.15 and Fig. 8.16 that both waves R_1 and R_2 have considerable errors for the broken rail, as does their sum.

Accordingly, it was found from the combined SSE/SSE models that relatively large errors are created by semi-infinite SSEs with blocked and free end conditions. The order of this error is about 10^{-4} to 10^{-3} at frequencies above 20 kHz. The reason for this relatively large error caused by the semi-infinite SSE has not yet clearly been identified. However, it is anticipated that this error would be reduced if more dofs are used in the cross-sectional modelling. To check that, the errors predicted from the finer cross-sectional model, i.e., model A used in Chapter 4, are shown in Fig. 8.17. The errors in R_1 which come from the blocked semi-infinite rail are illustrated in Fig. 8.17(a). In Fig. 8.17(b), the errors created from the semi-infinite rail with free end are presented. Comparing them to those in Fig. 8.15 and Fig. 8.16, it can be seen that the error is generally reduced with a finer mesh. However, this finer cross-sectional model could not be utilised in this chapter because it led to the FE model possessing too many dofs.

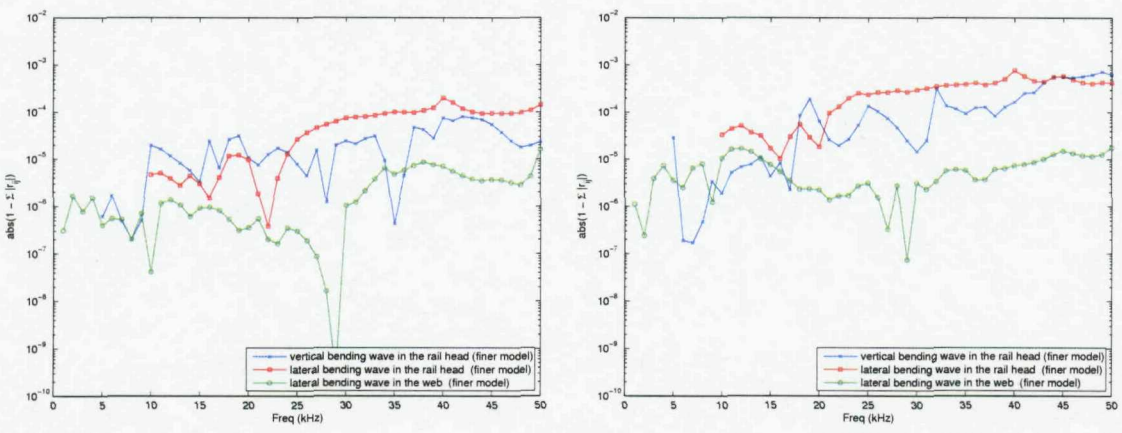

(a) (b)

Fig. 8.17. Errors created from the finer cross-sectional model for (a) the blocked semi-infinite rail shown in Fig. 8.13(a), (b) the combined SSE/SSE semi-infinite rail with free end as shown in Fig. 8.13(b).

8.3.2 Numerical error in combined SSE/FE models

In this section, numerical errors are predicted for combined SSE/FE models in terms of the power conservation. The same homogeneous and broken rails are considered here as shown in Fig. 8.13, simply replacing the finite SSEs with an FE mesh. The FE models in the homogeneous and broken rails have 25 and 12 sets of elements in 150 mm and 72 mm lengths, respectively.

For the homogeneous SSE/FE model, the errors are shown in Fig. 8.18, predicted from the reflected and transmitted waves for three incident waves. As presented in Fig. 8.18, the errors are of the order of 10^{-7} to 10^{-6} above 20 kHz for both reflected and transmitted waves. Comparing them with those in Fig. 8.14, it is clear that the combined SSE/FE model produces higher errors than the SSE/SSE one, but they are still fairly small. However, one should be aware that the error, coming from the blocked case, is still the same as presented in Fig. 8.15 because the blocked case does not involve the FE part.

For the broken SSE/FE rail, the errors predicted from the reflected waves are shown in Fig. 8.19. Since the errors in Fig. 8.19 are nearly the same as those in Fig. 8.16, it is clear that the errors contained in the reflected waves are generated mainly by the blocked semi-infinite SSE, not by the SSF/FE coupling.

Through the analysis of numerical error described above, it was identified that

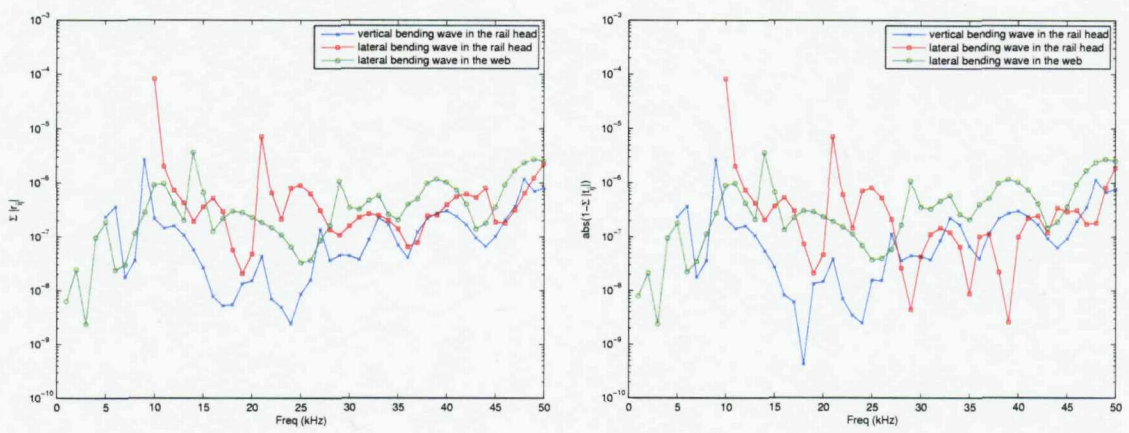

(a) (b)

Fig. 8.18. Errors predicted from the connected SSE/FE homogeneous rail, contained in (a) reflected waves, (b) transmitted waves.

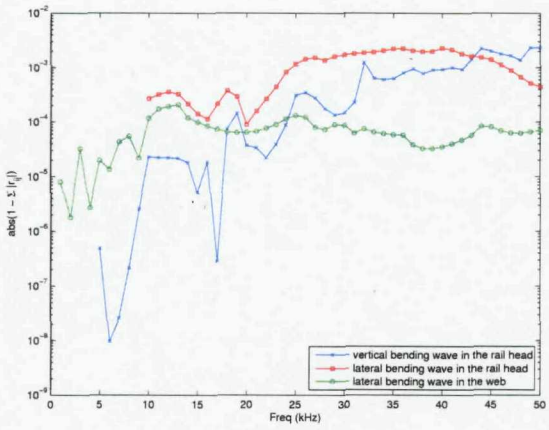

Fig. 8.19. Error predicted from the combined SSE/FE semi-infinite rail with free end.

the broken rail model creates an error of order about 10^{-3} above 20 kHz. It was also found that the error associated with SSE/FE coupling appears to be about 10^{-6} as shown in Fig. 8.18. However, since the total powers in multiple reflected and transmitted waves were compared, it is not possible to specify individual errors associated with each reflected and transmitted wave. The homogeneous and broken rails considered here correspond to two limit cases of a cracked rail. If a crack is introduced in the combined SSE/FE model, numerical errors of the model may fall between these two limit values and approach the broken one as the crack increases. So it is likely that the numerical error would increase with crack size.

8.4 Prediction of wave reflection and transmission due to cracks in rails

In this section, a crack is introduced to the combined SSE/FE rail model to estimate its reflection and transmission characteristics. As used above, the same three incident waves are imposed on the model with a crack and then their power reflection and transmission coefficients are predicted up to 50 kHz.

8.4.1 Crack modelling

There are various types of rail defects in practical railway tracks, such as vertical breaks which occur suddenly, cracks growing from an interior or surface defect of the rail, spalling, weld defects, etc. Some of the most common types of rail defects

are described in ref. [3]. However, transverse cracks in the rail have normally been considered in the literature because they are easy to model and create artificially in experiment [7, 8, 10]. Transverse cracks in the rail are regarded also in this section, which seems to be suitable for this feasibility study.

In the combined SSE/FE rail model, the length of the FE substructure was set to 150 mm with 25 elements in length. In that FE part, very simple vertical 'cracks' are generated simply by removing elements at a single slice at the middle of the model. As an example, the FE model with a crack reaching the middle of the web is illustrated in Fig. 8.20 with different view angles. In fact, this is not a commonly used geometry for a crack which is more usually modelled as a 'V' shaped notch. To make matters simpler, however, this crack model is considered in this feasibility study. In addition, the model used in this analysis could also be adopted to represent a short section of missing rail head or foot which is also of practical concern in railway tracks.

In order to investigate variations of reflection and transmission coefficients due to crack size, two sets of crack geometries are specified: a crack growing down from the top of the rail head and one growing up from the end of the foot, in each case to the full break of the rail. The increasing size of the crack is classified with the numbers from 0 to 9 as illustrated in Fig. 8.21. In this classification, crack sizes '0' and '9' represent homogeneous and fully broken rails, respectively. The vertical depths of each crack are listed in Table 8.2, which are the height of the cracks taken from the vertical mid-plane of the rail cross-section. Since only half of the rail cross-section is modelled, all the cracks specified in this study are symmetric with respect

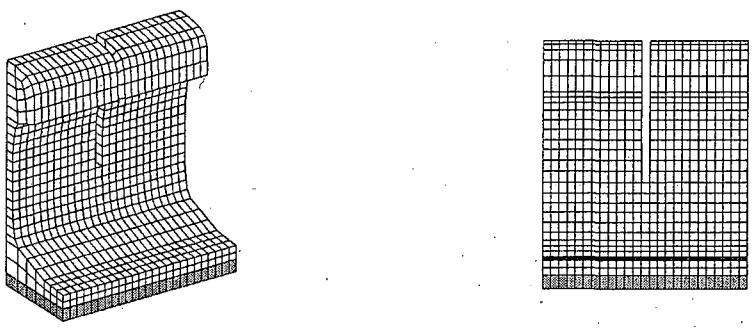

Fig. 8.20. An example of crack modelled by FEM seen by two different view angles.

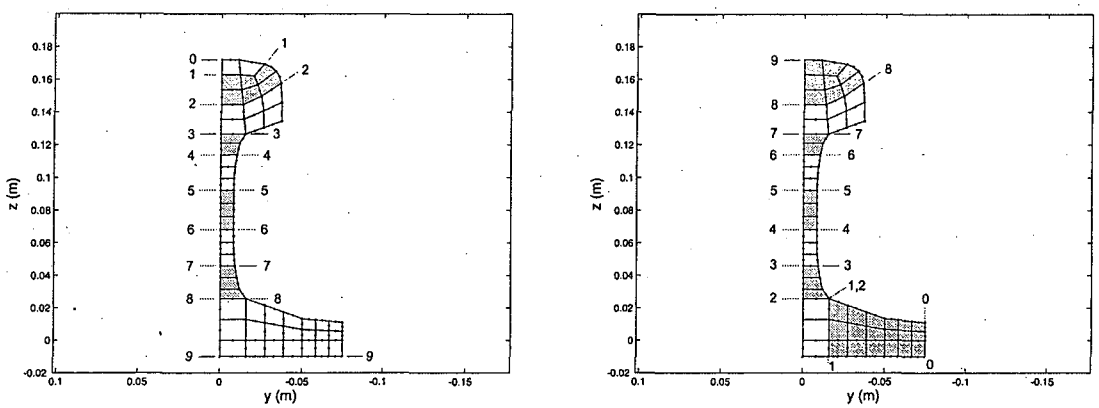

(a) (b)

Fig. 8.21. Two crack models (a) growing down from the top of the rail head, (b) growing up from the end of the rail foot. The increasing size of the crack is classified with the numbers from 0 to 9 and the depths of each crack are listed in Table 8.2.

Table 8.2. Depth of crack in the vertical direction (including depth of rail pad).

Crack number	Crack growing down from the top of the rail head	Crack growing up from the end of the rail foot
0	0 mm	0 mm
1	9 mm	36 mm
2	27 mm	36 mm
3	45 mm	56 mm
4	58 mm	78 mm
5	80 mm	102 mm
6	104 mm	124 mm
7	126 mm	137 mm
8	146 mm	155 mm
9 (full break)	182 mm	182 mm

to the vertical mid-plane of the rail cross-section.

8.4.2 Predicted reflection and transmission coefficients

Firstly, to understand how the numerical errors depend on the crack size, a power conservation check was executed for the two growing crack models. The predicted errors obtained from the power conservation check are illustrated in Appendix D. From that simulation, it was found that the errors in total power generally in-

crease with the crack size and approach those of the broken rail.

In the case of the crack growing down from the top of the rail head, the errors for crack sizes 3 and above in Fig. D.2(a) and (b) are nearly the same as those for the full break. For the web bending wave in Fig. D.2(c), however, the maximum error was obtained at crack size 6 which reaches to the middle of the web. For the crack growing up from the end of the foot, the errors for the vertical bending wave increase gradually with the crack size as shown in Fig. D.3(a) while the others in Fig. D.3(b) and (c) are in between about 10^{-5} to 10^{-3} for the crack sizes 1 and above. Similarly to those shown in Fig. D.2(c), the maximum error for the web bending wave was also appeared at crack size 4 which reaches to the middle of the web (Fig. D.3(c)). However, the reason for the these variations in numerical errors with respect to the crack size has not yet been identified.

In addition, to examine the effect of the FE model length on the prediction of reflection and transmission coefficients, the power conservation check was performed for three FE models with different lengths of 102 mm, 150 mm and 210 mm, respectively. For the crack size 3 in Fig. 8.21(a), the errors obtained from the three different FE lengths were nearly the same, regardless of the FE length. This implies that the variance caused by the FE model length is not significant.

For each crack size specified in Fig. 8.21, power reflection and transmission coefficients are predicted for the three wave types which are most measurable at the head and web and also propagate furthest along the rail. Although reflection and transmission may be in different wave types, most energy is retained in the same wave as is incident.

For the crack growing down from the top of the rail head, the reflection and transmission coefficients, r_{jj} and t_{jj}, are shown in Fig. 8.22. From Fig. 8.22(a), it was found that the vertical bending wave's reflection coefficients are nearly the same for crack sizes 3 and above. Also for the transmission coefficients, the similar variation is obtained as illustrated in Fig. 8.22(b). Note that since this wave chosen has global deformation below 16 kHz, only the coefficients above 16 kHz are for the vertical bending wave in the head. The results in Fig. 8.22(a) and (b) indicate that the propagation of this vertical bending wave in the rail head is not

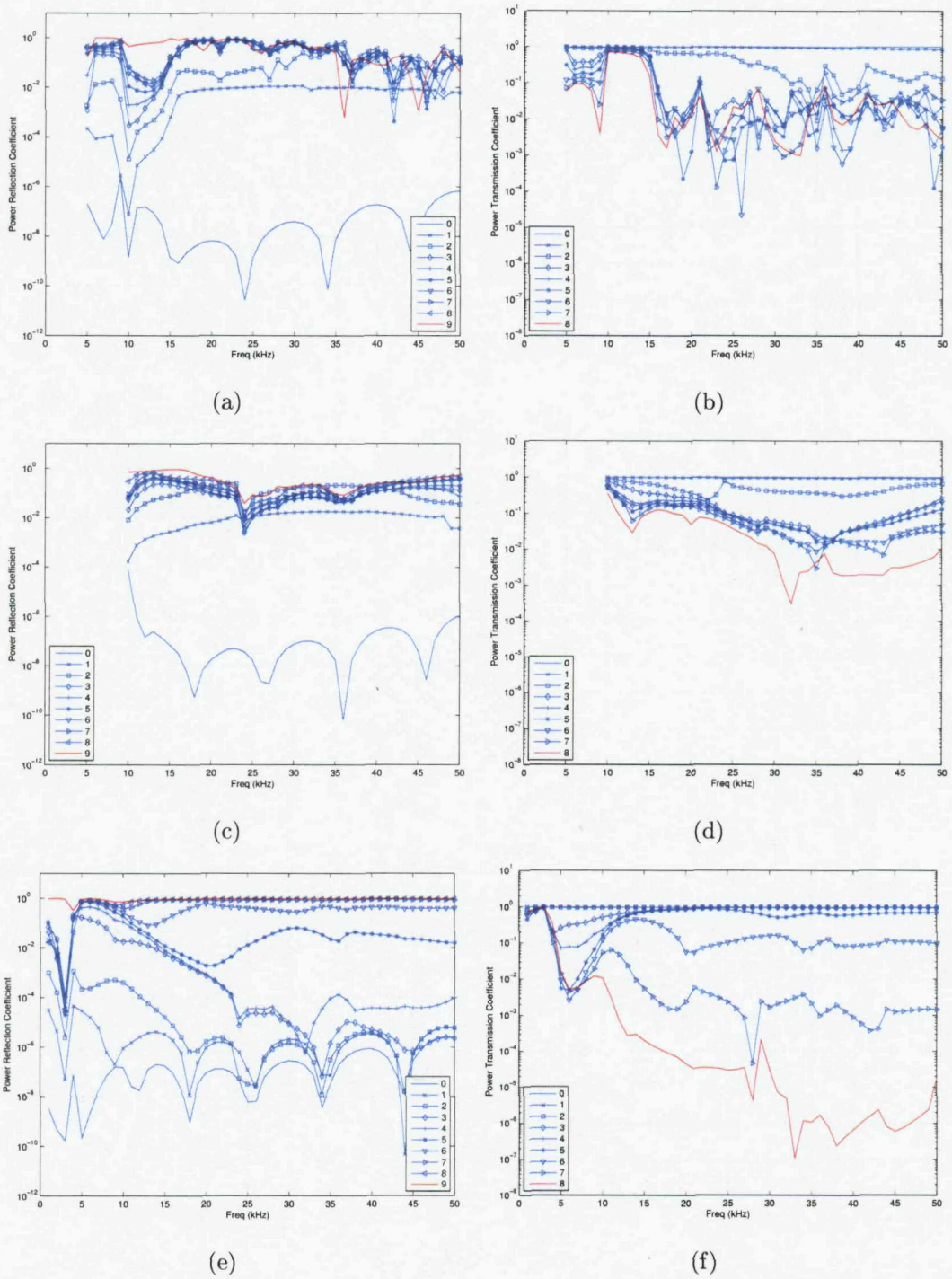

Fig. 8.22. Power reflection and transmission coefficients predicted from the combined SSE/FE rail with the crack shown in Fig. 8.21(a) for (a),(b) the vertical bending wave in the rail head, (c),(d) the lateral bending wave in the rail head, (e),(f) the 1^{st} order web bending wave.

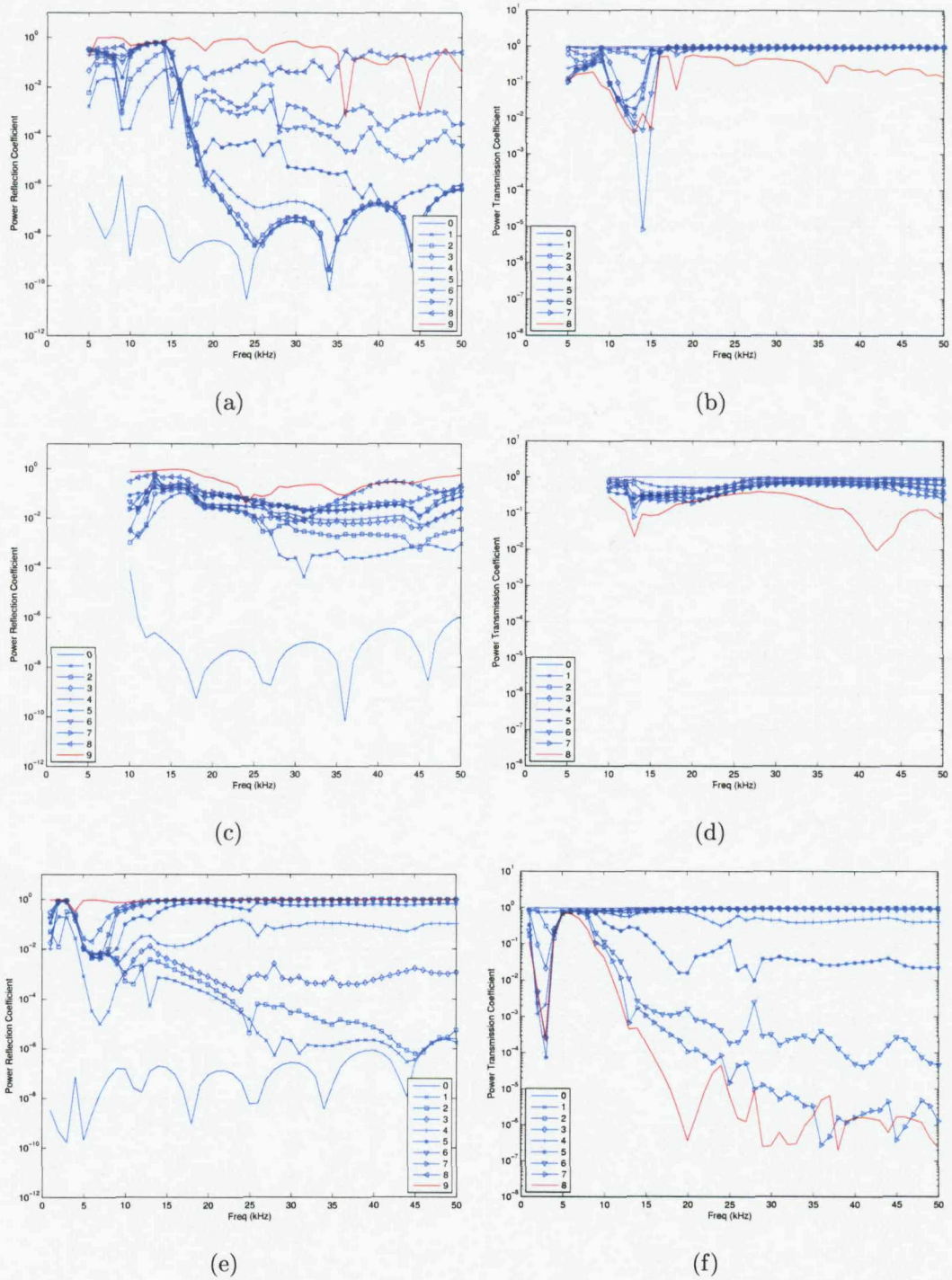

Fig. 8.23. Power reflection and transmission coefficients predicted from the combined SSE/FE rail with the crack shown in Fig. 8.21(b) for (a),(b) the vertical bending wave in the rail head, (c),(d) the lateral bending wave in the rail head, (e),(f) the 1^{st} order web bending wave.

much affected by the changes of the crack size in the web. A similar phenomenon is also found from the coefficients predicted for the lateral bending wave in the rail head and web (Fig. 8.22(c) and (d)). In the case of the web bending wave, it can be seen from Fig. 8.22(e) and (f) that the coefficients are not much affected for the crack sizes smaller than 6. On the other hand, for the crack growing up from the end of the foot, the reflection and transmission coefficients are shown in Fig. 8.23 and the similar variations of the coefficients are presented for the growing crack sizes.

In Fig. 8.22(a), dips of the reflection coefficients at 21 kHz and 27 kHz result from wave mode conversion of the incident wave. To illustrate this phenomenon, the reflection coefficients estimated at 20 kHz and 21 kHz are compared in Fig. 8.24 for all reflected waves propagating at crack size 3. As shown in Fig. 8.24, waves 8 and 9 cut on between these two frequencies and a significant part of the incident power is reflected in these newly cut-on waves at 21 kHz. Nevertheless, this figure confirms that most energy is retained in the same wave as is incident.

As presented in Fig. 8.22 and Fig. 8.23, the numerical error accumulated for all the reflected and transmitted waves propagating can be determined using the conservation of incident power. However, the level of error contained in each individual wave's reflection and transmission coefficients is unknown because only the accumulated error in all the multiple propagating waves could be quantified. This means that it may be possible for errors in individual reflected and transmitted waves to be larger than the accumulated one. In this analysis, nevertheless, the error obtained

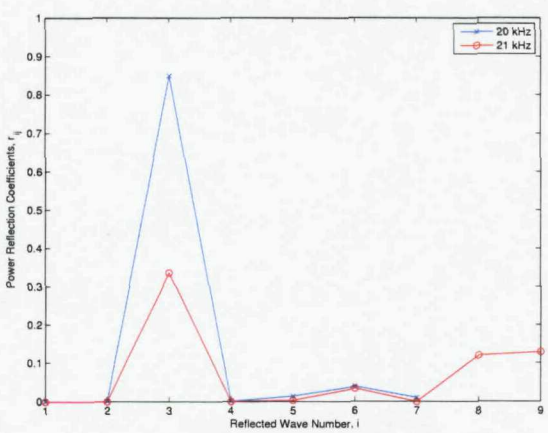

Fig. 8.24. Power reflection coefficients of all reflected waves propagating for the incident vertical bending wave in the rail head.

by the conservation of total power will be compared with the single wave's predicted reflection and transmission coefficients because that is the only estimate available.

The interesting frequency range in which waves propagate furthest along rails is between 20 kHz and 40 kHz as presented in previous chapters. The reflection and transmission coefficients averaged within this frequency band are presented in Fig. 8.25 and Fig. 8.26 with respect to crack size. The approximate errors are also shown in these figures, which were obtained from the results described in Appendix D by averaging them in the same frequency band. From Fig. 8.25 and Fig. 8.26, it can be seen that the errors are at least 15 dB lower than the predicted coefficients in general, excluding some cases where the reflection and transmission coefficients are very small.

To become an effective crack indicator, the waves chosen should have a large reflection coefficient and a small transmission coefficient even in the presence of small cracks. Fig. 8.25(a) shows that the vertical bending wave in the rail head reflects about half of its incident power for a crack larger than the size of the rail head. Conversely, the web bending wave propagates well regardless of a crack present in the rail head until it reaches crack size 6 in Fig. 8.21(a), i.e., most of the web is cracked. Since the lateral bending wave in the rail head has global deformation including the rail head and web, it generally gives less reflection than the vertical bending wave, which propagates mainly along the rail head. In transmission, the transmitted vertical bending wave has about 15 dB reduction of its incident power for cracks numbered 3 and above. The web bending wave gives a considerable drop in transmitted power from crack size 6.

From the predicted results for the crack growing down from the top of the rail head, it was identified that neither the vertical nor lateral waves that propagate along the rail head give significant reflections for small cracks located in the rail head (crack '1' which has a depth of about 10 mm). Also they are insensitive to changes in crack size once the crack is deeper than the rail head. In addition, the web bending wave does not create noticeable changes in its reflected and transmitted powers until a crack is deeper than half of the web from the top of the rail head.

For cracks growing up from the end of the foot, the predicted coefficients are

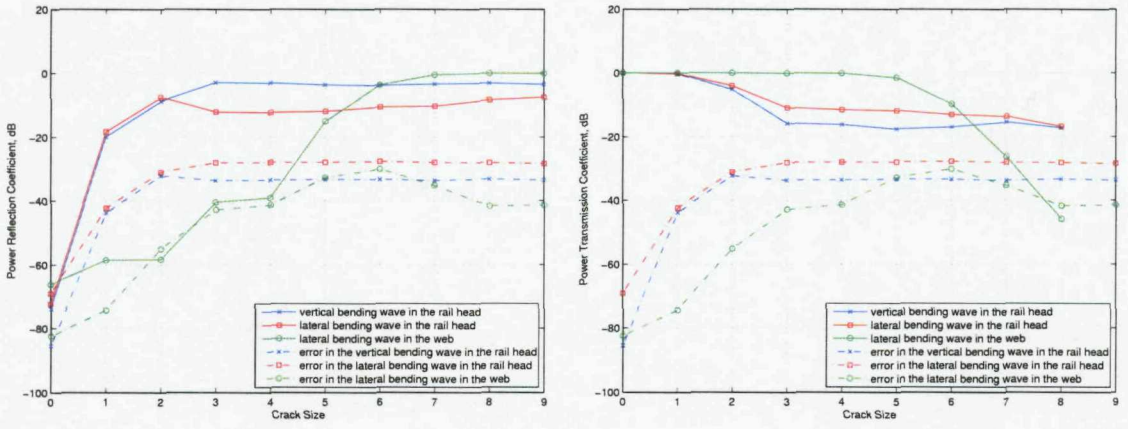

(a) (b)

Fig. 8.25. Power reflection and transmission coefficients averaged between 20 kHz and 40 kHz for the crack growing down from the top of the rail head. (a) Power reflection coefficients, (b) power transmission coefficients.

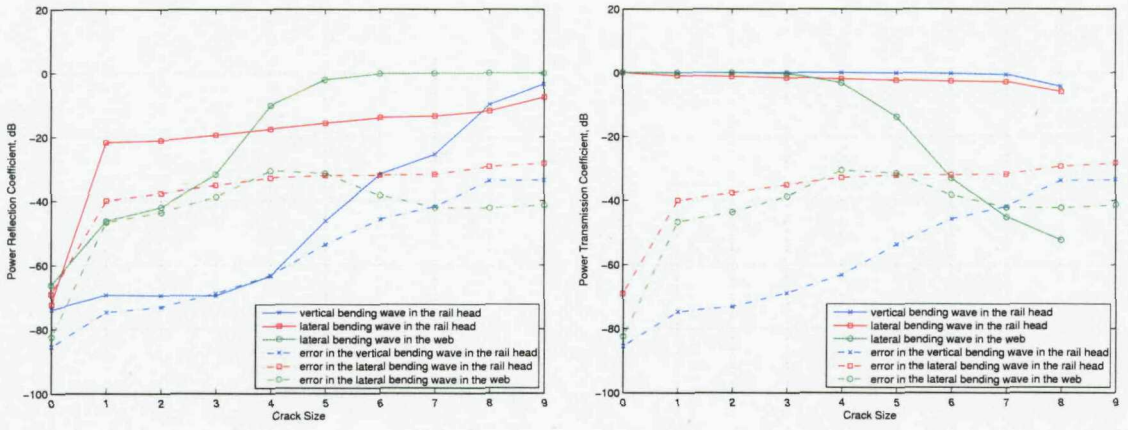

(a) (b)

Fig. 8.26. Power reflection and transmission coefficients averaged between 20 kHz and 40 kHz for the crack growing up from the end of the foot. (a) Power reflection coefficients, (b) power transmission coefficients.

illustrated in Fig. 8.26. Fig. 8.26 indicates that both waves measurable in the rail head are insensitive to the presence of a crack located in the bottom half of the rail, giving small reflections and large transmissions. Similar to the results in Fig. 8.25, when the crack becomes bigger than size 5, specified in Fig. 8.21(b), it could be detectable by the web bending wave, giving a large reflection and small transmission. From the predicted results shown in Fig. 8.26, it was identified that none of the wave types considered here can detect cracks growing from the end of the rail foot in the early stage.

For train-induced rail vibration, the transmitted waves would be more useful for long range crack detection because the reflected waves will be masked by the waves directly produced by the train. Consequently, from the results shown in Fig. 8.25(b) and Fig. 8.26(b), it was found that none of the transmitted wave types considered in this analysis are effective for the detection of small cracks in rails although they are the waves propagating furthest along the rail. This outcome indicates that using a single wave and measuring it at a single position on the rail cross-section is not sufficient to detect cracks efficiently, particularly small cracks, in rails excited by trains.

On the other hand, if artificial excitation is utilised, the reflected waves could also be used for crack detection. In this case, an reflection coefficient of -20 dB (or less, depending on the measurement system) would be usable. From the results in Fig. 8.25(a) and Fig. 8.26(a), therefore, it was found that the reflection coefficients would be more useful than the transmition coefficients for the artificial excitation.

Since it was found that using a single response measured on the rail cross-section is not effective to identify cracks in rails, it would be better to use more responses of the rail vibration and quantify mode conversion of the incident wave. This approach would not be relevant for train excitation which allows only a limited access to the rail because it requires multiple responses along the rail and around the perimeter of the rail cross-section. If an artificial excitation is considered instead, it would be possible to use multiple transducers, such as a transducer array mounted along the length of the rail and around the perimeter of the rail cross-section, to excite and measure specific wave modes effectively. In this way, matrices of reflection and transmission coefficients for each incident wave may be constructed. These matrices would present the mode conversions of the incident waves, which arise from the presence of cracks.

8.5 Summary

In this chapter, as a feasible application of the findings in the previous chapters, wave reflection and transmission due to cracks in rails were investigated by means of numerical simulations. Since the railway track has a complex cross-section and the frequency of interest is up to 50 kHz, a new numerical approach was developed to achieve this in this analysis.

Firstly, the SSEs for semi-finite waveguide structure were newly developed. Then combining them with a FE part, a new method, named the combined SSE/FE method, was introduced in this chapter. In this method, an infinite rail with a defect is subdivided into three parts: two semi-infinite rails (SSEs) and a finite length one containing the local defect (FE). Because of the computational limitation, a coarse cross-sectional model used in the previous FE analysis (Chapter 3) was utilised in this chapter. Since all the homogeneous wave solutions at a given frequency are required in this analysis, wavenumbers and mode shapes including propagating and nearfield waves were obtained and the relations between them for the positive- and negative-going waves were described briefly. Also cracks in the rail were modelled simply by removing elements at a single slice of the FE model.

Before entering the main part of the analysis, numerical errors caused by the combined SSE/FE method were investigated for three incident waves up to 50 kHz in order to check the reliability of the method. In this analysis of numerical error, the accumulated errors in all the multiple propagating waves were quantified by examining the conservation of incident power. Note that the level of error contained in each individual wave's reflection and transmission coefficients could not be predicted in this analysis. From this investigation, it was found that the maximum errors are of the order of 10^{-4} to 10^{-3} at frequencies above 20 kHz and are created from the semi-infinite SSE model, not from the SSE/FE coupling. This order of numerical error seems to be rather large for the application for the crack detection, particularly for small cracks, which may reflect a tiny amount of the incident power. Also this error may mask the transmitted power at a large crack which only a little amount of the incident power can pass through. The error would be reduced if more dofs are used in the cross-sectional modelling.

For two sets of cracks growing from the top of the rail head and from the end of the foot, power reflection and transmission coefficients were estimated for three waves that propagate furthest along the rail, measurable on the rail head and the middle of the web. From this calculation, it was found that neither the vertical nor lateral bending waves that propagate along the rail head experience considerable energy drops in their transmission in the presence of small cracks located in the rail head. Also the web bending wave did not create noticeable changes in its trans-

mitted powers until a crack was deeper than half the rail. Accordingly, this result indicates that measuring rail vibration at a single position on the rail cross-section is not efficient to detect cracks in rails, particularly small cracks.

In this chapter, the fully broken rail was assumed to consist of two parts that are well separated from each other. However, as stated before, they may be held together by the compressive stress in the rail in practice and this full break will still have some reflection and transmission. However, an appropriate model for this kind of full break is beyond the scope of the present work.

Chapter 9

Conclusions and Suggestions for Further Work

9.1 Conclusions

In this thesis, the characteristics of waves propagating in railway tracks have been investigated at frequencies up to 80 kHz by means of numerical simulations and experiments. In terms of the long range wave propagation, the work has focused on answering the fundamental question: *how far along a rail can vibration travel?* Through the research presented in this thesis, the specific answers to this question have been clearly identified. Above all, the efficient wave types for long range propagation and their decay rates were found by numerical simulations and validated by experiments. It was also found which part of the rail cross-section gives the best measurement of these waves and in which frequency range the waves travel furthest along the rail. Based on these results, the travelling distances of waves propagating along rails were identified. Additionally, using the waves found which propagate furthest as incident waves, the reflection and transmission characteristics due to cracks in rails have been investigated by introducing a new numerical method.

In Chapter 2, works published in literature, which are associated with the wave propagation in waveguide structures, particularly in rails, were reviewed briefly. There was only a limited amount of work on wave propagation in rails at frequencies of several tens of kilohertz, especially in experiments. The difficulties are caused mainly by the presence of multiple dispersive waves in this frequency range, which

leads to very complicated dispersion relations. Based on the findings of the literature, the frequency range up to 80 kHz was set for the present work for studying the long range wave propagation in rails.

As a numerical approach, the conventional finite element (FE) method has been employed in Chapter 3, which has been previously used for noise modelling of a rail at frequencies below 5 kHz or 6 kHz. From this simulation, dispersion relations and decay rates were predicted up to 80 kHz. It was found that the FE method would be a useful tool even for frequencies up to 80 kHz, but this method had several drawbacks for dealing with wave propagation in structures efficiently. The FE method was therefore not considered suitable for repeated use.

As an alternative approach to the conventional FE method, the wavenumber finite element (WFE) method has been discussed in Chapter 4. In this method, group velocity and decay rates were readily evaluated theoretically for each individual wave. From the results produced from the FE and WFE methods, it was observed that both methods produce almost the same dispersion relations and decay rates but the WFE method produces smoother curves, particularly for the group velocities, more easily. So the WFE method was more relevant for the present study because it was much faster and more efficient than the FE method.

Also in Chapter 4, the waves measurable on the rail surface were predicted by quantifying deformation energies at several regions of the rail cross-section. The most measurable waves which have the lowest decay rates were the vertical bending wave which has a local deformation in the rail head, lateral bending wave which has global deformation in the rail head and web and the 1^{st} order web bending wave, respectively. In this prediction for measurable waves, furthermore, it was found that the longitudinal waves do not have lower decay rates than other types of waves. This is probably because they normally induce considerable deformations of the rail foundation which has a large damping loss factor.

In the numerical simulations above, the track was modelled as a rail on a continuous foundation. This model has two damping components: damping for the rail and the foundation, respectively. These were set to constants in the simulations but the parameter study performed in Chapter 4 revealed that the minimum decay rates

are directly related to the damping of the rail, not of the foundation. So damping loss factors of rails were measured from several rail samples in Chapter 5 in order to improve the predicted decay rates. From the structural damping measurement, it was found that the measured damping loss factor reduces as the frequency increases, although it does not deviate much from the estimated value of 0.0002 used for the previous FE and WFE analyses. Introducing this frequency dependency into the damping of the rail has produced some changes in the predicted decay rates. In addition it has to be emphasised that the damping loss factors tend not to be significantly dependent on the different rail geometries or steels. From the recalculated decay rates, it was identified that the minimum decay rates are about 0.04 to 0.05 dB/m at frequencies between 20 kHz and 40 kHz.

The effective wave types for long range wave propagation, predicted from the numerical simulations, were validated in Chapter 6 by the experiments carried out on the ISVR test track. In this experiment group velocities were measured along the short section of rail using first an impact hammer and then a piezoceramic transducer as exciters. It was validated from the measured signals that the measured group velocities give an excellent agreement with the simulated ones for measurable waves. It was also found from this measurement that waves do not travel large distances along the rail foot. In addition, the measured data revealed that a considerable reflection occurs for waves in the web due to welds. In practice, every track has welds along the rail although at different spacing from those present in the ISVR test track used in this experiment. They would thus affect the long range propagation of a wave by reflecting a certain amount of travelling energy.

In Chapter 7, the decay rates were measured on an operational track because a long section of rail was required to extract them reliably. In this measurement train-induced rail vibration was acquired for several service trains for measurement positions at the rail head and web. Through this experiment, features of the train-induced rail vibration were identified and it was revealed that service trains are very effective in exciting rail vibration even at high frequencies. Also frequency bands which are more likely to give the furthest detection range were identified from the measured data at the rail head and web. Consequently, it was validated from this field test that the measured decay rates coincide very well with the simulated ones in almost the entire frequency range up to 80 kHz. Furthermore, the characteristics

of rail vibration induced by the different trains that were measured were almost the same, despite differences in running speeds and number of coaches. This may be because the trains measured were all EMUs, mainly of the same class. Nevertheless, this is a very desirable result in terms of the practical application. It would be clearer if more rail responses were measured for other types of railway vehicles, such as freight trains.

Finally, the question of *how far along a rail can vibration travel?* could be answered clearly from the simulated and experimental results. The measured minimum decay rates and their corresponding frequency ranges are

- about 0.035 dB/m at the underside of the rail head around 25 kHz
- about 0.035 dB/m at the side of the rail head around 25 kHz
- about 0.04 dB/m at the middle of the web around 29 kHz.

These outcomes indicate that the most effective frequency range is between 20 kHz and 40 kHz, not the higher range of 40 kHz to 80 kHz suggested in ref. [11]. In the latter range, the decay rates measured were 0.04 to 0.06 dB/m at the underside of the rail head, 0.04 to 0.08 dB/m at the side of the rail head and 0.05 to 0.1 dB/m at the middle of the web, respectively. It was seen from the field measurement that an amplitude range of more than 50 dB is measurable in the rail vibration. So in terms of travelling distance, if a 50 dB level reduction is assumed, the maximum propagating distances will be about 1.2 km at the rail head and about 1.0 km at the web, respectively. It has to be noted that high excitation signals were induced by running trains at specific frequencies between 20 kHz and 40 kHz. These frequencies might be different at other sites and with different trains. Their origin is not known.

In terms of monitoring and detecting defects in railway tracks, a diagram such as the acceleration level versus distance could be used because abrupt level changes due to rail defects could be observed in this diagram which can be created for each train running on the track. These sudden level changes will be associated with reflection and, more likely, transmission characteristics of the defects. So, in Chapter 8, as a feasible application of the findings on long range wave propagation in rails, wave reflection and transmission due to cracks in rails was investigated. For this analysis, the SSE for the semi-infinite rail was formulated and then the combined SSE/FE

method was developed. In this method, an infinite length track was subdivided into three elements: two semi-infinite rails modelled by the SSE method and a finite length rail containing a crack modelled by the FE method. Before introducing a crack into this track model, numerical errors were examined up to 50 kHz in terms of the incident power conservation in order to check the reliability of the combined SSE/FE method. From this investigation, it was observed that the maximum errors are of the order of 10^{-4} to 10^{-3} at frequencies above 20 kHz and are created from the semi-infinite SSE model, not from the SSE/FE coupling. (However, it was not possible to predict the level of error contained in each individual wave's reflection and transmission coefficients in this analysis.) The reason for this error caused by the semi-infinite SSE has not yet been clearly identified, but it was found that a finer cross-sectional model gives a reduced error. For two sets of cracks of various sizes, power reflection and transmission coefficients were estimated for the three waves that propagate furthest along rails. From this calculation, it was found that none of these three waves could be used to detect small cracks localized in the rail head or foot on the basis of train-induced vibration. This result indicates that measuring rail vibration at a single position on the rail cross-section is not efficient to detect cracks in rails, particularly small cracks.

9.2 Suggestions for Further Work

Through the work presented in this thesis, it was well identified how far along a rail vibration can travel. However, there are still several interesting aspects unidentified in this thesis. In this section some suggestions for future research are highlighted.

In the field measurement, more study and experiment may be necessary to identify the origin of the rail vibration and to establish why the rail has higher vibration at several particular frequencies. This would require more rail responses to be measured during the passage of several different types of railway vehicles, including freight, as well as more investigation on the wheel/track interaction at high frequencies. Also it will be important, particularly from a practical point of view, to identify the reason for a sudden energy drop which appeared in the spectrograms measured from the field test. Measurements at other sites would be required to check whether these findings are particular to the present site. Those measurements would also be necessary to investigate the variation of the decay rates for other tracks.

In the field measurements, the accelerometers were mounted on the rail surface to detect waves propagating along rails. However, from the practical point of view, using non-contact type transducers as sensors may give several advantages for the practical implementation. So, it would be helpful to investigate and search appropriate non-contact type sensors.

In the prediction of power reflection and transmission coefficients due to rail defects, the origin of numerical error needs to be clearly identified to improve the reliability of the combined SSE/FE method for further application. Also, for the vertical rail defects modelled in this thesis, it would be possible to replace the FE section which requires long computation times with a short section of SSE which only has reduced cross-section. If it is feasible, it would make the work finding origins of the numerical error easier.

There are various types of rail defects in practical railway tracks, like cracks growing in the lateral or oblique directions and growing from the interior of the rail, etc. Further investigation on the reflection and transmission characteristics for these different types of defects may be necessary. In addition, cracks with asymmetric geometries with respect to the vertical mid-plane of the rail cross-section were not considered in the crack modelling because only half of the rail cross-section was modelled in this thesis. It would be required to evaluate reflection and transmission coefficients for these asymmetric cracks by modelling the entire cross-section of the rail.

In order to validate the predicted reflection and transmission coefficients, experiments need to be performed on a long section of rail with similar defects to those used in simulation. Since it would be impracticable to do it on defective operational tracks for running trains, cracks made artificially, like saw-cuts, in a long rail specimen may be sufficient for this purpose. Also to improve the detection performance, it seems to be necessary to use more responses obtained from several points on the rail cross-section in order to quantify wave mode conversion by using artificial excitations. In this approach, matrices of reflection and transmission coefficients for each incident wave would present the mode conversions of the incident waves, which arise from the presence of cracks. In this situation, it could be

an important issue how to decompose each mode reliably from the measured signals.

References

[1] V. Weise and G. Waite, "Developments of flaw inspection techniques within the UK rail industry," *Railway Engineering 2004, 7th International Conference and Exhibition, London, UK*, 6-7 July 2004.

[2] P. Aknin and H. Cygan, "Improving the detection of internal rail cracks by using radon transform of bscan image," *Railway Engineering 2004, 7th International Conference and Exhibition, London, UK*, 6-7 July 2004.

[3] C. Esveld, *Modern railway track.* 2nd Edition, MRT-Productions, 2001.

[4] J. L. Rose, "Standing on the shoulders of giants: an example of guided wave inspection," *Materials Evaluation*, vol. 60, pp. 53–59, 2002.

[5] Research and Development Department in Guided Ultrasonic Ltd, "Long range screening of rail using guided waves," *Third Vehicle/Track Interaction Course, Emmanuel College, Cambridge, UK*, Sep. 2001.

[6] P. Wilcox, M. Evans, D. Alleyne, B. Pavlakovic, K. Vine, P. Cawley and M. Lowe, "Long range inspection of rail using guided waves," *Railway Engineering 2002, 5th International Conference and Exhibition, London, UK*, 3-4 July 2002.

[7] J. L. Rose, M. J. Avioli and W-J. Song, "Application and potential of guided wave rail inspection," *Insight*, vol. 44, no. 6, pp. 353–358, 2002.

[8] P. Cawley, M. J. S. Lowe, D. N. Alleyne, B. Pavlakovic and P. Wilcox, "Practical long range guided wave testing: applications to pipes and rail," *Material Evaluation*, vol. 61, pp. 66–74, 2003.

[9] F. Lanza di Scalea and J. McNamara, "Ultrasonic NDE of railroad tracks: Air-coupled cross-sectional inspection and long-range inspection," *Insight*, vol. 45, no. 6, pp. 394–401, 2003.

[10] P. Cawley, P. Wilcox, D. N. Alleyne, B. Pavlakovic, M. Evans, K. Vine and M. J. S. Lowe, "Long range inspection of rail using guided waves - field experience," *16th World Conference on NDT, Montreal, Canada*, 2004.

[11] J. L. Rose, M. J. Avioli, P. Mudge and R. Sanderson, "Guided wave inspection potential of defects in rail," *Railway Engineering 2002, 5th International Conference and Exhibition, London, UK*, 3-4 July 2002.

[12] K. Knothe and S. L. Grassie, "Modelling of railway track and vehicle/track interaction at high frequencies," *Vehicle System Dynamics*, vol. 22, pp. 209–262, 1993.

[13] D. J. Thompson and N. Vincent, "Track dynamic behaviour at high frequencies. part 1: Theoretical models and laboratory measurements," *Vehicle System Dynamics Supplement*, vol. 24, pp. 86–99, 1995.

[14] D. J. Thompson, "Wheel-rail noise generation, part III: Rail vibration," *Journal of Sound and Vibration*, vol. 161, no. 3, pp. 421–446, 1993.

[15] R. Sanderson and S. Smith, "The application of finite element modelling to guided ultrasonic waves in rails," *Insight*, vol. 44, no. 6, pp. 359–363, 2002.

[16] S. Finnveden, "Exact spectral finite element analysis of stationary vibrations in a railway car structure," *Acta Acoustica*, vol. 2, pp. 461–482, 1994.

[17] F. Birgersson, *Modelling with the dynamic stiffness and the spectral finite element methods for distributed sources.* M.Sc. Thesis, ISVR at University of Southampton, 2000.

[18] F. Birgersson, N. S. Ferguson and S. Finnveden, "Application of the spectral finite element method to turbulent boundary layer induced vibration of plates," *Journal of Sound and Vibration*, vol. 259, no. 4, pp. 873–891, 2003.

[19] J. F. Doyle, *Wave Propagation in Structures: Spectral analysis using fast discrete fourier transforms.* 2nd Edition, Springer, New York, 1997.

[20] F. Birgersson, S. Finnveden and C.-M. Nilsson, "A spectral super element for modelling of plate vibration. part 1: general theory," *Journal of Sound and Vibration*, vol. 287, no. 1-2, pp. 297–314, 2005.

[21] L. Gry and C. Gontier, "Dynamic modelling of railway track: A periodic model based on a generalized beam formulation," *Journal of Sound and Vibration*, vol. 199, no. 4, pp. 531–558, 1997.

[22] B. R. Mace, D. Duhamel, M. J. Brennan and L. Hinke, "Finite element prediction of wave motion in structural waveguides," *Journal of Acoustical Society of America*, vol. 117, no. 5, pp. 2835–2843, 2005.

[23] B. Aalami, "Waves in prismatic guideds of arbitrary cross section," *Journal of Applied Mechanics*, vol. 40, pp. 1067–1072, 1973.

[24] L. Gavric, "Computation of propagative waves in free rail using a finite element technique," *Journal of Sound and Vibration*, vol. 183, no. 3, pp. 531–543, 1995.

[25] X. Sheng, C. J. C. Jones and D. J. Thompson, "Computer programs for the discrete wavenumber finite/boundary element model for ground vibration and noise from railway tunnels," *ISVR Technical Memorandum*, No. 915, 2003.

[26] C.-M. Nilsson, *Waveguide finite elements applied on a car tyre.* Ph. D. Thesis, KTH, Stockholm, 2004.

[27] S. Finnveden, "Evaluation of modal density and group velocity by a finite element method," *Journal of Sound and Vibration*, vol. 273, pp. 51–75, 2004.

[28] T. Hayashi, W-J. Song and J. L. Rose, "Guided wave dispersion curves for a bar with an arbitrary cross-section, a rod and rail example," *Ultrasonics*, vol. 41, pp. 175–183, 2003.

[29] I. Bartoli, A. Marzani, F. Lanza di Scalea and E. Viola, "Modeling wave propagation in damped waveguides of arbitrary cross-section," *Journal of Sound and Vibration*, vol. 295, pp. 685–707, 2006.

[30] N. Vincent and D. J. Thompson, "Track dynamic behaviour at high frequencies. part 2: Experimental results and comparisons with theory," *Vehicle System Dynamics Supplement*, vol. 24, pp. 100–114, 1995.

[31] D. J. Thompson, "Experimental analysis of wave propagation in railway tracks," *Journal of Sound and Vibration*, vol. 203, no. 5, pp. 867–888, 1997.

[32] D. J. Ewins, *Modal testing: theory and practice.* Research Studies Press Ltd., Letchworth, 1984.

[33] F. Lanza di Scalea and J. McNamara, "Measuring high-frequency wave propagation in railroad tracks by joint time-frequency analysis," *Journal of Sound and Vibration*, vol. 273, pp. 637–651, 2004.

[34] A. K. Gurvich, V. N. Kozlov, A. A. Samokrutov and V. G. Shevaldykin, "Non-destructive testing of rails in case of guided waves use," *16th World Conference on NDT, Montreal, Canada*, 2004.

[35] J. L. Rose and M. J. Avioli, "Elastic wave analysis for broken rail detection," *15th World Conference on NDT, Rome, Italy*, 2000.

[36] B. R. Mace, "Wave reflection and transmission in beams," *Journal of Sound and Vibration*, vol. 97, no. 2, pp. 237–246, 1984.

[37] J. F. Doyle and S. Kamle, "An experimental study of the reflection and transmission of flexural waves at discontinuities," *Journal of Applied Mechanics*, vol. 52, pp. 669–673, 1985.

[38] J. F. Doyle and S. Kamle, "An experimental study of the reflection and transmission of flexural waves at an arbitrary T-joint," *Journal of Applied Mechanics*, vol. 54, pp. 136–140, 1987.

[39] M. Martin, S. Gopalakrishnan and J. F. Doyle, "Wave propagation in multiply connected deep waveguides," *Journal of Sound and Vibration*, vol. 174, no. 4, pp. 521–538, 1994.

[40] S. Gopalakrishnan and J. F. Doyle, "Spectral super-elements for wave propagation in structures with local non-uniformities," *Computer Methods in Applied Mechanics and Engineering*, vol. 121, pp. 77–90, 1995.

[41] S. P. Shone, B. R. Mace and T. P. Waters, "Reflection and transmission coefficients using the spectral element method: application to crack modelling in beams," *Preceedings of the Institute of Acoustics, Spring conference, Southampton, UK*, pp. 115–128, 2004.

[42] S. P. Shone, B. R. Mace and T. P. Waters, "Reflection of waves from cracks in beams," *Preceedings of ISMA2004, Leuven, Belgium*, pp. 531–543, 2004.

[43] U. Orrenius and S. Finnveden, "Calculation of wave propagation in rib-stiffened plate structures," *Journal of Sound and Vibration*, vol. 198, no. 2, pp. 203–224, 1996.

[44] A. Peplow and S. Finnveden, "A super-spectral finite element method for sound transmission in waveguides," *Journal of Acoustical Society of America*, vol. 116, no. 3, pp. 1389–1400, 2004.

[45] G. de France, *Railway track: effect of rail support stiffness on vibration and noise.* M.Sc. Thesis, ISVR, University of Southampton, 1998.

[46] S. H. Crandall, N. C. Dahl and T. J. Lardner, *An introduction to the mechanics of solids (2nd edition with SI units).* McGraw-Hill, 1978.

[47] http://www.efunda.com/formulae/solid_mechanics/mat_mechanics/hooke_orthotropic.cfm. (date accessed: 23. Sep. 2005).

[48] A. D. Nashif, D. I. G. Jones and J. P. Henderson, *Vibration damping.* John Wiley & Sons, 1985.

[49] C. M. Harris, *Shock and vibration handbook.* Chapter 10, 3rd Edition, McGraw-Hill, New York, 1988.

[50] L. Cremer, M. Heckl and E. E. Ungar, *Structure-borne sound: structural vibrations and sound radiation at audio frequencies.* Springer-Verlag, 1973.

[51] N. C. Perkins and C. D. Mote, Jr., "Comments on curve veering in eigenvalue problems," *Journal of Sound and Vibration*, vol. 106, no. 3, pp. 451–463, 1986.

[52] Y. Waki, *On the application of finite element analysis to wave motion in one-dimensional waveguides.* Ph. D. Thesis, ISVR, University of Southampton, 2007.

[53] C. J. C. Jones and D. J. Thompson, "Rolling noise generated by railway wheels with visco-elastic layers," *Journal of Sound and Vibration*, vol. 231, no. 3, pp. 779–790, 1999.

[54] X. Sheng, C. J. C. Jones and D. J. Thompson, "Modelling ground vibration from rail traffic using the discrete wavenumber finite and boundary element method," *ISVR Technical Memorandum*, No. 899, 2002.

[55] C-M. Nilsson and C. J. C. Jones, "Theory manual for WANDS 2.1 wavenumber-domain FE-BE software for structures and fluids," *ISVR Technical Memorandum*, No. 975, 2007.

[56] C-M. Nilsson and C. J. C. Jones, "Manual for WANDS 2.1 wavenumber domain software for solids and fluids," *ISVR Technical Memorandum*, No. 976, 2007.

[57] M. Petyt, *Introduction to finite element vibration analysis.* Cambridge University Press, 1990.

[58] J. Ryue, D. J. Thompson and P. R. White, "Wave propagation in railway tracks at high frequencies," *ISVR Contract Report*, No. 06/06, 2006.

[59] S. Qian and D. Chen, *Joint time-frequency analysis: methods and applications.* Prentice Hall, 1996.

[60] http://www.ferroperm−piezo.com/. (date accessed: 20. Sep. 2006).

[61] D. J. Thompson and C. J. C. Jones, "A review on the modelling of wheel/rail noise generation," *Journal of Sound and Vibration*, vol. 231, no. 3, pp. 519–536, 2000.

[62] A. V. Oppenheim and R. W. Schafer, *Discrete-time signal processing.* Prentice-Hall International, Inc., 1989.

[63] L. Gavric, "Finite element computation of dispersion properties of thin-walled waveguides," *Journal of Sound and Vibration*, vol. 173, no. 1, pp. 113–124, 1994.

Appendix A

A Rail Model on Discrete Rail Pads

The track model with continuous support neglects the discrete nature of the support. Therefore, a modified track model with discrete support was created here in order to identify the periodicity effect of a discrete support. Since the contribution of the sleeper and ballast are limited to the low frequency region below 1 kHz, only the rail pad was included in this model. The rail pad spacing was 0.6 m. Fig. A.1 shows the FE model with discrete rail pad. The model has a length of 0.3 m and includes half a rail pad with length 0.072 m. The stiffnesses of the rail pad were given as below by compensating for the shorter length of the foundation.

$$E_{p,x} = E_{p,y} = E_{p,z} = 1.667 \times 10^8 \text{ N/m}^2 \times (300/72) = 6.95 \times 10^8 \text{ N/m}^2 \quad \text{(A.1)}$$

$$G_{p,xy} = G_{p,yz} = G_{p,xz} = 2.23 \times 10^8 \text{ N/m}^2 \times (300/72) = 9.29 \times 10^8 \text{ N/m}^2 \quad \text{(A.2)}$$

Due to the presence of the discrete rail pad the symmetric-symmetric and antisymmetric-antisymmetric boundary conditions at both ends of the rail segment will provide different natural frequencies. They will also be different for the symmetric-antisymmetric and antisymmetric-symmetric boundary conditions. So four different combinations of boundary conditions are applied. The FE analysis result shows that this discrete foundation model has some difficulties to draw dispersion curves. Firstly, as shown in Fig. A.2, the wavelengths of some modes are not clearly defined since they have uneven deformation shapes, particularly at low frequencies. Another difficulty with this model is that different wavelengths take place in different parts of the rail as shown in Fig. A.3.

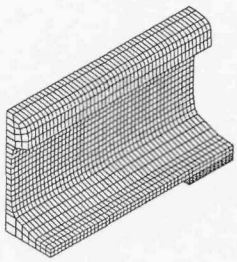

Fig. A.1. FE model for a rail on discrete rail pads

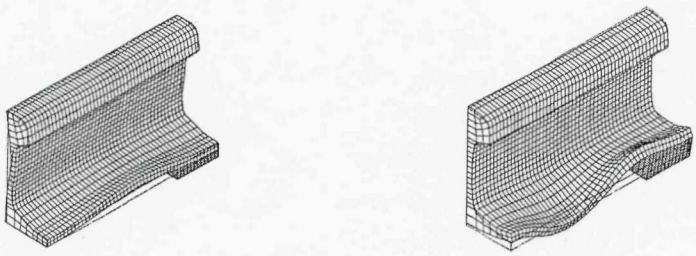

(a) (b)

Fig. A.2. Two examples of uneven deformation shapes along the rail. (a) 3875 Hz, (b) 5996 Hz.

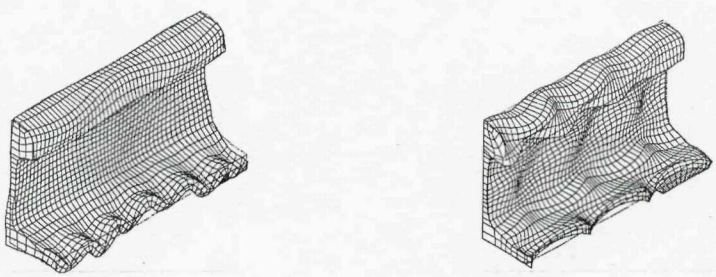

(a) (b)

Fig. A.3. Two examples of uneven deformation shapes along the rail. (a) 32712 Hz, (b) 57859 Hz.

Nevertheless, simply by selecting one of the possible values for the cases where the results are ambiguous, the discrete frequency-wavenumber plots are generated and compared with the dispersion curves obtained from the rail model with continuous foundation, as shown in Fig. A.4. From this figure, it is clear that the contribution of the discrete foundation on the frequency-wavenumber relation occurs only at low frequency, mainly below 10 kHz.

In addition, the damping loss factors predicted from the discrete and continuous foundation models are compared in Fig. A.5. Unlike the result shown in Fig. A.4, there is a considerable difference between the damping loss factors from the two track models. This discrepancy is strongly dependent on the nature of the rail pad's deformation because the different boundary conditions of the discretely supported rail model make different deformations of the rail pad. For example, in the continuously supported rail model, the symmetric-symmetric boundary condition will create exactly the same deformation shapes as those produced by the antisymmetric-antisymmetric boundary condition at the same frequency, having 90 ° phase shift in space. This implies that the rail pad has the same deformation regardless of these two boundary conditions. Conversely in the discretely supported rail model the symmetric-symmetric and antisymmetric-antisymmetric boundary conditions will exhibit different deformation shapes: one with large pad deformations, the other with small pad deformations. (See Fig. A.6). Therefore, the damping loss factors will be altered even at the same frequency. That is the reason why two different values of damping loss factor, marked '×' and '+' in Fig. A.5, occur even at the same natural frequency. However, as depicted in Fig. A.5, the damping loss factors of the discrete foundation model approach those of the continuous foundation model as frequency increases. In other words, the difference between two damping loss factors marked by '×' and '+' decreases and they tend towards those produced from the continuous foundation model at high frequencies. The kinds of rail pad deformations found at low and high frequency are shown graphically in Fig. A.6 and Fig. A.7 for the different boundary conditions. Since the length of the rail pad was modelled as 144 mm in this discretely supported rail model, the wavelength for a shear wave which travels along the rail at 3100 m/s will be shorter than 144 mm above about 22 kHz. It can be confirmed from Fig. A.5 that the two damping loss factors become similar above 22 kHz.

Based on the results shown in Fig. A.4 and Fig. A.5, it could be said that the contribution of the discrete foundation is limited to the low frequency region. Furthermore, from a practical point of view, if one measures the damping loss factors for a wave travelling in the rail at a certain frequency, then the result would be somewhere between the two values generated by the two different boundary conditions of the discretely supported track model which represent standing waves rather than propagating waves. On the basis of these simulation results, it was considered in this study that the continuously supported track model could give a reliable outcome.

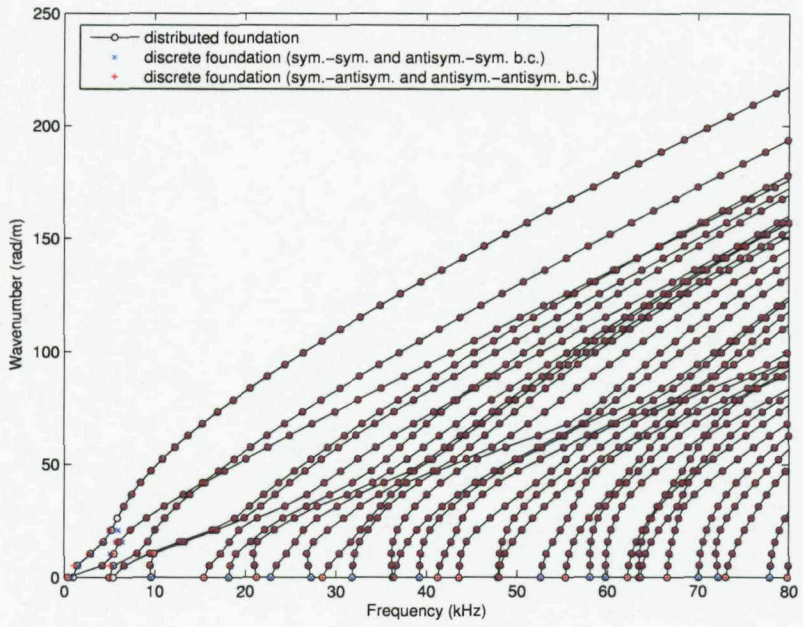

(a)

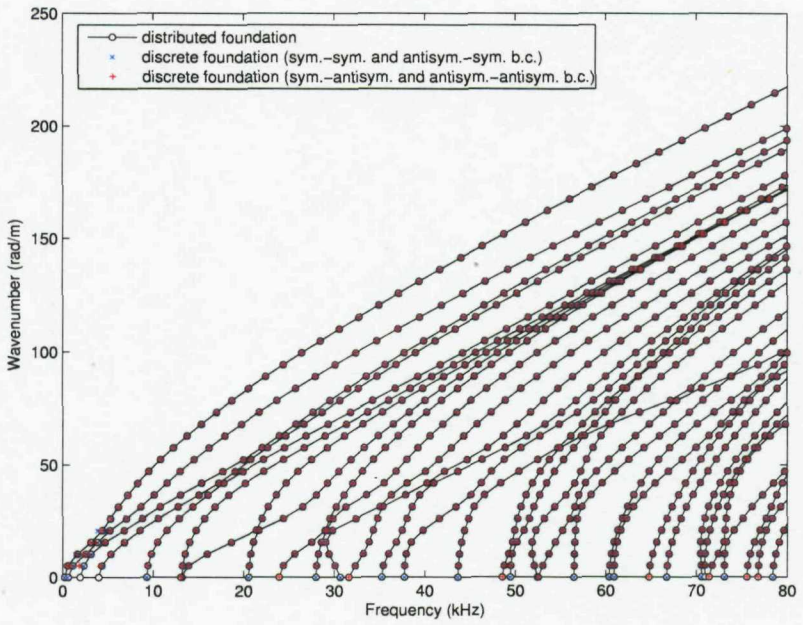

(b)

Fig. A.4. Comparison of frequency-wavenumber relations for the rail on distributed and discrete foundations for (a) the vertical and longitudinal modes, (b) the lateral and torsional modes.

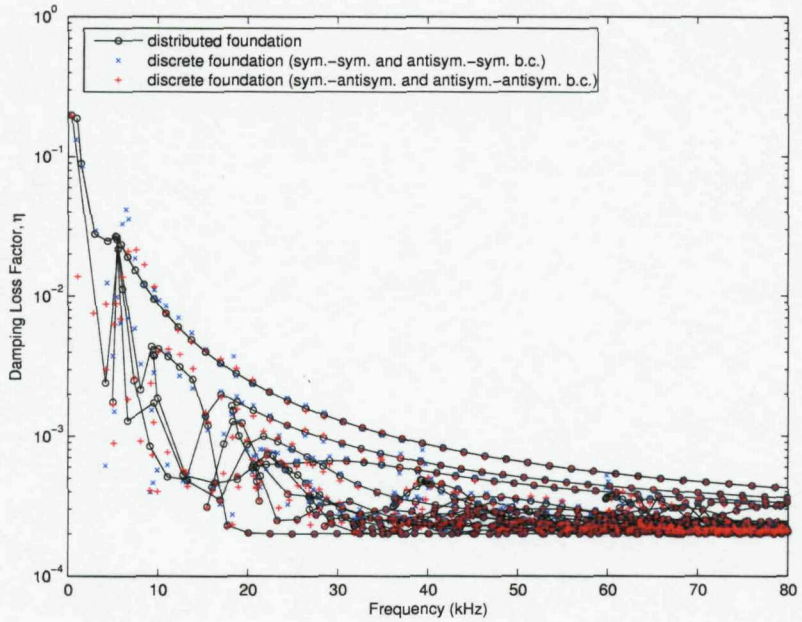

(a)

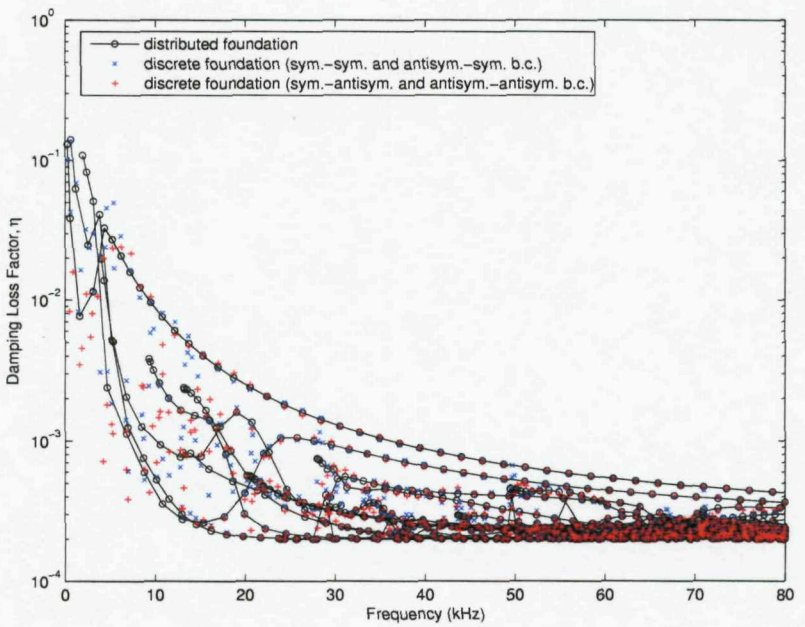

(b)

Fig. A.5. Comparison of damping loss factors for the rail on distributed and discrete foundations for (a) the vertical and longitudinal modes, (b) the lateral and torsional modes.

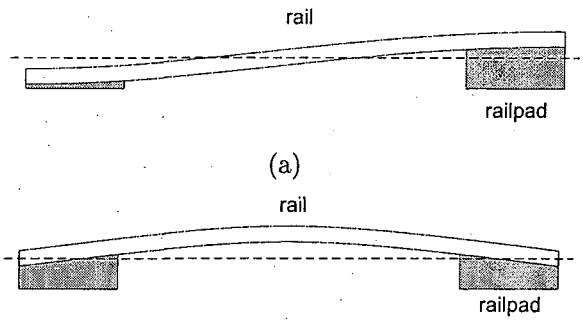

Fig. A.6. Schematic deformations of the rail pad at low frequency for (a) the antisymmetric-symmetric boundary condition for the model shown in Fig. A.1, (b) the symmetric-antisymmetric boundary condition for the model shown in Fig. A.1

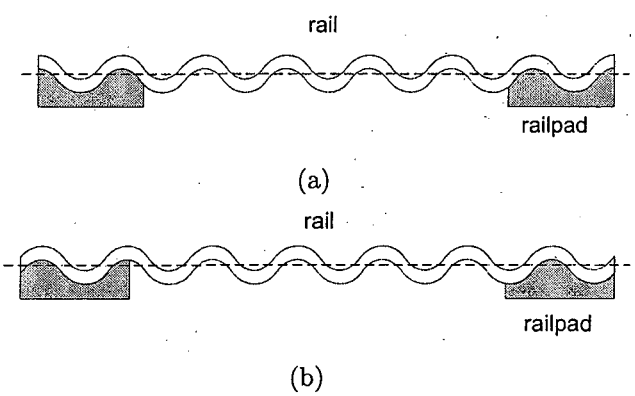

Fig. A.7. Schematic deformations of the rail pad at high frequency for (a) the antisymmetric-symmetric boundary condition for the model in Fig. A.1, (b) the symmetric-antisymmetric boundary condition for the model in Fig. A.1

Appendix B

Results Measured on the ISVR Test Track

B.1 Using an Impact Hammer

B.1.1 Time signals

The time signals measured along the rail of the ISVR track are shown below for the four different points in the rail cross-section.

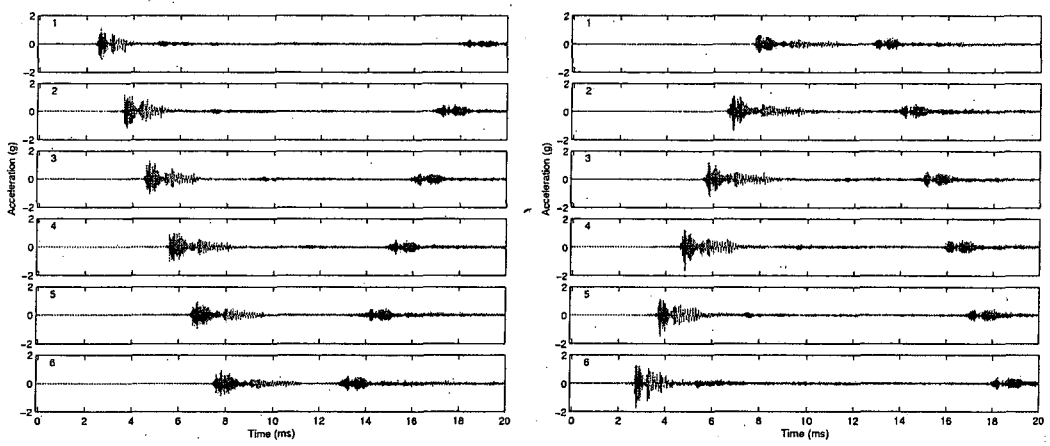

(a) (b)

Fig. B.1. An example of time signals measured at the top of the rail head along the rail in the vertical direction. (a) When the point 'a' was excited, (b) when the point 'b' was excited.

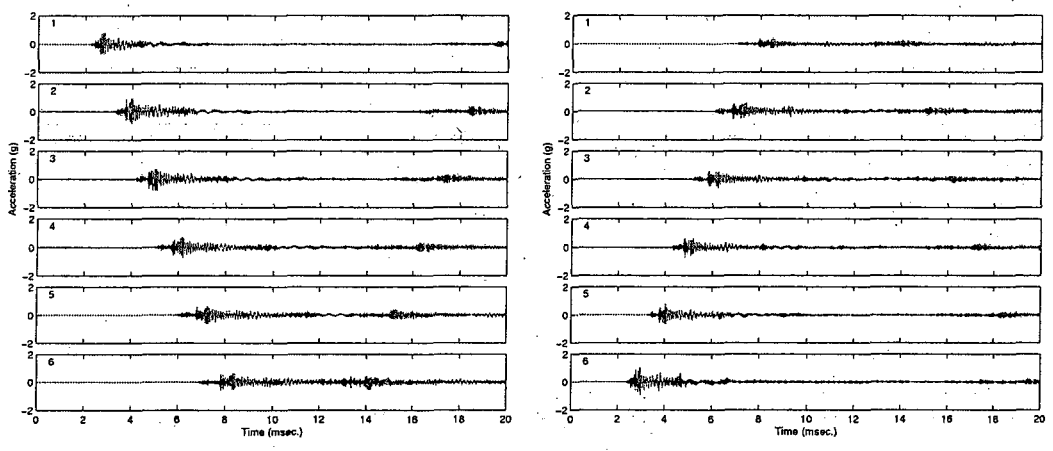

(a) (b)

Fig. B.2. An example of time signals measured at the side of the rail head along the rail in the lateral direction. (a) When the point 'a' was excited, (b) when the point 'b' was excited.

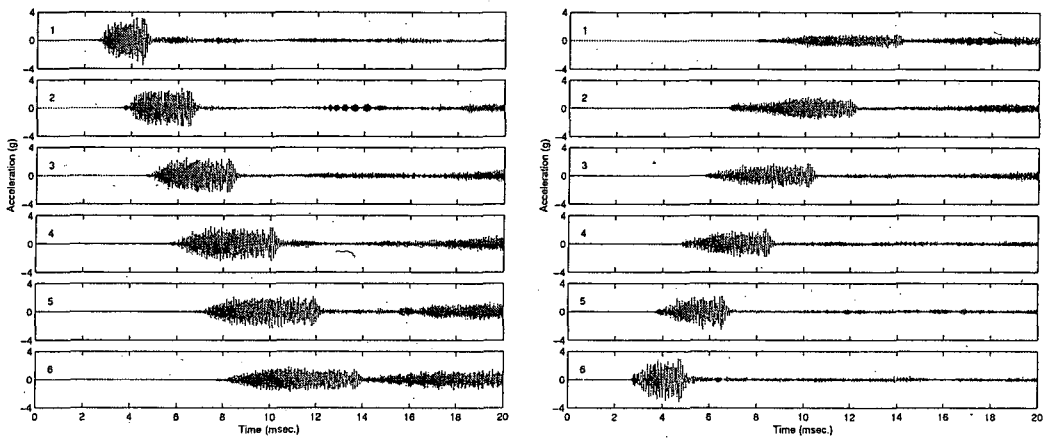

(a) (b)

Fig. B.3. An example of time signals measured at the middle of the web along the rail in the lateral direction. (a) When the point 'a' was excited, (b) when the point 'b' was excited.

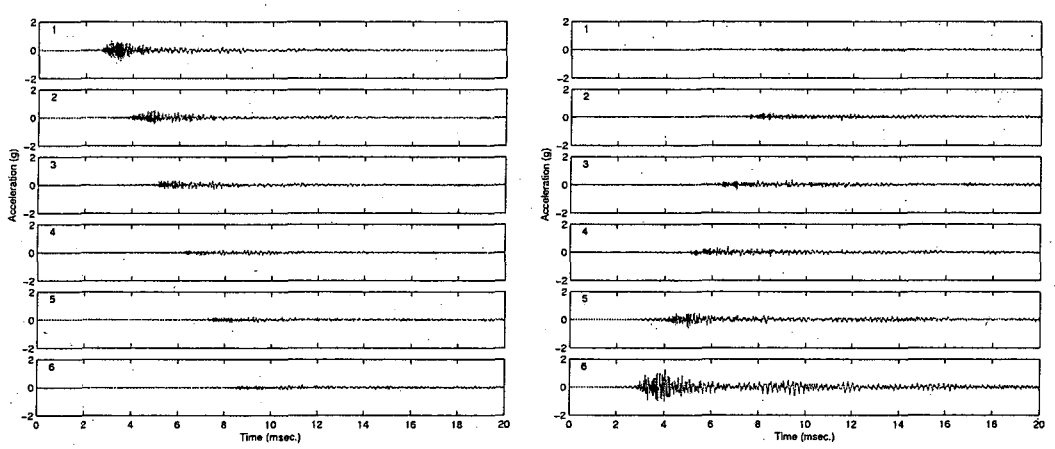

(a) (b)

Fig. B.4. An example of time signals measured at the top of the foot along the rail in the vertical direction. (a) When the point 'a' was excited, (b) when the point 'b' was excited.

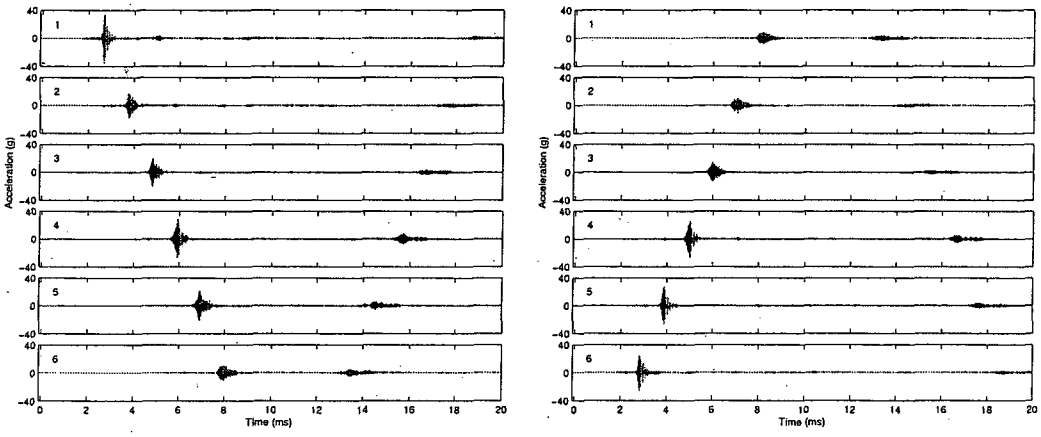

(a) (b)

Fig. B.5. An example of time signals measured at the top of the rail head along the rail in the longitudinal direction. (a) When the point 'a' was excited, (b) when the point 'b' was excited.

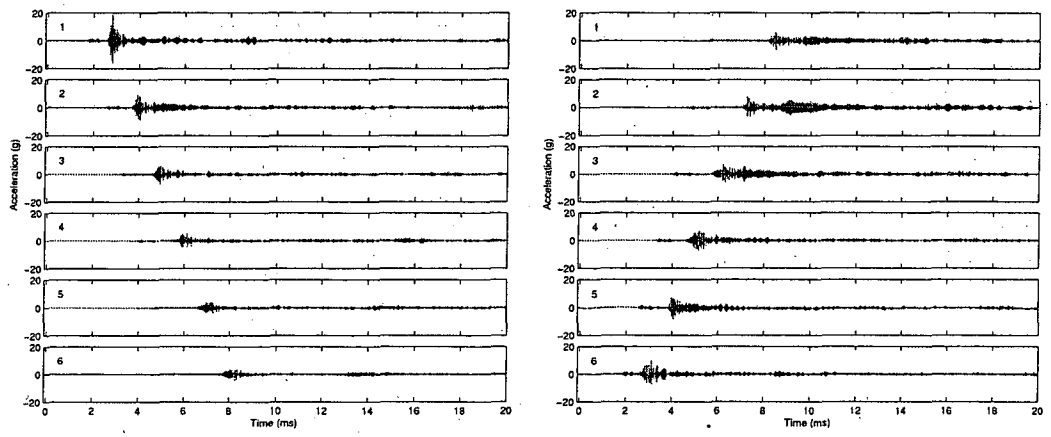

(a) (b)

Fig. B.6. An example of time signals measured at the side of the rail head along the rail in the longitudinal direction. (a) When the point 'a' was excited, (b) when the point 'b' was excited.

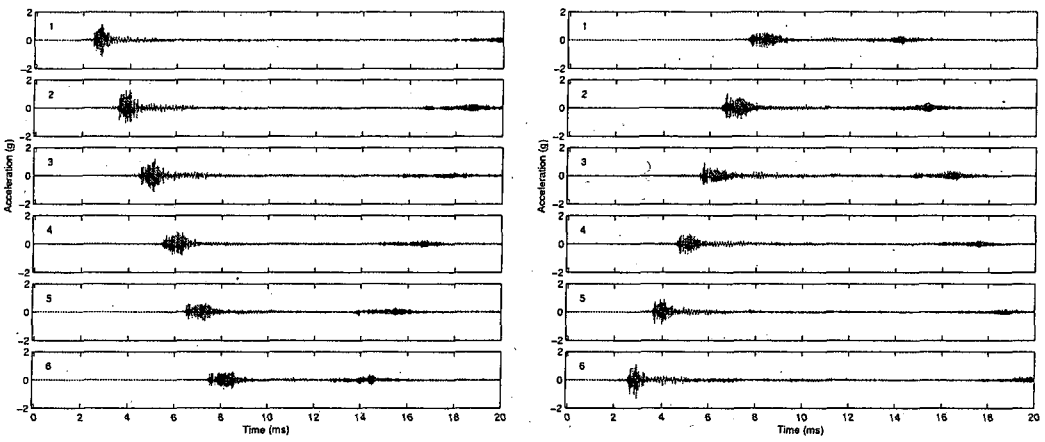

(a) (b)

Fig. B.7. An example of time signals measured at the underside of the rail head along the rail in the vertical direction. (a) When the point 'a' was excited, (b) when the point 'b' was excited.

B.1.2 Spectrograms

The averaged spectrograms along the rail in ISVR are shown below for the four different points in the rail cross-section.

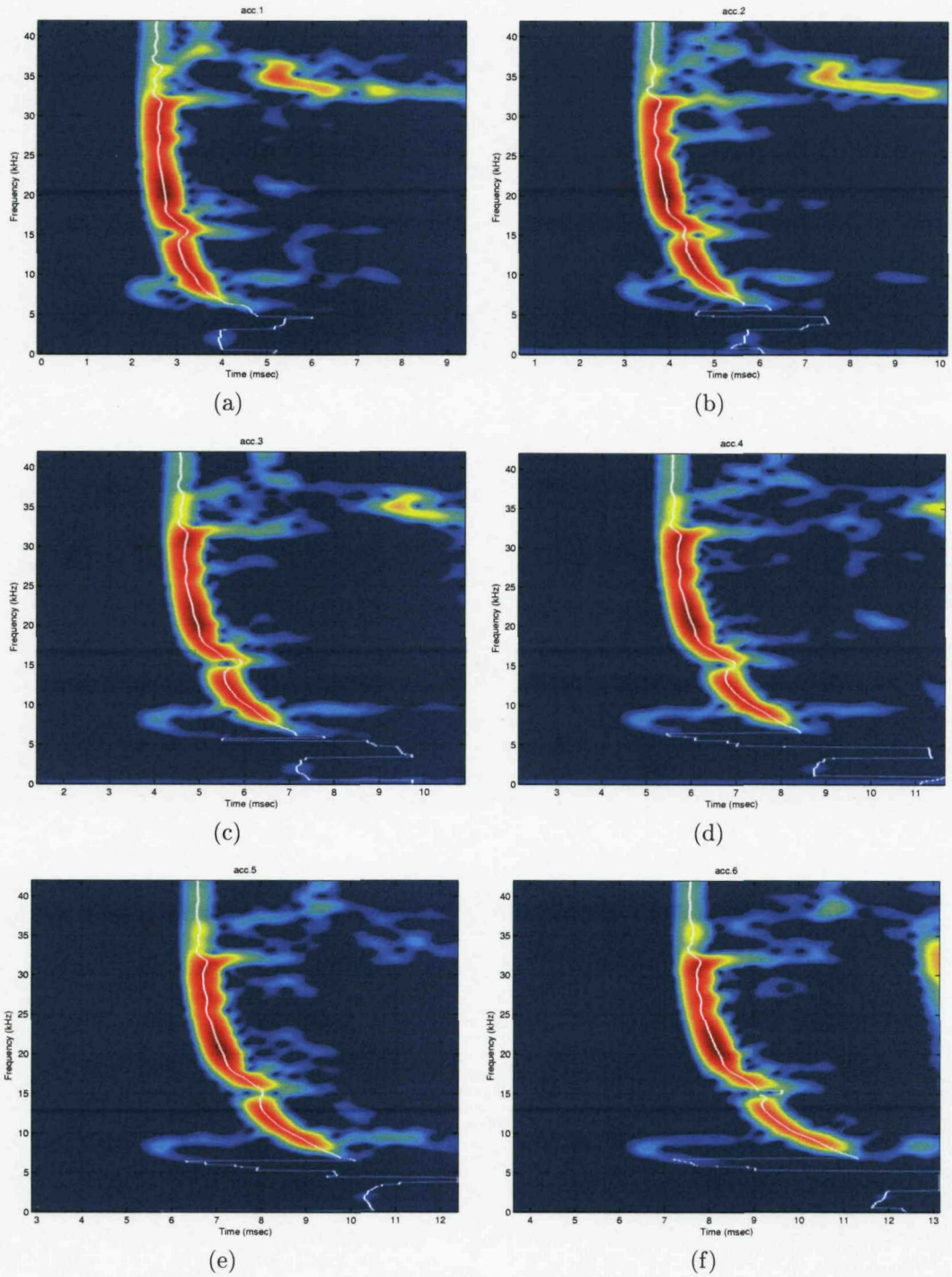

Fig. B.8. Spectrograms measured at the top of the rail head in the vertical direction at different positions along the rail by using impact hammer. White lines indicate wave ridges selected for the calculation of decay rate described in Section B.3.

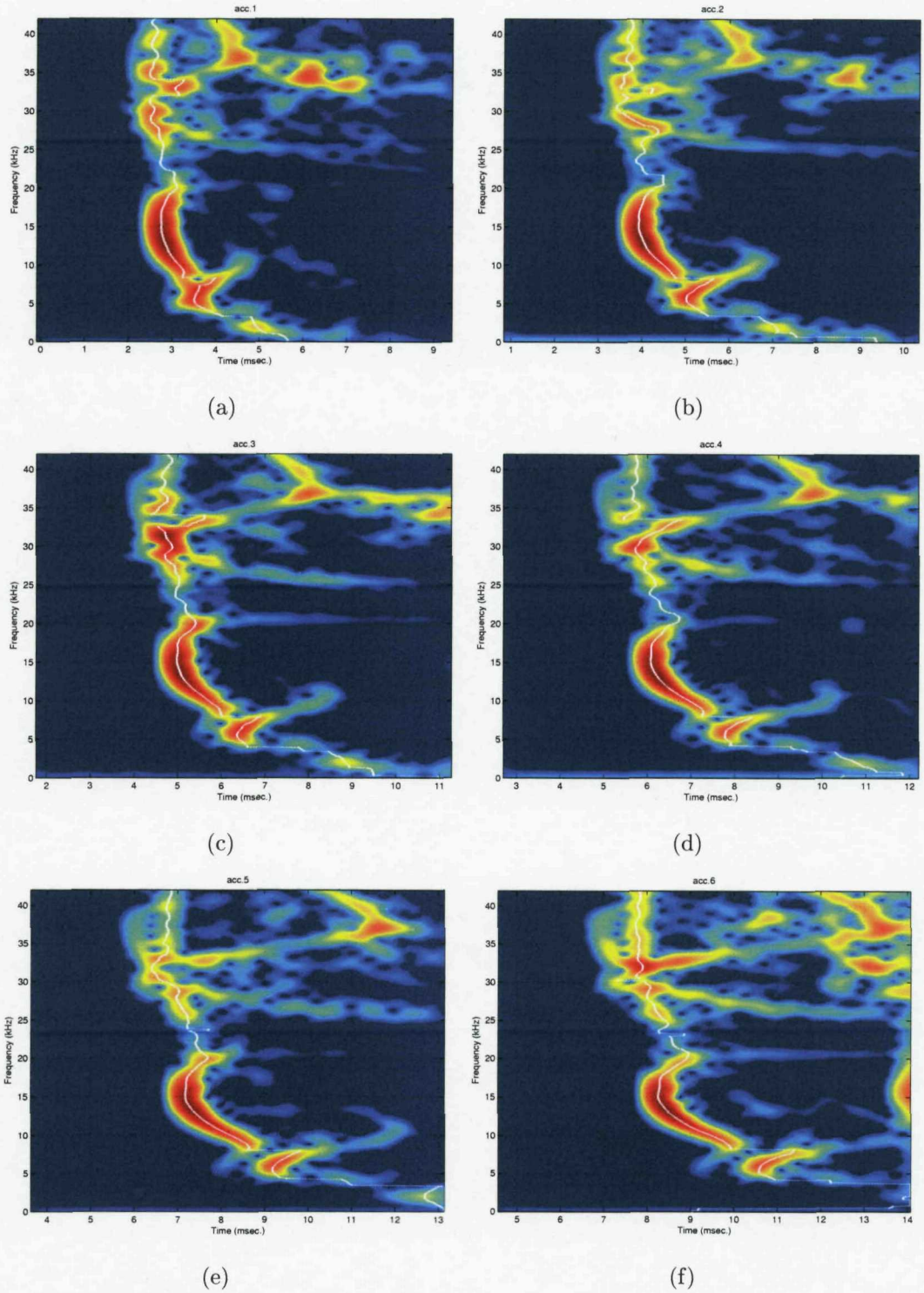

Fig. B.9. Spectrograms measured at the side of the rail head in the lateral direction at different positions along the rail by using impact hammer. White lines indicate wave ridges selected for the calculation of decay rate described in Section B.3.

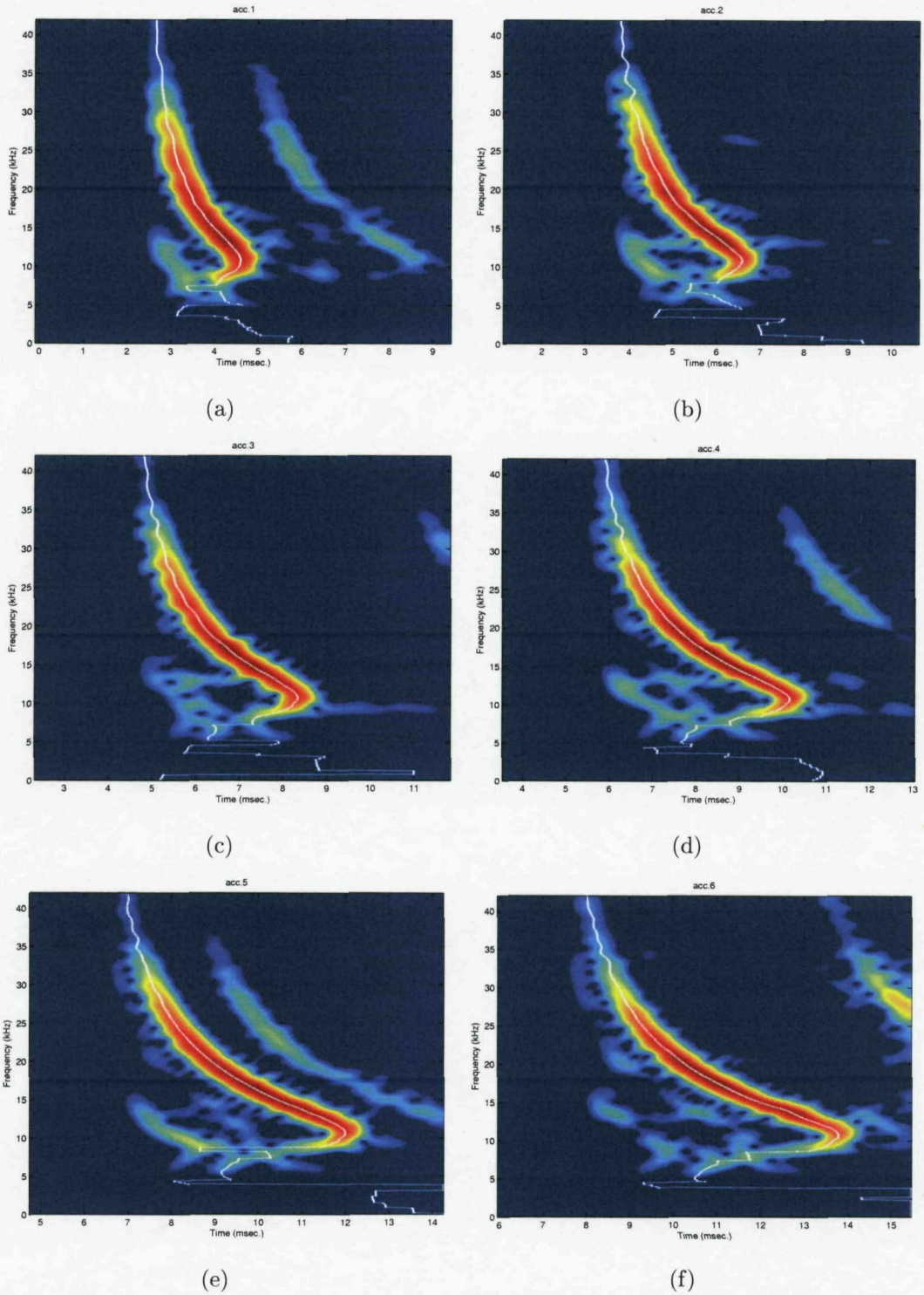

Fig. B.10. Spectrograms measured at the middle of the web in the lateral direction at different positions along the rail by using impact hammer. White lines indicate wave ridges selected for the calculation of decay rate described in Section B.3.

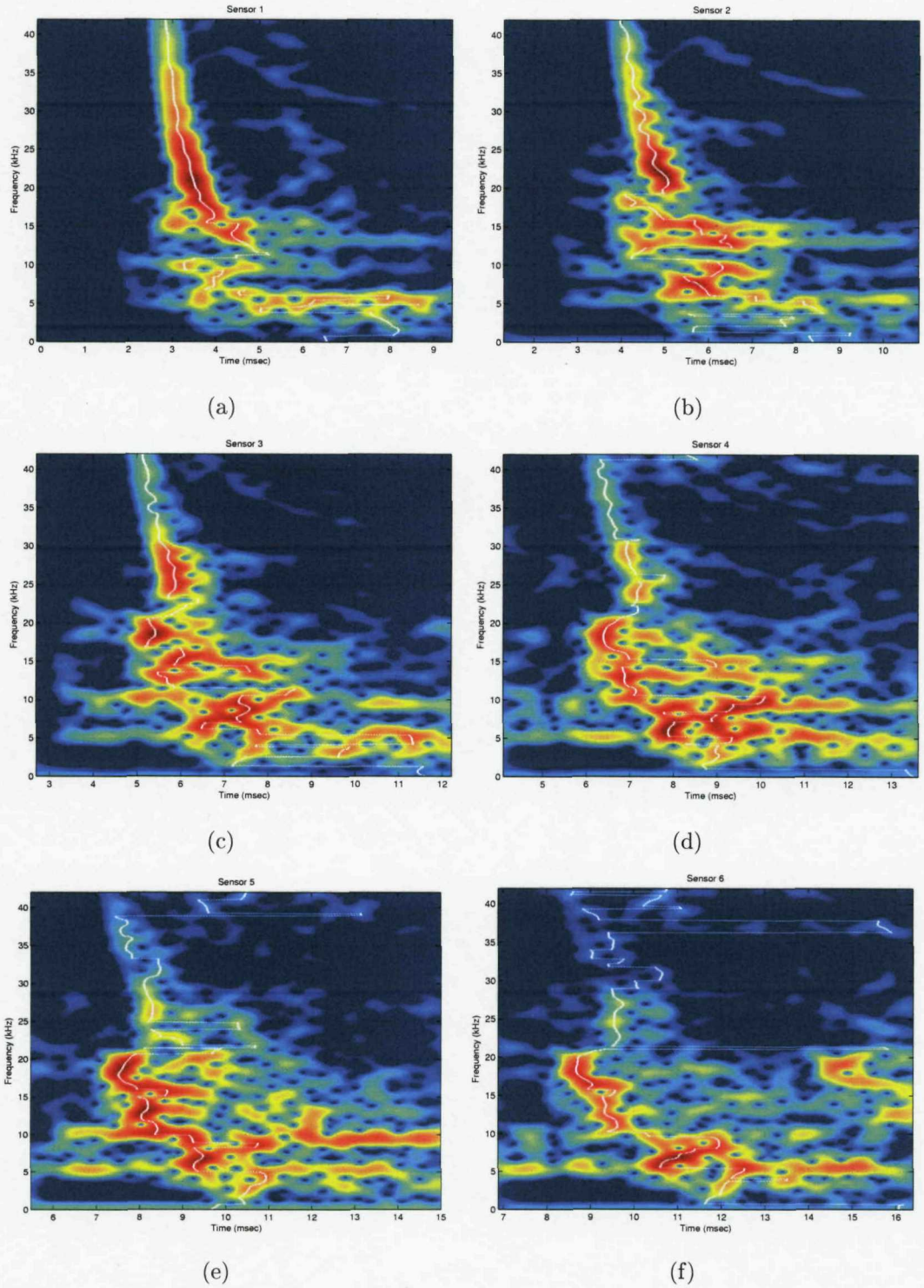

Fig. B.11. Spectrograms measured at the top of the rail foot in the vertical direction at different positions along the rail by using impact hammer. White lines indicate wave ridges selected for the calculation of decay rate described in Section B.3.

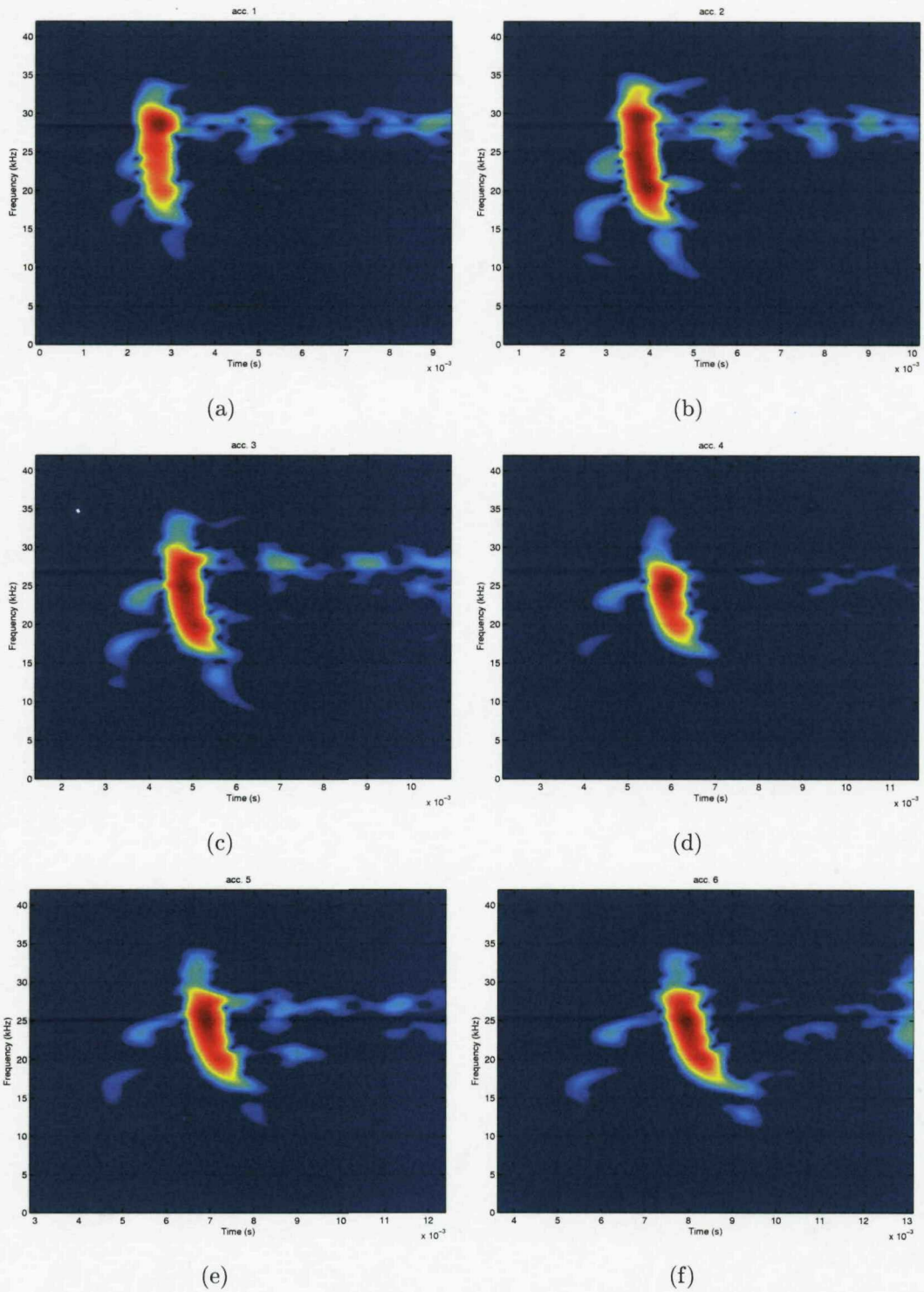

Fig. B.12. Spectrograms measured at the top of the rail head in the longitudinal direction at different positions along the rail by using impact hammer.

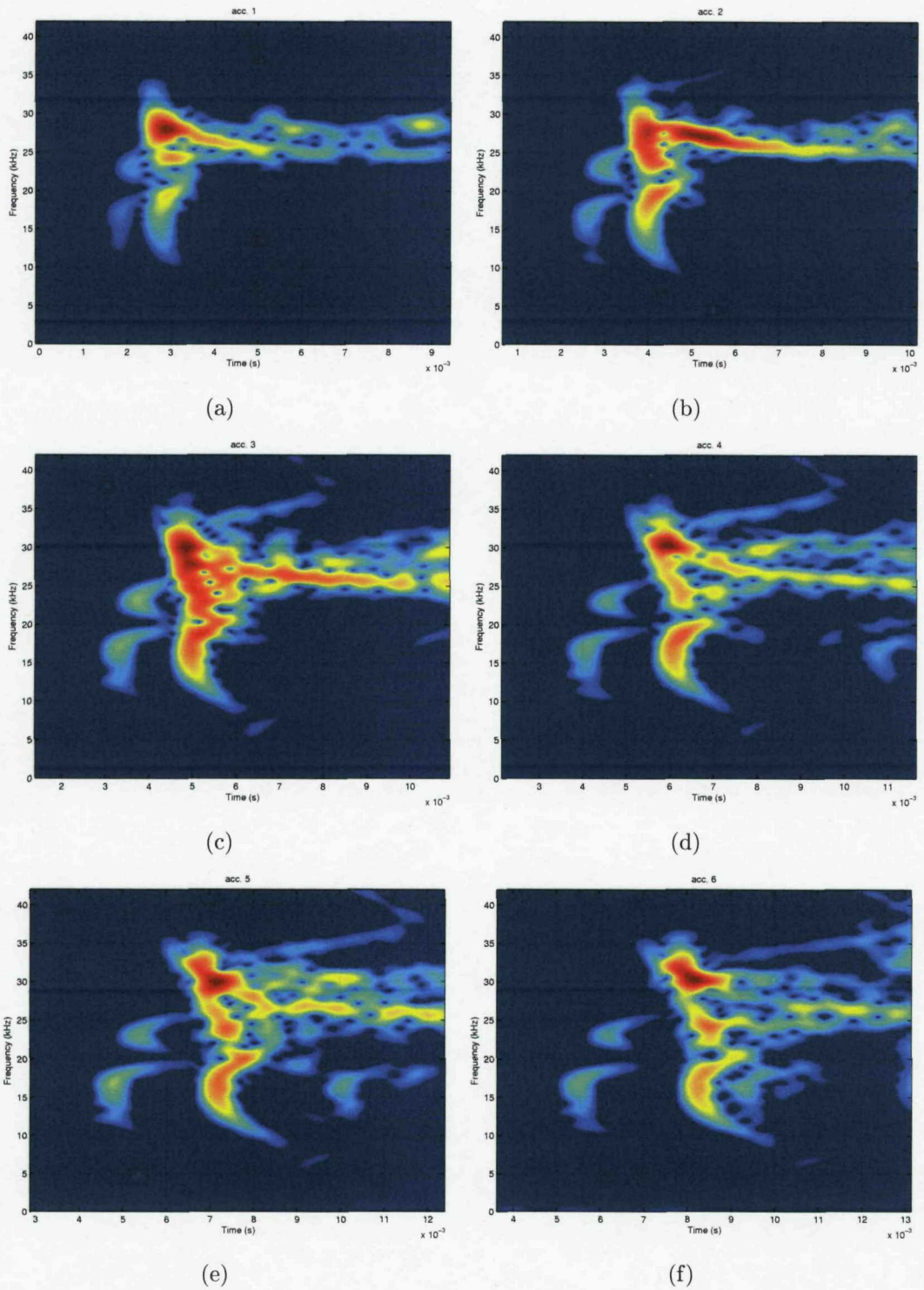

Fig. B.13. Spectrograms measured at the side of the rail head in the longitudinal direction at different positions along the rail by using impact hammer.

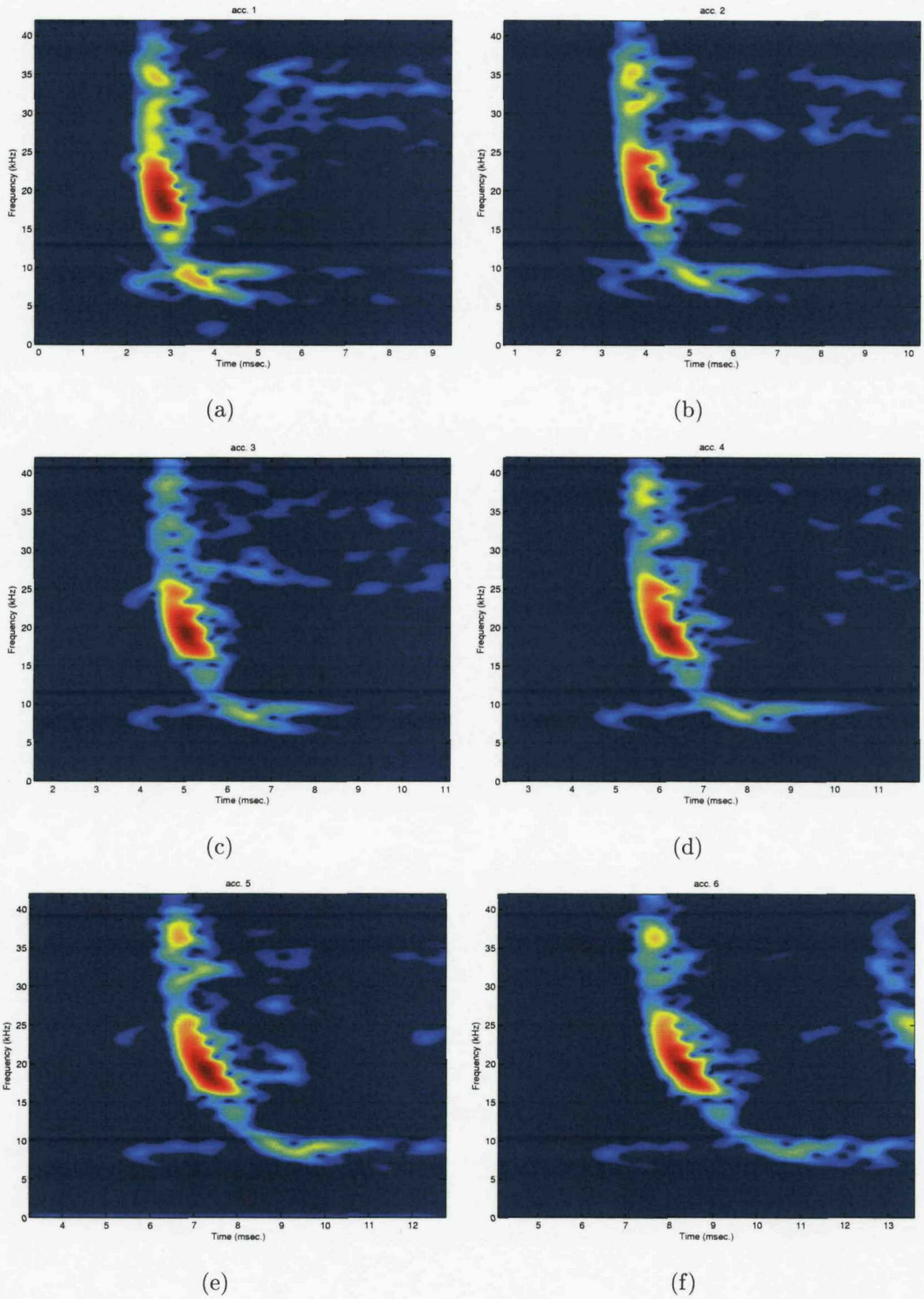

Fig. B.14. Spectrograms measured at the underside of the rail head in the longitudinal direction at different positions along the rail by using impact hammer.

B.2 Using Piezoceramic Transducers

B.2.1 Time signals

The time signals measured along the rail of the ISVR track are shown below for the three different measuring points in the rail cross-section.

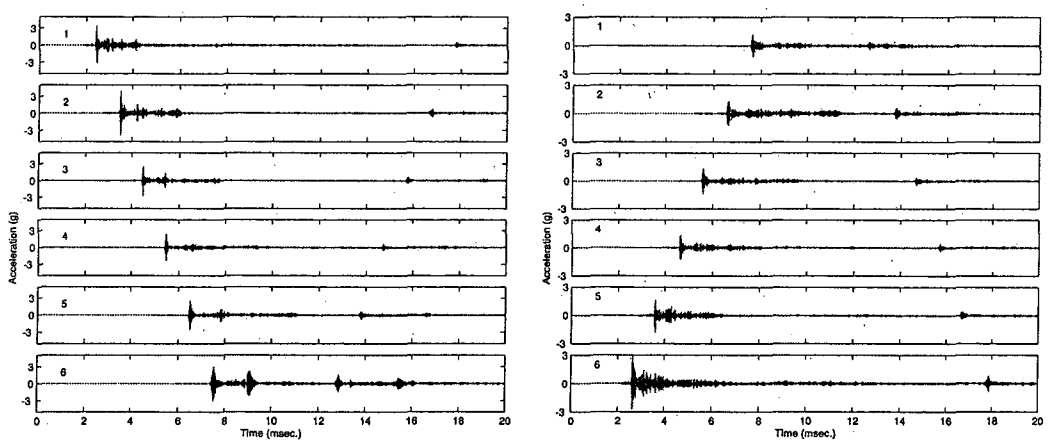

(a) (b)

Fig. B.15. An example of time signals measured at the top of the rail head along the rail in the vertical direction. (a) When the point 'a' was excited, (b) when the point 'b' was excited by a PZT.

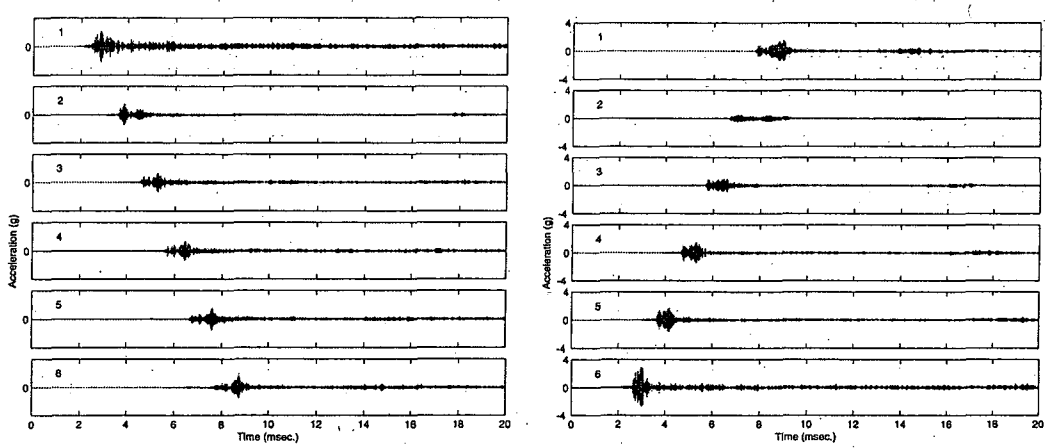

(a) (b)

Fig. B.16. An example of time signals measured at the side of the rail head along the rail in the lateral direction. (a) When the point 'a' was excited, (b) when the point 'b' was excited by a PZT.

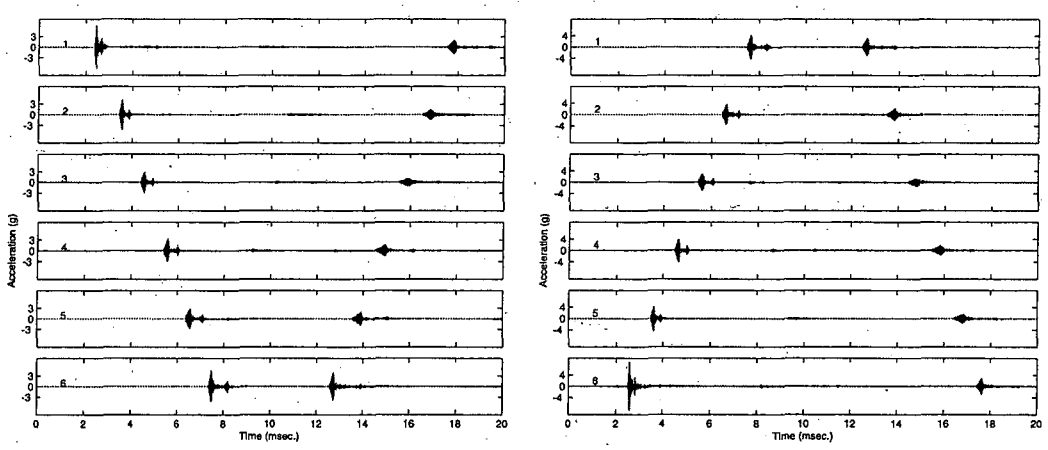

(a) (b)

Fig. B.17. An example of time signals measured at the middle of the web along the rail in the lateral direction. (a) When the point 'a' was excited, (b) when the point 'b' was excited by a PZT.

B.2.2 Spectrograms

The averaged spectrograms along the rail of the ISVR test track are shown below for the three different points in the rail cross-section.

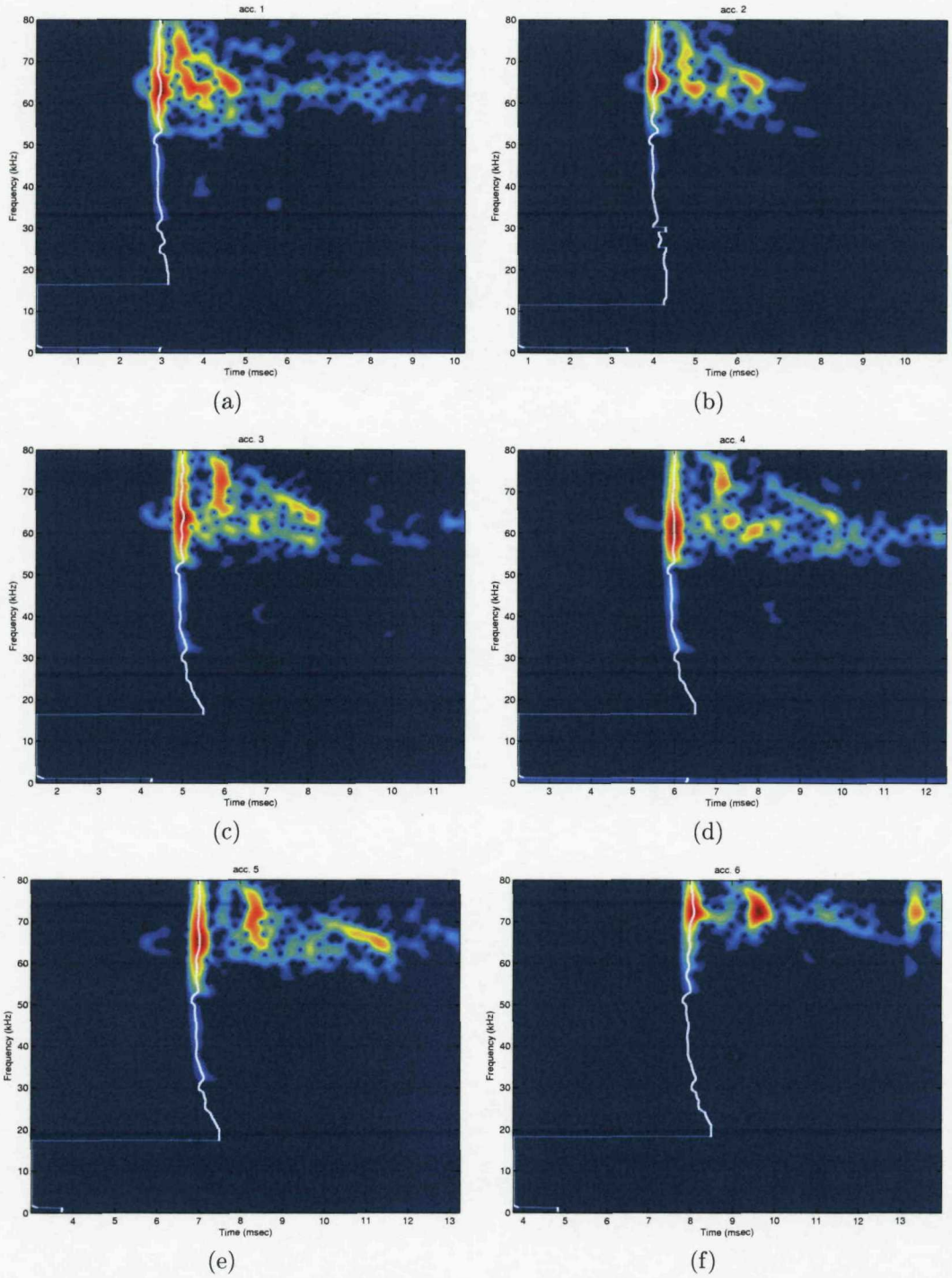

Fig. B.18. Spectrograms measured at the top of the rail head in the vertical direction at different positions along the rail by using PZT. White lines indicate wave ridges selected for the calculation of decay rate described in Section B.3.

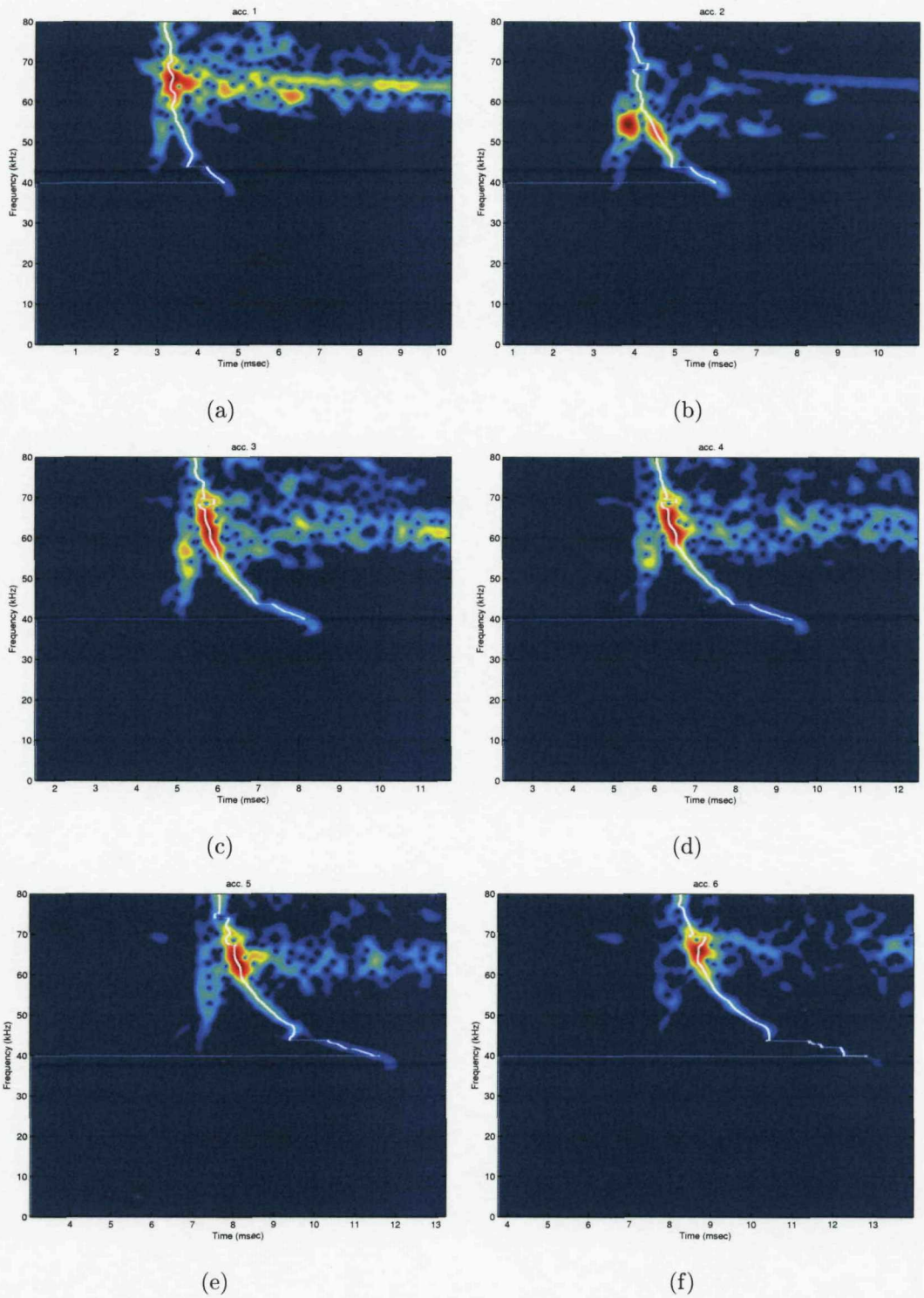

Fig. B.19. Spectrograms measured at the side of the rail head in the lateral direction at different positions along the rail by using PZT. White lines indicate wave ridges selected for the calculation of decay rate described in Section B.3.

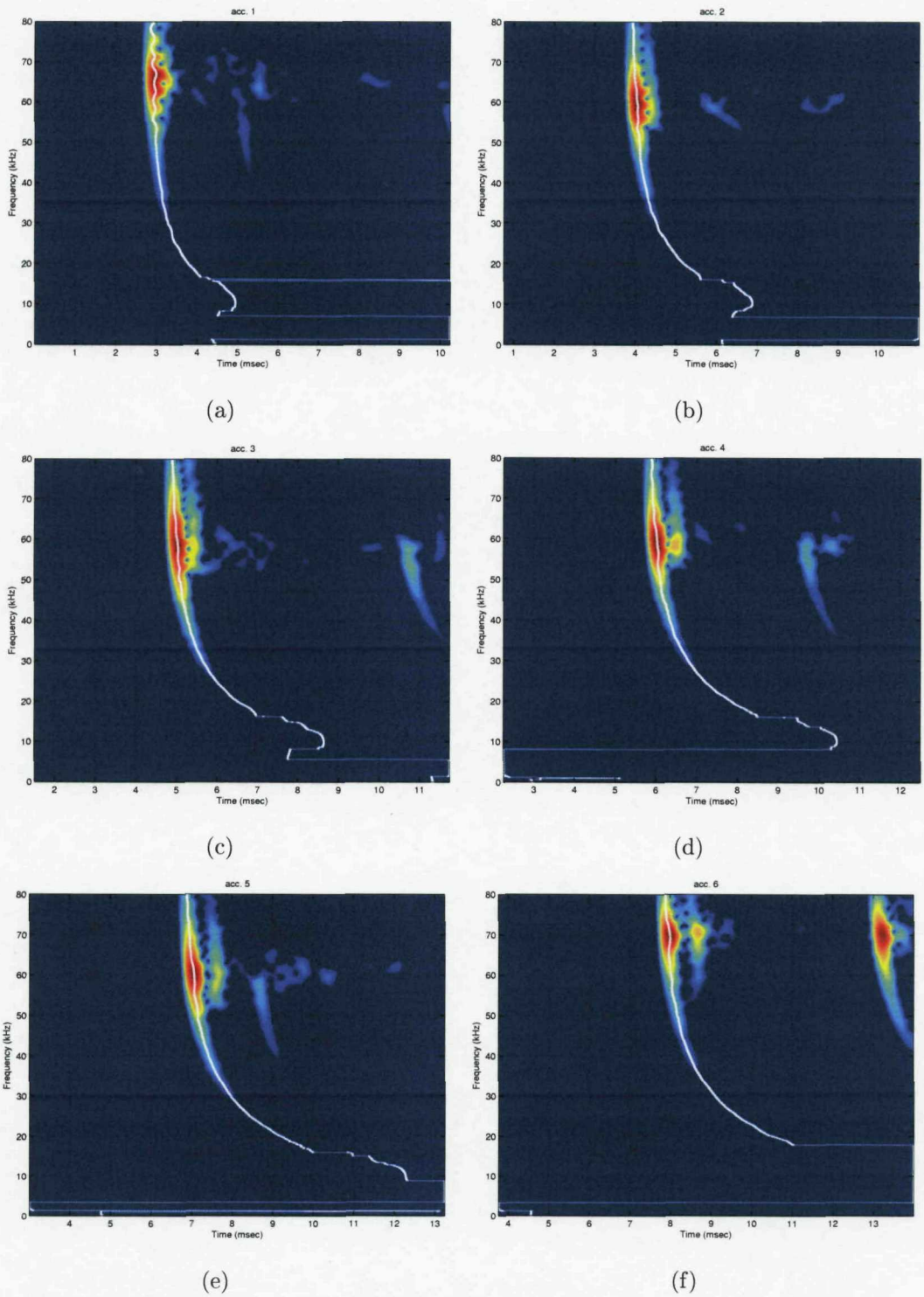

Fig. B.20. Spectrograms measured at the middle of the web in the lateral direction at different positions along the rail by using PZT. White lines indicate wave ridges selected for the calculation of decay rate described in Section B.3.

B.3 Extraction of Decay Rates

It seems that the ISVR test track is not long enough to measure decay rates reliably, particularly for the slowly decaying waves of interest. In this section, nevertheless, it is attempted to extract the decay rates of the main waves propagating from the data measured. To detect waves propagating along the rail in the measurement, multiple sensors were attached by means of the beeswax; this gives a less reliable response at high frequencies. Therefore, sensor calibration is an important factor which can affect the levels of decay rates determined. In order to eliminate each sensor's frequency-dependent sensitivities, the same measurements were performed twice by exciting at both ends of the rail as depicted in Fig. B.21. In the measurement using PZTs, the excitation at both ends of the rail was applied in the same manner. Calibrated decay rates between any two sensors can be obtained from the two level differences between them created by the excitations at both ends of the rail.

The analysis procedure used for the decay rate extraction is briefly presented in Fig. B.22 as a flow chart. Since the rail was excited at both its ends, i.e., a and b as shown in Fig. B.21, the decay rates between any two sensors i and j, can be predicted by

$$\Delta_{ij}(f) = \frac{1}{2d_{ij}}\left[\{A_{ai}(f) - A_{aj}(f)\} + \{A_{bj}(f) - A_{bi}(f)\}\right] \tag{B.1}$$

where A_{aj} denotes the output level in dB measured at point j when the rail is excited

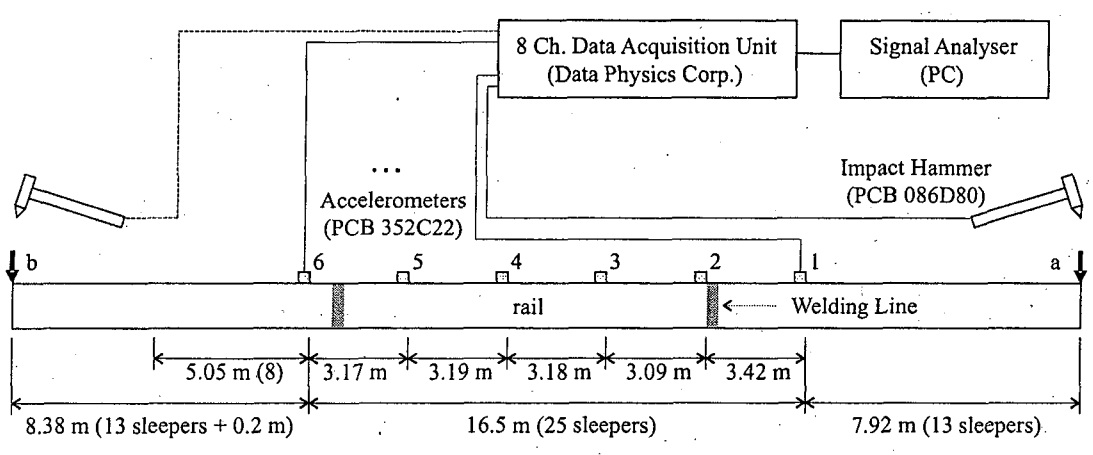

(a)

Fig. B.21. Experimental setup for decay rate extraction using an impact hammer.

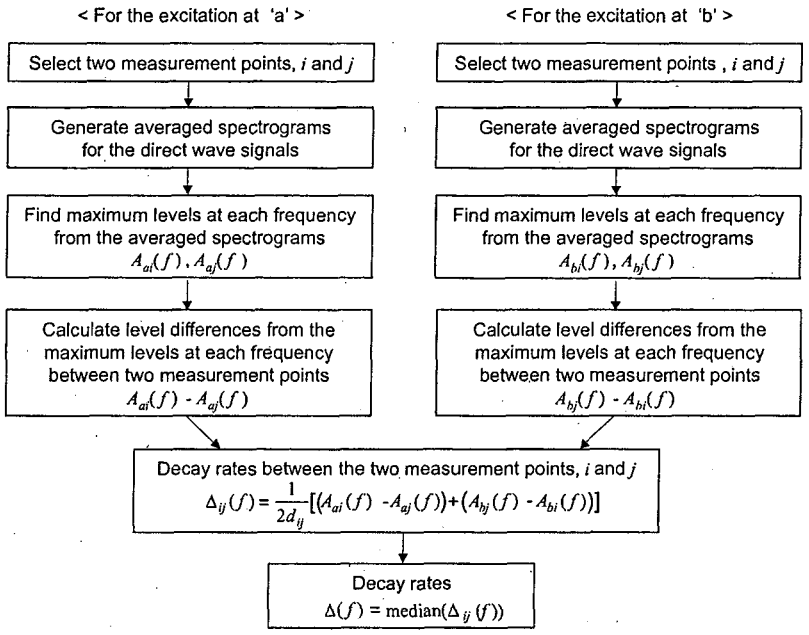

Fig. B.22. Flow chart for the decay rate calculation

at a, similarly for b and d_{ij} is the distance between two sensors i and j. In detail, the uncalibrated output level measured at position i, A_{ai}, can be expressed as a sum of the calibrated output, A^c_{ai}, and the calibration error, C_i, in dB scale. Then Eq. (B.1) can be rewritten as

$$\begin{aligned}\Delta_{ij}(f) &= \frac{1}{2d_{ij}}\left[(A^c_{ai} + C_i) - (A^c_{aj} + C_j) + (A^c_{bj} + C_j) - (A^c_{bi} + C_i)\right] \\ &= \frac{1}{2d_{ij}}\left[(A^c_{ai} - A^c_{bi}) + (A^c_{bj} - A^c_{aj})\right] . \end{aligned} \tag{B.2}$$

Therefore, it is clear from Eq. (B.1) and Eq. (B.2) that any calibration error in sensor i is eliminated by taking the level difference $A_{ai} - A_{bi}$. For instance, Fig. 6.6(b) shows that the accelerometer located at position 1 gives a smaller response to the same input signal than the others. However, these characteristics of each sensor are eliminated in the process of the decay rate extraction. Finally the decay rate was determined by means of the median of Δ_{ij} for different combinations i and j.

It should be noted that, even for the maximum distance between sensors, 16.5 m, decay rates of the order of 0.06 dB/m correspond to a 1 dB attenuation in that distance, which is likely to be at the limit of what can be measured reliably. Also to reduce the measurement error, the decay rates calculated from two adjacent sensors are neglected because the distance between them (i.e., about 3 m) does not seem to

be long enough.

In order to be able to predict a propagation distance from the measurement spectrograms, the wave which has the lowest decay rate at each frequency has to be identified. As seen in the spectrograms in sections B.1 and B.2, however, there are several waves which have different decay rates. The waves which are expected to have the lowest decay rate are selected from the spectrograms on the basis of comparison with the WFE analysis results. For instance, the simulated decay rates in Fig. B.23(a) indicate that the green and red coloured waves have the lowest decay rates in the range 7 kHz to 15 kHz and 15 kHz to 60 kHz, respectively. The corresponding group velocities of these waves predicted are presented in Fig. 6.9(b). By comparing them with the measured group velocity diagrams, the waves having the slowest decay rates were selected from the measured results. The selected wave ridges for the calculation of decay rate are marked in the spectrograms in sections B.1 and B.2 with white lines. Below about 10 kHz, the ridge was created by simply picking the maximum values so it will be less reliable.

The decay rates extracted from the data measured on the ISVR test track are shown in Fig. B.23. In this figure, the decay rates obtained from the experiment using PZT were confined to frequencies above 30 kHz (Fig. B.23(a) and (c)) and 40 kHz (Fig. B.23(b)), because they will be less accurate at low frequencies. For the same reason, in frequencies between 30 kHz and 42 kHz where two decay rate results are present, the decay rates measured from the impact hammer test are expected to be more reliable than those obtained by using PZTs.

It can be seen from Fig. B.23(a) that the minimum decay rate of 0.04 dB/m seems to occur between 20 kHz and 35 kHz at the top of the rail head. Also Fig. B.23(b) shows that the minimum decay rate of 0.05 dB/m seems to appear between 20 kHz and 40 kHz at the side of the rail head. Note that the measured minimum decay rate, 0.02 dB/m, shown around 25 kHz does not seem to be reliable because the decay rate at that frequency would be vulnerable to noise as anticipated from spectrograms measured. In Fig. B.23(c), the measured and predicted decay rates are shown up to 80 kHz at the middle of the web. According to the experimental results, the measured minimum decay rate on the web is 0.07 to 0.08 dB/m and occurs at around 20 kHz and around 45 kHz.

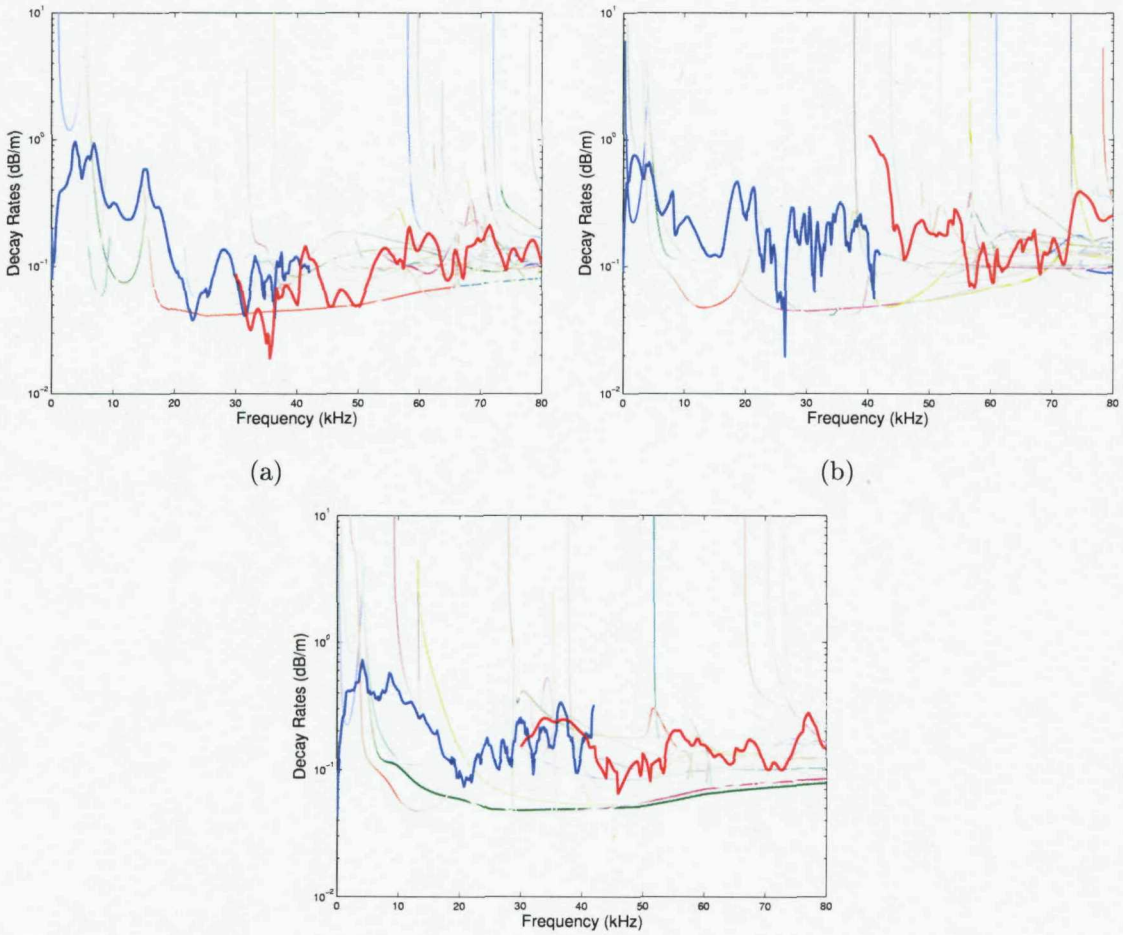

Fig. B.23. Comparison of measured and predicted decay rates (a) at the top of the rail head in the vertical direction, (b) at the side of the rail head in the lateral direction, (c) at the middle of the web in the lateral direction. The solid blue line was obtained from the impact hammer test and the solid red line was obtained from the measurement using the PZT, the other lines show the predicted decay rates produced by the WFE analysis.

As revealed in this figure, the measured decay rates present a very similar trend to the simulated ones but there are some variations in levels between them. That is, the measured decay rate is higher than the predicted ones in general. Moreover the measurements show considerable variation with frequency not found in the simulation. Accordingly, it can be said that the decay rates measured at the ISVR test track seem to be less reliable because the ISVR test track is too short to measure low decay rates precisely.

Appendix C

Results Measured on an Operational Track

C.1 Time Signals

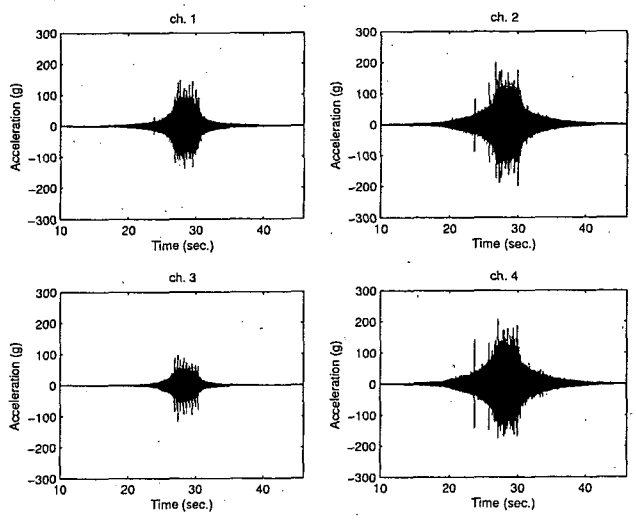

(a)

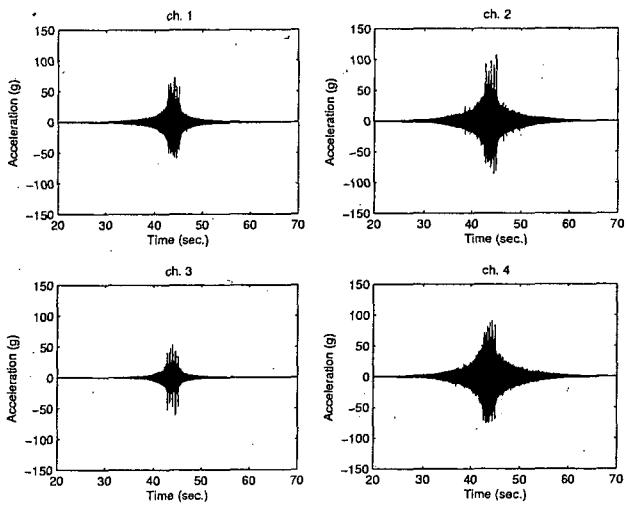

(b)

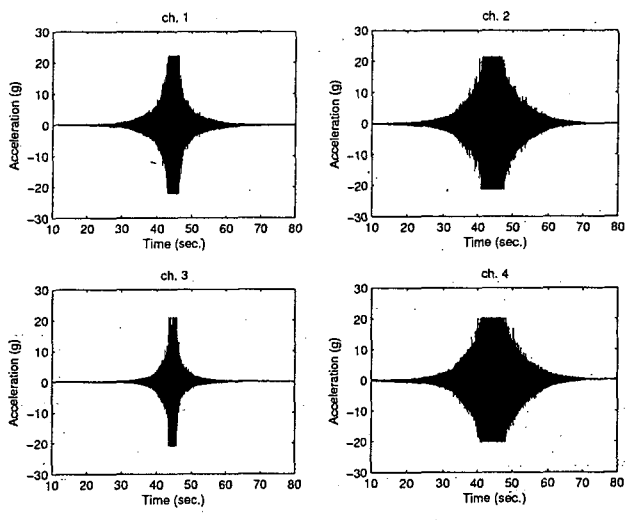

(c)

Fig. C.1. Time signals measured for (a) train 1, (b) train 2, (c) train 3.

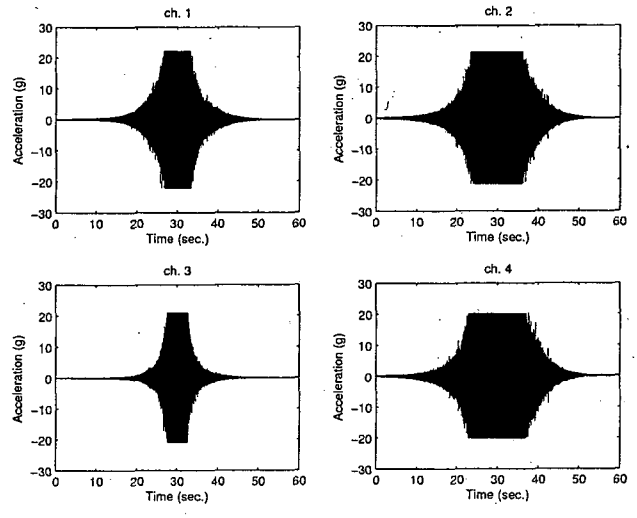

(a)

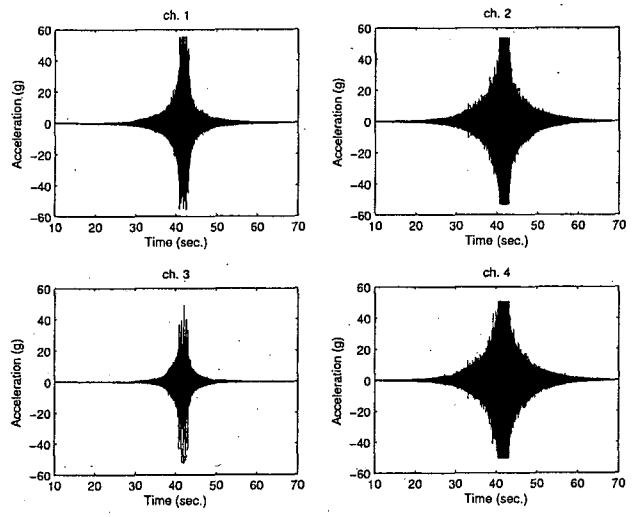

(b)

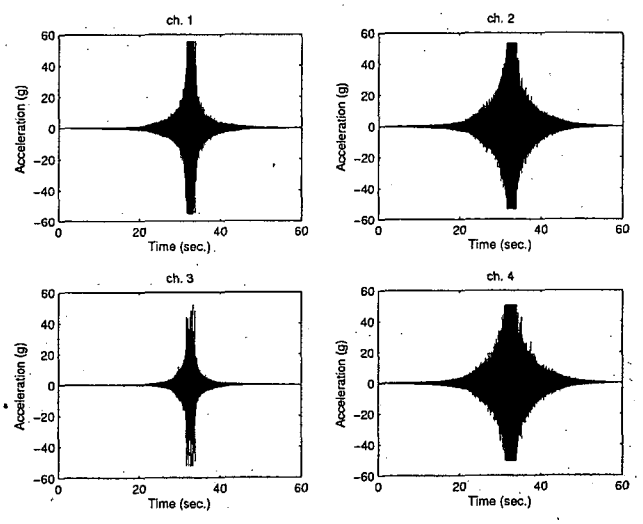

(c)

Fig. C.2. Time signals measured for (a) train 4, (b) train 5, (c) train 6.

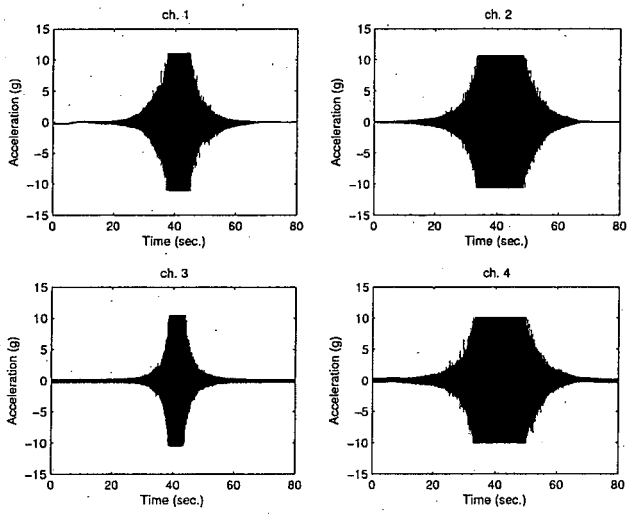

(a)

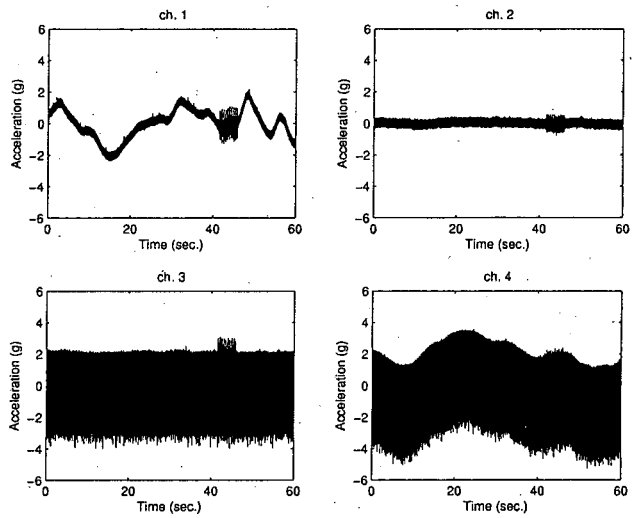

(b)

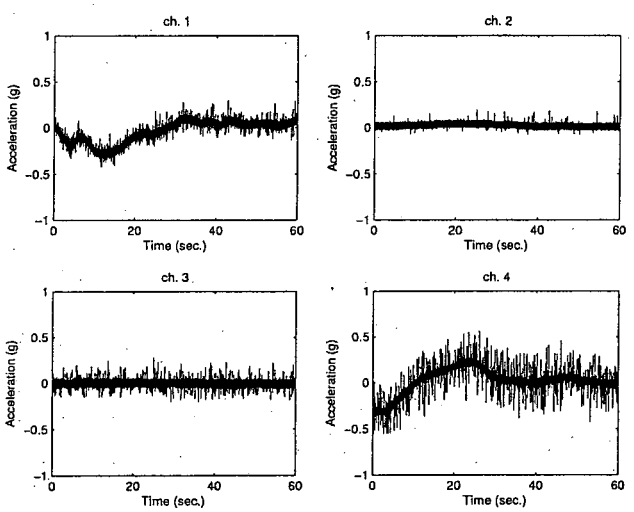

(c)

Fig. C.3. Time signals measured for (a) train 7, (b) ambient 1, (c) ambient 2.

C.2 Spectrograms

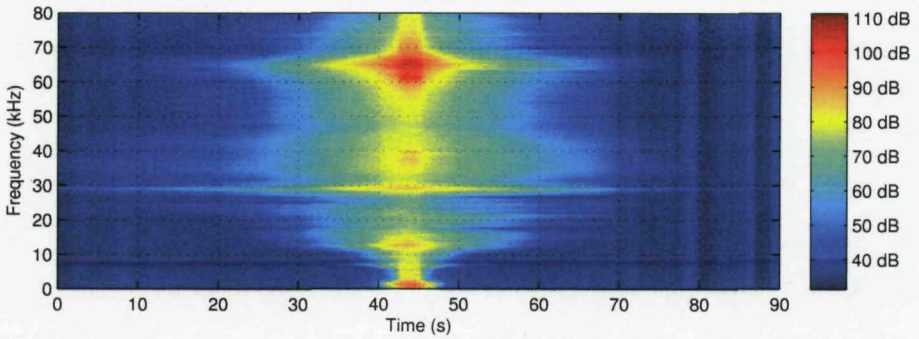

(a)

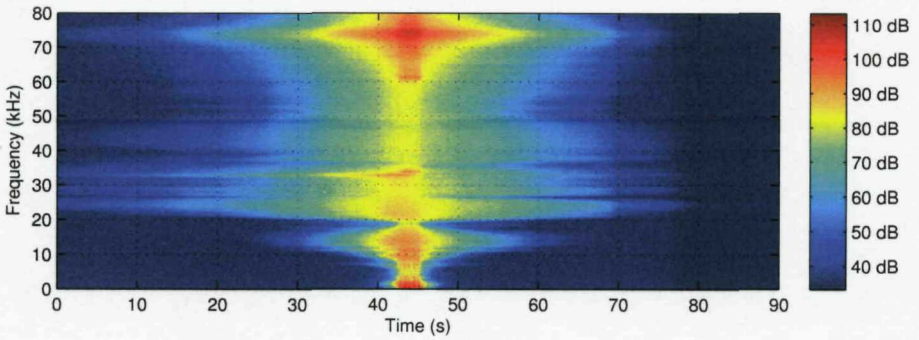

(b)

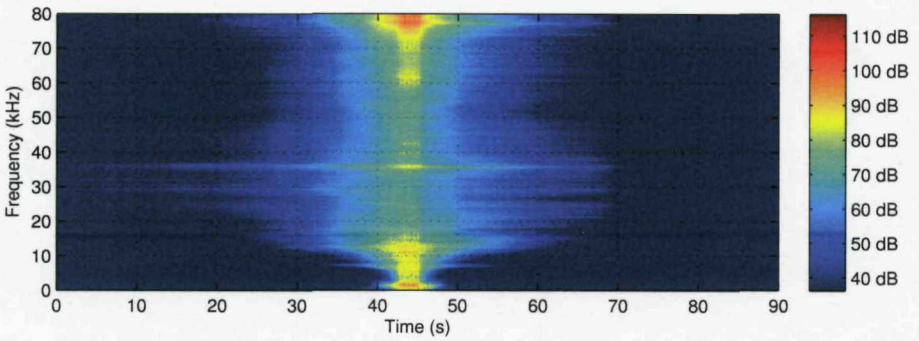

(c)

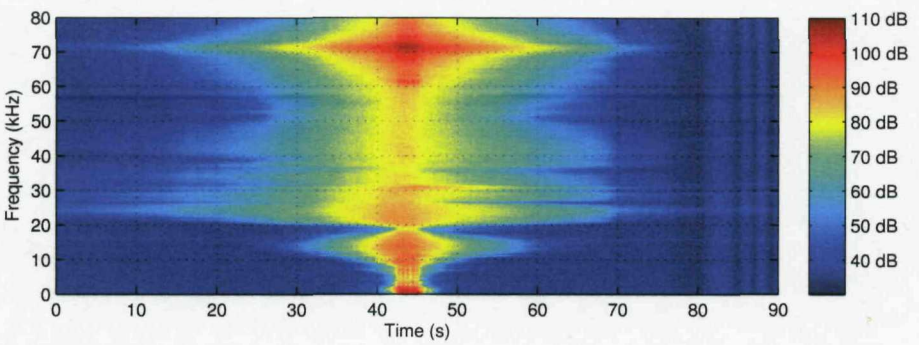

(d)

Fig. C.4. Spectrograms for train 2. (a) At the side of the rail head (ch. 1), (b) at the underside of the rail head (ch. 2), (c) at the middle of the web (ch. 3) and (d) at the underside of the rail head (ch. 4).

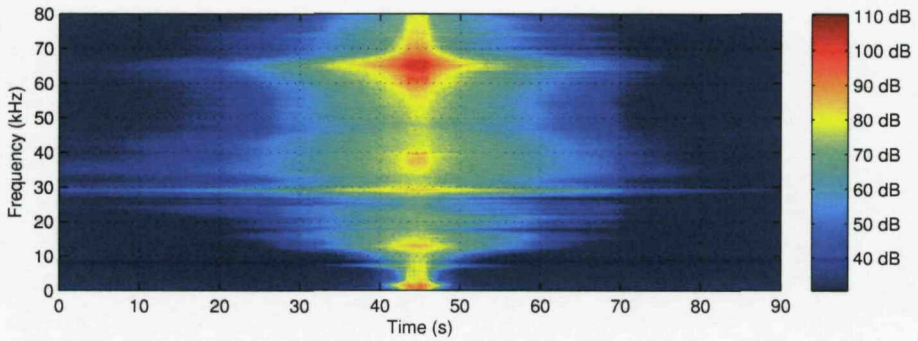

(a)

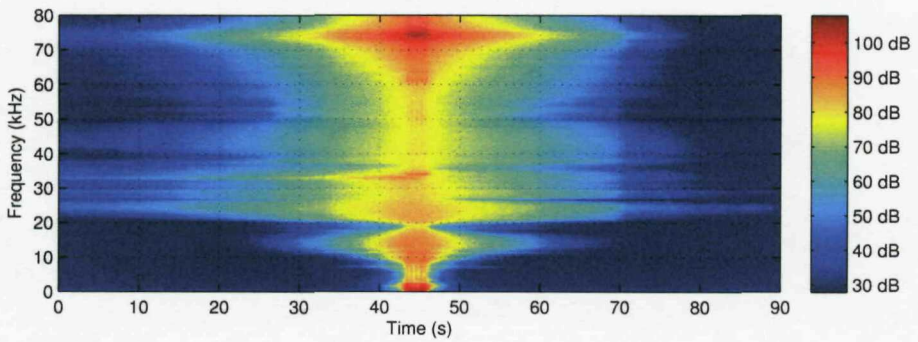

(b)

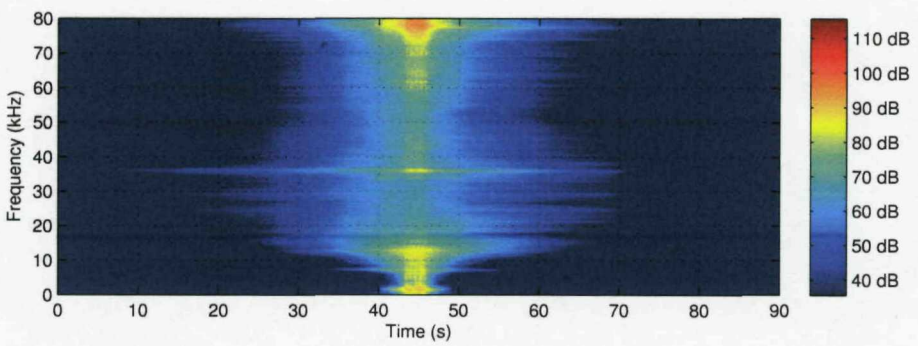

(c)

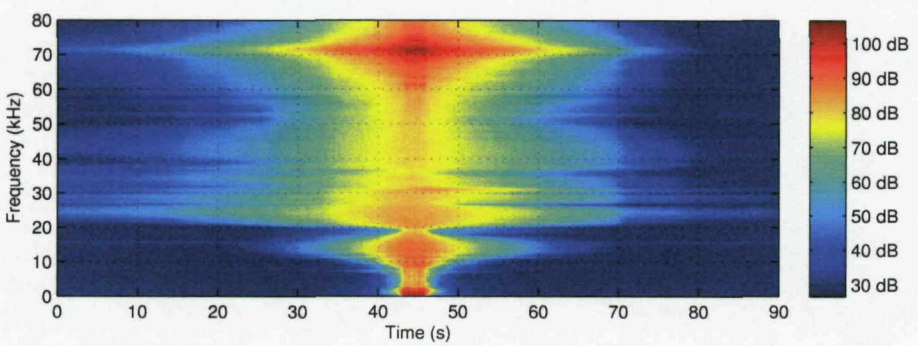

(d)

Fig. C.5. Spectrograms for train 3. (a) At the side of the rail head (ch. 1), (b) at the underside of the rail head (ch. 2), (c) at the middle of the web (ch. 3) and (d) at the underside of the rail head (ch. 4).

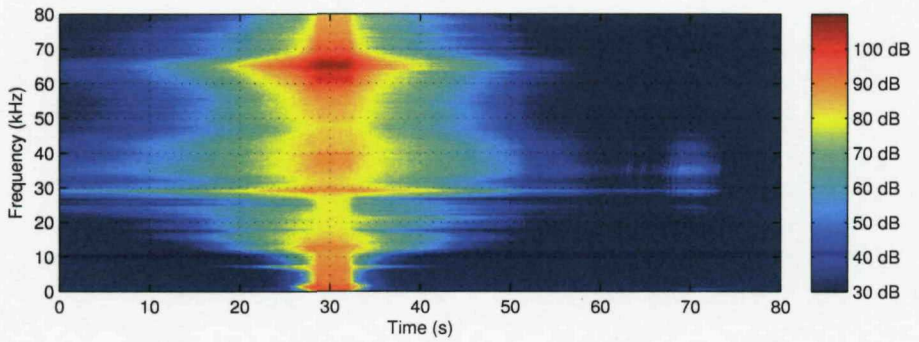

(a)

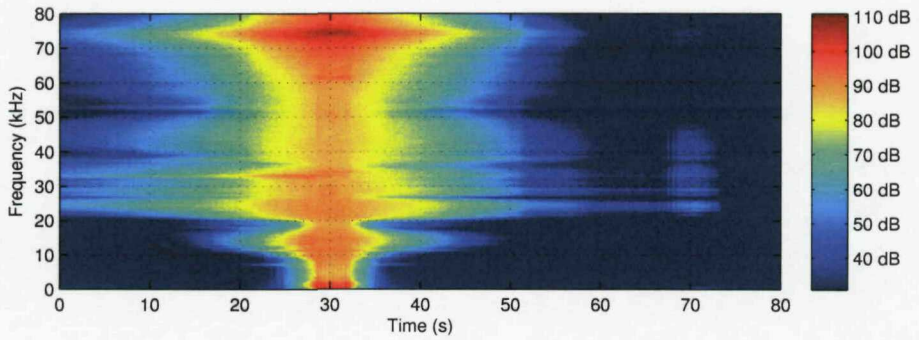

(b)

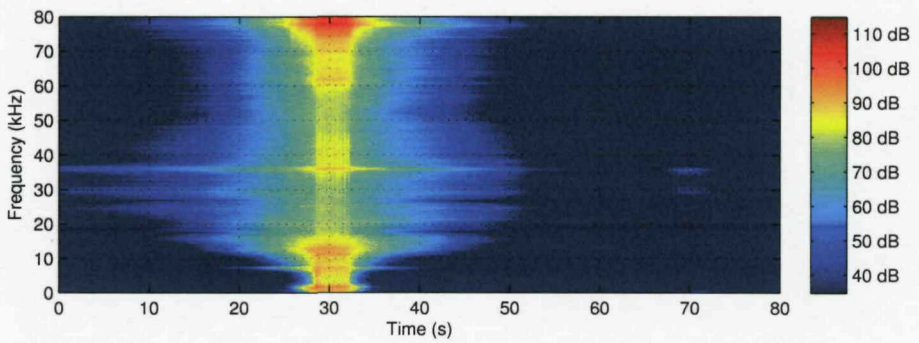

(c)

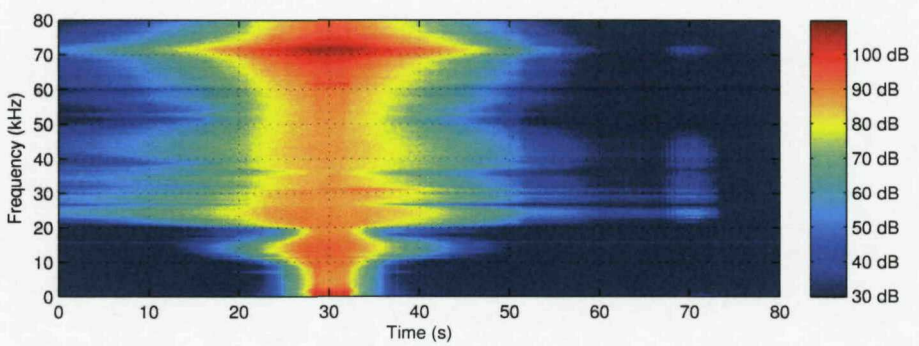

(d)

Fig. C.6. Spectrograms for train 4. (a) At the side of the rail head (ch. 1), (b) at the underside of the rail head (ch. 2), (c) at the middle of the web (ch. 3) and (d) at the underside of the rail head (ch. 4).

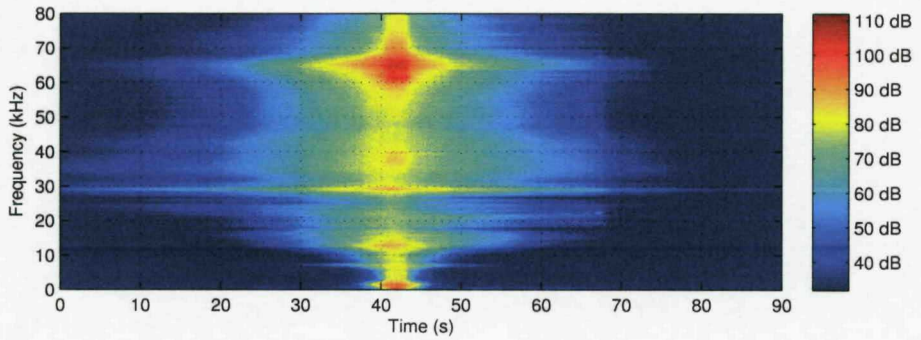

(a)

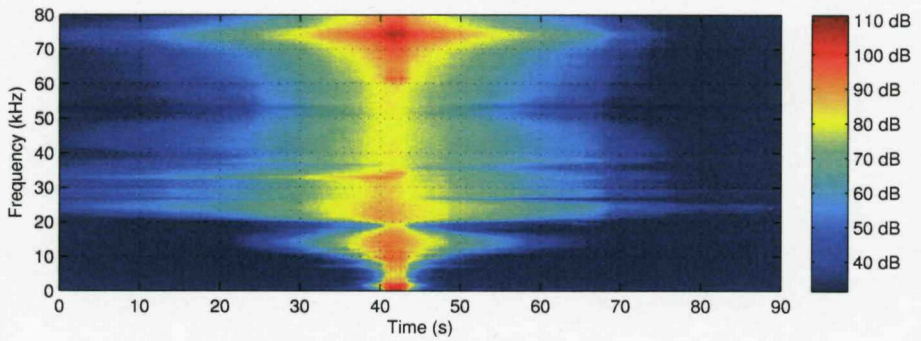

(b)

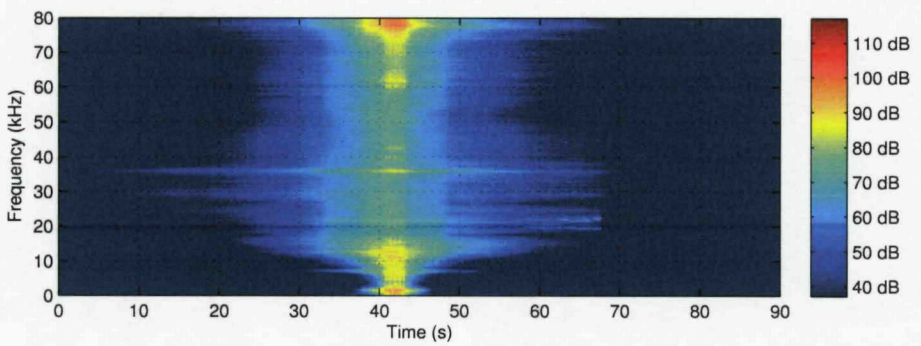

(c)

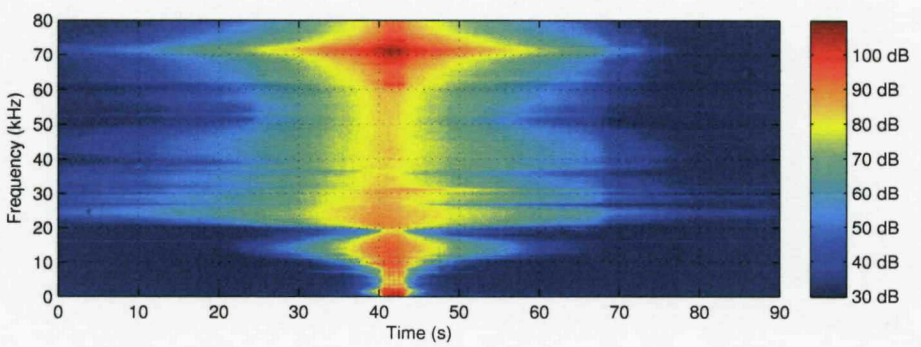

(d)

Fig. C.7. Spectrograms for train 5. (a) At the side of the rail head (ch. 1), (b) at the underside of the rail head (ch. 2), (c) at the middle of the web (ch. 3) and (d) at the underside of the rail head (ch. 4).

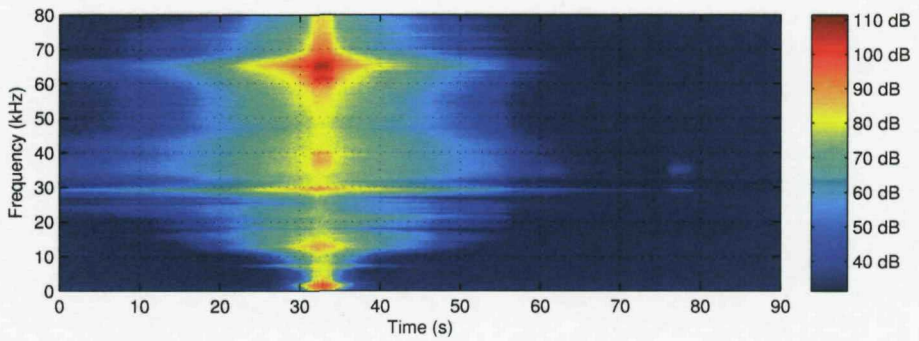

(a)

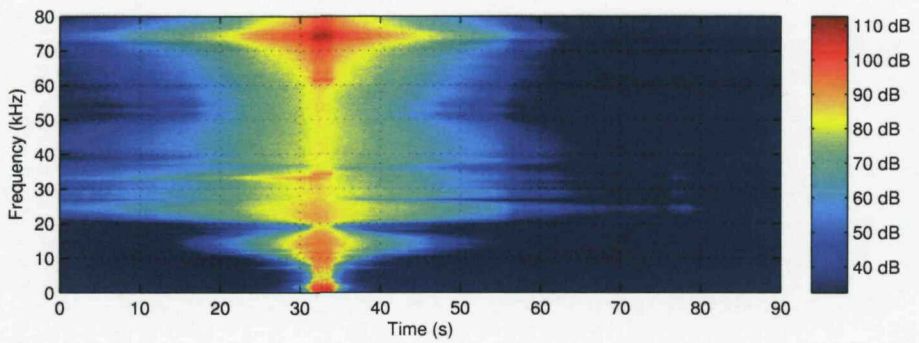

(b)

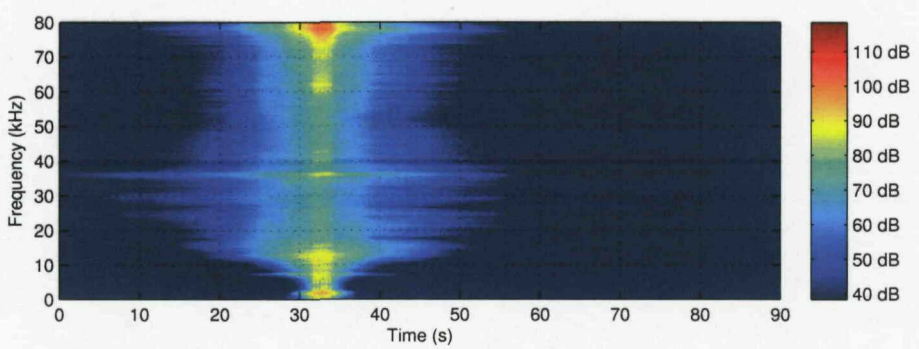

(c)

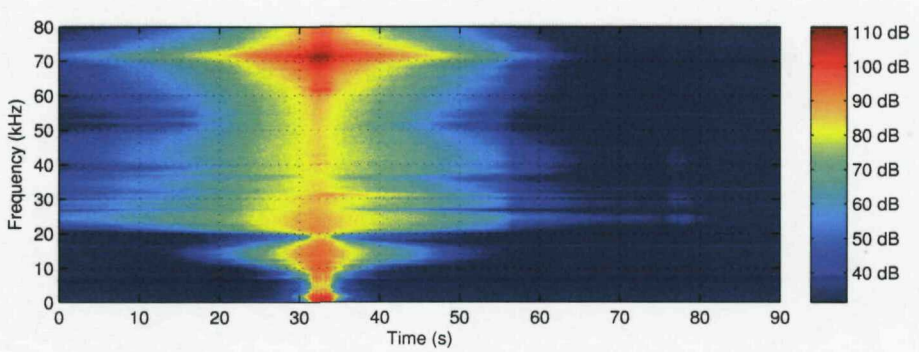

(d)

Fig. C.8. Spectrograms for train 6. (a) At the side of the rail head (ch. 1), (b) at the underside of the rail head (ch. 2), (c) at the middle of the web (ch. 3) and (d) at the underside of the rail head (ch. 4).

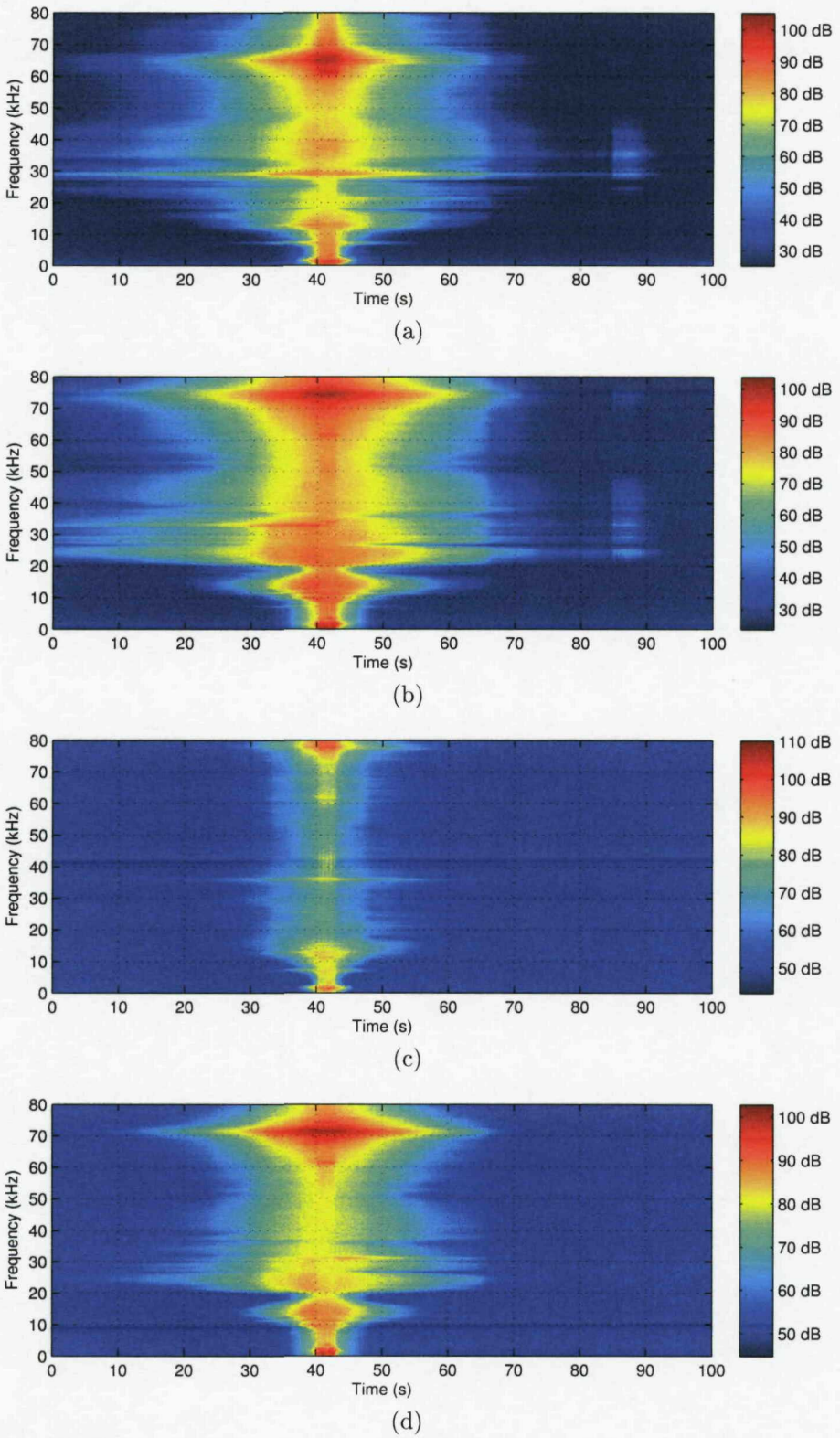

Fig. C.9. Spectrograms for train 7. (a) At the side of the rail head (ch. 1), (b) at the underside of the rail head (ch. 2), (c) at the middle of the web (ch. 3) and (d) at the underside of the rail head (ch. 4).

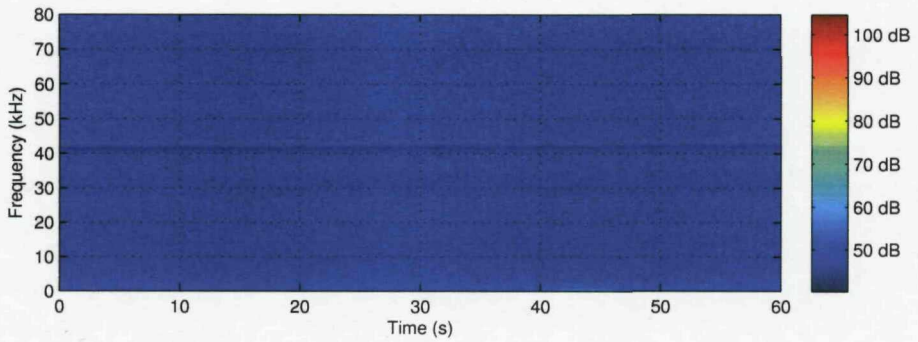

(a)

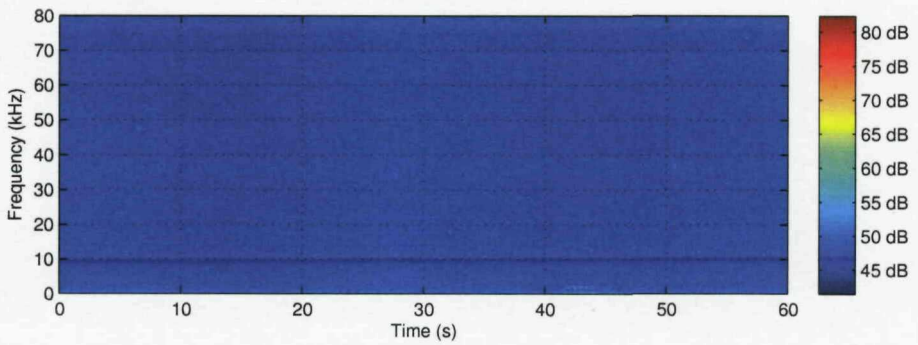

(b)

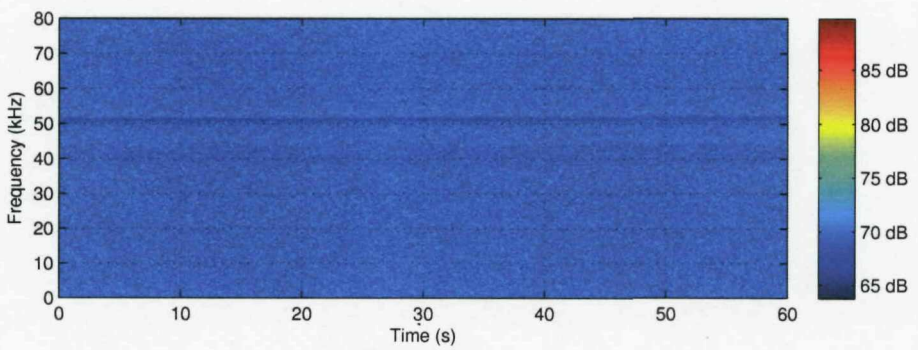

(c)

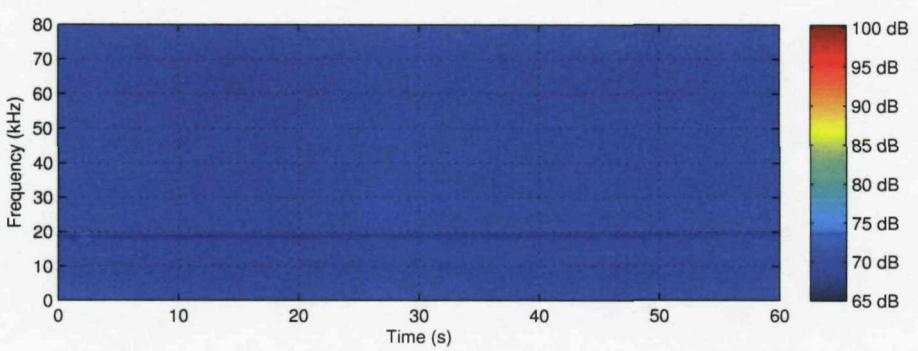

(d)

Fig. C.10. Spectrograms for ambient noise 1. (a) At the side of the rail head (ch. 1), (b) at the underside of the rail head (ch. 2), (c) at the middle of the web (ch. 3) and (d) at the underside of the rail head (ch. 4).

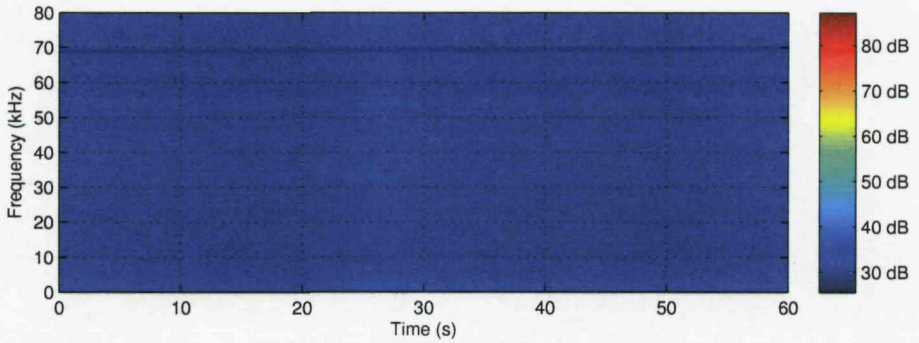

(a)

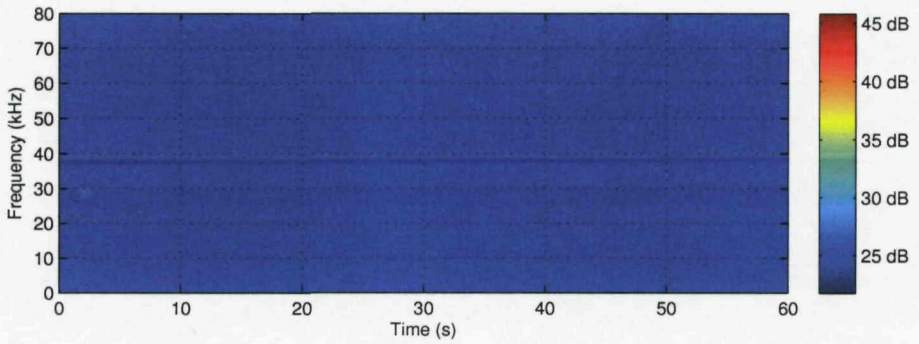

(b)

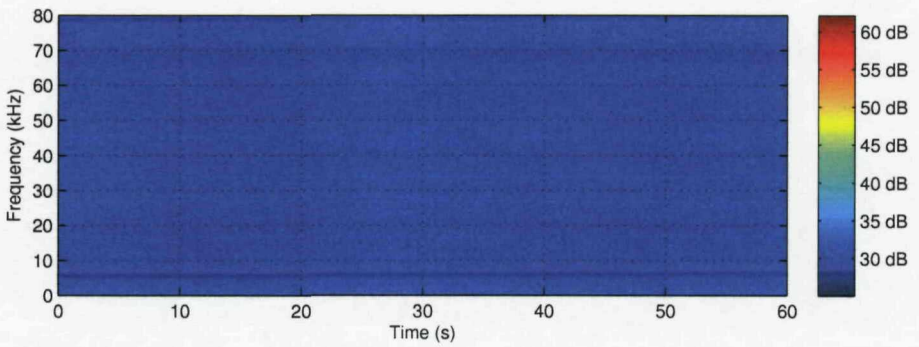

(c)

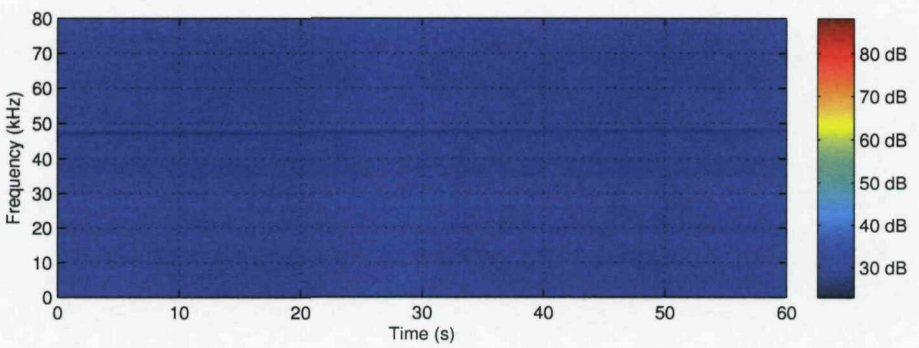

(d)

Fig. C.11. Spectrograms for ambient noise 2. (a) At the side of the rail head (ch. 1), (b) at the underside of the rail head (ch. 2), (c) at the middle of the web (ch. 3) and (d) at the underside of the rail head (ch. 4).

C.3 Acceleration Levels versus Distance

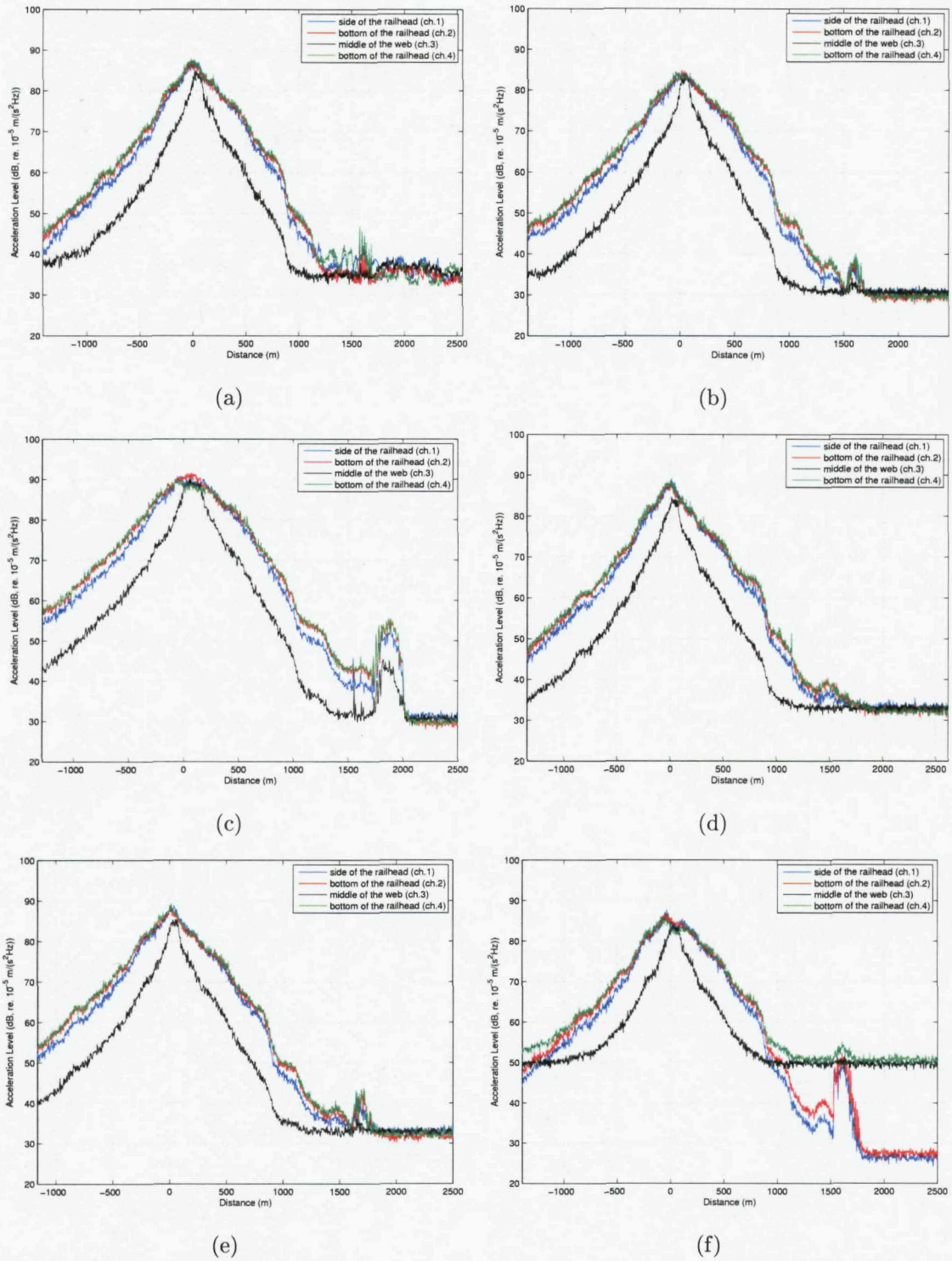

Fig. C.12. Variations of acceleration levels versus distance at each measuring point for (a) train 2, (b) train 3, (c) train 4, (d) train 5, (e) train 6 and (f) train 7. At each channel, the selected frequencies are around 29 kHz (ch.1), around 25 kHz (ch.2 and 4) and around 36 kHz (ch.3)

Appendix D

Errors Predicted from the Combined SSE/FE Model with Cracks

D.1 For a Crack Growing Down from the Top of the Rail Head

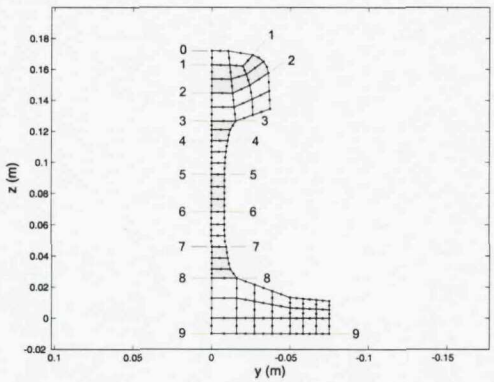

Fig. D.1. A crack model growing down from the top of the rail head.

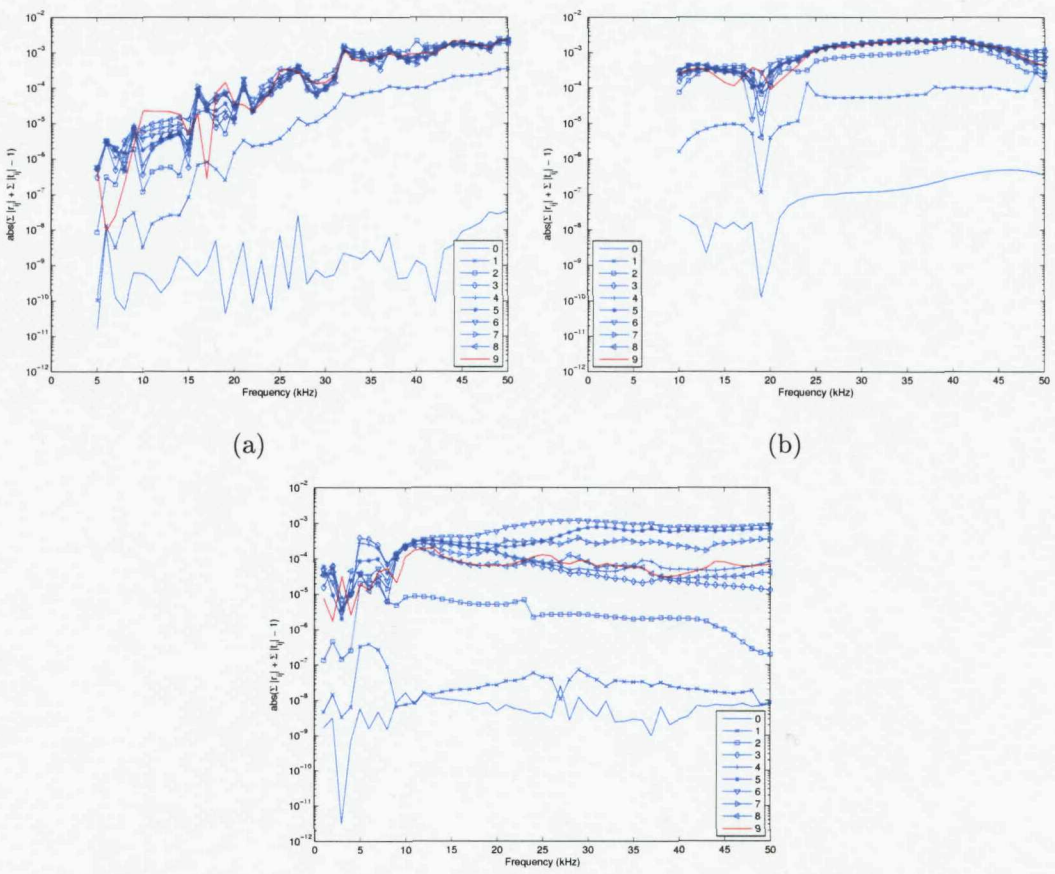

(a) (b)

(c)

Fig. D.2. Errors predicted from the connected SSE/FE rail with the crack shown in Fig. D.1 for (a) the vertical bending wave in the rail head, (b) the lateral bending wave in the rail head, (c) the 1^{st} order web bending wave.

D.2 For a Crack Growing Up from the End of the Foot

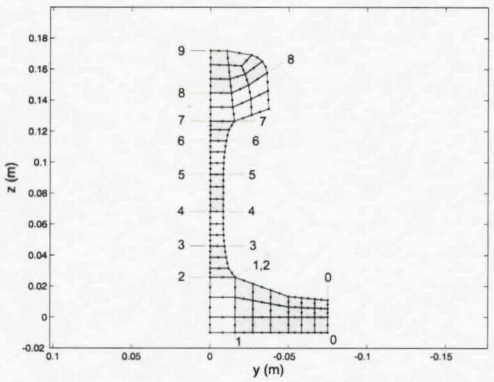

Fig. D.3. A crack model growing up from the end of the foot.

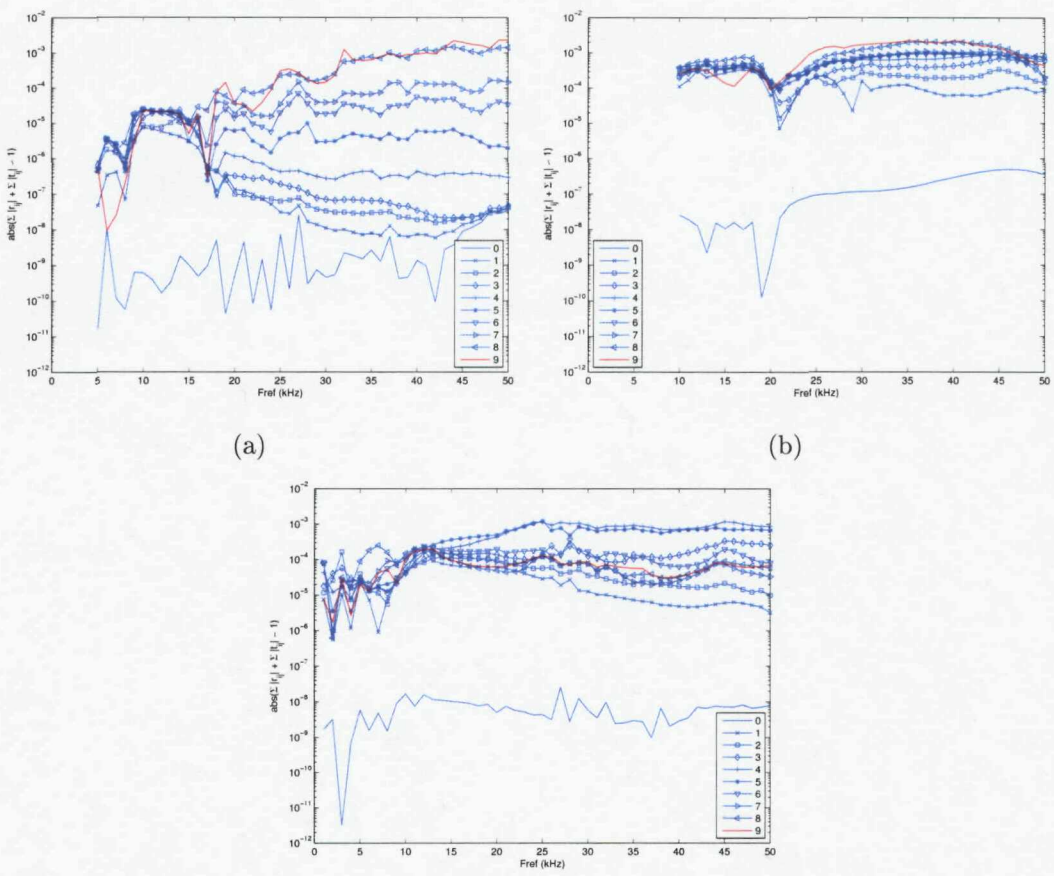

(a) (b)

(c)

Fig. D.4. Errors predicted from the connected SSE/FE rail with the crack shown in Fig. D.3 for (a) the vertical bending wave in the rail head, (b) the lateral bending wave in the rail head, (c) the 1^{st} order web bending wave.